

Some parts of this thesis may have been removed for copyright restrictions.

If you have discovered material in AURA which is unlawful e.g. breaches copyright, (either yours or that of a third party) or any other law, including but not limited to those relating to patent, trademark, confidentiality, data protection, obscenity, defamation, libel, then please read our [Takedown Policy](#) and [contact the service](#) immediately

FINITE ELEMENT ANALYSIS OF PARTICLE IMPACT PROBLEMS

CHUAN-YU WU, BSc, MSc

Doctor of Philosophy

THE UNIVERSITY OF ASTON IN BIRMINGHAM

October 2001

This copy of the thesis has been supplied on condition that anyone who consults it is understood to recognise that its copyright rests with its author and that no quotation from the thesis and no information derived from it may be published without proper acknowledgement.

FINITE ELEMENT ANALYSIS OF PARTICLE IMPACT PROBLEMS

Chuan-Yu Wu, BSc, MSc (Civil Engineering)
Doctor of Philosophy
2001

SUMMARY

Particle impacts are of fundamental importance in many areas and there has been a renewed interest in research on particle impact problems. A comprehensive investigation of the particle impact problems, using finite element (FE) methods, is presented in this thesis. The capability of FE procedures for modelling particle impacts is demonstrated by excellent agreements between FE analysis results and previous theoretical, experimental and numerical results.

For normal impacts of elastic particles, it is found that the energy loss due to stress wave propagation is negligible if it can reflect more than three times during the impact, for which Hertz theory provides a good prediction of impact behaviour provided that the contact deformation is sufficiently small. For normal impact of plastic particles, the energy loss due to stress wave propagation is also generally negligible so that the energy loss is mainly due to plastic deformation. Finite-deformation plastic impact is addressed in this thesis so that plastic impacts can be categorised into elastic-plastic impact and finite-deformation plastic impact. Criteria for the onset of finite-deformation plastic impacts are proposed in terms of impact velocity and material properties. It is found that the coefficient of restitution depends mainly upon the ratio of impact velocity to yield velocity V_{ni}/V_{y0} for elastic-plastic impacts, but it is proportional to $[(V_{ni}/V_{y0}) * (Y/E^*)]^{-1/2}$, where Y/E^* is the representative yield strain for finite-deformation plastic impacts. A theoretical model for elastic-plastic impacts is also developed and compares favourably with FEA and previous experimental results. The effect of work hardening is also investigated.

Traction distributions during the frictional contact with tangential loading are obtained for both elastic and plastic bodies. The influence of dissimilarity in material properties is discussed. For oblique impacts of elastic particles, the effects of initial velocity conditions, friction and Poisson's ratio on the impact behaviour are investigated. The major finding is that the peak tangential force first reaches its limiting value at the same critical impact angle as the tangential coefficient of restitution reaches its minimum; at this critical angle sliding occurs throughout the compression stage. For oblique impacts of plastic particles, the effects of friction and plastic deformation are explored. The effect of the change in the local contact plane orientation on the apparent impact behaviour is discussed. It is demonstrated that the change in the orientation of local contact plane significantly affects the apparent impact behaviour. This is significant to experimentalists studying high speed glancing impacts since they will invariably measure the vertical and horizontal rebound velocities. The investigation of the impact of a plastic sphere with an elastic or rigid substrate demonstrates that the tangential interaction does affect the normal response.

KEY WORDS: Contact mechanics; Impact dynamics; Finite element; Elastic-plastic; Particle technology

ACKNOWLEDGEMENTS

Among many people who have contributed to making my stay at Aston enjoyable and rewarding, I would like to thank my supervisor, Dr. Long-Yuan Li, for his encouragement, enthusiasm and support throughout the course of my research work on this project. In addition to the many scientific points I learnt from him, I am grateful for his advice, guidance and for his comments and suggestions on the preparation of this thesis.

I am especially privileged to acknowledge my research adviser and associate supervisor, Dr. Colin Thornton. He sacrificed much of his valuable time to deliberately correct all my reports and drafts throughout the project. I am grateful for his helpful discussions and comments on the direction in which I was going. Most importantly, I would like to thank him for sharing with me his extraordinary insight into contact mechanics and particle technology.

I would like to acknowledge the financial support provided partly by EPSRC/ERCOS and by the Committee of Vice-Chancellors and Principals of the universities of U.K. through the Overseas Research Studentship (ORS) awards. I also acknowledge the Methods Development Group at the Lawrence Livermore National Laboratory, USA, for providing us DYNA2D/DYNA3D codes.

To Rob Poole and Andy Crowcombe, I give my thanks for their excellent technical support. I did much of the writing-up of this thesis using the facility in Dr. Thornton's Granular Dynamics Group. I appreciate the generous support from Dr. Colin Thornton and Dr. David Kafui. I finished the final version of this thesis at my new position at Leicester University, so I would like to thank Prof. Alan Cocks for doing much to make it easier for me. I am grateful to the help and discussions from my colleague Yu Wang.

I am also indebted to my family for all their kinship, support, encouragement and understanding throughout the whole period of my study.

Finally and most importantly, My sincere appreciation attributes to my wife, Ling Zhang, who sacrificed and suffered so much throughout the course of my study yet kept cheerful, patient and supportive. I also thank her for carefully checking my draft of this thesis. It is to her that this thesis is dedicated.

Contents

1	Introduction	22
1.1	General background	22
1.2	Background of the project	23
1.3	Why finite element analysis?	24
1.4	Order of presentation	25
2	Literature Review	27
2.1	Introduction	27
2.2	Normal impact	28
2.2.1	Hertz theory of elastic contact/impact	28
2.2.2	Non-Hertzian contact/impact of elastic bodies	35
2.2.3	Contact/impact of elastic-plastic bodies	39
2.2.3.1	Yield	39
2.2.3.2	Contact pressure	40
2.2.3.3	Contact force-displacement relationship	47
2.2.3.4	Coefficient of restitution	49
2.3	Oblique impact	54
2.3.1	Rigid body dynamics	54
2.3.2	Frictional contacts with tangential loading	57
2.3.3	The elastic model of oblique impact (Maw <i>et al.</i> 1976)	61
2.3.4	Lumped parameter model (Stronge 1994)	64
2.3.5	Other previous works on oblique impacts	67
2.4	Summary	69
3	Finite Element Analysis Models	71
3.1	Introduction	71
3.2	Finite element models for normal impacts	71
3.2.1	FE models for normal impacts of a sphere with a rigid wall	72
3.2.2	FE models for normal impacts of a sphere with a half-space	74
3.3	FE models for friction contacts under tangential loading	77
3.4	FE models for oblique impacts of a sphere with a half-space	80
3.5	Summary	84
4	Normal Impact of Elastic Particles	85

4.1	Introduction	85
4.2	Normal impact of elastic spheres at a rigid boundary	86
4.2.1	Pressure distribution	86
4.2.2	Stress distribution	89
4.2.3	Evolution of impact parameters	90
4.2.4	Force-displacement relationship	94
4.2.5	Coefficient of restitution	97
4.3	Normal impact of elastic sphere at an elastic boundary	99
4.3.1	Pressure distribution	99
4.3.2	Stress distribution	100
4.3.3	Evolution of impact parameters	101
4.3.4	Force-displacement relationship	103
4.4	Summary	104
5	Normal Impact of Particles Involving Plastic Deformation	106
5.1	Introduction	106
5.2	Typical impact behaviour of an elastic sphere with an elastic- perfectly plastic half-space	107
5.2.1	Pressure distribution	108
5.2.2	Evolution of the stress and strain distribution	112
5.2.3	Evolution of impact parameters	115
5.2.4	Force-displacement relationship	117
5.2.5	Energy dissipation and coefficients of restitution	118
5.3	Parametric dependence of the rebound behaviour	120
5.3.1	Impact cases considered	121
5.3.2	The parametric dependence of the coefficient of restitution	121
5.4	Mathematical modelling of the impact of elastic-perfectly plastic particles---LWT model (Li <i>et. al.</i> 2001)	131
5.5	The influence of work hardening	139
5.5.1	Pressure distribution	139
5.5.2	Evolution of kinetic energy	140
5.5.3	Evolution of contact force.....	141
5.5.4	Contact force-displacement relationship	142
5.5.5	Coefficient of restitution	143
5.6	Summary	144
6	Frictional Contacts under Tangential Loading	146

6.1	Introduction	146
6.2	Elastic contact	146
6.2.1	Normal contact pressure distribution.....	147
6.2.2	Tangential traction distribution	149
6.3	Plastic contact	152
6.3.1	Normal contact pressure distribution.....	153
6.3.2	Tangential traction distribution	155
6.4	Summary	158
7	Oblique Impact of Elastic Particles	159
7.1	Introduction	159
7.2	Theoretical aspects	159
7.2.1	The classical rigid body dynamics.....	162
7.2.2	Model of elastic bodies	163
7.3	Typical time evolutions of the impact parameters	165
7.4	Typical features of the interaction during oblique impact of elastic particles.....	168
7.5	The peak tangential force	171
7.5.1	The influence of initial velocity conditions	171
7.5.2	The influence of friction	173
7.5.3	The influence of Poisson's ratio.....	174
7.6	Impulse ratio	176
7.6.1	The influence of initial velocity conditions	177
7.6.2	The influence of friction	177
7.6.3	The influence of Poisson's ratio.....	178
7.7	Coefficient of restitution and kinetic energy loss.....	179
7.7.1	The influence of initial velocity conditions	180
7.7.2	The influence of friction	187
7.7.3	The influence of Poisson's ratio.....	187
7.8	Reflection angle of the contact patch.....	189
7.8.1	The influence of initial velocity conditions	189
7.8.2	The influence of friction	190
7.8.3	The influence of Poisson's ratio.....	190
7.9	Rebound angular rotational velocity	191
7.9.1	The influence of initial velocity conditions	192
7.9.2	The influence of friction	193

7.9.3	The influence of Poisson's ratio	194
7.10	Summary	194
8	Oblique Impact of Plastic Particles	196
8.1	Introduction	196
8.2	Contact deformation	196
8.3	Yield and residual plastic strain distribution.....	199
8.3.1	Yield	199
8.3.2	Residual plastic strain distribution.....	201
8.4	Typical interaction behaviour.....	207
8.4.1	Time evolution of normal contact force	207
8.4.2	Normal force-displacement relationships	211
8.4.3	Tangential force evolution	214
8.4.4	Normal-tangential force relationship.....	216
8.5	Maximum tangential force	219
8.5.1	Impacts involving plastic deformation in the sphere	219
8.5.2	Impacts involving plastic deformation in the substrate	222
8.6	Impulse ratio	224
8.6.1	Impacts involving plastic deformation in the sphere	224
8.6.2	Impacts involving plastic deformation in the substrate	225
8.7	Kinetic energy loss and coefficient of restitution.....	227
8.7.1	Impacts involving plastic deformation in the sphere	228
8.7.2	Impacts involving plastic deformation in the substrate	231
8.8	Reflection angle of the contact patch.....	237
8.8.1	Impacts involving plastic deformation in the sphere	237
8.8.2	Impacts involving plastic deformation in the substrate	238
8.9	Rebound angular velocity	239
8.9.1	Impacts involving plastic deformation in the sphere	239
8.9.2	Impacts involving plastic deformation in the substrate	241
8.10	summary	242
9	Conclusions	244
9.1	Normal impacts of particles	244
9.2	Oblique impacts of particles	245
9.3	Limitations and future work	246
	References	248

Appendix A	Finite Element Methods for Contact/Impact Problems	256
A.1	Introduction	256
A.2	General formulations for contact/impact problems	256
A.3	Time integration methods	260
A.3.1	The central difference method	260
A.3.2	The Newmark method.....	261
A.4	Contact modelling techniques in finite element methods	262
A.4.1	Finite element discretization of contact interfaces	263
A.4.2	Contact searching procedure	267
A.4.3	Contact constraint method	271
A.4.3.1	Kinematic constraint method	272
A.4.3.2	Penalty method	273
A.4.4	Calculations of the contact traction	274
A.5	Introduction of DYNA2D/DYNA3D	277
A.6	Summary	279
Appendix B	Significance of the Substrate Size in FE Simulations of the Normal Impact of a Sphere with a Half-Space	280
B.1	Introduction	280
B.2	Finite element models	281
B.3	The influence of substrate size	282
B.4	The influence of stress waves.....	288
B.5	Summary	291
Appendix C	Significance of the Substrate Size in FE Simulations of the Oblique Impact of a Sphere with a Half-Space	293
Appendix D	The Influence of Rigidity on Oblique Impact Behaviour of a Sphere with an Elastic Substrate	297

List of Figures

Figure 2.1	Stress-strain curves for (a) elastic, (b) elastic-perfectly plastic, and (c) elastic-plastic with work hardening solids.....	28
Figure 2.2	Plastic deformation process during the compression of a spherical indenter into a plastic solid: (a) the onset of plastic deformation which is underneath the surface; (b) the plastic zone is expanded to the contact surface and fully plastic deformation occurs.....	41
Figure 2.3	The contact of elastic-plastic solid: (a) the expanding cavity model; (b) the variation of p_m/Y with E^*a/YR^* (Johnson 1985).....	43
Figure 2.4	The pressure distribution for the indentation of an elastic-plastic half-space by a rigid sphere.....	45
Figure 2.5	(a) Force-time curves for the impact of two 1-in-diameter crossed lead cylinders (Goldsmith 1960) and (b) force-displacement relationship for the impacts of harder steel by a hard steel sphere (Goldsmith and Lyman 1960).....	49
Figure 2.6	Tangential traction distribution (Mindlin 1949).....	58
Figure 2.7	Influence of a difference in elastic constants on the normal pressure and tangential traction distribution during (a) sliding contact with $\mu = 1.0$ (Johnson 1985); (b) tangential loading of elastic cylinder with $\beta = 0.4$ and $\mu = 0.5$ (Hills <i>et al.</i> 1993).....	59
Figure 2.8	Tangential traction distribution during the rolling contact (From Johnson 1985, p265): solid line-numerical theory (Kalker 1967a); circle-photo-elastic measurements (Haines and Ollerton 1963).....	60
Figure 2.9	Tangential traction distribution proposed by Poritsky (1950).....	60
Figure 2.10	Tangential force evolution during the impact of homogeneous solid spheres (Maw <i>et al.</i> 1976, 1981).....	64
Figure 2.11	The reflection angle of the contact patch for the oblique of homogeneous solid spheres (Maw <i>et al.</i> 1976, 1981).....	64
Figure 2.12	The reflection angle of the contact patch for different values of normal coefficient of restitution (Stronge 1994, 2000).....	67
Figure 3.1	Illustration of the normal impact of a sphere with a target wall.....	72
Figure 3.2	The analysis model for the normal impact of a sphere with a rigid wall.....	72
Figure 3.3	Finite element meshes for the sphere that collides with a rigid wall.....	73
Figure 3.4	The analysis model for the impact of a sphere with a half-space.....	75
Figure 3.5	(a) Finite element model for the impact of a sphere with a half-space; (b) Magnified view of contact region.....	76
Figure 3.6	The analysis model for frictional contacts under tangential loading.....	78
Figure 3.7	FE model for frictional contacts under tangential loading.....	79
Figure 3.8	The load curves.....	80
Figure 3.9	Diagram of the oblique impact of a sphere with a plane surface.....	81

Figure 3.10	FE model for the oblique impact of a sphere with a half-space.....	81
Figure 3.11	The approaches to specify the impact angles.....	82
Figure 4.1	The pressure distribution over the contact area at the maximum compression ($t = 11.2ns$) during the impact of an elastic sphere with a rigid wall at $V_{ni} = 50m/s$ using: a) Model I; b) Model II.....	87
Figure 4.2	The pressure distribution over the contact area during the impact of an elastic sphere with a rigid wall.....	88
Figure 4.3	The variation of the maximum contact pressure p_0 with the contact radius a for the impact of an elastic sphere with a rigid wall using Model I.....	89
Figure 4.4	The stress distributions of the sphere at the maximum compression ($t = 11.2ns$) with $V_{ni} = 50m/s$ using Model I.....	89
Figure 4.5	Time histories of nodal displacements during the impact of an elastic sphere with a rigid wall using Model I at: a) $V_{ni} = 2.0m/s$; b) $V_{ni} = 50m/s$	91
Figure 4.6	Time histories of nodal velocities during the impact of an elastic sphere with a rigid wall using Model I at: a) $V_{ni} = 2.0m/s$; b) $V_{ni} = 50m/s$	91
Figure 4.7	Time histories of kinetic energy during the impact of an elastic sphere with a rigid wall using Model I and II at: a) $V_{ni} = 2.0m/s$; b) $V_{ni} = 50m/s$	92
Figure 4.8	Time histories of contact force during the impact of an elastic sphere with a rigid wall using Model I and II at: a) $V_{ni} = 2.0m/s$; b) $V_{ni} = 50m/s$	93
Figure 4.9	Contact force-displacement relationships for the impact of an elastic sphere with a rigid wall using Model I and II at: a) $V_{ni} = 2.0m/s$; b) $V_{ni} = 50m/s$	94
Figure 4.10	Illustration of the contact deformation at high velocities.....	95
Figure 4.11	The variation of the contact force F_n with the contact radius a	96
Figure 4.12	The variation of a^2 with the displacement α	96
Figure 4.13	The pressure distributions at various instants during the impact of an elastic sphere with an elastic half-space at $V_{ni} = 5.0m/s$	100
Figure 4.14	The variation of the maximum contact pressure p_0 with the contact radius a during the impact of an elastic sphere with an elastic half-space at $V_{ni} = 5.0m/s$	100
Figure 4.15	Stress distributions inside the sphere and the half-space at the maximum compression ($t = 2.5ns$) during the impact at $V_{ni} = 5.0m/s$	101
Figure 4.16	Time histories of (a) nodal displacements and (b) velocities during the impact of an elastic sphere with an elastic half-space at	

	$V_{ni} = 5.0m/s$	102
Figure 4.17	Time histories of (a) kinetic energy and (b) impact force during the impact of an elastic sphere with an elastic half-space at $V_{ni} = 5.0m/s$	102
Figure 4.18	The force-displacement relationship for the impact of an elastic sphere with an elastic half-space at $V_{ni} = 5.0m/s$	103
Figure 4.19	(a) The variation of F_n with a ; (b) the variation of a^2 with α for the impact of an elastic sphere with an elastic half-space at $V_{ni} = 5.0m/s$	104
Figure 5.1	The typical evolution of contact pressure distributions for the impact of an elastic sphere against an elastic-perfectly plastic half-space with $V_{ni} = 30m/s$ at various instants: (a) during the compression; (b) the restitution.....	108
Figure 5.2	The contact pressure distribution at the maximum compression ($t = 21ns$) during the impact of an elastic sphere with an elastic-perfectly plastic half-space at $V_{ni} = 30m/s$	110
Figure 5.3	The topography of the contact deformation at the maximum compression ($t = 21ns$) during the impact of an elastic sphere with an elastic-perfectly plastic substrate at $V_{ni} = 30m/s$	110
Figure 5.4	Topographies of the contact deformation at the maximum compression during the impact of an elastic sphere with a elastic-perfectly plastic half-space at (a) $V_{ni} = 40m/s$; (b) $V_{ni} = 60m/s$ and (c) $V_{ni} = 80m/s$	111
Figure 5.5	The influence of piling-up upon the contact pressure distribution during the impact of an elastic sphere with an elastic-perfectly plastic half-space.....	112
Figure 5.6	The distributions of effective stress within the substrate at various instants during the compression of the impact of an elastic sphere with an elastic-perfectly plastic substrate at $V_{ni} = 30m/s$	113
Figure 5.7	The distributions of effective stress within the substrate at various instants during the restitution of the impact of an elastic sphere with an elastic-perfectly plastic substrate at $V_{ni} = 30m/s$	114
Figure 5.8	The evolution of effective plastic strain within the substrate at various instants during the restitution of the impact of an elastic sphere with an elastic-perfectly plastic substrate at $V_{ni} = 30m/s$	114
Figure 5.9	Time histories of (a) nodal displacement and (b) nodal velocity for the impact of an elastic sphere with an elastic-perfectly plastic substrate at $V_{ni} = 30m/s$	115
Figure 5.10	Time histories of normalised kinetic energy during the impact of an elastic sphere with an elastic-perfectly plastic substrate at various impact velocities.....	116
Figure 5.11	Time histories of contact force during the impact of an elastic	

	sphere with an elastic-perfectly plastic substrate at various impact velocities.....	117
Figure 5.12	Contact force-displacement relationships for the impact of an elastic sphere with an elastic-perfectly plastic substrate at various impact velocities.....	118
Figure 5.13	Coefficient of restitution for the impact of an elastic sphere with an elastic-perfectly plastic half-space.....	119
Figure 5.14	Coefficient of restitution as a function of impact velocity V_{ni} for all impact cases considered.....	123
Figure 5.15	Coefficient of restitution as a function of the normalised impact velocity V_{ni}/V_{y0} for all impact cases considered.....	124
Figure 5.16	$e_n(E^*/Y)^{1/2}$ versus $(V_{ni}/V_{y0})/(E^*/Y)^2$ for all impact cases considered.....	127
Figure 5.17	Coefficient of restitution as a function of V_{ni}/V_{y0} for all impacts at velocities less than the critical velocity \bar{V}_{ni} for the onset of finite-deformation plastic impact.....	129
Figure 5.18	Coefficient of restitution as a function of $(V_{ni}/V_{y0})/(E^*/Y)$ within finite-deformation range for all impact cases considered.....	129
Figure 5.19	The dimensionless cut-off pressure as a function of the dimensionless contact radius.....	132
Figure 5.20	Variation of the radius of curvature with the contact radius and displacement.....	135
Figure 5.21	Force-displacement relationships for the impact of elastic-perfectly plastic particles.....	138
Figure 5.22	Variation of coefficient of restitution with normalised impact velocity.....	139
Figure 5.23	The typical evolution of contact pressure distributions for the impact of an elastic sphere with an elastic-plastic work hardening half-space at $V_{ni} = 10m/s$: (a) during compression; (b) during restitution.....	140
Figure 5.24	Time evolution of the normalised kinetic energy for impacts of an elastic sphere with an elastic-plastic half-space with and without work hardening at various impact velocities.....	141
Figure 5.25	Time evolution of the contact force for impacts of an elastic sphere with an elastic-plastic half-space with and without work hardening at various impact velocities.....	142
Figure 5.26	Force-displacement relationships for impacts of an elastic sphere with an elastic-plastic half-space with and without work hardening at various impact velocities.....	142
Figure 5.27	Coefficient of restitution for the impact of an elastic sphere with an elastic-plastic half-space with and without work hardening.....	143
Figure 6.1	The evolution of contact forces during the frictional contact of a	

	rigid indenter with an elastic substrate.....	147
Figure 6.2	Normal contact pressure distributions at various instants for the frictional contact of a rigid indenter with an elastic substrate.....	148
Figure 6.3	Influence of tangential traction on the normal pressure distribution in the symmetry plane.....	149
Figure 6.4	Tangential traction distributions at various instants for the frictional contact of a rigid indenter with an elastic substrate.....	150
Figure 6.5	Tangential traction distributions within the symmetry plane (y-z plane) at various instants for the contact of a rigid indenter with an elastic substrate.....	151
Figure 6.6	The distributions of the normal pressure and tangential traction in the symmetry plane (y-z plane) at various instants.....	152
Figure 6.7	The evolution of contact forces during the frictional contact of a rigid indenter and an elastic-perfectly plastic substrate.....	153
Figure 6.8	Normal contact pressure distributions at various instants for the frictional contact of a rigid indenter with an elastic-perfectly plastic substrate.....	154
Figure 6.9	Influence of tangential traction on the normal pressure distribution in the symmetry plane.....	155
Figure 6.10	Tangential traction distributions at various instants for the frictional contact of a rigid indenter with an elastic-perfectly plastic substrate.....	156
Figure 6.11	The distributions of the normal pressure and tangential traction in the symmetry plane (y-z plane) at various instants.....	157
Figure 7.1	Typical time evolutions of the impact parameters during the impact of a rigid sphere against an elastic substrate with $V_{ni} = 5.0m/s$ at $\theta = 45^\circ$	165
Figure 7.2	The typical evolutions of the relative displacement between nodes C and D for the impacts of a rigid sphere against an elastic substrate at different angles with a fixed initial normal velocity $V_{ni} = 5.0m/s$	168
Figure 7.3	The time evolutions of the normal contact force for the impacts of a rigid sphere against an elastic substrate at various impact angles with a fixed initial normal velocity $V_{ni} = 5.0m/s$	169
Figure 7.4	Normal force-displacement relationships for the impacts of a rigid sphere against an elastic substrate at various angles with a fixed initial normal velocity $V_{ni} = 5.0m/s$	169
Figure 7.5	The typical time histories of the tangential force for impacts of a rigid sphere with an elastic substrate at various impact angles with a fixed initial normal velocity $V_{ni} = 5.0m/s$	170
Figure 7.6	The variation of tangential force with normal force for impacts of a rigid sphere with an elastic substrate at various impact angles with a fixed initial normal velocity $V_{ni} = 5.0m/s$	170

Figure 7.7	The typical tangential force-displacement relationships for impacts of a rigid sphere with an elastic substrate at various impact angles with a fixed initial normal velocity $V_{ni} = 5.0m/s$	171
Figure 7.8	The variation of the peak tangential force $F_{t,max}$ with impact angle θ for various impact cases.....	172
Figure 7.9	The variation of $F_{t,max} / \mu F_{n,max}$ with impact angle θ for various impact cases.....	172
Figure 7.10	The variation of $F_{t,max} / \mu F_{n,max}$ with the impact angle for impacts with different coefficients of friction.....	174
Figure 7.11	The variation of $F_{t,max} / \mu F_{n,max}$ with $\tan \theta / \mu$ for impacts with different coefficients of friction.....	174
Figure 7.12	The variation of $F_{t,max} / \mu F_{n,max}$ with $\tan \theta / \mu$ for the impacts with different Poisson's ratios.....	175
Figure 7.13	The variation of $F_{t,max} / \mu F_{n,max}$ with $\kappa \tan \theta / \mu(7\kappa - 3)$ for the impacts with different Poisson's ratios.....	175
Figure 7.14	The variation of impulse ratio f with impact angle θ for impacts with different initial velocity conditions.....	177
Figure 7.15	The variation of f / μ with normalised impact angle $\tan \theta / \mu$ for impacts with different friction coefficients.....	178
Figure 7.16	The variation of f / μ with normalised impact angle $\tan \theta / \mu$ for impacts with different Poisson's ratios.....	178
Figure 7.17	The variation of f / μ with $\kappa \tan \theta / \mu(7\kappa - 1)$ for impacts with different Poisson's ratios.....	178
Figure 7.18	The change in normalised kinetic energies at various impact angles for impacts with different initial velocity conditions.....	180
Figure 7.19	Transformation of kinetic energy during the oblique impact of elastic particles.....	182
Figure 7.20	Transformation of initial linear kinetic energy in the tangential direction at various impact angles during the impact of a rigid sphere against an elastic substrate with a fixed initial normal velocity of $V_{ni} = 5.0m/s$	183
Figure 7.21	Transformation of initial linear kinetic energy in the tangential direction at various impact angles during the impact of a rigid sphere against an elastic substrate with a fixed initial speed of $V_i = 5.0m/s$	183
Figure 7.22	The change in tangential kinetic energies at various impact angle for the impacts with different initial velocity conditions.....	185
Figure 7.23	The coefficients of restitution at various impact angle for the impacts with different initial velocity conditions.....	186
Figure 7.24	The coefficients of restitution at various impact angles for impacts with different friction coefficients.....	187
Figure 7.25	The variation of tangential coefficients of restitution with	

	normalised impact angle $\tan \theta / \mu$ for impacts with different friction coefficients.....	187
Figure 7.26	The coefficients of restitution at various impact angles for impacts with different Poisson's ratios.....	188
Figure 7.27	The variation of the tangential coefficients of restitution with $\kappa \tan \theta / \mu(7\kappa - 3)$ for impacts with different friction coefficients.....	188
Figure 7.28	The variation of normalised reflection angle of the contact patch $v_{ir} / \mu V_{ni}$ with normalised impact angle $V_{ii} / \mu V_{ni}$ for impacts with different initial velocity conditions.....	189
Figure 7.29	The variation of normalised reflection angle of the contact patch $v_{ir} / \mu V_{ni}$ with normalised impact angle $V_{ii} / \mu V_{ni}$ for impacts with different friction coefficients.....	190
Figure 7.30	The variation of the normalised reflection angle of the contact patch $v_{ir} / \mu V_{ni}$ with normalised impact angle $V_{ii} / \mu V_{ni}$ for impacts with different Poisson's ratios.....	191
Figure 7.31	The variation of the dimensionless reflection angle of the contact patch $\kappa v_{ir} / \mu V_{ni}$ with dimensionless impact angle $\kappa V_{ii} / \mu V_{ni}$ for impacts with different Poisson's ratios.....	191
Figure 7.32	The rebound angular rotational velocity at various impact angles for impacts with different initial velocity conditions.....	192
Figure 7.33	The normalised rebound angular rotational velocity versus the normalised impact angle for impacts with different initial velocity conditions.....	192
Figure 7.34	The rebound angular rotational velocity at various impact angles for impacts with different friction coefficients.....	193
Figure 7.35	The normalised rebound angular rotational velocity versus the normalised impact angle for impacts with different friction coefficients.....	193
Figure 7.36	The rebound angular rotational velocity at various impact angles for impacts with different Poisson's ratios.....	194
Figure 7.37	The normalised rebound angular rotational velocity versus the normalised impact angle for impacts with different Poisson's ratios.....	194
Figure 8.1	Profiles of the contact deformation over the interface for PR impact at $\theta = 85^\circ$ with $V_{ni} = 5.0m/s$ and $\mu = 0.3$	197
Figure 8.2	Profiles of the contact deformation over the interface for PE impact at $\theta = 85^\circ$ with $V_{ni} = 5.0m/s$ and $\mu = 0.3$	197
Figure 8.3	Profiles of the contact deformation over the interface for RP impact at $\theta = 85^\circ$ with $V_{ni} = 5.0m/s$ and $\mu = 0.3$	198
Figure 8.4	Profiles of the contact deformation over the interface for RP impact at $\theta = 85^\circ$ with $V_{ni} = 5.0m/s$ and $\mu = 0.0$	198
Figure 8.5	Profiles of the contact deformation over the interface for EP impact at $\theta = 85^\circ$ with $V_{ni} = 5.0m/s$ and $\mu = 0.3$	199

Figure 8.6	The evolution of von Mises stress distribution during the impact of an elastic sphere with a plastic substrate at $\theta = 0^\circ$ with $V_{ni} = 5.0m/s$	200
Figure 8.7	The evolution of von Mises stress distribution during the impact of an elastic sphere with a plastic substrate at $\theta = 85^\circ$ with $V_{ni} = 5.0m/s$	201
Figure 8.8	Residual effective plastic strain distribution for PR impacts with $V_{ni} = 5.0m/s$ and $\mu = 0.3$	203
Figure 8.9	Residual effective plastic strain distribution for PE impacts with $V_{ni} = 5.0m/s$ and $\mu = 0.3$	204
Figure 8.10	Residual effective plastic strain distribution for RP impacts with $V_{ni} = 5.0m/s$ and $\mu = 0.3$	205
Figure 8.11	Residual effective plastic strain distribution for EP impacts with $V_{ni} = 5.0m/s$ and $\mu = 0.3$	206
Figure 8.12	The time histories of the normal contact force at various impact angles for PR impacts with $V_{ni} = 5.0m/s$ and $\mu = 0.3$	208
Figure 8.13	The time histories of the normal contact force at various impact angles for PE impacts with $V_{ni} = 5.0m/s$ and $\mu = 0.3$	208
Figure 8.14	The time histories of apparent normal contact force at various impact angles for RP impacts with $V_{ni} = 5.0m/s$ and $\mu = 0.3$	209
Figure 8.15	The time histories of apparent normal contact force at various impact angles for EP impacts with $V_{ni} = 5.0m/s$ and $\mu = 0.3$	209
Figure 8.16	The time histories of apparent normal contact force at various impact angles for frictionless RP impacts with $V_{ni} = 5.0m/s$	210
Figure 8.17	The effect of indentation and prow.....	210
Figure 8.18	The normal force-displacement relationships for PR impacts at various impact angles with $V_{ni} = 5.0m/s$ and $\mu = 0.3$	212
Figure 8.19	The normal force-displacement relationships for PE impacts at various impact angles with $V_{ni} = 5.0m/s$ and $\mu = 0.3$	212
Figure 8.20	The normal force-displacement relationships for RP impacts at various impact angles with $V_{ni} = 5.0m/s$ and $\mu = 0.3$	213
Figure 8.21	The normal force-displacement relationships for EP impacts at various impact angles with $V_{ni} = 5.0m/s$ and $\mu = 0.3$	213
Figure 8.22	The normal force-displacement relationships for frictionless RP impacts at various impact angles with $V_{ni} = 5.0m/s$	214
Figure 8.23	The time evolutions of tangential force for PR impacts at various impact angles with $V_{ni} = 5.0m/s$ and $\mu = 0.3$	215
Figure 8.24	The time evolutions of tangential force for PE impacts at various impact angles with $V_{ni} = 5.0m/s$ and $\mu = 0.3$	215

Figure 8.25	The time evolutions of tangential force for RP impacts at various impact angles with $V_{ni} = 5.0m/s$ and $\mu = 0.3$	216
Figure 8.26	The time evolutions of tangential force for EP impacts at various impact angles with $V_{ni} = 5.0m/s$ and $\mu = 0.3$	216
Figure 8.27	The normal-tangential force relationships for PR impacts at various impact angles with $V_{ni} = 5.0m/s$ and $\mu = 0.3$	217
Figure 8.28	The normal-tangential force relationships for PE impacts at various impact angles with $V_{ni} = 5.0m/s$ and $\mu = 0.3$	217
Figure 8.29	The normal-tangential force relationships for RP impacts at various impact angles with $V_{ni} = 5.0m/s$ and $\mu = 0.3$	218
Figure 8.30	The normal-tangential force relationships for EP impacts at various impact angles with $V_{ni} = 5.0m/s$ and $\mu = 0.3$	218
Figure 8.31	The variation of peak tangential force with impact angle for impacts involving plastic deformation in the sphere with $\mu = 0.3$	220
Figure 8.32	The variation of $F_{t,max} / \mu F_{n,max}$ with impact angle for impacts involving plastic deformation in the sphere with $\mu = 0.3$	221
Figure 8.33	The variation of peak tangential force with impact angle for impacts involving plastic deformation in the substrate with $\mu = 0.3$	222
Figure 8.34	The variation of $F_{t,max} / \mu F_{n,max}$ with impact angle for impacts involving plastic deformation in the substrate with $\mu = 0.3$	223
Figure 8.35	The variation of $F_{t,max} / F_{n,max}$ with impact angle for the frictional ($\mu = 0.3$) and frictionless RP impacts with constant normal velocity $V_{ni} = 5.0m/s$	223
Figure 8.36	The variation of f / μ with impact angle for impacts involving plastic deformation in the sphere with $\mu = 0.3$	225
Figure 8.37	The variation of f / μ with impact angle for impacts involving plastic deformation in the substrate with $\mu = 0.3$	226
Figure 8.38	The variation of impulse ratio f with impact angle for the frictional ($\mu = 0.3$) and frictionless RP impacts with constant normal velocity $V_{ni} = 5.0m/s$	227
Figure 8.39	Transformation of kinetic energy during the oblique impact of plastic particles.....	228
Figure 8.40	The variation of normal coefficient of restitution with impact angle for impacts involving plastic deformation in the sphere with $\mu = 0.3$	229
Figure 8.41	The variation of tangential coefficient of restitution with impact angle for impacts involving plastic deformation in the sphere with $\mu = 0.3$	230
Figure 8.42	The variation of the normal coefficient of restitution with impact	

	angle for impacts involving plastic deformation in the substrate with $\mu = 0.3$	231
Figure 8.43	The effect of the change in orientation of the local contact plane on the rebound of particles.....	232
Figure 8.44	Effect of contact plane inclination on the variation of local coefficients of restitution for the RP impact with $V_{ni} = 5.0m/s$ at $\theta = 85^\circ$	233
Figure 8.45	The variation of tangential coefficient of restitution with impact angle for impacts involving plastic deformation in the substrate with $\mu = 0.3$	233
Figure 8.46	The variation of total coefficient of restitution with impact angle for impacts involving plastic deformation in the substrate with $\mu = 0.3$	234
Figure 8.47	Comparison of the normal coefficient of restitution obtained for (i) oblique impacts with fixed initial speeds and (ii) normal impacts with the same initial normal velocity ($\mu = 0.3$).....	235
Figure 8.48	The (a) normal and (b) tangential coefficients of restitution of frictional ($\mu = 0.3$) and frictionless RP and PR impacts with a fixed initial normal velocity of $V_{ni} = 5.0m/s$	235
Figure 8.49	Effect of the change in orientation of the local contact plane on the coefficients of restitution for frictionless RP impacts.....	236
Figure 8.50	The variation of the dimensionless reflection angle of contact patch with dimensionless impact angle for impacts with plastic spheres ($\mu = 0.3$).....	238
Figure 8.51	The variation of the normalised reflection angle of contact patch with normalised impact angle for impacts with plastic spheres ($\mu = 0.3$).....	238
Figure 8.52	The variation of the dimensionless reflection angle of contact patch with dimensionless impact angle for impacts with plastic substrates ($\mu = 0.3$).....	239
Figure 8.53	The variation of the normalised reflection angle of contact patch with normalised impact angle for impacts with plastic substrates ($\mu = 0.3$).....	239
Figure 8.54	The variation of the rebound angular velocity with impact angle for impacts with plastic spheres ($\mu = 0.3$).....	240
Figure 8.55	The variation of the normalised rebound angular velocity with normalised impact angle for impacts with plastic spheres ($\mu = 0.3$).....	240
Figure 8.56	The variation of the rebound angular velocity with impact angle for impacts with plastic substrates ($\mu = 0.3$).....	241

Figure 8.57	The variation of the normalised rebound angular velocity with normalised impact angle for impacts with plastic substrates ($\mu = 0.3$)....	241
Figure 8.58	The variation of the rebound angular velocity with impact angle for frictional ($\mu = 0.3$) and frictionless impacts.....	242
Figure A.1	The contacting system configuration.....	257
Figure A.2	A hierarchical contact system.....	263
Figure A.3	(a) A 4-node contact segment. (b) A 3-node contact segment (c) A line segment.....	264
Figure A.4	Illustration of the contact searching.....	269
Figure A.5	Projection of g onto master segment s_i	270
Figure A.6	Location of contact target point when n_i lies above master segment.....	271
Figure A.7	Illustration of the penalty method.....	274
Figure A.8	The contact traction over a contact segment.....	275
Figure A.9	Possible errors in calculation of contact tractions at the contact edge.....	276
Figure B.1	Finite element meshes for the substrate of: (a) $R \times R$; (b) $2R \times 2R$; (c) $10R \times 10R$ and (d) $20R \times 20R$	281
Figure B.2	Time histories of displacement at the sphere centre for the impact of an elastic sphere with an elastic substrate of various sizes.....	284
Figure B.3	Time histories of velocity at the sphere centre for the impact of an elastic sphere with an elastic substrate of various sizes at: (a) $V_{ni} = 5.0m/s$; (b) $V_{ni} = 150m/s$	284
Figure B.4	Time histories of kinetic energy of the sphere for the impact of an elastic sphere with an elastic substrate of various sizes at: (a) $V_{ni} = 5.0m/s$; (b) $V_{ni} = 150m/s$	285
Figure B.5	Time histories of contact force for the impact of an elastic sphere with an elastic substrate of various sizes at: (a) $V_{ni} = 5.0m/s$; (b) $V_{ni} = 150m/s$	285
Figure B.6	Force-displacement relationships for the impact of an elastic sphere with an elastic substrate of various sizes at: (a) $V_{ni} = 5.0m/s$; (b) $V_{ni} = 150m/s$	286
Figure B.7	Time histories of (a) displacement and (b) velocity at the sphere centre for the impact of an elastic sphere with an elastic-perfectly plastic substrate of two different sizes at $V_{ni} = 150m/s$	286
Figure B.8	Time histories of kinetic energy of the sphere for the impact of an elastic sphere with an elastic-perfectly plastic substrate of two different sizes at $V_{ni} = 150m/s$	287

Figure B.9	(a) Time histories of contact force and (b) force-displacement relationships for the impact of an elastic sphere with an elastic-perfectly plastic substrate of two different sizes at $V_{ni} = 150m/s$287
Figure B.10	Coefficients of restitution for the impacts of an elastic sphere with an elastic substrate.....288
Figure B.11	The variation of energy loss ratio λ with impact velocity for the impact of an elastic sphere with an elastic substrate.....290
Figure C.1	Finite element model with a large substrate ($d/r=6$): (a) the whole model; (b) a close view of the meshes in the contact region.....294
Figure C.2	The variation of $F_{t,max} / \mu F_{n,max}$ with impact angle θ obtained using two different FE models.....294
Figure C.3	The variation of f / μ with impact angle θ obtained using two different FE models.....295
Figure C.4	The coefficients of restitution at various impact angles obtained using two different FE models.....295
Figure C.5	The variation of the normalised reflection angle at the contact patch with normalised impact angle obtained using two different FE models.....296
Figure C.6	The rebound angular velocities at various impact angles obtained using two different FE models.....296
Figure D.1	The variation of $F_{t,max} / \mu F_{n,max}$ with impact angle θ for different impact cases.....298
Figure D.2	The variation of normalised impulse ratio f / μ with impact angle θ for different impact cases.....298
Figure D.3	The coefficients of restitution at various impact angles for different impact cases.....299
Figure D.4	The variation of normalised reflection angle of the contact patch $v_{tr} / \mu V_{ni}$ with normalised impact angle $V_{it} / \mu V_{ni}$ for different impact cases.....299
Figure D.5	The rebound angular velocities at various impact angles for different impact cases.....300
Figure D.6	The normalised rebound angular velocity versus the normalised impact angles for different impact cases.....300

List of Tables

Table 3.1	model parameters for the impact of a sphere with a rigid wall.....	74
Table 3.2	model parameters for the impact of a sphere with a half-space.....	77
Table 3.3	model parameters for the frictional contact between a sphere and a half-space with tangential loading.....	80
Table 3.4	Various cases investigated for oblique impacts of a sphere with a half-space.....	83
Table 3.5	Material properties for oblique impacts of a sphere with a half-space.....	84
Table 4.1	The coefficient of restitution for the impact of an elastic sphere with a rigid wall.....	99
Table 5.1	The duration of impact at various impact velocities	117
Table 5.2	Material and geometric properties for various impact cases considered.....	122
Table 7.1	Critical angles for the impacts with different friction coefficients.....	174
Table 7.2	Critical angles for the impacts with different Poisson's ratios.....	175
Table B.1	The number of elements and nodes for the substrates.....	282
Table B.2	The duration of the impact.....	289
Table B.3	The coefficient of restitution for the impact of an elastic sphere with an elastic-perfectly plastic substrate of different sizes.....	291

Chapter 1 Introduction

1.1 General background

Contact phenomena are very common in mechanical engineering. The response of contacting solids provides information of central interest to such important phenomena as erosion, wear, and fracture strength. Most analyses of contact problems involve the contact of a sphere or a cylinder with a target, which is also a frequently occurring phenomenon in many areas of engineering application. The most direct macroscopic applications of such an investigation include hardness testing, the action of ball bearings in races, the impact damage to compressor blades by the ingestion of dust clouds in vehicles such as helicopters, hovercraft *etc.*, and the erosion of surfaces by low-velocity particle impacts. On a smaller scale, the mechanics of precision machinery with smooth surfaces involves the contact of small surface asperities. Knowledge of the stresses and deformations arising in contacting media, in conjunction with the resulting wear, is especially crucial for computer hard disk drives and micro-electromechanical devices, in which even small amounts of wear can be disastrous to the performance of the product. Thus, understanding the contact mechanical characteristics, such as stress and deformation, involved in the mechanics of contacting bodies is also of paramount importance in engineering practice.

In addition to the domain of mechanical engineering, contact mechanics is also the basis to understand the mechanical behaviour of granular materials, which is of particular interest in a wide variety of industrial, engineering, and scientific fields including such areas as the flow of solids through chemical processing plants, handling of granular materials in the agricultural industry, processing drug powder in the pharmaceutical industry, predicting and avoiding landslides and snow avalanches in civil and environmental engineering, assessing safety in the nuclear industry, and understanding planetary rings in astrophysics. Better understanding the behaviour of granular flow is therefore crucial not only to improve the quality of granular products but also to avoid disasters with the loss of fortune and human lives. Some important features of the mechanical behaviour of granular materials are clearly related to the internal structure of the material, which is typically composed of individual particles that interact with each other. Therefore, understanding and rigorous analytical modelling of granular media requires a prior understanding and

modelling of the response at the micro-mechanical level involving one or several contacts. Computer simulations of granular flows, such as using discrete element methods (DEM), have recently proved to be powerful to test and validate theoretical models, to complement and interpret experimental findings and to gain more information about the flow behaviour of granular materials. In numerical simulations the individual particles, commonly idealised as disks or spheres, interact through binary collisions or contacts. The effectiveness and accuracy of the computer simulations, therefore, depend primarily on the exact representation of the physical contact behaviour between individual particles.

However, it is very difficult to fully understand the impact behaviour of a particle with a substrate or between two particles because of the complexities of the impact mechanisms and the diversity of material properties. The impact behaviour is dominated by many factors, such as initial velocity conditions, material properties, interfacial properties, *etc.* The mode of contact deformation may be elastic, plastic, visco-elastic, or visco-plastic, depending on material properties and the initial velocity conditions.

1.2 Background of the project

As mentioned above, numerical simulations are very powerful for investigating the mechanical behaviour of granular materials. However, the accuracy and effectiveness of these simulations significantly depend upon the understanding of the contact/impact behaviour of a particle with a surface or between two particles. For example, forces, moments and deformations of the colliding bodies should be understood exactly and explicitly for the simulation based on granular dynamics. For simulation methods based on "event driven" algorithms (Brilliantov *et al.* 1996), the transformation rules for the relative velocities of colliding bodies after the impact as a function of the incident velocity should be accurately given in a simple manner. Otherwise, these simulations would be extremely time-consuming, and thus only granular systems with a relatively small number of particles could be investigated, which will prevent the characteristics of granular materials being well understood.

The elastic-plastic behaviour of the material plays an important role in the deformation behaviour in most impact cases. Thus methods based on elastic-plastic impact models are necessary and more representative of the real material behaviour than simple models based on either pure elastic material, such as the elastic impact theory, or rigid-perfectly plastic

material, such as the slip-line theory of plasticity. The theoretical solution to elastic-plastic impact problems presents extreme analytical difficulties since the mechanism of elastic-plastic deformation is very complex. Although several impact models based on some approximate assumptions have been developed, their accuracy and effectiveness need to be tested extensively by experimental and numerical data. While some experiments have been conducted to verify the theoretical models, the range and reliability are however limited owing to availability of materials and inevitable measurement errors. Our understanding of the impact behaviour of particles, especially elastic-plastic particles, is far from complete. Moreover, accurate and extensively effective impact models of particles, which must be based on a better understanding of the impact behaviour of particles, and can be incorporated in numerical simulations of elastic-plastic granular flow, still need to be delivered. Therefore, further investigation of the impact of particles needs to be undertaken in order to understand the impact behaviour better and more comprehensively.

1.3 Why finite element analysis?

The finite element method (FEM) was first introduced in the late 1950s as a computer-aided mathematical technique for obtaining approximate numerical solutions to the equations of calculus that predict the response of complicated physical systems, and has been extensively advanced since then. It is now widely used and accepted in many areas of engineering, science, and applied mathematics. The FEM can successfully handle numerous problems including steady state problems, eigenvalue problems and transient problems. With the rapid advances in computer technology and computing power, it has been possible to analyse larger and more complex problems with higher accuracy. For example, the application of finite element methods in the car industry is not limited to analysing the strength of individual components any more, but to analyse the strength of the car as a whole, as well as its impact behaviour and crashworthiness.

Finite element methods have been extended to handle contact/impact problems since the early 1970's. It has recently been advanced sufficiently to model the contact/impact phenomena. It can readily deal with the non-linear characteristics of contact boundary conditions that prevent the interesting problems from being solved analytically. In addition, it has neither limitations of material properties nor uncertainties of initial conditions, which normally results in extremely low levels of reproducibility in real experimental tests. In other words, finite element analysis (FEA) can readily handle the

material properties and initial conditions. Furthermore, the FE analysis can provide such detailed information as the contact deformation, the stress and strain distributions within the contacting bodies, the contact force and pressure distributions developed over the interface and the velocity profiles, which generally cannot easily be obtained from experimental measurements.

Therefore, the purpose of this study is to provide a comprehensive investigation of the impact behaviour of particles using FEM and to better understand the impact behaviour of particles. In this study, we will concentrate our attention on the impact of spherical particles. In all the finite element analyses presented in the thesis, the diameter of the impacting sphere is $20\mu\text{m}$. In reality, particles of size less than *ca.* $50\mu\text{m}$ tend to adhere together due to van der Waals forces and it had been the original intent to include a study of impacting autoadhesive spheres in the research programme. Consequently, it may be considered that the magnitudes of the normal and tangential contact forces and the durations of the impacts reported are not realistic although, by appropriate scaling, the corresponding values for larger spheres can be obtained. Furthermore, the size of a (non-adhesive) sphere has no effect on the rebound kinematics.

The FEA simulated impacts are implicitly carried out in a vacuum and, therefore, only the mechanical solid-solid interaction between the two bodies is examined. The effect of gravity and other forces due to the ambient fluid are neglected.

1.4 Order of presentation

A detailed review of previous research on contact/impact problems is presented in Chapter 2. Starting with normal impact, Chapter 2 describes the historic development of contact/impact mechanics, which is categorised into two groups: normal impact and oblique impact. The finite element models are presented in Chapter 3.

In Chapter 4, we discuss the normal impact of elastic particles. The interaction during the impact of an elastic sphere with an elastic substrate is investigated in detail. The impact behaviour of the sphere including energy dissipation and coefficient of restitution is presented. The effect of finite deformation on the normal impact behaviour of elastic particles is also discussed. The effect of plastic deformation on the normal impact behaviour of a sphere with a substrate is investigated in Chapter 5, in which a

comprehensive investigation of the impact behaviour during plastic normal impact is presented. A theoretical model is also presented. In addition, the finite-deformation plastic impact is addressed. The effect of work hardening on the impact behaviour of elastic-plastic particles is also investigated.

Chapter 6 provides a preliminary study on the frictional contact with tangential loading and the focus is placed on the traction distribution over the interface. The normal contact pressure distribution and the tangential traction distribution for both elastic and plastic contacts are reported and effects of the dissimilarity of elastic material properties and plastic deformation are discussed.

Oblique impacts of particles are discussed in Chapters 7 and 8. In Chapter 7, we present the oblique impact of elastic particles. Comparison of FEA results with those given by previous theories, experimental and other numerical analyses are made. The effects of initial velocity condition, friction and Poisson's ratio are investigated. The effect of plastic deformation on the oblique impact behaviour is studied in Chapter 8. Different impact cases are modelled. The effects of friction and contact deformation on the oblique impact behaviour of plastic particles are discussed. The coupling of normal and tangential responses is addressed, so is the effect of the change in local contact plane orientation.

Conclusions drawn from the work that has been done during this research project are given in Chapter 9 and future work on this topic is suggested.

In addition to the chapters in the main body of this thesis, there are four appendices dealing with various topics, as noted by the appendix heading in the contents. Appendix A presents finite element methods for contact/impact problems, including general formulations for contact/impact problems, time integration methods and contact modelling techniques.

Significance of the substrate size in FE simulation of the normal impact of a sphere with a half-space is discussed in Appendix B, in which the effect of stress waves on the normal impact behaviour of a sphere with a half-space is also investigated. Significance of the substrate size in simulations of oblique impacts of a sphere with a half-space is presented in Appendix C. In Appendix D, the influence of rigidity on the oblique impact behaviour of a sphere with an elastic substrate is presented.

Chapter 2 Literature Review

2.1 Introduction

The classical paper “on the contact of elastic solids” published by H. Hertz in 1882 may be the pioneer work of contact mechanics, which is usually referred to as Hertz theory. From then on Hertz theory has attracted considerable interest and has stood the test of time. Many scientists have studied this problem and advanced it by different means. Hertz theory has been advanced and extended to such aspects as that including the influence of friction at the interface (Smith and Liu 1953), the effect of tangential loading (Mindlin 1949; Mindlin and Deresiewicz 1953) and elastic wave propagation (Hunter 1957; Reed 1985), the influence of elastic-plastic deformation (Bitter 1963; Johnson 1985; Thornton 1997) and adhesion (Johnson *et al.* 1971; Rogers and Reed 1984; Thornton and Yin 1991; Thornton and Ning 1998; Johnson 1997, 1998). Meanwhile, a number of experimental investigations have been undertaken to verify the theoretical models (Zener 1941; Tillet 1954; Maw *et al.* 1976, 1981; Labous *et al.* 1997; Gorham and Kharaz 2000). In addition, since the early 1970's, finite element methods have been developed and applied to study contact/impact problems (Hardy *et al.* 1971; Lee *et al.* 1972; Hong and Saka 1991; Shih *et al.* 1992; Kral *et al.* 1993, 1995a, 1995b; Kral and Komvopoulos 1996a, 1996b; Mesarovic and Fleck 1999, 2000; Li *et al.* 2000).

Impacts can generally be categorised into normal impact and oblique impact, according to whether the direction of initial velocity coincides with the normal direction of the initial contact plane. In this chapter, a literature review is presented first for normal impact, then for oblique impact. We focus on the contact/impact behaviour of a sphere with a half-space, since most collisions involving spheres in engineering applications can be generalised as a sphere impacting with a half-space without losing the principal mechanisms of the impact. For more details of the contact/impact analysis, readers are referred to books by Tabor (1951), Goldsmith (1960), Kolsky (1963), Johnson (1985), Hills *et al.* (1993) and Stronge (2000), which describe general aspects of the contact/impact behaviour of solids, and recent reviews of Bhushan (1996) with emphasis on modelling of a single asperity contact or indentation problems, of Tabor (1986) concerning the

understanding of indentation hardness, of Adams and Mosonovsky (2000) focusing on contact forces and their relationship to the properties of the contacting bodies.

During contact/impact, the deformation behaviour of the contacting body generally depends on the nature of the solid bodies, such as elastic, elastic-perfectly plastic, elastic-plastic with work hardening, visco-elastic and visco-plastic solids. In this study, we consider only the contact/impact of bodies of either elastic, or elastic-perfectly plastic, or elastic-plastic with work hardening solids. Figure 2.1 shows the stress-strain curves for various materials considered in this study. We refer readers to Johnson (1985) for more details on the contact/impact of visco-elastic and visco-plastic bodies.

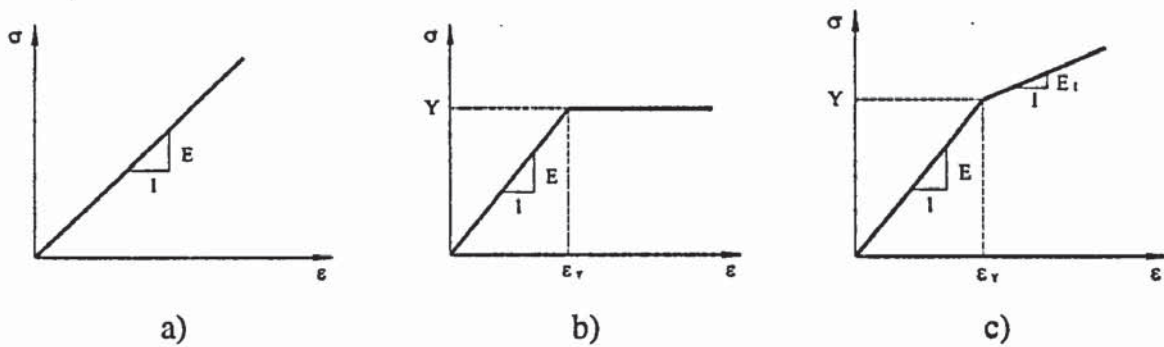


Fig. 2.1 Stress-strain curves for (a) elastic, (b) elastic-perfectly plastic, and (c) elastic-plastic with work hardening solids.

2.2 Normal impact

2.2.1 Hertz theory of elastic contact/impact

The solution for the contact of two elastic bodies was first given by Hertz (1896). Hertz's interest in the problem was aroused by experiments on optical interference between glass lenses when he was investigating Newton's optical interference fringes. He was concerned about the possible influence of elastic deformation of the lenses caused by contact pressure. Hertz theory of elastic contact has three fundamental hypothesis: 1) the contact area is, in general, elliptical; 2) Each body can be regarded as an elastic half-space loaded over a small elliptical region of its plane surface, which requires that the dimensions of the contact area must be small compared both with the dimensions of each body and with the relative radii of curvature of the contacting surfaces; 3) The surfaces are assumed to be frictionless so that only a normal pressure is transmitted. The above assumptions can be summarized as follows:

- 1) Each solid is considered as a linear elastic half-space;

- 2) The bodies are homogeneous and isotropic;
- 3) The strains are small;
- 4) The contacting surfaces are continuous and non-conforming, and their profiles are described by quadratic formulae;
- 5) The surfaces are frictionless and the surface tractions are only induced by normal contact forces, i.e., neither tangential forces nor adhesive forces are considered.

Based on the above assumptions, Hertz obtained an analytical solution for the elastic contact problem. Hertz (1896) proposed that the contact pressure between two frictionless elastic solids in contact is given by

$$p(r) = p_0 \left[1 - \left(\frac{r}{a} \right)^2 \right]^{1/2} \quad (2.1)$$

where p_0 is the maximum pressure at the contact centre; a is the contact radius and r is the distance from the contact centre. The total contact force F_n is then given by

$$F_n = \int_0^a p(r) 2\pi r dr = \frac{2}{3} \pi a^2 p_0 \quad (2.2)$$

Hence

$$p_0 = \frac{3F_n}{2\pi a^2} \quad (2.3)$$

For any arbitrary points at a distance r from the contact centre, the normal displacement w induced by the contact pressure is obtained as (Johnson 1985)

$$w(r) = \frac{1-\nu^2}{E} \frac{\pi p_0}{4a} (2a^2 - r^2) \quad (2.4)$$

where E and ν are the Young's modulus and Poisson's ratio of the body, respectively.

For two spheres in contact, the boundary condition for displacements within the contact area can be written as

$$w_1(r) + w_2(r) = \alpha - \frac{r^2}{2R^*} \quad (2.5)$$

where w_1 and w_2 are normal displacements of any arbitrary points on the contact surfaces at a distance r from the contact centre ($r \leq a$), α is the relative approach of the centroids of the two spheres and

$$\frac{1}{R^*} = \frac{1}{R_1} + \frac{1}{R_2} \quad (2.6)$$

in which R_1 and R_2 are the radii of the two spheres, respectively.

Substituting the expressions for w_1 and w_2 into Eq.(2.5), we have

$$\frac{\pi p_0}{4aE^*} (2a^2 - r^2) = \alpha - \frac{r^2}{2R^*} \quad (2.7)$$

where

$$\frac{1}{E^*} = \frac{1-\nu_1^2}{E_1} + \frac{1-\nu_2^2}{E_2} \quad (2.8)$$

E_i and ν_i ($i=1,2$) denote the Young's moduli and Poisson's ratios of the contacting bodies, respectively. Since Eq.(2.7) is applicable for any point within the contact area, *i.e.*, independent of the value of r , we have

$$a = \frac{\pi p_0 R^*}{2E^*} \quad (2.9)$$

$$\alpha = \frac{\pi a p_0}{2E^*} \quad (2.10)$$

Using Eq.(2.9) and (2.10), we have

$$\alpha = \frac{a^2}{R^*} \quad (2.11)$$

From Eqs.(2.3), (2.10) and (2.11), we can obtain the contact force-displacement relationship

$$F_n = \frac{4E^*}{3R^*} a^3 = \frac{4}{3} E^* R^{*1/2} \alpha^{3/2} \quad (2.12)$$

For the elastic sphere exerted by the Hertz pressure (Eq.(2.1)), the analytical solutions for stress distributions were calculated by many researchers (see, among others, Morton and Close 1922; Davies 1949; Hamilton and Goodman 1966), which are generalised in Johnson's book (Johnson 1985).

Hughes *et al.* (1976) studied the contact between an elastic sphere and a rigid surface using finite element method. The contact region and the contact pressure distribution over a wide

range of loading were reported. The contact pressures were determined from the nodal contact forces by a tributary area method. The results showed that the Hertzian solution indeed gives very good prediction compared with the FEA results. Shih *et al.* (1992) experimentally observed the stress distribution for two elastic spheres of different sizes compressed together using a photo-elastic stress-freezing technique. The stress distribution was compared with both FEA results and Hertz theory. The comparison reveals that the normal pressure distribution obtained from FEA is consistent with Hertz theory except in the vicinity of the contact point. The pressure obtained from FEA is larger than those given by Hertz theory at the contact centre. The deviation was attributed to be the result of large deformation in the two contacting spheres. The maximum shear stress distribution in the larger sphere is closer to that of the Hertzian solution than that in the smaller one for contacts between different size spheres, which indicated that Hertz theory is limited to small deformation as assumed.

Following directly from the theory of elastic contact, Hertz also analysed the impact of frictionless elastic bodies. Hertzian impact theory of elastic bodies is essentially quasi-static and based on the following assumptions (Johnson 1985): 1) The deformation is assumed to be restricted to the vicinity of the contact area and to be given by the static theory; 2) Elastic wave motion in the bodies is ignored; 3) The total mass of each body is assumed to be moving with the velocity of its centre of mass at any instant. Hertz theory makes it possible to obtain an approximate solution to the normal impact of elastic bodies. For instance, the duration of impact was determined as (see Timoshenko and Goodier 1951; Johnson 1985)

$$t = 2.87 \left(\frac{m^{*2}}{R^* E^{*2} V_{ni}} \right)^{1/5} \quad (2.13)$$

in which V_{ni} is the initial relative velocity of two bodies and

$$\frac{1}{m^*} = \frac{1}{m_1} + \frac{1}{m_2} \quad (2.14)$$

where m_i denotes the masses of the contacting bodies, respectively.

For the special impact case of an elastic sphere with an elastic half-space, Eq.(2.13) reduces to

$$t = 5.09 \left(\frac{\rho}{E^*} \right)^{2/5} \frac{R}{V_{ni}^{1/5}} \quad (2.15)$$

where ρ is the density of the sphere. It can be seen that the duration of impact is proportional to the radius of the sphere and inversely proportional to $V_{ni}^{1/5}$.

Generally the impact period can be divided into two phases: an initial phase of compression and a subsequent phase of restitution. When collision occurs between two elastic bodies, the initial kinetic energy is converted to elastic strain energy stored in the contacting bodies and energy for elastic waves to propagate during compression. Hence the relative velocity gradually reduces and vanishes at the instant when the maximum compression is reached. During restitution, the stored elastic strain energy is gradually recovered with the relaxation of compression deformation, and the relative velocity correspondingly increases until the restitution is terminated at the instant when the contacting bodies separate. The contacting bodies then rebound with a rebound kinetic energy that is somewhat less than the initial kinetic energy as a portion of the initial energy is dissipated by the stress wave propagation.

The coefficient of restitution, which is usually used to characterise the change in kinetic energy during the impact, is among the important parameters needed to predict post-impact motion of the spheres. There are several definitions for the coefficient of restitution, which were proposed by Newton, Poisson and Stronge (see Smith and Liu 1992; Adams and Tran 1993; Stronge 1990):

- 1) In *Newton's* definition, the coefficient of restitution e is defined as ratio of the rebound velocity V_r to the incident velocity V_i . This is usually referred to as *Newton's Law of restitution* or the *kinematic coefficient*;
- 2) *Poisson* defined the coefficient of restitution as the ratio of the impulse during the restitution phase to the impulse during the compression phase of the impact, which is normally known as *Poisson's hypothesis* or the *kinetic coefficient*;
- 3) An energetic coefficient of restitution is proposed by *Stronge* (1990) in terms of energy dissipation. In this definition, the coefficient of restitution is expressed as the ratio of work done by the normal force during the restitution to that during the compression.

It was pointed out by Stronge (1990) that the above three definitions are consistent and give the same results for collinear impact. Since in this study we only consider the impact of spherical particles, which are all collinear, we will adopt *Newton's* definition for simplicity.

Since the energy dissipation due to elastic wave motion is neglected in Hertz theory, the initial kinetic energy W_i is assumed to be completely converted to elastic strain energy stored in the contact bodies during the compression. We hence have

$$W_i = \frac{1}{2} m^* V_{ni}^2 = \int_0^{\alpha^*} F_n d\alpha = \frac{8}{15} E^* R^{*1/2} \alpha^{*5/2} = \frac{8}{15} \frac{E^* a^{*5}}{R^{*2}} \quad (2.16)$$

where α^* and a^* are the maximum relative approach and maximum contact radius during the impact.

Owing to the reversibility of elastic deformation, the elastic strain energy could almost be recovered and becomes the rebound kinetic energy W_r of the contacting bodies during the restitution. For a sphere striking a fixed target, the rebound velocity V_{nr} is hence almost identical to the initial impact velocity V_{ni} . Therefore, the coefficient of restitution e_n defined as

$$e_n = \frac{V_{nr}}{V_{ni}} \quad (2.17)$$

is close to unity.

The Hertzian assumptions have been validated by Andrews (1930) and Crook (1953). Andrews (1930) experimentally investigated the impact of two equal spheres of soft metal with low impact velocities. He found that the duration of impact varies inversely as $V_i^{1/5}$, as given by Eqs.(2.13) and (2.15), and the coefficient of restitution is very close to unity, which indicated that elastic wave motion can be ignored. Crook (1952) measured the impact force throughout the impact between a hard sphere and metal substrate using the piezo-electric method. A quantitative comparison of the experimental results with Hertz theory was made. It is shown that the experimental results agree closely with those given by Hertz theory.

Hughes *et al.* (1976) also investigated the impacts of an elastic sphere onto a rigid plane and of two dissimilar elastic spheres using FEM. It was shown that, for the impact of an elastic sphere with a rigid plane, the normal pressure distribution over the contact area at the instant when the contact radius reaches its maximum compares favourably with Hertzian quasi-static solution. For the impact of two dissimilar elastic spheres, the variation

of the relative approach with the contact radius was reported and was in good agreement with Hertz theory.

Hertian elastic impact theory is in nature quasi-static. By analogy to the impact of a thin rod, Love (1952) suggested that the deformation would be quasi-static if the duration of the impact was long enough to permit stress waves to traverse the impacting bodies many times. For the impact of a sphere with a substrate of dimension $L \times L$ (see Fig. 3.4), the time for a longitudinal wave to travel a distance of two sphere diameters is

$$\bar{T} = 4R/c_0 \quad (2.18)$$

and to travel two substrate dimensions is

$$\bar{T} = 2L/c_0 \quad (2.19)$$

where c_0 is the velocity of the stress wave in one-dimension and

$$c_0 = \sqrt{E/\rho} \quad (2.20)$$

According to Love's criterion, for a quasi-static analysis of the impact to be valid, the ratio of \bar{T} to the duration of impact t should be much less than unity, i.e.

$$\bar{T}/t \ll 1 \quad (2.21)$$

where t is given by Eq.(2.15). This implies that the initial impact velocity must be low enough to satisfy the quasi-static condition since the duration of impact t is inversely proportional to $V_{ni}^{1/5}$, see Eqs.(2.13) and (2.15).

However, for a sphere impacting with a substrate that is so large that no reflected waves return to the contact point, Love's criterion is obviously not the appropriate one. Based on the study of Hunter (1956), Johnson (1985) suggested an alternative criterion, by which the deformation is regarded as quasi-static provided the time constant of the system \tilde{T} is short compared with the period of the force pulse applied to the system. Hence the following condition should be satisfied for quasi-static conditions to be approached (Johnson 1985),

$$\frac{\tilde{T}}{t} \approx 0.4 \frac{RV_{ni}}{a^* c_0} \ll 1 \quad (2.22)$$

where a^* can be determined from Eq.(2.16).

2.2.2 Non-Hertzian contact/impact of elastic bodies

The classical Hertz theory is based on some assumptions as mentioned before. However some of the assumptions cannot be satisfied in special circumstances. Consequently, many works have been done to extend Hertz theory by relaxing some of the restrictions. In this section previous works on non-Hertzian contact/impact of elastic bodies are briefly reviewed.

The classical Hertz contact theory is considered valid in the case of very small deformations (Goldsmith 1960). In addition, it is assumed that each body is considered as a semi-infinite elastic body---half-space. Tatara (1989) extended Hertzian elastic contact theory by considering each of the contacting spheres as a finite elastic medium and developed force-displacement relationships for the contact and impact of two elastic spheres. For the contact of elastic spheres, Tatara (1989) considered the compression of two elastic spheres pressed against each other by a compressive force F_n and suggested that for any points within the contact area at a distance r from the initial contact centre the following expression stands

$$(w_1 + w_2)_T = \alpha - \frac{r^2}{2R^*} \quad (2.23)$$

where α is the relative approach of the two centres of masses, $(w_1 + w_2)_T$ denote the relative approach of the spheres at the position of radius r on the mutual surface of contact and is given by

$$(w_1 + w_2)_T = w_1 + w_2 - (w_1 + w_2)_E \quad (2.24)$$

where $w_1 + w_2$ represents the displacement of the contact surface given by Hertz theory (Eq.(2.5)) and $(w_1 + w_2)_E$ represents the expansive displacement of the contact surface due to the compressive force F_n . Since it is very difficult to obtain a general solution of $(w_1 + w_2)_E$ for arbitrary values of r , two special cases were considered by supposing: I) the deflection of any points over the contacting surfaces is constant and equal to that at $r = 0$, *i.e.*, $(w_1 + w_2)_{E1}$; II) the deflection of any points over the contacting surfaces is constant and equal to that at $r = a$, *i.e.*, $(w_1 + w_2)_{E2}$. Obviously, the actual value of $(w_1 + w_2)_E$ lies between $(w_1 + w_2)_{E1}$ and $(w_1 + w_2)_{E2}$, *i.e.*,

$$(w_1 + w_2)_{E2} \leq (w_1 + w_2)_E \leq (w_1 + w_2)_{E1} \quad (2.25)$$

Relations between the contact force and relative approach were obtained for the two special cases. For case I,

$$\alpha = \left(\frac{F_n}{k} \right)^{2/3} - \frac{F_n}{k_c} \quad (2.26)$$

For case II,

$$\alpha = \left(\frac{F_n}{k} \right)^{2/3} - \frac{F_n}{k_c} + \left[\frac{K'_1}{(2R_1)^2} + \frac{K'_2}{(2R_2)^2} \right] a^2 F_n \quad (2.27)$$

where $k = \frac{4}{3} E^* R^{1/2}$, k_c , K'_1 and K'_2 are parameters related to the material constants.

It is clear that the first item on the right-hand sides of Eq.(2.26) and (2.27) is identical to the Hertz equation. At high compressive forces, Tatara (1989) showed that, for hard materials such as steel and glass, the effects of the additional items in Eqs.(2.26) and (2.27) are negligible so the results given by Eqs.(2.26) and (2.27) are close to the Hertz solution. However, for soft materials such as polyethylene and rubber, the expansive displacements given by the additional items of Eqs.(2.26) and (2.27) become significant and cannot be neglected. Experimental results for solid rubber sphere verified the extensive force-displacement relationships and demonstrated that the extended theory can be applicable to the case of large deformations. It should be noted that the actual relative approach α lies between those given by Eqs.(2.26) and (2.27) since they were derived for two extreme cases (Tatara 1989).

For the impact of spheres, Tatara (1989) pointed out that this would be a different case from that for the contact of spheres since there is no compressive force. Tatara then considered the deformation of the entire sphere induced by the contact force F_n generated over the contact surface, rather than regarding the sphere as a half-space. As a result of the deformation of the entire sphere, the relative approach of the two sphere centres α will be decreased and smaller than the relative approach given by Hertz theory, α_H , *i.e.*

$$\alpha = \alpha_H - z_G \quad (2.28)$$

where z_G denotes the relative receding displacement of the centres and given by

$$z_G = \left[\frac{(1+\nu_1)(13-10\nu_1)}{10\pi E_1 R_1} + \frac{(1+\nu_2)(13-10\nu_2)}{10\pi E_2 R_2} \right] F_n \quad (2.29)$$

From Eqs.(2.28) and (2.29), the relative approach can be determined as

$$\alpha = \left(\frac{F_n}{k} \right)^{2/3} - \frac{F_n}{k_T} \quad (2.30)$$

in which

$$k_T = \left[\frac{(1+\nu_1)(13-10\nu_1)}{10\pi E_1 R_1} + \frac{(1+\nu_2)(13-10\nu_2)}{10\pi E_2 R_2} \right]^{-1} \quad (2.31)$$

It can be seen from Eq.(2.30) that, for the same contact force F_n , Eq.(2.30) gives a lower value of relative approach than that given by Hertz theory.

Taking account of the curvature and the global deformability of the sphere, Bondareva (1970) obtained an elastic solution for the contact between a heavy sphere and a rigid plane. Based on Bondareva's analysis, Villaggio (1996) investigated the normal impact of an elastic sphere against a rigid plane based on the assumption that the effect of the stress wave can be neglected. The force-displacement relationship was given by

$$F_n = \frac{4}{3} E^* R^{*1/2} \alpha^{3/2} \left[1 - \frac{2}{3\pi} \frac{(1-2\nu)^2}{1-\nu} \left(\frac{\alpha}{R^*} \right)^{1/2} \left(\ln 2 - \frac{2}{3} + \ln \left(\frac{\alpha}{R^*} \right)^{1/2} \right) + \frac{1}{2\pi} \frac{1-2\nu}{1-\nu^2} \left(\frac{\alpha}{R^*} \right)^{1/2} \right]^{-1} \quad (2.32)$$

where ν is the Poisson's ratio of the sphere, E^* and R^* are defined by Eqs.(2.8) and (2.6), respectively.

For incompressible materials $\nu = 0.5$, the corrective terms within the square bracket in Eq.(2.32) become unity, Eq.(2.32) then reproduces Hertz's formula (Eq.(2.12)). Moreover, for small values of α/R^* , the sum of the corrective terms does not differ appreciably from unity so that Eq.(2.32) may be replaced by Hertz's solution (Eq.(2.12)). However, for large values of α/R^* , the value of the corrective terms may deviate from unity and Eq.(2.32) hence gives a considerable different result from that given by Hertz theory. For example, if $\alpha/R^* = 0.27$ and $\nu = 0.0$, Eq.(2.32) becomes (Villaggio 1996)

$$F = 0.8678 \times \frac{4}{3} E^* R^{*1/2} \alpha^{3/2} \quad (2.33)$$

Villaggio (1996) also obtained a solution for the duration of impact and showed that it is slightly longer than that given by Eq.(2.15).

Conforming elastic contact was investigated by Goodman and Keer (1965), who investigated the elastic contact between a sphere and a spherical cavity. They showed that the contact stiffness for conforming contacts is considerably harder than that for the non-conforming contacts given by Hertz theory. Singh and Paul (1974) removed the restriction

that the profiles of the contact surfaces are quadratic and developed a numerical analysis method for frictionless, non-conformable, non-Hertzian contact of elastic bodies of arbitrary shape, i.e., the surface may not be locally quadratic. As an example, the contact of rounded indenters with local flat spots was analysed, and it was found that there is a dip in the pressure distribution near the axis of symmetry. They attributed this to the extremely flat profile at the contact centre.

In the classical Hertz contact theory, the influence of friction is ignored and the surfaces in contact are assumed to be perfectly smooth. However, in reality, surfaces are never frictionless. The influence of dry friction without tangential loading was incorporated into a study of contacting spheres by Goodman (1962). Even for the contact between spheres with different elastic materials, it was found that the coupling between normal and shear stresses was small and could normally be neglected. Conway (1971) also investigated the effect of friction on normal contact stresses. A severe case investigated is that a thin elastic sheet is compressed between and pulled through two identical rigid stationary cylinders, in which the effect of the shearing on the normal stresses is likely to be much larger than that encountered in many other practical contact problems, like simple normal compression of a layer between equal cylindrical indenters. However, it was shown that the effects on the normal contact stresses are quite small. The function of friction in oblique contacts/impacts will be discussed in detail in section 2.3.

According to Hertz's assumption that the elastic wave motion in the bodies is ignored, there is no energy loss due to elastic stress waves during the impact. It is implied that the coefficient of restitution is a constant of unity during the Hertz impact. This has been examined by some researchers. Saint-Venant first mentioned the effect of the elastic waves within the bodies for the impact of long rods and showed that, as a consequence, even perfectly elastic materials will have a coefficient of restitution less than one (see Love 1952). Hunter (1957) analysed the energy losses due to the elastic wave propagation during the elastic impact and showed that for a steel ball impinging on a large block of steel or glass, less than 1 per cent of the kinetic energy of the ball is converted into elastic wave. These energy losses were re-evaluated by Reed (1985), who predicted the energy loss as being some 4.5 times greater than that estimated by Hunter (1957).

Hertz theory was also extended to investigate the impact of elastic spheres with elastic plates. Zener (1941) gave an elaborate treatment of the theoretical problem involved in the

impact of a sphere with a plate using the premise of Hertz. In his analysis, the force-approach relationship established by Hertz was used to predict the relation between the reaction force F_n of the plate on the sphere and their relative approach α . The coefficient of restitution was obtained as a function of a single impact parameter that depends on the geometry and material properties of the sphere and the plate. Tillett (1954) experimentally investigated the impact of steel balls on plates of glass and plastics. Both the coefficient of restitution and the duration of impact were measured. The energy loss due to stress wave propagation was estimated and it was found that the energy losses were of the order of 3 per cent for a steel ball impacting on glass. The coefficient of restitution was found to be dependent upon the size of the specimen as well as its material properties.

By removing the constraint that each solid is considered as a homogeneous and isotropic elastic half-space, Conway *et al.* (1972) investigated the impact between a rigid sphere and a thin elastic layer supported by a rigid substrate. Several models were developed to predict the force-time relationships and the duration of impact by assuming either frictionless support or complete adherence between the layer and substrate. The theoretical predictions were in good agreement with experimental results obtained by Goodier *et al.* (1959). Experiments on the impact of a steel ball on nylon layers were also carried out and the experimental results were consistent with the theoretical predictions (Conway *et al.* 1972). Further to the investigation of Conway *et al.* (1972), Fisher (1975) studied the impact of an elastic sphere on a thin elastic plate supported by a Winkler foundation, rather than supported by rigid substrate. Winkler hypothesis that the reaction pressure is considered to be proportional to the local deflection was used to estimate the contact pressure between the plate and the foundation. The contact force, coefficient of restitution and duration of impact are computed for a wide variation of problems. For two extreme cases, one is for the impact of an elastic sphere with a half-space and the other is for the impact of the sphere on a thin plate supported by a rigid foundation, the durations of impact were found to correlate with the predictions of Hertz and Conway *et al.* (1972).

2.2.3 Contact/impact of elastic-plastic bodies

2.2.3.1 Yield

In many practical cases, plastic deformation is involved during the impact because of the localisation of stresses. According to the theory of plasticity, there are two yield criteria

commonly employed: one is the distortion energy theory, or von Mises yield criterion; the other is the maximum shear theory, or Tresca criterion.

In von Mises yield criterion, yield begins when the distortion energy equals the distortion energy at yield in simple tension. Hence yield occurs when the second invariant J_2 of the stress deviator tensor (s_{ij}) reaches a critical value, *i.e.*,

$$J_2 = \frac{1}{2} s_{ij} s_{ij} = \frac{1}{6} [(\sigma_1 - \sigma_2)^2 + (\sigma_2 - \sigma_3)^2 + (\sigma_3 - \sigma_1)^2] = k^2 = \frac{Y^2}{3} \quad (2.34)$$

where σ_1 , σ_2 and σ_3 are the principal stresses in the state of complex stress, k and Y are the yield stress in simple shear and in simple tension, respectively. The maximum shear theory (Tresca criterion) assumes that yield will occur when the maximum shear stress reaches the same value as the maximum shear stress for yield occurring under simple tension,

$$\max \{ |\sigma_1 - \sigma_2|, |\sigma_2 - \sigma_3|, |\sigma_3 - \sigma_1| \} = 2k = Y \quad (2.35)$$

For the case of axisymmetric contact of two spheres with Poisson's ratio $\nu = 0.3$, both the von Mises and Tresca criteria predict that yield occurs when (Johnson 1985)

$$p_{yo} = 1.60Y \quad (2.36)$$

where p_{yo} is the maximum contact pressure when yield initiates. In terms of the mean contact pressure, the onset of plastic deformation occurs when (Tabor 1951)

$$p_{ym} = 1.10Y \quad (2.37)$$

where p_{ym} denotes the mean contact pressure at the onset of yield.

2.2.3.2 Contact pressure

The solution for Hertz contact remains valid until yield initiates in the body with a lower yield strength. The yield will be first developed inside the body at some distance from the centre of the contact surface and a small amount of plastic flow occurs within the larger elastic hinterland (Tabor 1951). As the load and contact pressure continue to be increased, the plastic zone grows. With the further increase of the load and contact pressure, the plastic zone gradually reaches the contact surface, and eventually the whole of the material around the contact area undergoes plastic deformation (see Fig. 2.2). This implies that in

the whole process the deformation changes from purely elastic to elastic-plastic then to fully plastic, which is the common phenomena for most engineering materials in contact. Thus, the contact deformation process can be categorised into three phases:

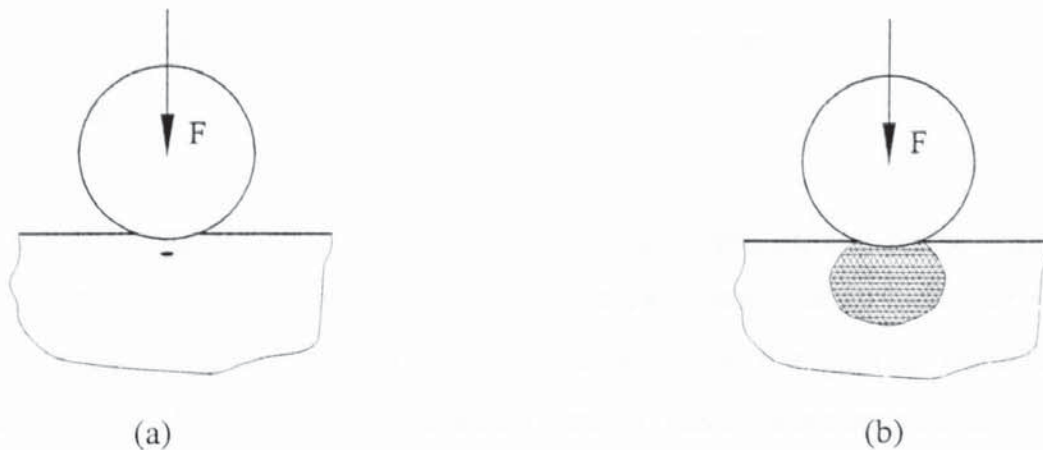


Fig. 2.2 Plastic deformation process during the compression of a spherical indenter into a plastic solid: (a) the onset of plastic deformation which is underneath the surface; (b) the plastic zone is expanded to the contact surface and fully plastic deformation occurs.

- 1) Elastic phase: the deformations of both contacting bodies are elastic and the solution of Hertz theory holds;
- 2) Elastic-plastic phase: this is a transitional phase from purely elastic to fully plastic. It begins once yield occurs in the body with a lower yield strength and terminates by the fully plastic phase;
- 3) Fully plastic phase: this becomes dominant once the plastic zone reaches the surface and the material surrounding the contact area undergoes plastic deformation.

Note that plastic deformation will be initiated first in one of the two contacting bodies, but as the contact deformation proceeds, the maximum contact pressure increases and as soon as it exceeds $1.60Y$ of another contacting body, it begins to deform plastically as well. As a result, both bodies will be permanently deformed.

The contact pressure can be determined by Hertz theory for the contact of elastic bodies or within elastic regime of elastic-plastic bodies, as discussed in Section 2.2.1. The fully plastic contact was analysed using the slip-line method by Ishlinshy (see Tabor 1951), who investigated the contact of a rigid sphere and a rigid perfectly plastic half-space. The analytical solution for the contact pressure was obtained. It was shown that the pressure over the contact area is not uniform but is somewhat higher in the centre than at the edge (Tabor 1951). The mean contact pressure p_m was obtained as follows

$$p_m = 2.8Y \sim 3.0Y \quad (2.38)$$

Based on available numerical analyses and experimental measurements of the spherical indentation of an elastic-plastic half-space, with or without work hardening, in the literature, Francis (1976) and Johnson (1985) have given a relationship between the mean contact pressure p_m and the yield stress Y for fully plastic contact,

$$p_m \approx 2.8Y \quad (2.39)$$

General theoretical solutions for the contact pressure in the transitional elastic-plastic phase are not available in the literature. Nevertheless, an expanding cavity model as shown in Fig. 2.3a has been used with some success in soft metals with negligible work hardening (see Johnson 1985, Hill 1950). The expanding cavity model assumes that, if the contact area has a diameter $d = 2a$, the contact surface is encased in a hemispherical core of radius a . Within the core, the material is under hydrostatic pressure equal to the mean contact pressure p_m . This material under hydrostatic pressure could not yield. Outside the core, it is assumed that the stresses and displacements have radial symmetry and are the same as an infinite elastic-perfectly plastic body with a spherical cavity under a pressure p_m . From the boundary of the core, plastic flow spreads into the surrounding material, and the plastic strains gradually diminish until they match the elastic strains in the hinterland at some radius c ($c > a$), at which the plastic-elastic boundary lies. Johnson (1985) illustrated that the pressure in the hydrostatic core is a function of the critical parameter $(E^*/Y)(a/R^*)$ for a spherical indenter. For an incompressible material indented by a spherical indenter of radius R , the pressure p_m in the core is given by

$$\frac{p_m}{Y} = \frac{2}{3} \left\{ 1 + \ln \left[\frac{1}{3} \frac{E^*}{Y} \frac{a}{R^*} \right] \right\} \quad (2.40)$$

Figure 2.3b shows how the mean contact pressure increases from $p_m \sim 1.1Y$ (the onset of plastic deformation) to $\sim 3.0Y$ (fully plastic deformation) as the size of the contact a/R^* increases, based on the prediction of Eq.(2.40) for the spherical indentation. Fully plastic deformation occurs at a value of $E^*a/YR^* \approx 40$, which is about 16 times greater than the value for the occurrence of yield. For the case of a hard steel sphere pressed into the surface of a fully work-hardened mild steel specimen, Tabor (1970) showed the load increases by a factor of about 300 and the contact radius increases by a factor of about 10

from the onset of plastic deformation until fully plastic deformation, which is consistent with that described in Fig. 2.3b.



Fig. 2.3 The contact of elastic-plastic solid: (a) the expanding cavity model; (b) the variation of p_m/Y with E^*a/YR^* (Johnson 1985).

However, the expanding cavity model breaks down in harder materials with pronounced work hardening characteristics since it is based on the assumption that the material has a constant yield stress Y , that is, that no work hardening is produced during the indentation process. For most materials, the yield or flow stress increases as a result of plastic deformation or work hardening. Consequently, the deformation process during the contact induces an increase in the flow stress. Tabor (1951) suggested that there is an effective strain such that the mean contact pressure is

$$p_m = cY_R \quad (2.41)$$

where Y_R is the uniaxial flow stress and c is a constant. For a spherical indenter of diameter D , producing an indentation of chordal diameter, d , the effective strain is a function of the dimensionless ratio d/D . Experiments (Tabor 1948) showed that for full plasticity the mean contact pressure increases with the size of the indentation in a manner consistent with the empirical assumption that the effective strain ϵ_R is approximately equal to $0.2(d/D)$, *i.e.*

$$\epsilon_R = 0.2 \frac{d}{D} = 0.2 \frac{a}{R} \quad (2.42)$$

This is confirmed by the analysis of Lee *et al.* (1972). They investigated this problem with a material of specified flow stress-plastic strain characteristics using slip-line field theory. It also involved a finite element analysis at incremental stages of the indentation process.

Matthews (1980) presented an approximate analysis of the spherical indentation of an annealed material. It was assumed that the yield of the annealed material in uni-axial tension or compression might be written as

$$\frac{\varepsilon}{\varepsilon_0} = \left(\frac{Y}{Y_0} \right)^n \quad (2.43)$$

where ε is the strain, Y is the stress, ε_0 and Y_0 are appropriate material constants which may be found by fitting the data to a simple tension or compression test, and n is the reciprocal of the usual work hardening index. Note that if $n = 1$, Eq.(2.43) represents a linear elastic solid with Young's modulus $E = Y/\varepsilon = Y_0/\varepsilon_0$. If $n \rightarrow \infty$, Eq.(2.43) represents an ideal rigid-plastic material of yield stress $Y = Y_0$. For n between 1 and ∞ , Eq.(2.43) represents an annealed plastic material with a general work hardening behaviour. The contact pressure distribution proposed by Matthews (1980) is of the form

$$p(r) = p_m \frac{2n+1}{2n} \left(1 - \frac{r^2}{a^2} \right)^{1/2n} \quad (2.44)$$

The mean pressure p_m over the contact area is

$$p_m = \frac{F_n}{\pi a^2} = \frac{6nY_0}{2n+1} \left(\frac{8a}{9\pi R \varepsilon_0} \right)^{1/n} \quad (2.45)$$

It can be seen that if $n = 1$, Equations (2.44) and (2.45) reduce to the classical Hertzian equations for elastic contacts; if $n \rightarrow \infty$, the pressure distribution becomes uniform, of magnitude $3Y_0$, which is close to the behaviour of an ideal rigid-plastic solid predicted by slip-line field theory (Matthews 1980).

Based on Matthews's analysis, Tabor (1985) estimated the effective yield stress Y_R of the solid for fully plastic indentation using a semi-empirical relation

$$Y_R = \frac{p_m}{3} = \frac{2nY_0}{2n+1} \left(\frac{8}{9\pi \varepsilon_0} \frac{a}{R} \right)^{1/n} \quad (2.46)$$

Using Eqs.(2.43) and (2.46), the effective strain ε_R can be obtained as

$$\varepsilon_R = \frac{8}{9\pi} \left(\frac{2n}{2n+1} \right)^n \frac{a}{R} \quad (2.47)$$

The effective strain ε_R has a value ranging from $0.189(a/R)$ to $0.172(a/R)$ as n varies from 1 to ∞ . This may be compared with Eq.(2.42) given by Tabor (1951).

Finite element methods have been extensively used to investigate the contact problems of elastic-plastic bodies since the late 1960's. Finite element methods were first employed by Akyuz and Merwin (1968) to investigate the two-dimensional stresses beneath a cylindrical indenter. Since then, Hardy *et al.* (1971), Lee *et al.* (1972), Follansbee and Sinclair (1984), Sinclair *et al.* (1985), Hill *et al.* (1989), Kral *et al.* (1993), Yu *et al.* (1995) and Mesarovic and Fleck (1999, 2000) have also analysed the contact of elastic-plastic spheres using FEMs.



Fig. 2.4 The pressure distribution for the indentation of an elastic-plastic half-space by a rigid sphere: F_{y_0} and a_{y_0} are the contact force and contact radius at onset of plastic deformation (Hardy *et al.* 1971).

Hardy *et al.* (1971) studied the deformations and stresses produced in an elastic-perfectly plastic half-space indented by a rigid sphere using FEM. The pressure distributions obtained by Hardy *et al.* (1971) are shown in Fig. 2.4. A flattening of the pressure distribution is apparent and at high loads the peak of the pressure distribution moves slightly towards the edge of the contact. Lee *et al.* (1972) used FEM to analyse the indentation process of an elastic-plastic material due to the impact of a sphere. The load-displacement curve, plastic zone development and indentation pressures were investigated. Follansbee and Sinclair (1984) and Sinclair *et al.* (1985) analysed quasi-static normal indentation of an elasto-plastic half-space by a rigid sphere under higher load levels using FEM, in which constant-strain-triangle elements were used. The indentation response with increasing pressure, contact and interior stresses during loading and unloading, yield region growth, strain distributions and surface displacement profiles were provided. Kral *et al.* (1993) investigated the elastic-plastic contact problem of a rigid sphere repeatedly

indenting a homogeneous half-space using FEM. The load range between elastic and fully plastic was considered. The material properties of the half-space were specified to be either elastic, elastic-perfectly plastic and elastic-plastic with isotropic work hardening. The results for the contact pressure distribution and the force-displacement relationship were presented.

Most recently, Mesarovic and Fleck (1999) performed a numerical study of the indentation of an elastic-plastic half-space by a rigid sphere using FEM. Indentation maps were constructed to distinguish between the regimes of deformation mode in terms of the ratio of contact radius a to the sphere radius R and the yield strain of the half-space Y/E . They showed that the fully plastic regime could be subdivided into two regimes: a plastic similarity regime and a finite deformation plastic regime. For the former that corresponds to relatively small contact sizes, a similarity solution for rigid plastic indentation applies. While for the latter where the contact size is relatively large, a finite-deformation mode dominates. They found that for the deformations within the plastic similarity regime, the degree of deformation could be defined by a single non-dimensional parameter aE^*/RY . However for finite deformation plastic contact, this parameter ceases to uniquely define the degree of deformation. Instead, the normalised contact size a/R becomes the controlling non-dimensional parameter. For the indentation of an elastic-perfectly plastic half-space by a rigid sphere, they showed that the finite deformation plastic contact begins at

$$a/R = 0.16 \tag{2.48}$$

and the mean contact pressure begins to drop with increasing contact size, rather than keeping constant as it does in the plastic similarity regime. This result was found to be consistent with the experimental observation of Chaudhri *et al.* (1984), Timothy and Hutchings (1986a, 1986b) and Chaudhri (1987).

The contact of two spheres of different diameters and different material properties was modelled by Mesarovic and Fleck (2000) using FEM. The analysis showed that the onset of the finite deformation regime is not governed only by a critical value of a/R^* for all the cases considered. Moreover, it is dependent upon the relative size of the deformable spheres too: the smaller the relative size of the deformable spheres, the smaller is the critical value of the contact radius a/R^* for the onset of the finite deformation regime. It was shown that for the elastic-perfectly plastic solids the similarity/finite deformation boundaries differ by a factor of about 2 in a/R^* between the contact of two identical spheres and that of a sphere with a half-space.

2.2.3.3 Contact force-displacement relationship

The contact force-displacement relation is crucial for understanding the impact behaviour of elastic-plastic particles. The analytical derivation of the contact force-displacement relation should be based on the determination of both the contact pressure distribution and the relation between the relative approach and the contact radius. For fully plastic contact within the plastic similarity regime, it is generally accepted that the mean contact pressure is constant $(2.8 \sim 3.0)Y$ and the relative approach is related to the contact radius by $\alpha = a^2 / 2R^*$ provided that neither piling-up nor sinking-in occurs (see Johnson 1985; Tabor 1951; Crook 1953). The force-displacement relation can hence be determined. However, for fully plastic contact/impact within the finite deformation plastic regime, as shown by Mesarovic and Fleck (1999, 2000), the mean contact pressure no longer remains constant, instead, it decreases with the increased contact size. In addition, either piling-up or sinking-in is inevitable, so that the simplified relation $\alpha = a^2 / 2R^*$ does not hold. Thus the solution for this case becomes more complicated and has not been solved yet.

Several attempts have been made to bridge the gap between purely elastic contact and fully plastic contact. For the transition regime from purely elastic to fully plastic contact (elastic-plastic regime), an accurate determination of the contact pressure distribution and the correlation between relative approach and contact radius becomes more complicated. Therefore most analyses are based on some assumptions to simplify the problem. Bitter (1963) assumed that, after yield is initiated, the pressure is constant and the area that is loaded to the constant pressure increases upon further approach of the particle into the body. A flattened contact pressure distribution obtained by truncating the Hertzian pressure profile was proposed by Thornton (1997) and Thornton and Ning (1998), who also assumed that the Hertzian substitution $a^2 = R^* \alpha$ is still valid for the elastic-plastic regime. A relation between the relative approach and the contact radius was proposed by Chang *et al.* (1987) on the basis of volume conservation for plastically deformed spheres. However the model fails to evolve smoothly from the elastic regime to the plastic regime since a constant mean contact pressure was assumed for the whole deformation process. For the transition from elastic deformation to fully plastic deformation, Zhao *et al.* (2000) proposed a force-displacement relationship using a logarithmic function to model the relation of the mean contact pressure to the relative approach, and a fourth-order polynomial function to

model the relation between the contact radius and the relative approach. Vu-Quoc and his co-workers (Vu-Quoc and Zhang 1999; Vu-Quoc *et al.* 2000) developed elastoplastic normal force-displacement models in which the contact radius is decomposed into an “elastic” part and a “plastic” part, and the contact curvature is modified by an adjustable coefficient to account for plastic deformation. In addition, the pressure distribution is assumed to be of similar pattern to Hertzian distribution.

Yigit and Christoforou (1994) proposed a simplified model for the contact force-displacement relationship of plastic bodies by combining the classical Hertz theory and the elastic-plastic indentation theory given by Johnson (1985). The formulae for three phases (elastic loading; elastic-plastic loading and elastic unloading) were given as following:

Phase I: elastic loading (Hertz theory)

$$F_n = \frac{4}{3} E^* R^{*1/2} \alpha^{3/2} \quad 0 \leq \alpha \leq \alpha_{y0} \quad (2.49)$$

Phase II: Elastic-plastic loading

$$F_n = K_y (\alpha - \alpha_{y0}) + \frac{4}{3} E^* R^{*1/2} \alpha_{y0}^{3/2} \quad \alpha_{y0} \leq \alpha \leq \alpha^* \quad (2.50)$$

Phase III: Elastic unloading

$$F_n = \frac{4}{3} E^* R^{*1/2} (\alpha^{3/2} - \alpha^{*3/2} + \alpha_{y0}^{3/2}) + K_y (\alpha^* - \alpha_{y0}) \quad (2.51)$$

where α_{y0} and α^* are the relative approach at the onset of plastic yielding and at the maximum compression, respectively; K_y is obtained by equating the slope of the elastic-plastic loading phase to that of the elastic loading at $\alpha = \alpha_{y0}$ and is given by

$$K_y = 2E^* R^{*1/2} \alpha_{y0}^{1/2} \quad (2.52)$$

Goldsmith and his co-workers (Goldsmith 1960; Goldsmith and Lyman 1960) reported some experimental results for plastic impacts of spheres and cylinders. The force evolutions during the impact were recorded using a piezo-electric gauge. Some typical force-time curves are reproduced in Fig. 2.5a. Moreover, the force-displacement relationships governing the contact of hard-steel balls and plane surfaces of various metals under both static and dynamic conditions were calculated. The static and dynamic force-displacement relationships were compared with each other and with the predictions of both

Hertz theory and the postulation of a constant flow pressure. The results indicated that an increasing stiffness is exhibited for all materials at low values of displacement. The harder steel subsequently exhibits a range during which a reasonable constant stiffness is maintained (see Fig. 2.5b). The softer metals all show a distinctly downward concave curvature of the force-displacement relation for larger magnitudes of relative approach (Goldsmith and Lyman 1960).



Fig. 2.5 (a) Force-time curves for the impact of two 1-in-diameter crossed lead cylinders (Goldsmith 1960) and (b) force-displacement relationship for the impacts of harder steel by a hard steel sphere (Goldsmith and Lyman 1960): 1-- $V_i=151.0$ ft/sec; 2--- $V_i=151.4$ ft/sec; 3--- $V_i=205.0$ ft/sec; 4--- $V_i=292.0$ ft/sec; 5--- $V_i=294.0$ ft/sec; A---static.

2.2.3.4 Coefficient of restitution

When collision occurs between two plastic bodies, if the initial kinetic energy is so high that plastic deformation initiates during the compression, the initial kinetic energy becomes elastic strain energy stored in the contacting bodies, plastic strain energy to deform the material plastically and energy for elastic wave to propagate. Since the plastic deformation is irreversible, during the restitution, only the stored elastic strain energy can be recovered as the rebound kinetic energy. Some of initial kinetic energy is thus dissipated by plastic deformation and stress wave propagation. For the impact of plastic bodies with an impact velocity less than a certain value, the energy lost due to plastic deformation and stress waves is negligible. Hence the rebound velocity is almost the same as the initial impact velocity and the coefficient of restitution is close to unity. As the impact velocity is

increased, more energy loss due to both plastic deformation and elastic wave propagation is expected. Therefore the coefficient of restitution becomes lower and lower as the impact velocity is increased.

The energy dissipated by stress wave propagation during plastic impact was analysed by Hutchings (1979), who showed that only a few per cent of the initial kinetic energy is normally dissipated by stress waves. Comparing with the energy dissipated by plastic deformation, the fraction of the kinetic energy dissipated by stress waves is relatively small. For instance, when a hard steel sphere collides with a mild steel block at a velocity of about 70m/s, the coefficient of restitution measured is about 0.4, in which only about 3% of the kinetic energy is dissipated by stress waves. Thus only a very small portion of the kinetic energy is generally dissipated owing to stress wave propagation during the collision of plastic bodies.

Several theoretical models in which the energy losses due to stress waves are generally neglected have been developed to predict the coefficient of restitution during the impact of elastic-plastic spheres. Thornton (1997) developed a theoretical model for the collinear impact of two elastic-perfectly plastic spheres, in which a Hertzian pressure distribution with a cut-off was proposed. In addition, the cut-off pressure p_y , was assumed to be a constant during plastic loading, which makes it possible to obtain an explicit analytical solution for the coefficient of restitution as follows,

$$e_n = \left(\frac{6\sqrt{3}}{5} \right)^{1/2} \left[1 - \frac{1}{6} \left(\frac{V_y}{V_{ni}} \right)^2 \right]^{1/2} \left[\frac{V_y/V_{ni}}{V_y/V_{ni} + 2\sqrt{6/5 - (1/5)(V_y/V_{ni})^2}} \right]^{1/4} \quad (2.53)$$

where V_{ni} is the impact velocity and V_y is the impact velocity below which the contact deformation is assumed to be elastic and is defined by

$$V_y = \left(\frac{\pi}{2E^*} \right)^2 \left(\frac{8\pi R^{*3} p_y^5}{15m^*} \right)^{1/2} \quad (2.54)$$

It should be noted that p_y and V_y do not represent the maximum contact pressure and the impact velocity at the instant when yield is initiated. Instead, they correspond to the instant when significant flattening of the contact pressure distribution commences. According to the data provided by Hardy *et al.* (1971), it is suggested that $p_y \approx 2.8Y$ (Thornton *et al.* 2001)

By concentrating on the fully plastic deformation regime, Johnson (1985) proposed a simplified model by introducing the following assumptions: (1) the relative approach is related to the contact radius by:

$$\alpha = \frac{a^2}{2R^*} \quad (2.55)$$

i.e. neither “pile-up” nor “sinking in” occurs at the edge of the indentation; (2) the mean contact pressure p_{dm} is constant and equal to $3.0Y$. Johnson then obtained an expression for the coefficient of restitution e_n which was written as

$$e_n^2 = \frac{W_r}{W_t} = \frac{V_{nr}^2}{V_{ni}^2} = \frac{3\sqrt{2}\pi^{5/4}}{5} \left(\frac{p_{dm}}{E^*} \right) \left(\frac{\frac{1}{2}m^*V_{ni}^2}{p_{dm}R^{*3}} \right)^{-1/4} \quad (2.56)$$

For the case of a sphere impacting a wall, Equation (2.56) can be rewritten as

$$e_n = 1.718 \left(\frac{p_{dm}^5}{E^{*4} \rho} \right)^{1/8} V_{ni}^{-1/4} \quad (2.57)$$

Tabor (1951) proposed a model for the plastic impact based on the following main assumptions: i) the energy involved in the release of the elastic stresses is equal to the energy of rebound of the indenter; ii) the difference between the initial kinetic energy and the rebound kinetic energy is the energy in producing the indentation and given by the multiplication of the mean contact pressure and the volume of the remaining permanent plastic deformation (indentation). An expression was then derived in terms of the impact and rebound velocities as

$$V_{nr}^8 = \hbar \left(V_{ni}^2 - \frac{3}{8} V_{nr}^2 \right)^3 \quad (2.58)$$

in which

$$\hbar = \frac{2 \cdot 3^4 \cdot 4^3 \pi^5 p_{ym}^5 R^3}{10^4 m^* E^{*4}} \quad (2.59)$$

By numerically solving Eq.(2.58), the coefficient of restitution can be calculated.

Based on the elastic-plastic loading model introduced by Chang *et al.* (1987), Chang and Ling (1992) developed an impact model for elastic-plastic spheres. The coefficient of restitution e_n was written as

$$e_n^2 = \frac{W_r}{W_i} = \frac{\frac{8}{15} E^* R^{1/2} \alpha_{y0} \alpha^{*3/2} \left(2 - \frac{\alpha_{y0}}{\alpha^*}\right)^{3/2}}{\frac{8}{15} E^* R^{1/2} \alpha_{y0}^{5/2} + \pi \bar{p}_{y0} R \alpha^* (\alpha^* - \alpha_{y0})} \quad (2.60)$$

where α_{y0} and α^* are the relative approach at the onset of plastic yielding and at the maximum compression, respectively.

Stronge (1995) derived an analytical expression for the energetic coefficient of restitution introduced by Stronge (1990) for the impact of elasto-plastic bodies with moderate impact speed and small maximum indentation. Using the mean contact pressure in the elastic-plastic regime obtained by Johnson (1985) (see Eq.(2.40)) and subdividing the relative approach α for plastic contact/impact into the residual permanent approach α_r and the elastic recovered approach α_e , Levy and Parry (1981) studied the elastic-plastic impact.

Most of the theoretical models discussed above generally ignored the effect of work hardening. Only Tabor (1951) extended his impact model of elastic-perfectly plastic bodies to take account of the work hardening, in which the total contact force F_n is related to the contact radius a or the relative approach α by

$$F_n = k_1 a^n \approx k_2 \alpha^{n/2} \quad (2.61)$$

where k_1 and k_2 are constants and n is the Meyer index typically varying between values of 2 for an elastic-perfectly plastic metal and 2.5 for a fully annealed metal. A value of $n = 3$ corresponds to the Hertzian analysis of elastic contact. Then an expression for the rebound velocity was obtained

$$V_r = \hbar (V_i^2 - \mathfrak{R} V_r^2)^\beta \quad (2.62)$$

where \mathfrak{R} is related to the Meyer index n by

$$\mathfrak{R} = \frac{2n-1}{2n+4} \quad (2.63)$$

Some experimental results for the collision of elastic-plastic spheres have also been published in the literature (see Tabor 1948; Goldsmith and Lyman 1960; Bridges *et al.* 1984; Labous *et al.* 1997; Kharaz and Gorham 2000). The experimental results for coefficient of restitution were given by Tabor (1948) for cast steel and drawn brass balls with impact velocities up to 4.5m/s. It was shown that the coefficient of restitution is not constant in general. Experimental results of the collision of a hard steel sphere against plane surface of various metals were reported by Goldsmith and Lyman (1960), who calculated the coefficient of restitution from the initial and rebound velocities of the ball measured with a stroboscopic camera. Bridges *et al.* (1984) reported some preliminary experimental results of the coefficient of restitution for the collision of ice particles at impact velocities relevant to Saturn's rings, in order to better understand ice-particle collision processes. They obtained the following empirical expression for the coefficient of restitution:

$$e = (0.32 \pm 0.02)V_i^{-0.234 \pm 0.008} \quad (2.64)$$

for the range of the impact velocity $0.015\text{cm/s} < V_i < 5.1\text{cm/s}$.

The impact of two nylon spheres was experimentally studied by Labous *et al.* (1997) using high-speed video analysis. The size and velocity dependences of the coefficient of restitution were investigated. It was suggested that there were two basic energy dissipation regimes: i) plastic deformation at high impact velocity and ii) visco-elastic dissipation at lower impact velocities. More recently, accurate measurements of the coefficient of restitution have been made by Kharaz and Gorham (2000) for the impact of 5mm elastic (aluminium oxide) spheres on thick plates of steel and aluminium alloy over a wide velocity range. The variations in the coefficient of restitution with the impact velocity were reported. The experimental results showed that the effect of work hardening was significant during the impact, which results in a higher coefficient of restitution than that predicted by elastic-perfectly plastic impact theory, such as Thornton theory (Thornton 1997). Some FEA results were reported by Walton (1992) using the non-linear, explicit finite element code DYNA2D for the impact of elastic-plastic spheres. Li *et al.* (2000) reported some FEA results for the impact of elastoplastic spheres. Influences of material behaviour were discussed and their effect on the coefficient of restitution was demonstrated. The coefficients of restitution for normal impact of elastoplastic particles were also presented by Ning and Thornton (1994) and Ning (1995) using DEM. The dependence of the coefficient of restitution upon the impact velocity was illustrated.

2.3 Oblique impact

So far we have reviewed research works dealing with the normal impact. Oblique impacts between rough bodies are also common phenomena in engineering applications. Thus the mechanisms involved in the oblique impact have become the topics of many publications. In this section, a review on the oblique impact of rough particles is presented.

2.3.1 Rigid body dynamics

Rigid body dynamics was first developed as an initial simple approach to predict the impact behaviour of objects (see, for example, Goldsmith 1960), and has been extensively advanced (see Keller 1986; Brach 1988, 1998; Smith 1991; Wang and Mason 1992; Stronge 1993; *etc.*). Rigid body dynamics is in principle based on the impulse-momentum law, in which the tangential effects are limited by Coulomb friction. It is assumed that the effect of impact may be modelled by applying a single point impulse to each contacting body at the contact point. The impulse is generally decomposed into two components, P_n and P_t , normal and tangential to the plane that is mutually tangent to the contacting bodies at the contact point. Once these impulsive components are known, the normal and tangential rebound velocities of the bodies at their centres of mass can be determined from the following impulse-momentum equations:

$$P_n = m_1(V_{nr}^1 - V_{ni}^1) = -m_2(V_{nr}^2 - V_{ni}^2) \quad (2.65a)$$

$$P_t = m_1(V_{tr}^1 - V_{ti}^1) = -m_2(V_{tr}^2 - V_{ti}^2) \quad (2.65b)$$

where m_i is the mass of the body i ($i=1, 2$), superscripts 1 and 2 refer to contacting bodies 1 and 2, respectively. Subscripts n and t refer to the components in the normal and tangential directions, and i and r denote the initial and rebound velocities of the sphere centres, respectively. Since the impact is modelled as the interaction at the contact patch imparted by a point impulse, the angular momentum of each body is conserved about the contact point. Hence, for the collision of two spheres, we have

$$I_1(\omega_r^1 - \omega_i^1) = P_t R_1 \quad (2.66a)$$

$$I_2(\omega_r^2 - \omega_i^2) = P_t R_2 \quad (2.66b)$$

where ω is the angular velocity, I_i is the mass moment of inertia of the body i ($i=1, 2$), R_1 and R_2 are the radii of the spheres 1 and 2, respectively.

It can be seen from Eqs.(2.65) and (2.66) that there are six unknowns, but only four equations. In order to solve the rebound velocities, two more equations are required. One of these two required equations can be obtained by relating the normal components of rebound velocities with those of initial velocities, for which the normal coefficient of restitution e_n is generally introduced and is defined as

$$e_n = \frac{V_{nr}}{V_{ni}} \quad (2.67)$$

For rigid body impacts, it is often assumed that the coefficient of restitution e_n is a constant.

The other required equation can generally be obtained by considering the correlation between normal and tangential response. The conventional rigid body dynamics assumes that (Whittaker 1904)

$$v_{tr} = 0 \quad \text{for } P_t \leq \mu P_n \quad (2.68a)$$

while if $v_{tr} > 0$

$$P_t = \mu P_n \quad (2.68b)$$

where the lower case v denotes the velocity of the contact patch. However, it has been shown by Maw *et al.* (1976, 1981) and Johnson (1983, 1985) that this assumption cannot accurately predict the rebound behaviour at small impact angles, in which the tangential velocity reverses its direction during the impact. Many works have been carried out to improve the accuracy of rigid body dynamics. An analytical solution was given by Keller (1986), who determined the relative tangential velocities at the contact point during the impact from the equations of motion of the two bodies. The tangential relative velocity and friction produce a time varying friction force exerted at the contact point. The tangential impulse during the impact was then obtained from the integral of the tangential force. The analysis indicated that the conventional rigid body dynamics is inapplicable for the impact cases during which the tangential velocity reverses its direction (Keller 1986).

Brach (1988) analysed the rigid body dynamics using an impulse ratio to correlate tangential and normal interactions, together with the classical coefficient of restitution e_n . The impulse ratio is defined as the ratio of tangential impulse to normal impulse

$$f = \frac{P_t}{P_n} \quad (2.69)$$

Brach (1988) pointed out that the impulse ratio f may or may not equal the coefficient of friction μ . It was shown that a distinction between the impulse ratio f and the friction coefficient μ is necessary for a proper interpretation of impact data. If f is known a priori, the system of equations can be solved explicitly for the rebound parameters.

Smith (1991) proposed that the tangential impulse P_t would be related to the normal impulse P_n by taking account of the tangential components of the initial and rebound velocity as follows

$$P_t = -\mu |P_n| \frac{|v_{ti}|v_{ti} + |v_{tr}|v_{tr}}{|v_{ti}|^2 + |v_{tr}|^2} \quad (2.70)$$

Equation (2.70) reduces to Eq.(2.68b) when v_{tr} and v_{ti} have the same direction. The analysis of the impact of two unstrained spheres using the above assumption illustrated that the proposed assumption leads to results that appear to be more reasonable than those given by Eq.(2.68).

Wang and Mason (1992) presented an analysis of two-dimensional rigid body collision with dry friction. The possible modes of impact were classified and analytical expressions for impulse were derived using Newton's and Poisson's definitions of coefficient of restitution, respectively. It was shown that the correct identification of the contact mode of impact is essential to accurately predict the rebound behaviour. Stronge (1993) employed the Coulomb coefficient of friction μ to relate the normal and tangential impulses during the relative sliding. The coefficient of friction is considered to be constant irrespective of static and dynamic condition. Analytical solutions were obtained for six different impact cases: sliding halting during compression, sliding reversing during compression, sliding halting during restitution, sliding reversing during restitution, sliding continuing throughout the impact with either decreasing or increasing velocity.

Since rigid body dynamics is of its nature based on the impulse-momentum law and does not include the material properties, the influence of the contact deformation is ignored and the tangential compliance of the bodies is not taken into account. It hence cannot predict the stresses and forces induced during the impact. Its accuracy in predicting the rebound behaviour of bodies is limited (Johnson 1985). To accurately predict the oblique impact behaviour of bodies, the contact deformation must be taken into account.

2.3.2 Frictional contacts with tangential loading

Consider now the application of a monotonically increasing tangential force to a Hertz contact with friction over the contact interface at constant normal force. It was shown by Mindlin (1949) that there is a central stick region surrounded by slip regions within the contact area. As the tangential force increases, the size of the stick region shrinks inwards until overall sliding begins. The sliding occurs with Coulomb's law of dry friction satisfied. According to Coulomb's law of dry friction, any points in the contact area must be in one of two states for frictional contact with tangential loading: i) sticking, during which there is no relative motion between adjacent points in the two contacting bodies and the resultant tangential traction is less than μp ; and ii) slip, during which relative motion occurs and the resultant tangential traction is of magnitude μp and opposes the instantaneous direction of slip. Mindlin (1949) also showed that when slip occurs over the contact surface, it starts at the circumference of the contact area and progresses radially inward so that the portion on which slip occurs is an annulus of outer radius a and inner radius c , where

$$c = a \left(1 - \frac{F_t}{\mu F_n} \right)^{1/2} \quad (2.71)$$

in which, F_n and F_t are the normal and tangential forces, respectively. The distribution of tangential traction over the total contact surface is given as

$$q(r) = \left(\frac{3\mu F_n}{2\pi a^2} \right) \left(1 - \frac{r^2}{a^2} \right)^{1/2} \quad c \leq r \leq a \quad (2.72a)$$

$$q(r) = \left(\frac{3\mu F_n}{2\pi a^2} \right) \left[\left(1 - \frac{r^2}{a^2} \right)^{1/2} - \frac{c}{a} \left(1 - \frac{r^2}{c^2} \right)^{1/2} \right] \quad 0 \leq r \leq c \quad (2.72b)$$

It is clear that the tangential traction in the slip region is given by $q(r) = \mu p(r)$, where $p(r)$ is defined in Eq.(2.1). The tangential traction distribution (2.72b) is obtained by superimposing on Eq.(2.72a) a negative traction over the stick region:

$$q'(r) = -\left(\frac{3\mu F_n}{2\pi a^2}\right) \frac{c}{a} \left(1 - \frac{r^2}{c^2}\right)^{1/2} \quad (2.72c)$$

as shown in Fig. 2.6.



Fig. 2.6 Tangential traction distribution (Mindlin 1949).

The relative tangential displacement of the centres of the two spheres δ is given by

$$\delta = \frac{3\mu F_n (2-\nu)}{8G^* a} \left[1 - \left(1 - \frac{F_t}{\mu F_n} \right)^{2/3} \right] \quad (2.73)$$

From Eq.(2.73), the tangential compliance S can be obtained

$$S = \frac{d\delta}{dF_t} = \frac{2-\nu}{4G^* a} \left(1 - \frac{F_t}{\mu F_n} \right)^{1/3} \quad (2.74)$$

where G^* is the shear modulus of the material. Mindlin's results were extended to other loading scenarios by Mindlin and Deresiewicz (1953). Their analysis showed that for the contact of two bodies the traction distribution over the interface at any instant depends not only upon the value of the normal and tangential loads but also upon the whole previous loading history.

The contact between dissimilar elastic materials was investigated by Bentall and Johnson (1967), Sackfield and Hills (1988) and Hills *et al.* (1993). A parameter β was introduced to denote the dissimilarity of the material properties (see Johnson 1985):

$$\beta = \frac{1}{2} \frac{[(1-2\nu_1)/G_1] - [(1-2\nu_2)/G_2]}{[(1-\nu_1)/G_1] + [(1-\nu_2)/G_2]} \quad (2.75)$$

Fig. 2.7 Influence of a difference in elastic constants on the normal pressure and tangential traction distribution during (a) sliding contact with $\mu = 1.0$ (Johnson 1985); (b) tangential loading of elastic cylinder with $\beta = 0.4$ and $\mu = 0.5$ (Hills *et al.* 1993).

It has been shown that, for sliding contact, the effect of the difference in material properties on the tangential traction is to shift the centre of the contact region towards the trailing edge, *i.e.*, the centre of pressure moves towards the trailing edge (Fig. 2.7a). However, the comparison with the Hertz pressure distribution shows that the effect is small (Johnson 1985). For the tangential loading of an elastic cylinder, Hills *et al.* (1993) showed that the stick zone is substantially offset when compared with that predicted by Mindlin's analysis (Mindlin 1949) and the traction distribution is not symmetric (see Fig. 2.7b). Nevertheless, the effect is modest for practical values of β and μ . Goodman (1962) also showed that for a pair of spheres with different elastic materials the coupling between normal and shear stresses is small and may be neglected.

Rolling contacts (rotation with translation motion) with friction have been extensively investigated by many researchers with special applications to the railway industry (see Johnson 1985). Similarly to the analysis of Mindlin (1949), it was recognised that there are two distinct regions within the contact area: stick and micro-slip. However, the stick region was found to be no longer centrally located. Experimental observations by Johnson (1962), in which a rubber ball was rolling on a transparent plane, showed the stick region is "pear" shaped and one edge coincides with the leading edge of the contact boundary (see also Johnson 1985). The typical traction distribution for rolling contacts obtained by Kalker (1967a, 1967b) and Haines and Ollerton (1963) is shown in Fig. 2.8. Similar results are

also obtained by Liu and Paul (1989). An intermediate case was proposed by Poritsky (1950), in which the stick region shifts towards the leading edge of the contact ellipse but does not coincide with the leading edge. The traction distribution for this case is shown in Fig. 2.9.



Fig. 2.8 Tangential traction distribution during the rolling contact (From Johnson 1985, p265): solid line-numerical theory (Kalker 1967a); circle-photo-elastic measurements (Haines and Ollerton 1963).



Fig. 2.9 Tangential traction distribution proposed by Poritsky (1950).

For frictional contacts with tangential loading, the effect of friction is to superimpose a stress that is induced by the tangential traction. This tangential traction alters the stresses in the contacting bodies and hence changes the loading condition at which plastic deformation is initiated. The internal stresses due to the combined effect of normal pressure and tangential traction in sliding contacts were analysed by Johnson and Jefferis (1963), Hamilton and Goodman (1966), Bryant and Keer (1982), and Sackfield and Hills (1983). The analysis showed that due to the effect of friction the point of maximum shear stress moves closer to the contacting surfaces. Both Tresca and von Mises yield criteria were adopted to determine the contact pressure for the onset of yield in sliding contacts by Johnson and Jefferis (1963). Their results showed that for low values of the coefficient of friction ($\mu \leq 0.25$ by Tresca criterion and $\mu \leq 0.3$ by von Mises criterion) the yield point is still reached at a point beneath the contact surface. For large value of μ , yielding first occurs at the interface, rather than in the subsurface. The prediction of Johnson and Jefferis (1963) was demonstrated by the finite element analysis of the sliding of a rigid cylinder

over a surface reported by Tengena and Hurkx (1985), who also illustrated that the formation of prow occurs when a rigid cylinder slides over an plastic substrate with high friction coefficients.

2.3.3 The elastic model of oblique impact (Maw *et al.* 1976)

For the oblique impact with friction, an accurate prediction of the rebound behaviour must take the contact deformation into account. Hence the problem is much more complicated. As concluded by Mindlin and Deresiewicz (1953), for contacts between two bodies, the response at any instant depends not only on the present value of the normal and tangential loads but also on the history of such loadings. Hence the variations of contact radius, the contact pressure and the tangential traction must be calculated step by step. This methodology was employed by Maw *et al.* (1976) to analyse the oblique impact of two elastic spheres. Here we refer to the analysis of Maw *et al.* (1976) as the elastic model of oblique impact.

In the elastic model of oblique impact, the normal interaction is predicted by Hertz theory (see Section 2.2.1). Although Hertzian theory in general predicts an elliptical contact area, the elastic model of oblique impact assumes the contacting bodies to be spherical at the contact point, giving a circular contact area to simplify the implementation of the tangential effect. In such a way, the system considered is symmetric with respect to the plane of motion. Coulomb's law of friction is employed to model tangential effects and it is assumed that the static and dynamic coefficients of friction are equal and constant. The model has been developed for a sphere striking against a half-space of the same material.

During the impact the maximum contact radius a^* is determined by Hertz theory of elastic impact (see Eq.(2.16))

$$a^* = \left(\frac{15 m^* R^{*2} V_{ni}^2}{16 E^*} \right)^{1/5} \quad (2.76)$$

In the elastic model of oblique impact, the maximum contact area is discretized into n annuli. At any given time t , the total tangential traction q at a radius r is in the direction of motion and can be equated to the following summation:

$$q_{(r)} = \sum_{i=j}^n q_{ii} \left[1 - \frac{n^2 r^2}{a^2 i^2} \right]^{1/5} \quad (2.77)$$

where j is the smallest integer bigger than nr/a^* and the traction coefficient q_{ii} are defined so that the equation holds. The system is solved for each time step once the n traction coefficients q_{ii} have been determined. This is achieved by creating a system of n equations for q_{ii} .

As the impact progresses, a given contact annulus is treated as sticking, sliding or not being in contact. In the stick region, the tangential displacement is prescribed, being the sum of the displacement of the sphere during the time increment and that before the time increment. Certain equations in q_{ii} can then be established. For sliding regions, tangential traction is given by multiplying the coefficient of friction by the Hertian normal pressure distribution, $q_{ii} = 0$ is given for the region outside the contact area. Each of the n annuli, whichever region it is in, contributes one equation towards a solvable system of equations for determining the n traction coefficients q_{ii} . In this manner the mixed boundary value problem involving displacements and tractions may be solved by a set of simultaneous equations.

Once every annulus has been described as either sticking, or sliding, or not in contact, the overall traction is found and checked for consistency over each annulus. The stick annuli are checked to ensure that the tangential traction does not exceed the product of the friction coefficient and the normal pressure. For sliding regions, the direction of sliding is checked to see if it is in the expected direction. If either of these conditions is not satisfied, the situation of the annulus is changed, for which the traction is found. The process is repeated until all the conditions are satisfied. Then the tangential force F_t at time t is found by integrating the traction distribution over the contact area

$$F_t = \frac{2\pi a^2}{3} \sum_{i=1}^n \frac{i^2 q_{ii}}{n^2} \quad (2.78)$$

This force is assumed constant over the time step and used to update the tangential relative velocity of the bodies at the contact patch.

With intensive numerical computations, both the interaction and the rebound behaviour of the elastic sphere were determined. Results showed that the response of oblique elastic

impacts could be characterised by two non-dimensional parameters. One of these parameters is related to the material and geometrical properties of the contacting bodies as follows

$$\chi = \frac{(1-\nu)(1+I/K^2)}{2-\nu} \quad (2.79)$$

where

$$K^2 = \frac{I}{mR^2} \quad (2.80)$$

in which, I is the mass moment of inertia.

Another parameter is the dimensionless impact angle related to the impact velocity,

$$\psi_i = \frac{\kappa V_{ti}}{\mu V_{ni}} \quad (2.81)$$

where V_{ni} and V_{ti} are the normal and tangential components of the initial velocity, respectively, κ is the ratio of the tangential to normal stiffness,

$$\kappa = \frac{(1-\nu_1)/G_1 + (1-\nu_2)/G_2}{\left(1-\frac{\nu_1}{2}\right)/G_1 + \left(1-\frac{\nu_2}{2}\right)/G_2} \quad (2.82)$$

G_1 and G_2 are the shear modulus of the contacting bodies, ν_1 and ν_2 are Poisson's ratios, respectively.

Figure 2.10 shows the variation of the tangential force throughout the impact process for similar homogeneous spheres under different incident conditions. For impact angles which are small compared with the angle of friction ($\psi_i \leq 1$) there is no sliding at the start of the impact. For larger impact angles ($1 < \psi_i < (4\chi - 1)$) the impact starts and finishes with sliding; in between no sliding is observed. If the impact angle is sufficiently high ($\psi_i \geq (4\chi - 1)$) sliding occurs throughout the impact. Provided that the impact angle is not too large it is clear from Fig. 2.10 that the tangential force undergoes a reversal during the impact, whereas the normal force completes a half cycle only. Figure 2.11 illustrates the variation of the reflection angle of the contact patch with the dimensionless impact angle. The reflection angle of the contact patch shown in Fig. 2.11 is also in the corresponding non-dimensional form

$$\psi_r = \frac{\kappa V_{tr}}{\mu V_{ni}} \quad (2.83)$$

where v_r is the tangential component of the rebound velocity at the contact patch. The reflection angle at the contact patch is found to be mainly negative except for $\psi_i \geq 4\chi$. This phenomenon has been substantiated by experiments (Maw *et al.* 1981; Johnson 1983; Gorham and Kharaz 2000). For large impact angles, every annulus in contact is sliding throughout the impact and the elastic model of oblique impact gives the same results as the rigid body dynamics with a coefficient of restitution of unity.



Fig. 2.10 Tangential force evolution during the impact of homogeneous solid spheres (Maw *et al.* 1976, 1981).

Fig. 2.11 The reflection angle of the contact patch for the oblique of homogeneous solid spheres (Maw *et al.* 1976, 1981).

In the elastic model of oblique impact, all the normal effects are handled by Hertz theory so that the normal impact is assumed to be purely elastic and the elastic wave effects are neglected. It does not account for any normal energy loss during the impact and assumes a coefficient of restitution of unity. Therefore it cannot be used to predict the rebound behaviour of oblique impact involving plastic deformation. An attempt to deal with plastic oblique impact has been made by Stronge (1994).

2.3.4 Lumped parameter model (Stronge 1994)

Stronge (1994) developed a lumped parameter model of contact between colliding bodies, in which it is assumed that both the colliding bodies are rigid except for an infinitesimally small deformable region that separates the bodies at the contact points. This infinitesimally small deformable region is modelled by applying two independent compliant elements (normal and tangential) to connect with a supposed massless particle located at the initial contact point. Both normal and tangential compliant elements are assumed to be

“piecewise” linear. During the compression, the normal elements has contact stiffness k_n while the tangential one has stiffness k_t , and

$$k_t = \kappa k_n \quad (2.84)$$

where κ is the ratio of tangential to normal stiffness at the contact point, as defined in Eq.(2.82). Introducing the normal coefficient of restitution e_n and assuming the normal unloading curve is “piecewise” linear, then the unloading stiffness can be related to the loading stiffness as following:

$$k_{nu} = \frac{k_n}{e_n^2} \quad (2.85)$$

For a linear compliant element, the colliding bodies undergo separate stages of simple harmonic motions during compression and restitution. Thus the normal component of the relative velocity during the impact is as follows,

$$V_n(t) = V_{ni} \cos \Omega_n t \quad (\text{during compression}) \quad (2.86a)$$

$$V_n(t) = e_n V_{ni} \cos \left[\frac{\Omega_n t}{e_n} + \frac{\pi}{2} \left(1 - \frac{1}{e_n} \right) \right] \quad (\text{during restitution}) \quad (2.86b)$$

where Ω_n is the normal natural frequencies and given by

$$\Omega_n = \sqrt{\frac{k_n}{m}} = \frac{\pi}{2t_c} \quad (2.87)$$

and t_c is the instant when the compression period terminates. The normal component of impulse that causes the changes in velocity can be obtained directly from Eq.(2.86) and the impulse can be differentiated to obtain the normal contact force.

For tangential impact response, the state of stick and sliding are treated separately. Suppose stick occurs at time $t = \tau$, in which instant the sphere has relative displacement $\delta(\tau)$ and velocity $v_t(\tau)$ at the initial contact patch. Since there is no sliding while stick occurs,

$$v_t(t) + \dot{\delta}(t) = 0 \quad t \geq \tau \quad (2.88)$$

where $\dot{\delta}(t) = d\delta / dt$. Assuming that simple harmonic motion also applies to the tangential response, the tangential displacement, velocity and the contact force can hence be expressed for $t \geq \tau$ as

$$\delta(t) = \delta(\tau) \cos \Omega_t (t - \tau) - \frac{1}{\Omega_t} v_t(\tau) \sin \Omega_t (t - \tau) \quad (2.89a)$$

$$v_t(t) = \Omega_t \delta(\tau) \sin \Omega_t (t - \tau) + v_t(\tau) \cos \Omega_t (t - \tau) \quad (2.89b)$$

$$F_t(t) = m_t \Omega_t^2 \delta(\tau) \cos \Omega_t (t - \tau) - m_t \Omega_t v_t(\tau) \sin \Omega_t (t - \tau) \quad (2.89c)$$

where Ω_t is the tangential natural frequencies

$$\Omega_t = \sqrt{\frac{k_t}{m_t}} = \sqrt{\frac{\kappa \kappa_n}{m_t}} = \frac{\pi \sqrt{\kappa}}{2t_c} \sqrt{\frac{m}{m_t}} \quad (2.90)$$

and

$$m_t = m \left(1 + \frac{1}{K^2} \right)^{-1} \quad (2.91)$$

For the state of sliding, Coulomb's law for dry friction is assumed to be applicable and the coefficients of static and dynamic friction are identical. Thus sliding begins only if

$$\left| \frac{F_t}{F_n} \right| = \mu \quad (2.92)$$

For sliding,

$$dP_t = -\mu s dP_n \quad (2.93a)$$

$$dP_n = m dV_n \quad (2.93b)$$

where $s \equiv \text{sgn}(v_t + \dot{\delta})$.

In the lumped parameter model, the tangential velocities of the contact patch are obtained for different ranges of impact angle. It has been shown by Stronge (1994) that the lumped parameter model has similar processes that develop at the contact patch in three ranges of impact angle to the solution of Maw *et al.* (1976) for elastic oblique impact. Although deviations between predictions of Stronge (1994) and Maw *et al.* (1976) exist at small and intermediate impact angles, it was suggested that in almost all respects the results of these models are practically identical. An advantage of the lumped parameter model is that the effect of the normal coefficient of restitution is taken into account. The significance of the normal coefficient of restitution e_n on the reflection angle at the contact patch predicted by the lumped parameter model is shown in Fig. 2.12. It is clear that the impact angle for sliding which occurs throughout the impact decreases as the normal coefficient of restitution decreases.

Fig. 2.12 The reflection angle of the contact patch for different values of normal coefficient of restitution (Stronge 1994, 2000).

The lumped parameter model can also predict the maximum tangential force during the oblique impact, which is of general interest in practical engineering since, for instance, wear rate of steel tubes is closely correlated with the maximum tangential force which varies with the impact angle (Ko 1985). An experimental investigation of the peak force was performed by Lewis and Rogers (1988). Piezoelectric force transducers were used to make separate measurements of the normal and tangential forces during the impact of a steel sphere of 25.4mm in diameter with a heavy steel plate at impact angles varying between 0° and 85° . Four series of tests at different impact speeds were conducted. Each gives a largest measurement of tangential force at an impact angle of about 40° . The analysis of Stronge (1994) showed that the maximum values vary with the impact angle and the coefficient of friction. For the same coefficient of friction as reported by Lewis and Rogers (1988), the lumped parameters model gave a maximum value of peak tangential force at about 35° irrespective of impact speed.

2.3.5 Other previous works on oblique impacts

Walton and Braun (1986) and Walton (1992) introduced a third parameter, the rotational coefficient of restitution e_r , and constructed a model in which three parameters (e_n , μ , e_r) were used to describe the rebound characteristics of inelastic and frictional impact. In the model, the rotational coefficient of restitution e_r was defined as the ratio of the tangential rebound velocity to the tangential initial impact velocity at the contact patch,

$$e_r = -\frac{v_{tr}}{v_{ti}} \quad (2.94)$$

It was shown that for impacts during which sliding occurs throughout the impact, e_r is proportional to $\tan\theta$, where θ is the impact angle, as indicated by Maw *et al.* (1976, 1981). Walton and Braun (1986) and Walton (1992) simply classified impacts during which sliding does not occur throughout the impact as rolling and a constant limiting value of the rotational coefficient of restitution e_{ro} is assumed for impact angles falling into this range. However, this is a crude approximation since, according to the analysis of Maw *et al.* (1976, 1981), the rebound angle of the contact patch varies with the impact angle for this range of impact angles. The expressions for e_r proposed by Walton and Braun (1986) and Walton (1992) can be generalised as

$$e_r = \begin{cases} -1 + \mu \left(1 + \frac{I}{K} \right) (1 + e_n) \frac{v_{ni}}{v_{ti}} & \text{for sliding} \\ e_{ro} & \text{for rolling} \end{cases} \quad (2.95)$$

where K is defined in Eq.(2.80).

Some experimental works on oblique impacts of particles have been reported in literature. Maw *et al.* (1981) conducted an experimental investigation of the oblique impact of a puck-like disk with a fixed target. The angles of incidence and reflection were measured. The experimental results obtained using steel and rubber showed good agreement with the theoretical predictions of Maw *et al.* (1976). The work of Maw *et al.* (1976, 1981) was also demonstrated by experiments undertaken by Johnson (1983), who measured the reflection and the incident angle of a “super-ball”, a solid rubber ball, impinging on a heavy steel plate at a small speed. The effects of material properties and plate thickness on the coefficient of restitution were experimentally investigated by Sondergaard *et al.* (1990), who studied the impact of solid spheres with flat plates. The experiments revealed that the data for the normal coefficient of restitution were quite consistent and repeatable but the data for the tangential coefficient of restitution exhibited a significant scatter. It was also shown that the impulse ratio defined by Eq.(2.69) increased systematically with the impact angle until a critical angle was reached. A high-speed video technique was used to measure the impact properties of spheres by Labous *et al.* (1997). They investigated the size and velocity dependence of the coefficient of restitution. By using the model of Walton and Braun (1986) and Walton (1992), the three impact parameters were obtained: $e_{ro} = 0.5 \pm 0.1$, $e_n = 0.97 \pm 0.07$ and $\mu = 0.175 \pm 0.1$. More recently, an experimental technique was proposed to measure the low velocity impact behaviour of spherical particles with high accuracy by Kharaz *et al.* (1999). By employing this technique, Gorham and

Kharaz (2000) reported some experimental results of 5mm aluminium oxide spheres impinging against a thick soda-lime glass anvil and an aluminium alloy anvil. The former was considered to deform fully elastically, while the latter exhibited some plastic deformation. The oblique impacts of a spherical particle with a target which was assumed to be ideal rigid-plastic were both theoretically and experimentally studied by Rickerby and Macmillan (1980), Hutchings *et al.* (1981) and Sundararajan and Shewmon (1987) with the emphasis on the erosion of the target.

Numerical simulations of oblique impacts of particles have been undertaken by Thornton and his co-workers. In their simulations, DEM was used and the impact behaviour of elastic and elastic-plastic particles were investigated. Thornton and Randall (1988) and Randall (1988) conducted the computer simulation of normal and oblique impacts of an elastic sphere against a wall. The coefficient of restitution was examined and the relationship between the rebound angle and the impact angle of the contact patch was reported and shown to be in good agreement with that predicted by Maw *et al.* (1976, 1981). More results of the oblique impact of elastic spheres were presented by Yin (1992) and Thornton and Yin (1991). The tangential force evolutions at various impact angles were reported and a good agreement with the analysis of Maw *et al.* (1976, 1981) was also observed. Thornton and Ning (1994) and Ning (1995) further investigated the oblique impact of elastic-plastic particles. The effects of friction, plastic deformation and impact angle on the rebound behaviour were investigated in detail.

2.4 Summary

In this chapter, we have reviewed the previous research on the contact/impact of spheres. It has been shown that the impact of spheres is a very interesting problem and has been the topic of many publications. Some theoretical models have been proposed to predict the rebound behaviour of spheres. In addition, many experimental works and numerical analyses have been conducted to verify these models. However, a proper and effective theoretical model would be established only on the basis of a full understanding of the impact behaviour. Although real experiments can reveal the impact characteristic very well, the accuracy and reproducibility of the experiment rely heavily on the experimental technique and high precision facilities. In addition, the availability and uncertainty of the real materials considerably limit our understanding of the impact behaviour by means of

real experiments. Furthermore, the development of DEM, which has proved powerful in modelling granular materials, requires more physical models for binary interactions of particles. Hence, further investigation needs to be carried out to gain a complete understanding of the impact of particles.

Fortunately, the advance in numerical methods, especially finite element methods, and the fast development of modern computer technology in recent years make it possible to release the limits of material properties and to avoid the uncertainty which is inevitably encountered in real experiments. It is believed that analysis using FEM would provide detailed information on particle impact problems. Therefore, the impact of spheres will be investigated using finite element methods in this study.

Chapter 3 Finite Element Analysis Models

3.1 Introduction

The contact between two bodies is a static problem whereas the impact is a dynamic one. Contact/impact problems usually involve friction. In addition, contact/impact problems are inherently non-linear, since the contact boundary conditions are unknown *a priori*. Specifically, neither the actual contact surface, nor the stresses and displacements on the contact surface are known prior to the solution of the problems. Additionally, general contact/impact problems may also involve geometry non-linearity and material non-linearity. All these make contact/impact problems more complex.

Owing to the extreme complexity of contact/impact problems, a rigorous analysis of such problems remains extremely difficult. However, with the rapid development of finite element techniques and the advance in computer power, it is now possible to effectively solve the contact/impact problems with desired accuracy. A detailed description of finite element techniques for contact/impact problems is a complicated topic and out of the scope of this study. For this, among others, we refer readers to Zienkiewicz and Taylor (1989), Hughes (1987), Bathe (1982), Oden (1972) and Zhong (1993). Nevertheless, we will briefly present some distinct aspects involved in finite element methods for contact/impact problems from the standard FEM in Appendix A, together with a brief description of FE codes DYNA2D/DYNA3D which are employed in this study.

In this chapter, finite element models employed in this study are given in three sections for modelling normal impacts, frictional contacts under tangential loading and oblique impacts, respectively. The detailed analysis results will be presented in subsequent chapters.

3.2 Finite element models for normal impacts

The normal impact of a sphere with a target is illustrated in Fig. 3.1, in which a sphere of radius R impinges against the target with an impact velocity V_{ni} . Note that the sphere and the target could deform either elastically or plastically, depending upon the material

properties and the value of the impact velocity V_{ni} . Obviously, the normal impact problem is geometrically axi-symmetric; it can thus be analysed using a 2D model. In this study, the analysis of the normal impacts will be performed using DYNA2D. We consider two types of normal impacts: one is the impact of a sphere with a rigid wall; the other is the impact of a sphere with a half-space. The corresponding FE models are presented in this section.

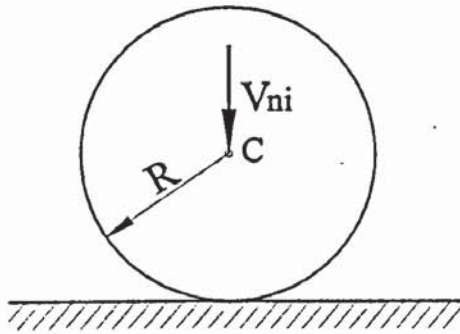


Fig. 3.1 Illustration of the normal impact of a sphere with a target wall.

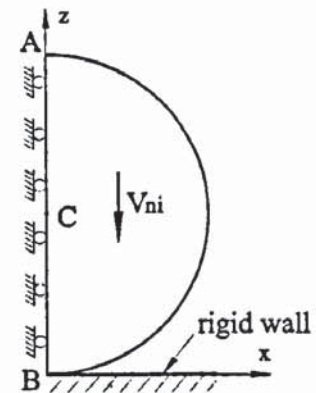


Fig. 3.2 The analysis model for the normal impact of a sphere with a rigid wall.

3.2.1 FE models for normal impacts of a sphere with a rigid wall

Owing to the symmetry of the loading condition, only half of the sphere needs to be considered for the normal impact of a sphere with a rigid wall. Figure 3.2 shows the finite element model and boundary conditions. The sphere is placed in such a way that only point B is initially in contact with the rigid wall which is stationary. The vertical boundary AB of the semi-sphere represents the axis of symmetry, and hence nodes on this boundary are restricted against displacement in the horizontal direction. The rigid target is modelled using a “rigid wall” in DYNA2D (Whirley and Engelmann 1992), which is a special purpose capability for treating the interaction between a body and a rigid target (see also Appendix A). The advantages of employing the “rigid wall” are two-fold: first of all, the computation is efficient since it permits modelling unilateral contact without requiring discretisation of the target; secondly, it avoids the influence of FE models for the target (such as boundary condition and the size of FE models), which may be significant as will be discussed in Appendix B for the normal impact of a sphere with a half-space.

In order to investigate the significance of finite element meshes, the semi-sphere is discretised with two different meshes, as shown in Fig. 3.3, which are referred to as Model

I and II, respectively. According to Hertz theory, the deformation of the sphere during impact occurs mainly in the vicinity of the initial contact point. Thus, for each model, finer meshes are used for the area near the initial contact point and coarser meshes for the remaining area. Figure 3.3a shows finite element meshes for Model I, which is constructed with the coarser overall meshes, and consists of 1250 four-node quadrilateral (axisymmetric) plane elements comprising 1316 nodes. Model I was first used in Li *et. al.* (2000). Model II is the finer model used here, which is discretised with 12780 four-node quadrilateral (axisymmetric) elements and 12961 nodes.

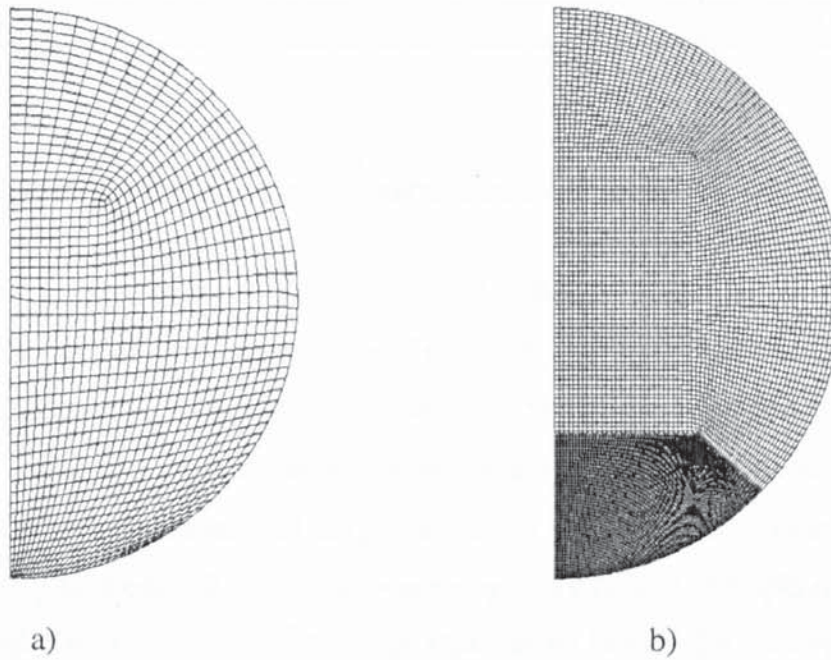


Fig. 3.3 Finite element meshes for the sphere that collides with a rigid wall: a) Model I; b) Model II.

For each model, the interaction between the sphere and the rigid wall is modelled by defining a slave slideline which is constructed with a set of nodes (slave nodes) along the bottom boundary of the sphere. These slave nodes are not permitted to penetrate the rigid wall. The contact searching is based on master-slave algorithm (see Appendix A.4.2). Only the nodes which are defined as slave nodes are checked for non-penetration, which means that the nodes, which are not listed as slave nodes, may penetrate the rigid wall without resistance. The slave slideline is hence constructed long enough to ensure that every potential contacting node is pre-defined as a slave node. The kinematic constraint method is used to exactly enforce the contact constraint conditions, by which the slave slideline is allowed to slide freely (frictionless) along the rigid wall and to separate from it, but cannot penetrate into the rigid wall. The impact is modelled by applying an initial downwards velocity V_{ni} to every node within the sphere.

The sphere is of $10\mu m$ in radius, and its material properties are assumed to be either elastic or elastic-perfectly plastic. The material parameters, which represent typical steel materials, are listed in Table 3.1, which also gives the sections where the corresponding FEA results can be found.

Table 3.1 model parameters for the impact of a sphere with a rigid wall

The sphere				Impact velocity, V_{ni} (m/s)	Results presented in Section
Young's modulus, E (GN/m ²)	Poisson's ratio, ν	Density, ρ (Mg/m ³)	Yield stress, Y (GN/m ²)		
208.0	0.3	7.85	---	2.0, 5.0	4.2
208.0	0.3	7.85	1.35	0.3~150.0	5.3

3.2.2 FE models for normal impacts of a sphere with a half-space

In the analysis model shown in Fig. 3.2, we introduce the idealistic concept, "rigid wall", to simplify the normal impact problems. However, in reality, both contacting bodies will deform simultaneously. Therefore it is instructive to analyse the impact of a sphere with a half-space in order to comprehensively understand the impact behaviour. For this purpose, FE models for normal impacts of a sphere with a half-space are constructed. Figure 3.4 shows the analysis model. Because of symmetry, only half of the sphere and the substrate are considered. The boundary condition is also shown in Fig. 3.4. Owing to the symmetry with respect to z -axis, the nodes along this axis are constrained against horizontal displacement. The bottom line and the side edge of the substrate are fixed. Compared with Fig. 3.2, it is clear that the model for the substrate has to be appropriately constructed.

It is recognised that the substrate in FE models should be large enough to represent a half-space so that the influence of the boundary constraints is negligible. To properly choose the size of the substrate, one needs to estimate the maximum deformation of the substrate by taking the loading condition and material properties into account. In literature, various relative sizes (L/R) were chosen in FE modelling of the contact of a sphere with a half space. For example, Kral *et al.* (1993) analysed the indentation of a half-space by a rigid sphere using a substrate of $L/R = 0.64$; Sen *et al.* (1998) chose $L/R = 3$ in FEA of the indentation between an elastic sphere and a half-space; and Mesarovic and Fleck (1999) used substrates of $L/R = 10$ and 20 when investigating the indentation of a half-space by a rigid sphere and they pointed out that the outer boundary conditions are unimportant for

FE models with a substrate larger than $L/R = 10$. Nevertheless, little attention has been paid to the FE analysis of dynamic problems---the impacts of a sphere with a half-space.

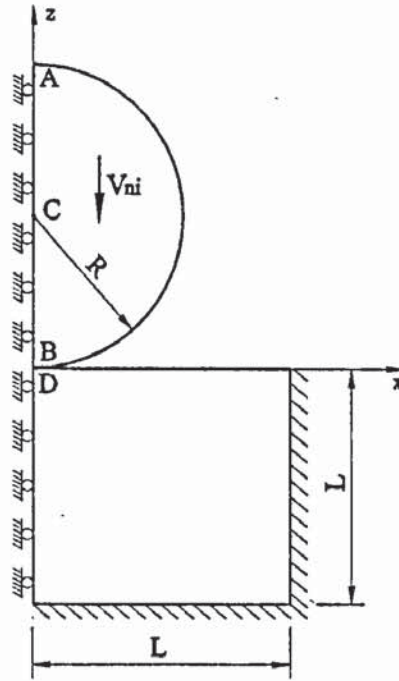


Fig. 3.4 The analysis model for the impact of a sphere with a half-space.

For the FEA of the impact of a sphere with a half-space, two factors need to be considered when choosing the substrate size: one is that, similar to the static case, the substrate should be large enough to minimise the influence of boundary constraints; on the other hand, the influence of the stress wave may become significant if a large substrate is used in the FE simulations, which may prevent a proper comparison with theoretical analysis being made since almost all theoretical models are based on the assumption that the effect of the stress wave is negligible. Therefore, a proper selection of the size of the substrate is crucial in FE modelling of the impact of a sphere with a half-space.

In this study, preliminary studies are undertaken to investigate possible effects of the substrate size by varying L/R from 1 to 20. The detailed analyses are presented in Appendix B. It is shown that, a substrate of dimension $L/R = 1$ is too small for modelling the impact even at low velocities. The effects of the boundary constraints and stress wave propagation are sufficiently small for the impact with a substrate of dimension $L/R \geq 2$. However, when the substrate is large (see $L/R \geq 10$) the effect of stress wave becomes significant. In this study, the effect of the stress wave is expected to be negligible and the quasi-static condition can be satisfied over a wide range of impact velocities. Therefore the substrate of dimension $L/R = 2$ is generally chosen and the FE model is shown in Fig. 3.5. Occasionally the substrate of dimension $L/R = 10$, for which the finite element model is

given in Appendix B, will be used in due course either to further validate the finite element model or to further investigate the energy losses due to stress waves.

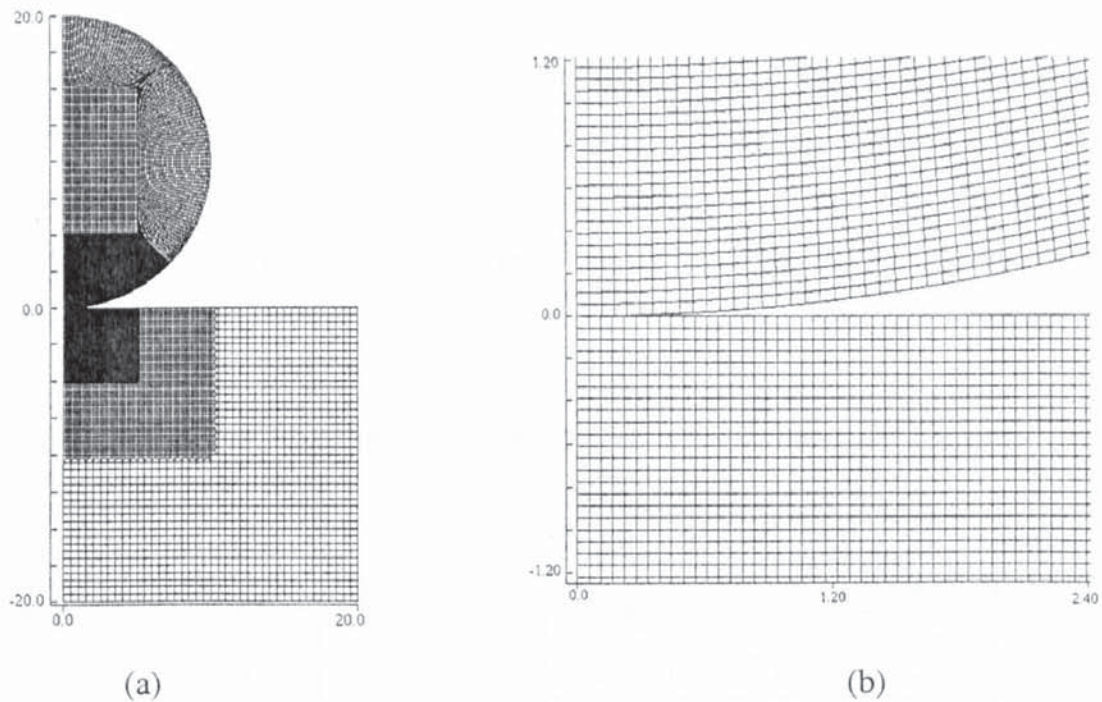


Fig. 3.5 (a) Finite element model for the impact of a sphere with a half-space; (b) Magnified view of contact region.

The sphere is discretised with the finer meshes shown in Fig. 3.3b in order to predict accurately the pressure distribution, the contact area and the deformation in this highly stressed region. An arrangement of 12,300 four-node quadrilateral (axi-symmetric) plane elements comprising 12,481 nodes is used to model the substrate. A refinement of the mesh near the contact zone is employed (Fig. 3.5b), because, according to Hertz theory, the deformation is mainly concentrated in the vicinity of the initial contact point.

The interaction between the sphere and the substrate is modelled by constructing a master-slave slideline, which consists of two contact lines: one is on the sphere side and the other on the substrate side. The “sliding with separation” option (Whirley and Engelmann 1992) is chosen to perform the contact modelling. This option allows two bodies to be either initially separate or in contact and the surfaces may separate and come together in a completely arbitrary fashion. Large relative motions are permitted and no friction is considered. Since this type of slideline is based on the master-slave contact searching algorithm and the kinematic constraint formulation to enforce the contact constraints, all potential nodes must be included in the set of the master and slave nodes *a priori*. Since in the kinematic method, only slave nodes are checked and restricted from penetrating master segments defined for the slide line, the master surface is constructed by a set of nodes on the sphere side which is discretised more coarsely, while the slave surface is constructed

by a set of nodes on the substrate side with finer meshes. The impact is again modelled by applying an initial downwards velocity V_{ni} to every node within the sphere.

For the impact of a sphere with a half-space, the sphere and the substrate are assumed to be either elastic, elastic-perfectly plastic or elastic-plastic with strain hardening. The material parameters of typical steel materials are chosen and listed in Table 3.2, together with the sections where the corresponding FEA results can be found. Again, the sphere is of $10\mu\text{m}$ in radius.

Table 3.2 model parameters for the impact of a sphere with a half-space

The sphere			The half-space					Results presented in Section
E_1 (GN/m ²)	ν_1	ρ_1 (Mg/m ³)	E_2 (GN/m ²)	ν_2	ρ_2 (Mg/m ³)	Y (GN/m ²)	E_T (GN/m ²)	
208.0	0.3	7.85	208.0	0.3	7.85	---	----	4.3
208.0	0.3	7.85	208.0	0.3	7.85	1.35	---	5.2; 5.3
208.0	0.3	7.85	208.0	0.3	7.85	1.35	10.4	5.5

3.3 FE models for friction contacts under tangential loading

Consider now that a spherical body is compressed into a substrate with a plane surface by a steady normal load \bar{F}_n while being subjected to a monotonically increasing tangential force \bar{F}_t of prescribed amplitude (see Fig. 3.6). For the case of two elastic bodies in contact, since the normal force remains constant at \bar{F}_n , the contact area and the normal pressure will remain constant as given by Hertz theory (see Section 2.2.1). Under the action of the tangential force \bar{F}_t ($\leq \mu\bar{F}_n$), where μ is the friction coefficient, Mindlin (1949) showed that the contact area consists of two parts: a central stick region ($r \leq c$) and a surrounding slip region ($c \leq r \leq a$) (See section 2.3.2), where c is given by Eq.(2.71). The tangential traction is shown in Fig. 2.6 and given by Eqs.(2.72a) and (2.72b) in the annulus $c \leq r \leq a$ and central circle $r \leq c$, respectively. As can be seen in Eq.(2.71), with the increase of tangential force, the size of the stick region shrinks to zero at which sliding occurs. This problem will be investigated in this study using FEM.

The FEA model is shown in Fig. 3.6 and Fig. 3.7, in which a spherical indenter with a radius R_1 is pressed onto a substrate with a plane surface by an applied normal force \bar{F}_n in

the opposite direction to the z-axis and is subjected to a tangential force \bar{F}_t at the initial contact point, in the opposite to the direction of the y-axis. The substrate is assumed to be a semi-sphere with a radius R_2 . In this study, both R_1 and R_2 are assumed to be $10\mu m$. The simulation is performed using DYNA3D (Whirley and Engelmann 1993).

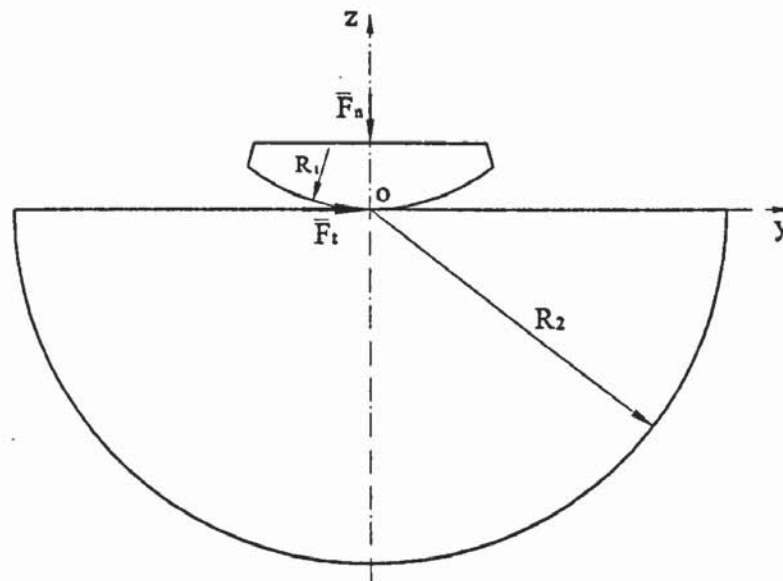


Fig. 3.6 The analysis model for frictional contacts under tangential loading.

To simulate the frictional contact under tangential loading, a three-dimensional finite element model as shown in Fig. 3.7 is constructed. Since the present contact problem is symmetric with respect to y-z plane, only half of the model is meshed, which consists of 9,800 eight-node solid elements with 12,780 nodes in the indenter and 29,400 elements with 32,580 nodes in the substrate. Refined meshes are used near the initial contact point in order to accurately describe the localised deformation. Interaction between the indenter and the substrate is modelled by employing a sliding interface defined as “sliding with separation and friction” (Whirley and Engelmann 1993), which allows two bodies to be either initially separate or in contact and permits large relative motions with friction. Two sets of slidelines are defined to construct the sliding interface: one is on the indenter side and the other is on the substrate side. The slidelines are constructed to be long enough to ensure every potential node being included in the interfacial node sets. Between the slidelines, the static and dynamics friction coefficients are assumed to be identical and remain constant. The contact searching is based on master-slave algorithm (see Section Appendix A.4.2), and the penalty method discussed in Appendix A.4.3.2 is used to enforce the contact constraint conditions. The assignment of which slideline as slave or master surface is trivial since the penalty method is symmetric, i.e., using the penalty method each

slideline is regarded once as the slave surface and once as the master surface to check the penetration. Since the accuracy of the solution using the penalty method depends upon the choice of the penalty parameters, several trial-and-error tests have been carried out to choose the appropriate parameters and to make sure that the penetration is controlled within an allowable range.

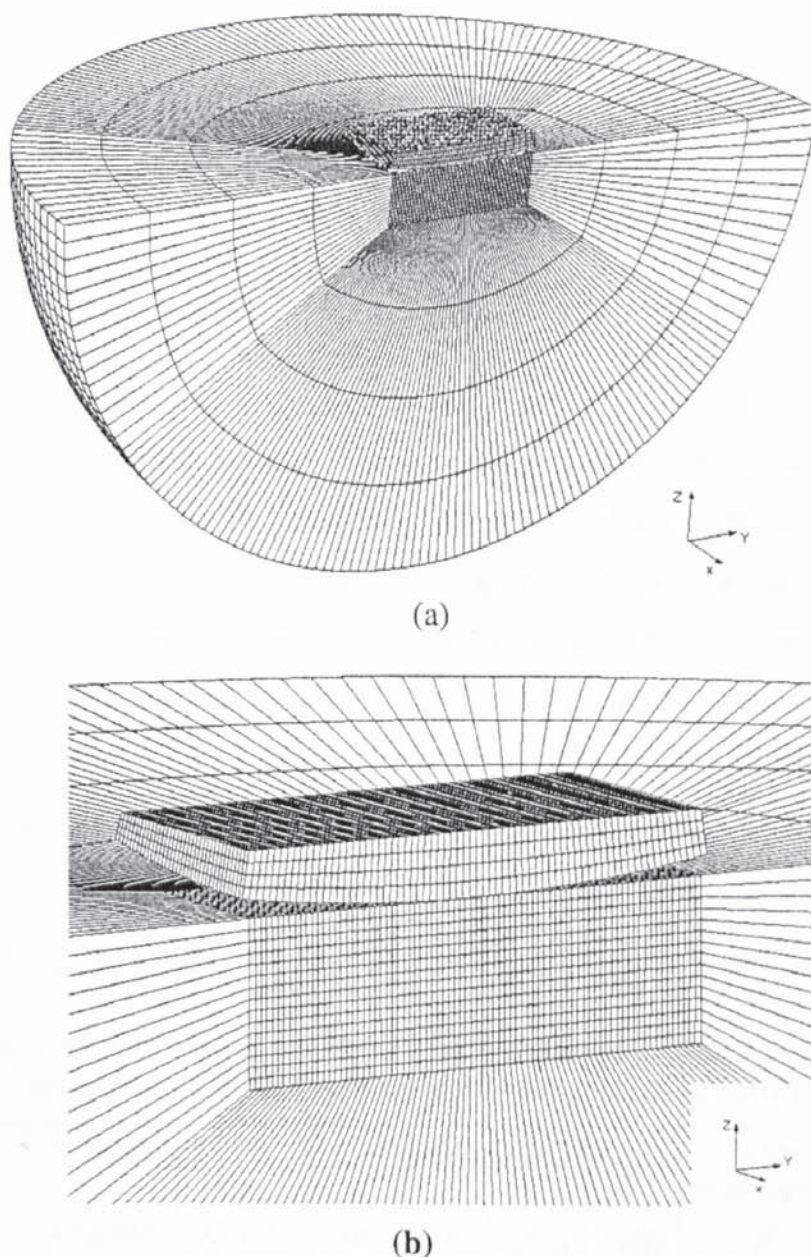


Fig. 3.7 FE model for frictional contacts under tangential loading: (a) the whole meshes; (b) a closer view of the meshes in the contact region.

Nodes on the symmetry plane (y - z plane) are restricted in the x -direction, while nodes on the outer boundary of the substrate are fixed. Two load curves are defined to prescribe the normal load \bar{F}_n and tangential load \bar{F}_t , respectively. The loading history is illustrated in Fig. 3.8. The normal load is first applied and prescribed to increase to a certain value (\bar{F}_{n0}) at instant t_1 , and then it is kept constant. The tangential loading is assumed to be started at

time t_1 when the normal force is constant and is increased to \bar{F}_{i0} at time t_2 , and then it remains unchanged. In order to reduce the oscillation induced by dynamic loading, mass proportional damping is introduced, as discussed in Appendix A.2.

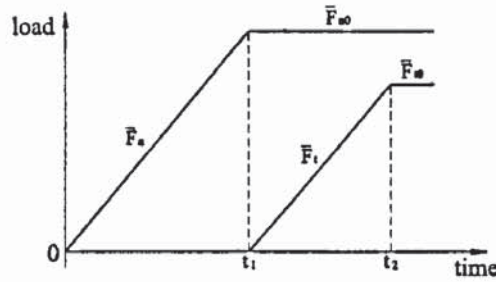


Fig. 3.8 The load curves.

In present study, we shall consider the frictional contact of a rigid indenter with half-space *i.e.*, the indenter is assumed to be rigid. The material properties for the substrate are shown in Table 3.3. Since in DYNA3D, elements that are rigid are bypassed in the element processing, but the realistic values for the material constants are required for determining sliding interface parameters, the same material constants as the substrate are assigned to the rigid indenter. The static and dynamic friction coefficients are assumed to be identical and constant at a value of μ . Table 3.3 also gives the control parameters for the load curves and the corresponding sections in which the FEA results will be reported. Note that negative values of \bar{F}_{n0} and \bar{F}_{i0} mean that the loading direction is opposite to the direction of the corresponding coordinate axis, as shown in Fig. 3.6.

Table 3.3 model parameters for the frictional contact between a sphere and a half-space with tangential loading

The half-space				Loading curves				Friction coefficient, μ	Results presented in Section
E (GN/m ²)	ν	ρ (Mg/m ³)	γ (GN/m ²)	t_1 (μ s)	t_2 (μ s)	\bar{F}_{n0} (mN)	\bar{F}_{i0} (mN)		
208.0	0.3	7.85	---	0.06	0.1	-9.0	4.2	0.5	6.2
208.0	0.3	7.85	2.5	0.06	0.1	-4.5	1.3	0.3	6.3

3.4 FE models for oblique impacts of a sphere with a half-space

Here we extend our attention to the dynamic problem---the oblique impact of a sphere with a half-space as illustrated in Fig. 3.9. Suppose that a sphere impinges onto a half-space with an incident velocity V_i at an impact angle θ ($\theta = 0^\circ$ for the normal impact) without

initial rotation. Due to the effect of friction, the sphere rotates during the impact. The rebound linear velocity and rotational angular speed of the sphere are designated by V_r and ω_r , respectively. Let V_{ni} and V_{ti} be the normal and tangential components of the initial impact velocity, V_{nr} and V_{tr} denote the normal and tangential components of the rebound velocity at the centre of the sphere. The problem we are interested in is how the sphere rebounds, i.e., to determine the rebound characteristics of the sphere during oblique impacts. The problem is now modelled using FEM.

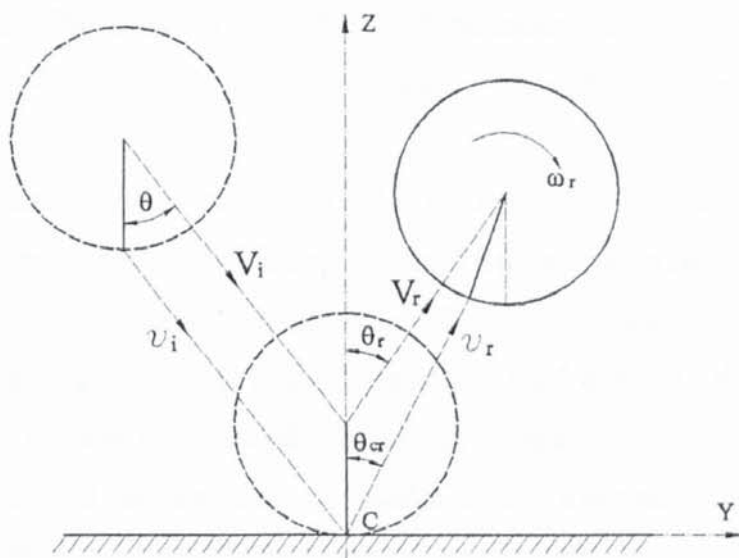


Fig. 3.9 Diagram of the oblique impact of a sphere with a plane surface.

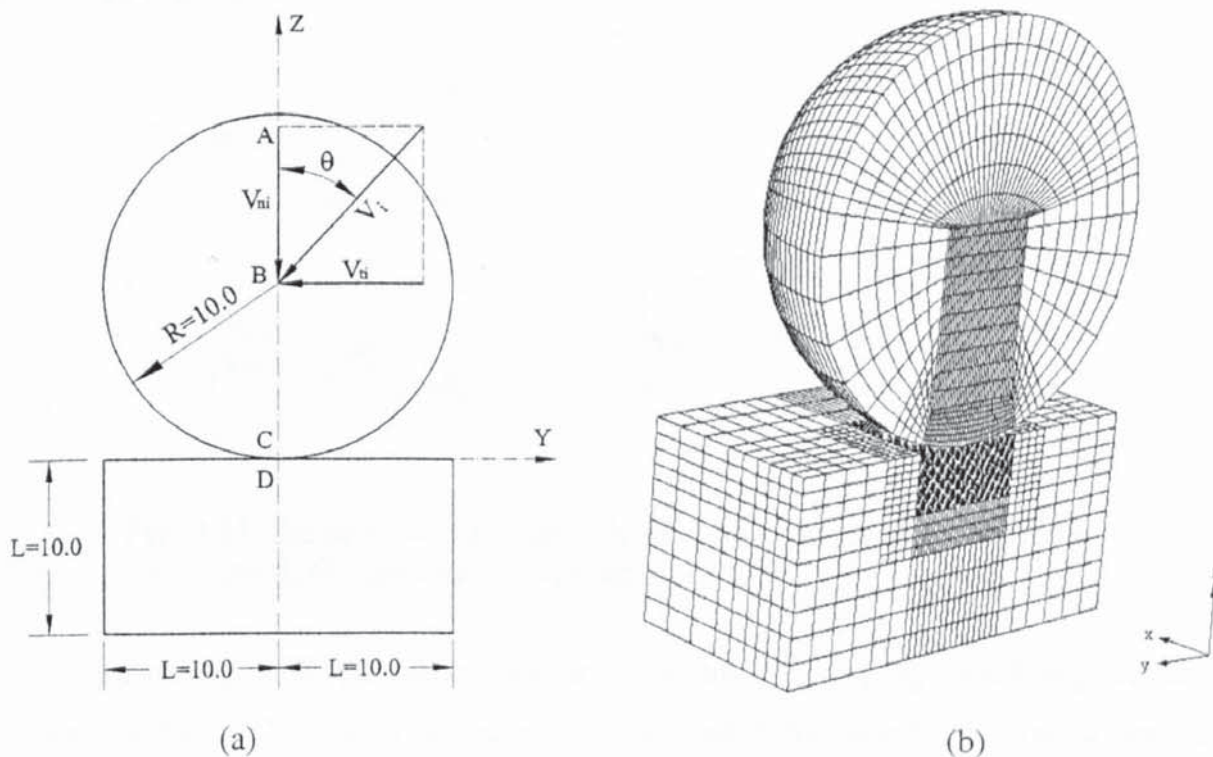


Fig. 3.10 FE model for the oblique impact of a sphere with a half-space (unit: μm).

To simulate the oblique impact of a sphere with a half-space, a three-dimensional finite element model, shown in Fig. 3.10, is used. Because of geometrical and loading symmetries, only half of the model is considered and discretised. The sphere is of a radius $R = 10\mu m$. The substrate is selected as $10\mu m$ in both x and z -directions, and $20\mu m$ in y -direction. As will be shown in Appendix C, further increasing the size of the substrate does not produce any difference in the results. Therefore, the size of the substrate is regarded large enough to represent a half-space under the velocities considered in this study. The meshes consist of 18,632 eight-node solid elements with 20,097 nodes in the sphere and 21,896 elements with 26,236 nodes in the substrate. Fine meshes are used in the vicinity of initial contact point in order to accurately describe the localised deformation.

The simulation is performed again using DYNA3D. Interaction between the sphere and half-space is modelled by employing a sliding interface defined as “sliding with separation and friction” (Whirley and Engelmann 1993), which allows two bodies to be either initially separate or in contact and permits large relative motions with friction. In the present study, Coulomb’s law of dry friction is used and coefficients of static and dynamic friction are assumed to be identical and remain constant. Nodes on the symmetry plane ($x = 0$) are restricted in the x direction. Nodes on boundaries (planes $x = 10$, $y = \pm 10$ and $z = -10$) are fixed. The impact is modelled by applying an initial velocity V_i to every node within the sphere at an angle θ .

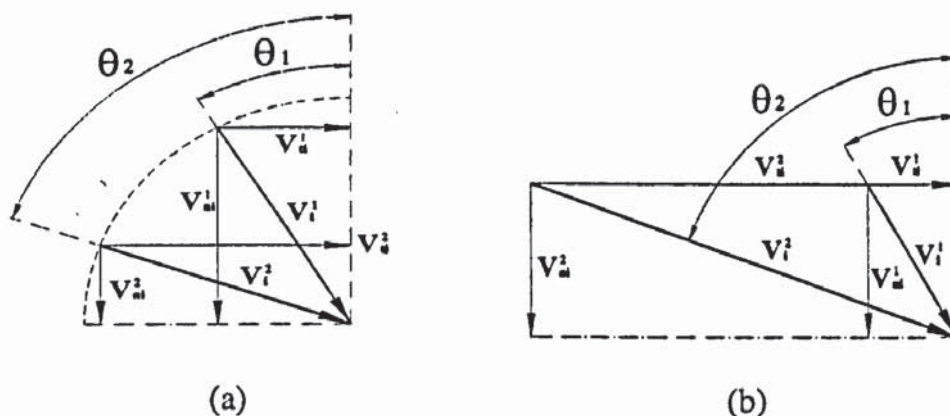


Fig. 3.11 The approaches to specify the impact angles: (a) Constant initial speed; (b) constant initial normal velocity.

For oblique impact, different impact angles are normally set up by specifying the initial velocity condition. Two approaches are usually used to specify the initial velocity condition: one is to keep the initial speed constant (see Fig. 3.11a), which has been commonly adopted in laboratory experiments (see, *e.g.*, Kharaz, *et al.* 1999); the other is to

keep the normal component of initial velocity fixed (see Fig. 3.11b). In the former, both normal and tangential responses vary with impact angle. Consequently, although the normal and tangential response may not interfere with each other, both responses would change with impact angle so that the coupling of normal and tangential responses may not be clearly identified. In the latter, the change in impact angle will only change the tangential component of the initial velocity and the effect of tangential response on the normal response can hence be explored. Both approaches are adopted in this study and comparisons between the results obtained by these two approaches are also made. Different impact angles that are varying from 0° (normal impact) to 85° (close to glancing) are considered in this study.

We consider various combinations of the sphere and the half-space with different material properties. Table 3.4 shows the combinations considered together with the Sections where the FEA results are reported. The corresponding material properties are listed in Table 3.5. For each combination, the static and dynamic friction coefficients are assumed to be identical and remain constant at μ . In finite element analyses, in order to reduce the computing costs, the ideal concept “rigid” is introduced. Since, in DYNA3D, elements that are rigid are bypassed in the element processing and the realistic values for the material constants are assigned to the rigid body for determining sliding interface parameters. It is hence expected that the simulations using a rigid body would give the similar results to those using an elastic body. This will be demonstrated in corresponding sections.

Table 3.4 Various cases investigated for oblique impacts of a sphere with a half-space

Case	The Sphere	The Half-Space	μ	Results presented in Section
RE	Rigid	Elastic	0.3	7.3~7.9
EE	Elastic	Elastic	0.3	App. D
RP	Rigid	Elastic-perfectly plastic	0.0, 0.3	8.2~8.9
PR	Elastic-perfectly plastic	Rigid	0.0, 0.3	8.2~8.9
EP	Elastic	Elastic-perfectly plastic	0.3	8.2~8.9
PE	Elastic-perfectly plastic	Elastic	0.3	8.2~8.9

The objective of employing the combination of the PR and PE impacts is to ensure that the orientation of the contact plane does not change during the impact by ensuring that the half-space is not deformed permanently. The effect of friction can hence be clearly investigated. In addition, it is instructive to simulate RP and EP impacts, where the focus is

placed on the effect of the plastic deformation of the half-space, in particular, the change in contact plane orientation induced due to permanent plastic deformation. In this way, the individual contributions of friction and plastic deformation to the oblique impact behaviour of plastic particles can be clearly identified.

Table 3.5 Material properties for oblique impacts of a sphere with a half-space

Material property	E (GN/m ²)	ν	Y (GN/m ²)	ρ (Mg/m ³)
Rigid	---	---	---	7.85
Elastic	208.0	0.3	---	7.85
Elastic-perfectly plastic	208.0	0.3	1.85	7.85

3.5 Summary

In this chapter, we have constructed various FE models for investigating the impact behaviour of a sphere with a half-space. The analysis results using these models will be presented in following chapters.

Chapter 4 Normal Impact of Elastic Particles

4.1 Introduction

As discussed in Chapter 2, the classical Hertz theory has been successfully applied to investigate the frictionless normal impact of spherical particles of homogeneous and isotropic elasticity with sufficiently small deformations induced. Some attempts have also been made to extend Hertz theory to be more applicable to a wider application range (see, *e.g.*, Tataru 1989; Villaggio 1996). All these theories are based on the quasi-static assumption so that the effect of stress waves is ignored. According to Love's and Johnson's criteria (see Eqs.(2.21)-(2.22)), the quasi-static assumption requires that the impact velocity is low enough to minimise the effect of stress wave propagation. Therefore, if the initial impact velocity is low enough that the quasi-static condition is satisfied, the energy losses due to stress wave propagation may be negligible. However, if the impact velocity is high enough, the quasi-static assumption is not warranted and the energy dissipation due to stress waves becomes significant. A detailed analysis of the influence of stress waves is presented in Appendix B.

As a preliminary study, finite element analysis of normal impacts of elastic particles is conducted using DYNA2D. The aim is to validate the FE model established in this study and to provide a comprehensive description of the normal impact of elastic particles. The FEA results are reported in this chapter, and some of the results were first reported in Li *et al.* (2000).

In this chapter we consider two impact cases of different configurations: one is for the impact of an elastic sphere at a rigid boundary, *i.e.*, a sphere striking against a rigid wall; and the other is for the impact of an elastic sphere at an elastic boundary, *i.e.*, a sphere impinging onto an elastic half-space. For each case, a wide range of impact velocities are considered, which implies that the deformation of the sphere and/or the substrate may be relative large and the effect of stress waves may become significant. The comparisons of FEA results with those given by theories available in literature are made.

4.2 Normal impact of elastic spheres at a rigid boundary

Consider now that an elastic sphere collides with a rigid wall as illustrated in Fig. 3.1. Assume that the contact surfaces are smooth so that the effect of friction can be neglected. The initial impact velocity of the sphere is specified to be V_{ni} . If V_{ni} is so small that the deformation of the sphere induced is also small, then the Hertz theory discussed in Section 2.2.1 is applicable. Hertz theory can thus be applied to analyse the impact behaviour of the sphere directly. For this specific case, Eqs.(2.6), (2.8) and (2.14) are replaced by

$$R^* = R \quad (4.1)$$

$$1/E^* = (1-\nu^2)/E \quad (4.2)$$

$$m^* = m \quad (4.3)$$

where E and ν are the Young's modulus and Poisson's ratio of the sphere, respectively, R is the radius of the sphere and m is the mass of the sphere.

In the following, the impact of an elastic sphere with a rigid wall is analysed using FEM. We simulate frictionless normal impacts using the two models presented in Fig. 3.3 of Section 3.2.1. The material properties were given in Table 3.1. To investigate the impact behaviour of the sphere over a wide velocity range, the initial impact velocity is prescribed to vary from $V_{ni} = 2.0m/s$ to $V_{ni} = 50.0m/s$, which is the highest velocity used for a sphere impinging against a rigid wall in this study.

4.2.1 Pressure distribution

Figure 4.1 shows the pressure distribution over the contact area at the maximum compression ($t = 11.2ns$) during the impact at $V_{ni} = 50m/s$. Figure 4.1a shows the results obtained with Model I (Fig. 3.3), while the pressure distributions obtained using Model II are presented in Fig. 4.1b. In Fig. 4.1 the thick curves are plotted by fitting Eq.(2.1) with the FEA results without accounting for those on the horizontal and vertical axes. At the contact centre, a sharp increase in the contact pressure is found in the FEA results obtained with Model I (Fig. 4.1a), although a slight increase is also found using Model II (Fig. 4.1b). We attribute the discrepancies between FEA results and Hertz theory in this region to the finite size of elements used, since it is clear that reducing the size of the elements reduces the divergences, as shown in Fig. 4.1. Again, the disagreements between FEA

results and Hertz theory at the contact edge are also apparently due to the finite size of elements used (see also Appendix A.4.4). Therefore it is suggested that we can omit the FEA results on the horizontal and vertical axis to minimise the effect of finite size of elements. This method is employed to produce Fig. 4.2, which shows the pressure distribution over the contact area at various instants during the impact of an elastic sphere with a rigid wall at two impact velocities considered. It can be seen that the FEA results obtained with the two different models are close and in excellent agreement with Hertzian predictions.

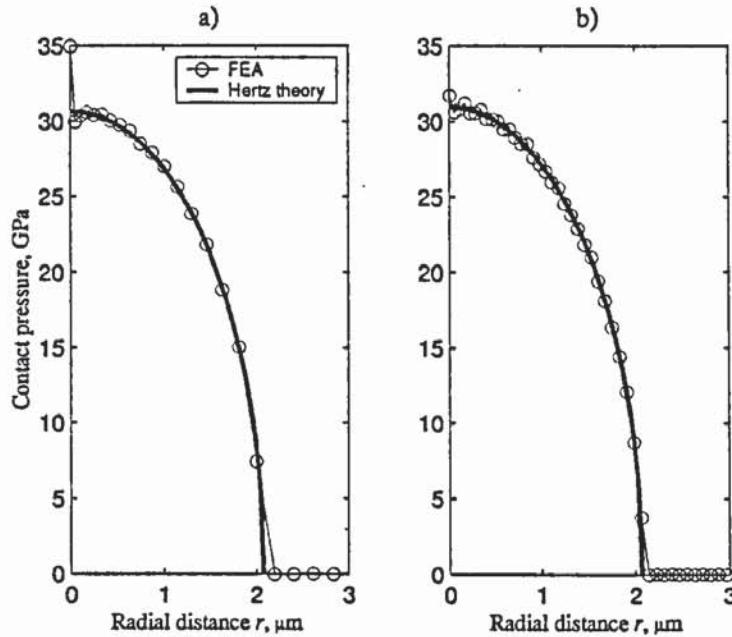


Fig. 4.1 The pressure distribution over the contact area at the maximum compression ($t = 11.2ns$) during the impact of an elastic sphere with a rigid wall at $V_{ni} = 50m/s$ using: a) Model I; b) Model II.

In Fig. 4.1, the intersections of the thick curves with the horizontal and vertical axes represent the contact radius a and the maximum contact pressure p_0 , respectively. From Fig. 4.1a we obtain $a = 2.069\mu m$ and $p_0 = 30.65GN/m^2$, while Fig. 4.1b gives $a = 2.064\mu m$ and $p_0 = 30.97GN/m^2$. It can be seen that, by omitting the FEA results on the horizontal and vertical axes, fitting the remaining FEA results obtained with two different models gives very close agreement for the overall pressure distribution which is governed by a and p_0 . This confirms that the effect of the finite size of elements used can be reduced if we omit the FEA results on the horizontal and vertical axes. It is also implied that the contact radius a and the maximum contact pressure p_0 can be appropriately estimated by this approach, which will be employed in the following study.

Figure 4.3 shows the variation of the maximum pressure p_0 with the contact radius a obtained using the above approach. In this figure, we also superimposed the results given by Hertz theory (see Eq.(2.9)). It can be seen that FEA results are in excellent agreement with Hertz theory. This also demonstrates that the above approach can be used to accurately determine the contact radius a and the maximum contact pressure p_0 . Furthermore, even at high velocities the pressure distribution still agrees well with the elliptical shape predicted by Hertz theory.

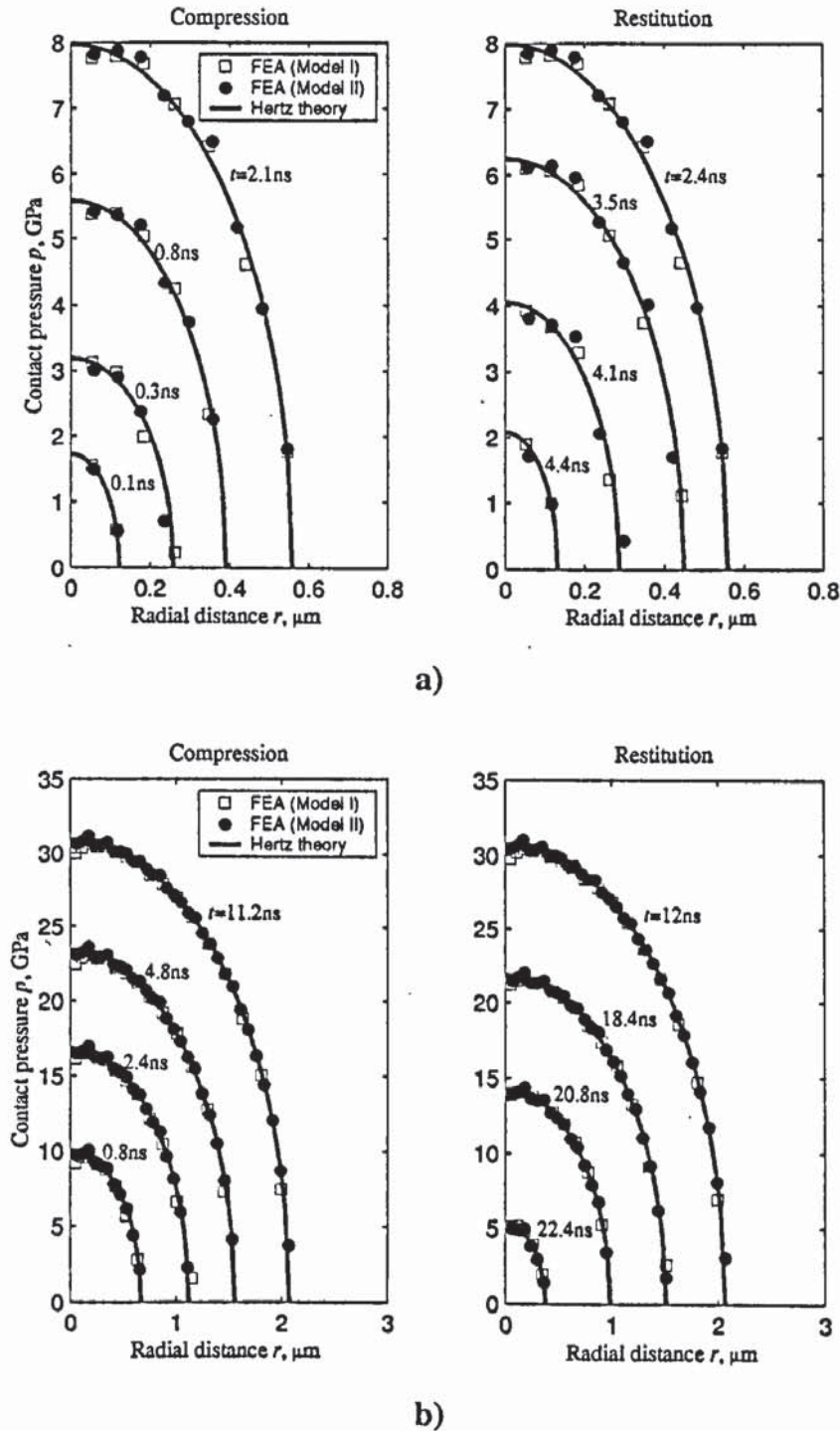


Fig. 4.2 The pressure distribution over the contact area during the impact of an elastic sphere with a rigid wall: a) $V_{ni} = 2.0m/s$; b) $V_{ni} = 50m/s$.

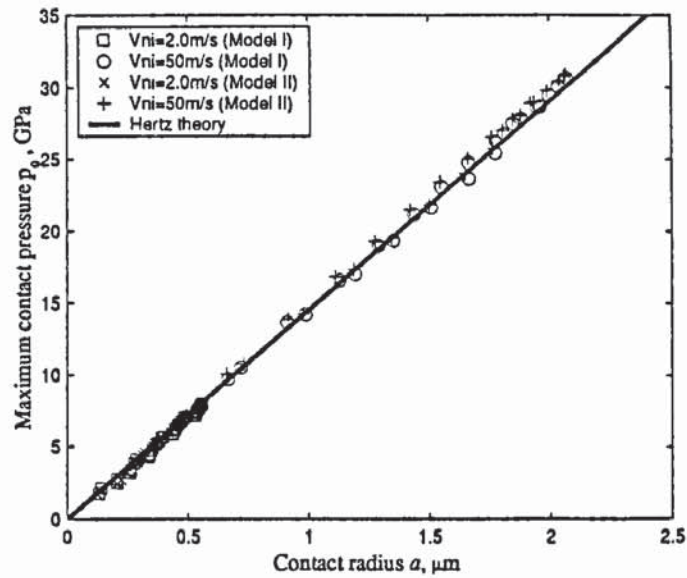


Fig. 4.3 The variation of the maximum contact pressure p_0 with the contact radius a for the impact of an elastic sphere with a rigid wall using Model I.

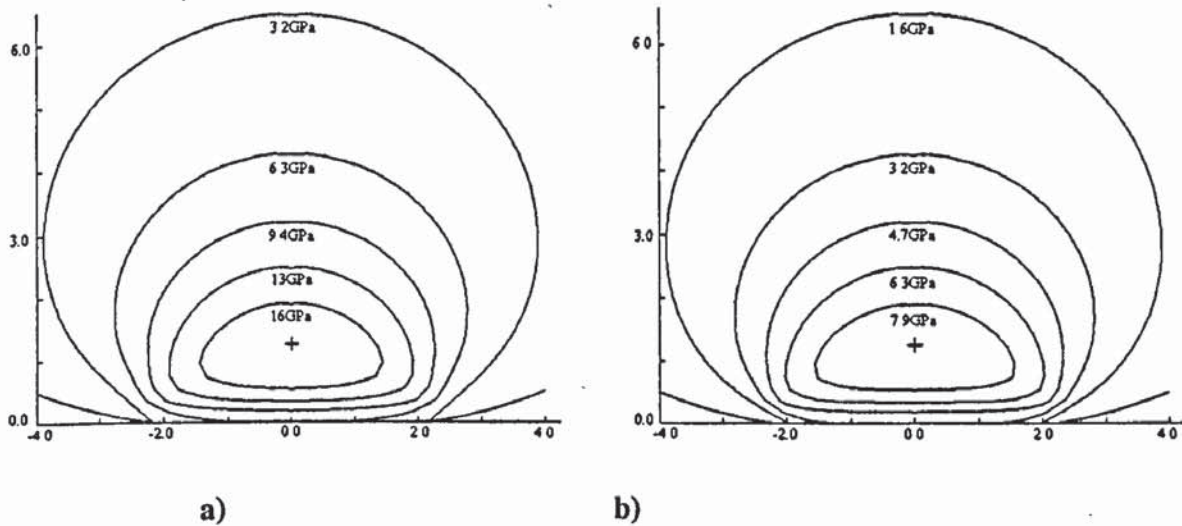


Fig. 4.4 The stress distributions of the sphere at the maximum compression ($t = 11.2ns$) with $V_{ni} = 50m/s$ using Model I: a) Effective stress (von Mises); b) Maximum shear stress.

4.2.2 Stress distribution

The typical patterns for the stress distribution inside the sphere are illustrated in Fig. 4.4, which shows (a) the effective stress or von Mises stress and (b) the maximum shear stress at the maximum compression ($t = 11.2ns$) during the impact at $V_{ni} = 50m/s$ using Model I. The patterns are quite similar to the experimental photo-elastic observations of Shih *et al.* (1992) and the theoretical predictions of Davies (1949). In Fig. 4.4, the plus signs “+” indicate the location of the maximum value of the corresponding stresses. It can be seen that the maximum values of the effective stress and maximum shear stress are lying inside

the sphere at a depth of *c.a.* $0.5a$. Hence the plastic yielding would be expected to initiate inside the sphere according to both von Mises and Tresca criteria. For the effective stress, the maximum value is $19GN/m^2$. While for the maximum shear stress, the value is $9.4GN/m^2$. Referring to Fig. 4.1, the maximum contact pressure p_0 is around $30.9 GN/m^2$ at $t = 11.2ns$. Therefore the maximum effective stress is equal to $0.61p_0$, while the maximum value of the maximum shear stress $0.31p_0$. This is consistent with the theoretical predictions (see Johnson 1985).

4.2.3 Evolution of impact parameters

Figure 4.5 shows the evolution of displacements at three nodes, the top (Node A), the centre (Node C) and the bottom (Node B) of the sphere (see Fig. 3.2), for the impact at $V_{ni} = 2.0m/s$ and $V_{ni} = 50m/s$ obtained with Model I. It can be seen that, owing to the resistance of the rigid wall to the sphere, there is no displacement at Node B until the separation of the sphere from the rigid wall at $t = t_s$, *i.e.*, the sphere rebounds from the rigid wall. During the impact, the magnitude of displacements at Nodes C and A increases until it reaches its maximum, then decreases and reduces to zero. It is apparent that the displacement at the top of the sphere (Node A) is very close to that at the centre of the sphere (Node C), even for the impacts at high initial impact velocities (say $V_{ni} = 50m/s$). This indicates that the deformation of the sphere is mainly concentrated in the bottom half of the sphere during the impact. After the sphere separating from the rigid wall, the displacements of the three nodes are identical, which implies that, after the separation, there is no deformation in the sphere and the sphere acts as a rigid body.

The period from the beginning of the contact ($t = 0$) until the separation ($t = t_s$) is referred to as the impact duration. The instant when the peak value of displacement at Node A or C is reached represents the instant of maximum compression, which is the demarcation between the compression and the restitution of the impact. It is also clear that the impact duration decreases from $t = 0.045\mu s$ at $V_{ni} = 2.0m/s$ to $t = 0.0232\mu s$ at $V_{ni} = 50m/s$, *i.e.*, the higher the initial impact velocity, the shorter the duration of impact. Furthermore, the duration of compression is identical to that of restitution.

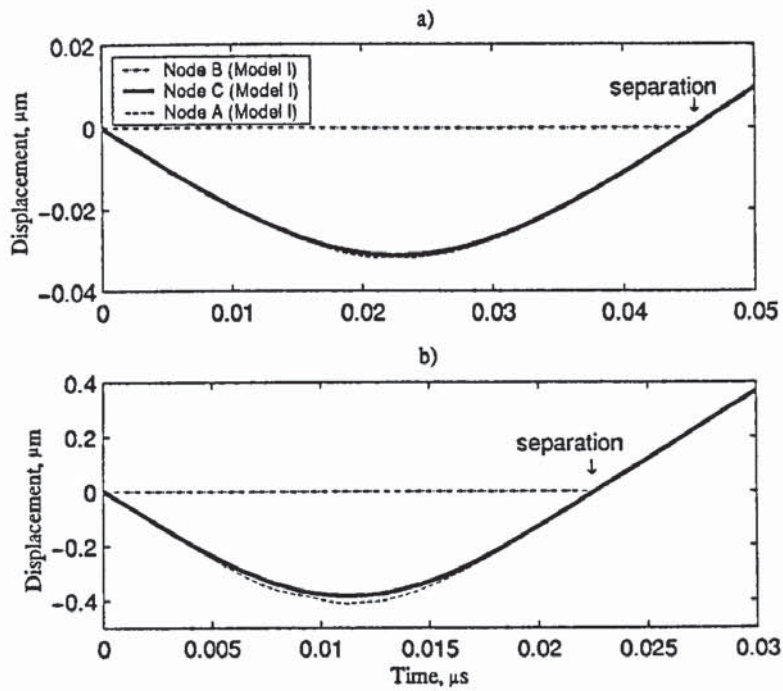


Fig. 4.5 Time histories of nodal displacements during the impact of an elastic sphere with a rigid wall using Model I at: a) $V_{ni} = 2.0\text{ m/s}$; b) $V_{ni} = 50\text{ m/s}$.

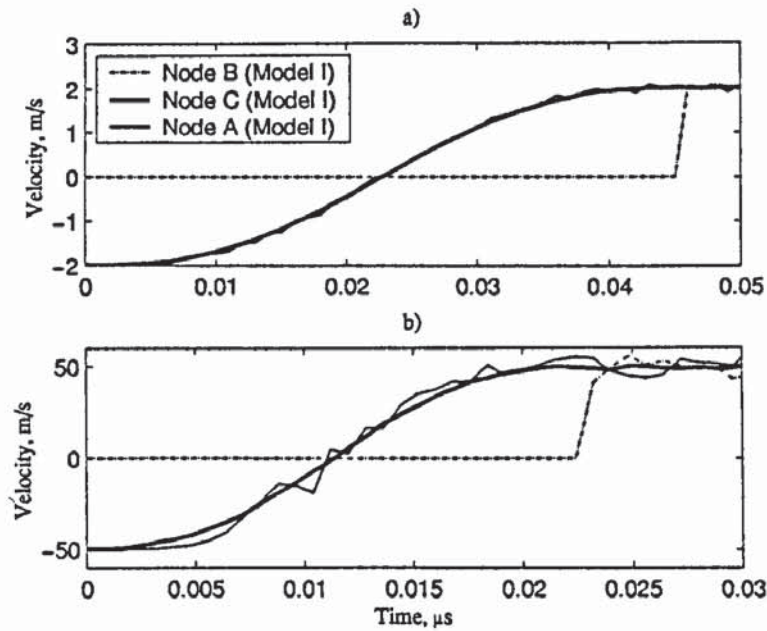


Fig. 4.6 Time histories of nodal velocities during the impact of an elastic sphere with a rigid wall using Model I at: a) $V_{ni} = 2.0\text{ m/s}$; b) $V_{ni} = 50\text{ m/s}$.

The evolution of the nodal velocities during the impacts at $V_{ni} = 2.0\text{ m/s}$ and $V_{ni} = 50\text{ m/s}$ is presented in Fig. 4.6. Again, because of the resistance of the rigid wall, the velocity of Node B remains unchanged at zero until separation occurs. It can be seen that a common feature for impacts at the two different initial impact velocities is the high frequency oscillations with small amplitude existing in the time histories of velocities for Nodes A

and C, which is also apparent for Node B after separation. Furthermore, stronger fluctuations occur at the node on the surface than at the centre of the sphere, and more significant oscillations can be observed for impact at higher initial impact velocity ($V_{ni} = 50m/s$). This is due to the influence of stress waves. However, the overall velocities of the nodes A and C are very close during the impact, while after separation all three nodes have very similar overall velocity profiles. The latter behaviour implies that after separation the sphere may be approximately treated as a rigid body if the oscillation is ignored (Li *et al.* 2000). It is also interesting to note that the velocities at nodes A and C are zero when the displacements of these nodes reach their maximum, which is corresponding to the kinetic theory of a single degree-of-freedom system (see Clough and Penzien 1993).

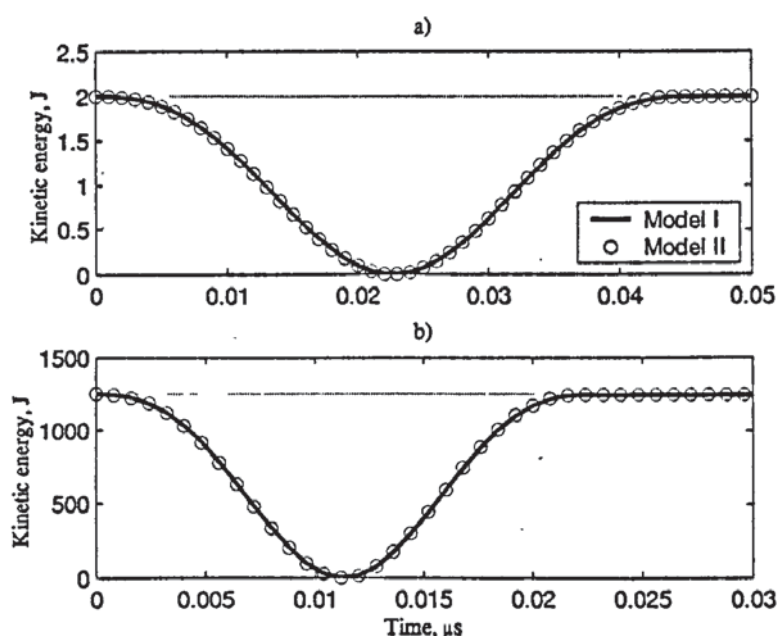


Fig. 4.7 Time histories of kinetic energy during the impact of an elastic sphere with a rigid wall using Model I and II at: a) $V_{ni} = 2.0m/s$; b) $V_{ni} = 50m/s$.

Figure 4.7 shows the comparisons of the evolution of kinetic energy obtained with Model I and II for the impacts at $V_{ni} = 2.0m/s$ and $V_{ni} = 50m/s$, respectively. It is clear that the results obtained for two models are identical for impacts both at low and high velocities. Unlike the velocity evolutions shown in Fig. 4.6, no oscillation is found in the evolution of kinetic energy. This demonstrates that the velocity oscillations are purely due to the interactions of stress wave propagation and reflection (Li *et al.* 2000). It can be seen that the kinetic energy gradually reduces to essentially zero during the compression phase, which indicates that the initial kinetic energy gradually transfers into the elastic strain energy stored in the sphere and/or the energy dissipated by stress wave propagation. At the

instant of maximum compression, the initial kinetic energy is completely transferred so that it reaches essentially zero. During the restitution, the kinetic energy gradually increases since the elastic strain energy stored in the sphere is gradually recovered and converted into kinetic energy that results in the sphere bouncing off. After the sphere separates from the rigid wall, the kinetic energy remains unaltered and is essentially identical to the initial kinetic energy, which implies the energy dissipated by stress waves is negligible.

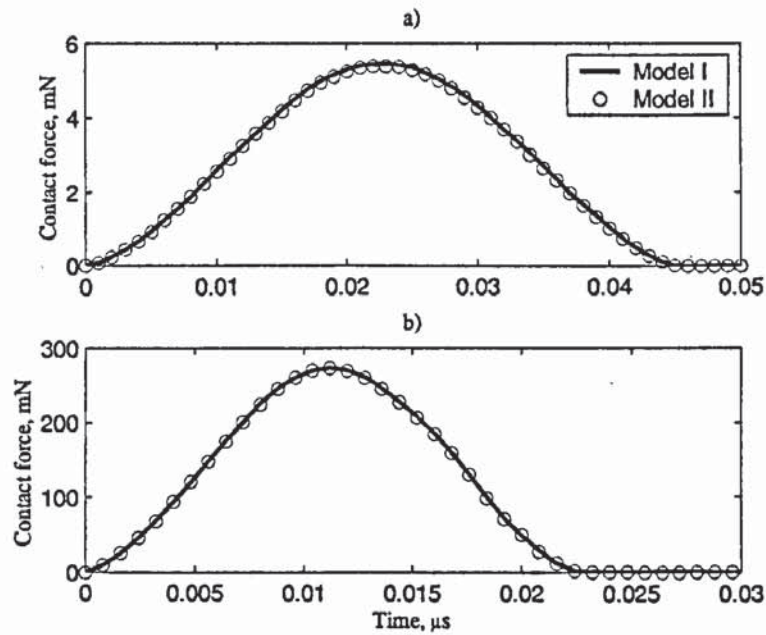


Fig. 4.8 Time histories of contact force during the impact of an elastic sphere with a rigid wall using Model I and II at: a) $V_{ni} = 2.0\text{m/s}$; b) $V_{ni} = 50\text{m/s}$.

As the kinetic energy decreases and the displacement of the centre of the sphere increases during compression, the contact force increases until it reaches a peak value at the maximum compression. Then, during restitution, the contact force decreases as the kinetic energy increases. Finally the contact force reduces to zero when the contact is terminated. After the sphere rebounds off, the contact force remains zero since there is no contact. The evolution of the contact force is illustrated in Fig. 4.8, in which the results obtained for impacts at $V_{ni} = 2.0\text{m/s}$ and $V_{ni} = 50\text{m/s}$ for the two different models are shown. It can be seen that the results obtained from the two models are essentially identical. In addition, it is clear that the duration of restitution is equal to that of compression and the higher the initial impact velocity, the shorter the duration of impact.

4.2.4 Force-displacement relationship

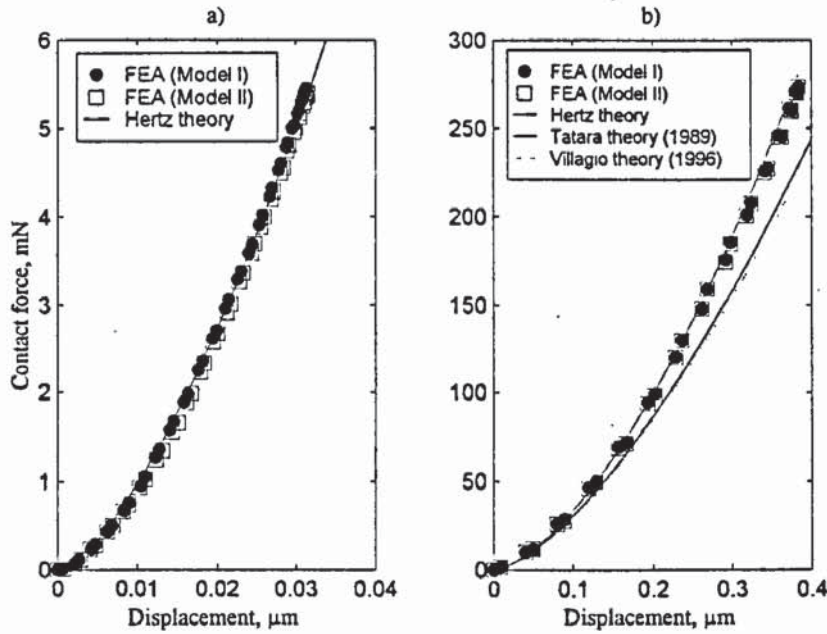


Fig. 4.9 Contact force-displacement relationships for the impact of an elastic sphere with a rigid wall using Model I and II at: a) $V_{ni} = 2.0\text{ m/s}$; b) $V_{ni} = 50\text{ m/s}$.

Figure 4.9 shows the contact force-displacement relations obtained using Model I and II. In this figure, the displacement is that of the sphere centre. Figure 4.9a shows the contact force-displacement relations for the impact at a low velocity ($V_{ni} = 2.0\text{ m/s}$), in which we superimpose the results given by Hertz theory. It can be seen that the FEA results obtained with the two models are identical and in excellent agreement with Hertz theory. Figure 4.9b presents the contact force-displacement relations for the impact at a high velocity ($V_{ni} = 50\text{ m/s}$), in which we also plot the results given by Hertz theory, Tataru theory (1989) and Villaggio Theory (1996). Again, the FEA results obtained with the two models are essential identical. The FEA results are found to diverge from Hertz theory at large displacements (say $\alpha > 0.1\mu\text{m}$). The discrepancies are attributed to the large deformation of the sphere at high velocities. Let us recall the assumptions proposed in Hertz theory that the deformation is relatively small and can hence be ignored. However, when the impact velocity is relatively high, the deformation induced would be so high that the assumption in Hertz theory is no longer satisfied. The large deformation of the sphere results in the lateral expansion of the sphere near the contact region as illustrated in Fig. 4.10.

Figure 4.10 illustrates the mechanism involved in the impact of an elastic sphere with a rigid surface at high velocities. In this figure, the dashed circle denotes the original position

of the sphere with its centre at C' and the solid curve indicates the real configuration of the impact system under large deformation at any arbitrary instant with the sphere centre located at C'' . The relative approach is then $C'C'' = \alpha$. If the deformation of the sphere is ignored, then the bottom of the sphere (Point B) moves to B'' as the sphere centre moves to point C'' . For a Hertzian interaction the contact diameter $2a_H$ is less than the length of the chord defined by the intersection of the rigid surface and the sphere that is centred at C'' ; and $BB'' = C'C'' = \alpha$ is the apparent overlap of the un-deformed sphere with the rigid surface. However, owing to the large deformation of the sphere, the bottom part of the sphere which is close to the contact region will expand outwards, this results in a real contact radius a and $a \geq a_H$.

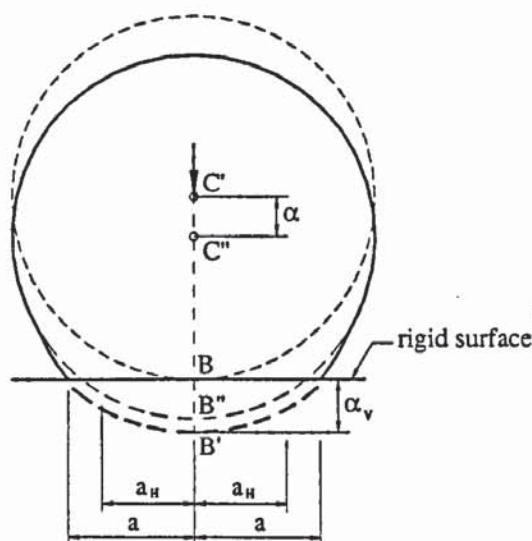


Fig. 4.10 Illustration of the contact deformation at high velocities.

Since at high velocities, as shown in Figs. 4.2 and 4.3, the contact pressure distribution still follow the elliptical shape as assumed in Hertz theory and the maximum contact pressure p_0 is still proportional to the contact radius a , Eqs.(2.1) and (2.2) are applicable. We hence have $F_n \propto a^3$. Although Hertz theory also predicts $\tilde{F}_n \propto a_H^3$ (Eq.(2.12)), it underestimates the contact force generated for a given relative approach since it predicts a smaller contact radius at large deformations by assuming the deformation of the sphere is insignificant. In other words, for the same value of the relative approach, the contact forces generated at large deformations are higher than those predicted by Hertz theory as shown in Fig. 4.9b.

The contact force is plotted against the contact radius in log-log scale in Fig. 4.11. Both the FEA results (symbols) and Hertz theory (the solid line) are presented. The FEA results are

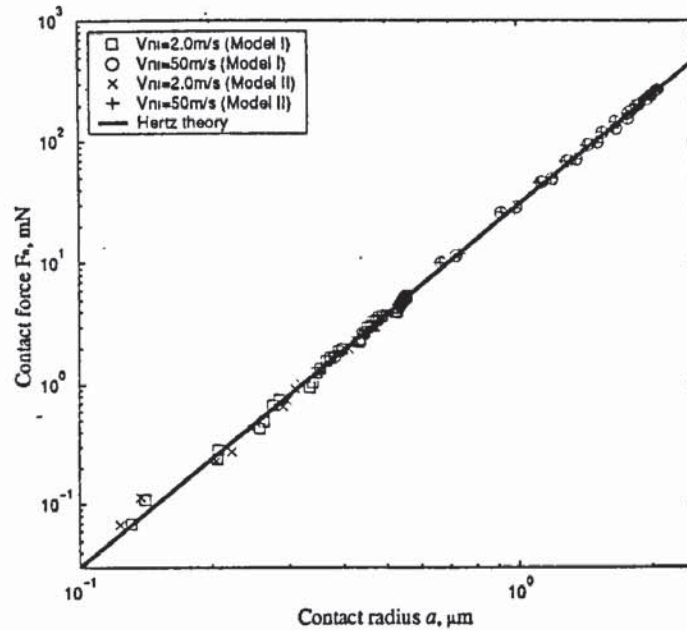


Fig. 4.11 The variation of the contact force F_n with the contact radius a .

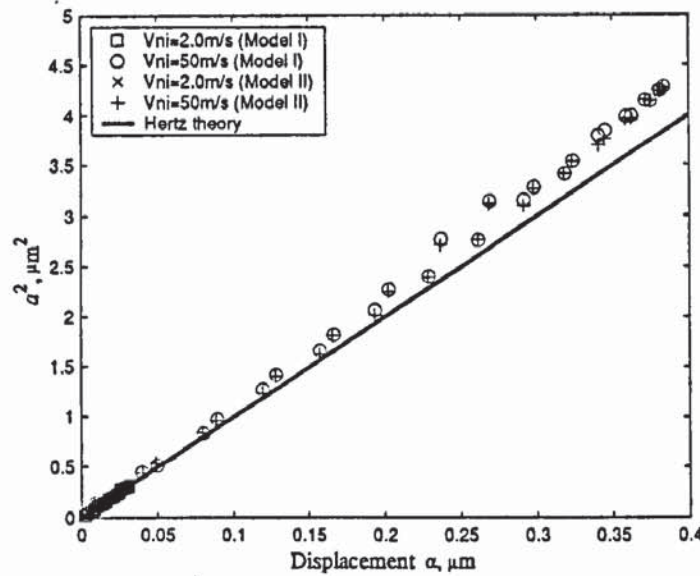


Fig. 4.12 The variation of a^2 with the displacement α .

obtained using the two models for the impacts at $V_{ni} = 2.0\text{ m/s}$ and $V_{ni} = 50\text{ m/s}$, respectively. In Hertz theory, the contact force F_n is given by Eq.(2.12). It can be seen from Fig. 4.11 that the variation of the contact force F_n with contact radius a obtained in FE analysis also agrees well with the predictions of Hertz theory, even for the impact at the high velocity ($V_{ni} = 50\text{ m/s}$). Figure 4.12 shows the variation of the displacement of the sphere centre α with the contact radius a , in which, again, the symbols represent the FEA results obtained with the two models for the impacts at $V_{ni} = 2.0\text{ m/s}$ and $V_{ni} = 50\text{ m/s}$, and the line is given by Eq.(2.11) in Hertz theory. It is clear that when the displacement α

is sufficient small (say $\alpha \leq 0.1\mu m = 0.01R$) FEA results are consistent with Hertz theory. However, with further increase in displacement, FEA results begin to diverge from Hertz theory and Hertz theory predicts a smaller contact radius than the FEA results as illustrated in Fig. 4.10. This is mainly due to the fact that the deformation of the sphere becomes significant. This leads to the lateral expansion of the sphere near the contact region and in turn results in a larger contact area than that predicted by Hertz theory. This also demonstrates that the disagreement in force-displacement relationship between the FEA results and Hertz theory as shown in Fig. 4.9b is mainly due to the large deformation of the sphere as discussed above.

Although Villaggio theory (Villaggio 1996) was developed for the contact of a sphere with a rigid plane taking account of the curvature and the global deformation of the sphere, it is not consistent with present FEA results. The reason for this is that it is assumed that the relative approach is equal to the overlap of the deformed sphere with the rigid surface (say, BB' in Fig. 4.10). In the present case, this is not true since significant deformation of the sphere takes place and the deformation is concentrated in the bottom half of the sphere. Therefore the overlap of the deformed sphere with the rigid plane is not equal to the approach of the sphere centre. It is clear from Fig. 4.10 that

$$\alpha_v \geq \alpha \quad (4.4)$$

where α_v is the displacement employed in Villaggio's theory (Villaggio 1996).

It is interesting to note that the FEA results for the impact at high velocity agree with Tatara theory (Tatara 1989), in which the induced deformation of the sphere is considered by assuming a concentrated force exerted at the initial contact point. This illustrates that the large deformation of the sphere results in a higher contact stiffness than given by Hertz theory.

4.2.5 Coefficient of restitution

As mentioned in Section 2.2.1, the coefficient of restitution can normally be defined by the ratio of the rebound velocity to the initial impact velocity of the sphere (Eq.(2.17)) for collinear impacts. However, it can be seen from Fig. 4.6 that the rebound velocity varies from node to node and from time to time due to the influence of stress wave propagation. Therefore, a key issue in calculating the coefficient of restitution is the definition of the

rebound velocity of the sphere. There are three possible approaches to define the rebound velocity (Li *et al.* 2000).

- 1) The rebound velocity of the sphere is defined as the average rebound velocity of the sphere centre over a suitable time period. This approach is rather simple but the rebound velocity is not unique since the time interval can be arbitrarily chosen.
- 2) An alternative is to treat the sphere as an ideal rigid body and use the law of conservation of momentum by equating the rebound momentum to impulse during the restitution. However, the contact force in FEMs is computed by either the kinematic method or the penalty method (see Appendix A), the accuracy of which is highly dependent on the sizes of contact elements used and the contact modelling techniques employed and is normally lower than that of the velocity and of the kinetic energy.
- 3) The third option is to determine the rebound velocity from the rebound kinetic energy as follows

$$V_{nr} = \sqrt{\frac{2W_r}{m}} \quad (4.5)$$

where W_r is the rebound kinetic energy of the sphere which is constant as shown in Fig. 4.7. The total rebound kinetic energy includes the oscillating energy and so the rebound velocity calculated in this way will be slightly higher than the true value. However, compared with the total rebound kinetic energy the oscillating energy is very small and its significance can be neglected. Therefore the third option generally provides a good approximation of the rebound velocity. Using Eqs.(2.16), (2.17) and (4.5), the coefficient of restitution can be rewritten as

$$e_n = \frac{V_{nr}}{V_{ni}} = \sqrt{\frac{W_r}{W_i}} \quad (4.6)$$

Table 4.1 shows the coefficient of restitution for the impact of an elastic sphere with a rigid wall at two different velocities using the two models. In Table 4.1, the coefficients of restitution calculated by two approaches (1 and 3) are presented. As expected, the coefficient of restitution obtained by approach 3 is slightly higher than that given by Approach 1, but the difference is insignificant. In the following, approach 3 is used to calculate the coefficient of restitution, except when specified otherwise. It is clear that all the coefficients of restitution presented in Table 4.1 are very close to unity, which implies

that the influence of the stress waves is negligible. To further evaluate the effect of stress waves, it is worth determining the reflection times of the longitudinal wave during the impact. As shown in the last column of Table 4.1, the longitudinal wave is reflected more than three times even during the impact at the higher velocity.

Table 4.1 The coefficient of restitution for the impact of an elastic sphere with a rigid wall

Impact Velocity V_{ni} (m/s)	Approach 1		Approach 3		Number of reflections of stress waves
	Model I	Model II	Model I	Model II	
2.0	.9978	.9979	.9992	.9998	5
50	.9940	.9970	.9985	.9991	3

4.3 Normal impact of elastic sphere at an elastic boundary

Since the rigid wall introduced in the last section is an idealisation and it is of interest to investigate more realistic cases in which both the sphere and the substrate can be deformed during the impact, we now consider the impact of an elastic sphere with an elastic half-space. The FE model was given in Section 3.2.2 and the material properties were listed in Table 3.2. Here we focus on the impact at an impact velocity of $V_{ni} = 5.0\text{ m/s}$, for which the quasi-static condition is satisfied so that a proper comparison with Hertz theory can be made. The effect of stress wave on the impact behaviour is discussed in Appendix B.

4.3.1 Pressure distribution

Figure 4.13 shows the pressure distribution at various instants. In the figure, the circles represents the FEA results and the solid lines denote the results given by Hertz theory. It is apparent that the FEA results are in excellent agreement with Hertz theory. The intersections of the thick lines with the horizontal and vertical axes represent the contact radius a and the maximum contact pressure p_0 , respectively. The contact radius a and the maximum contact pressure p_0 estimated by this approach is plotted in Fig. 4.14, in which p_0 is plotted as a function of a . We also superimpose the predictions of Hertz theory (Eq.(2.9)) as denoted by the solid line. It is clear that the FEA results are consistent with Hertz theory.

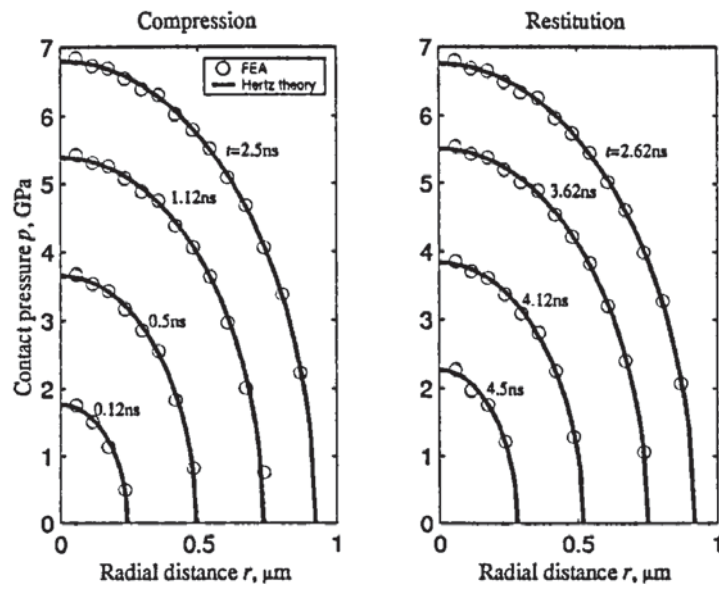


Fig. 4.13 The pressure distributions at various instants during the impact of an elastic sphere with an elastic half-space at $V_{ni} = 5.0m/s$.

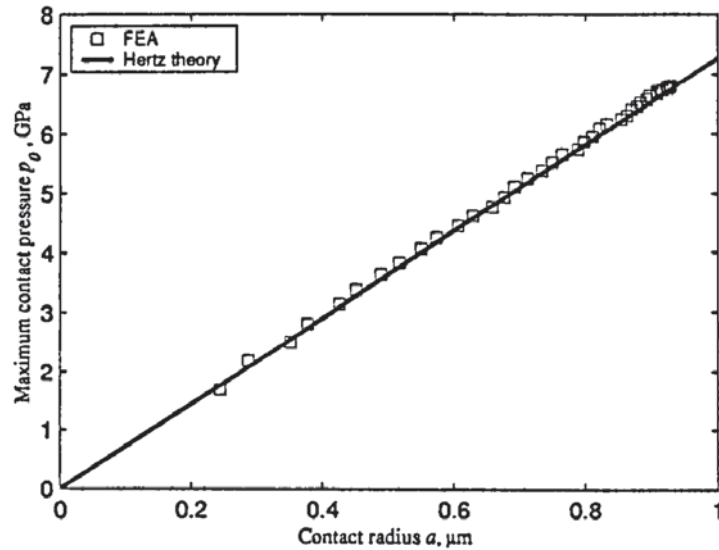


Fig. 4.14 The variation of the maximum contact pressure p_0 with the contact radius a during the impact of an elastic sphere with an elastic half-space at $V_{ni} = 5.0m/s$.

4.3.2 Stress distribution

Figure 4.15 shows the typical patterns for the stress distributions in the sphere and the half-space at the maximum compression ($t = 2.5ns$). The effective stress (or von Mises stress) is shown in Fig. 4.15a, while the maximum shear stress in Fig. 4.15b. It can be seen that the patterns for the stresses inside the sphere is quite similar to those inside the substrate. They are also consistent with the experimental photo-elastic observations of Shih *et. al.* (1992) and the theoretical predictions of Davies (1949). The plus signs “+” in Fig. 4.15 indicate the location of the maximum value of the corresponding stresses. It can be seen

that the maximum values of both the effective stress and maximum shear stress are located inside the substrate at a depth of *c.a.* $0.5a$. For the effective stress, the maximum value is 4.2GN/m^2 ; while for the maximum shear stress, the value is 2.1GN/m^2 . Referring to Fig. 4.13, the corresponding maximum contact pressure p_0 is around 6.8GN/m^2 at $t = 2.5\text{ns}$. Therefore the maximum effective stress is equal to $0.62p_0$, while the maximum value of the maximum shear stress is $0.31p_0$. This is in excellent agreement with the theoretical predictions (see Johnson 1985). According to both von Mises and Tresca criteria, it would be expected that yielding initiate inside the substrate if the contacting bodies are elastic-plastic.

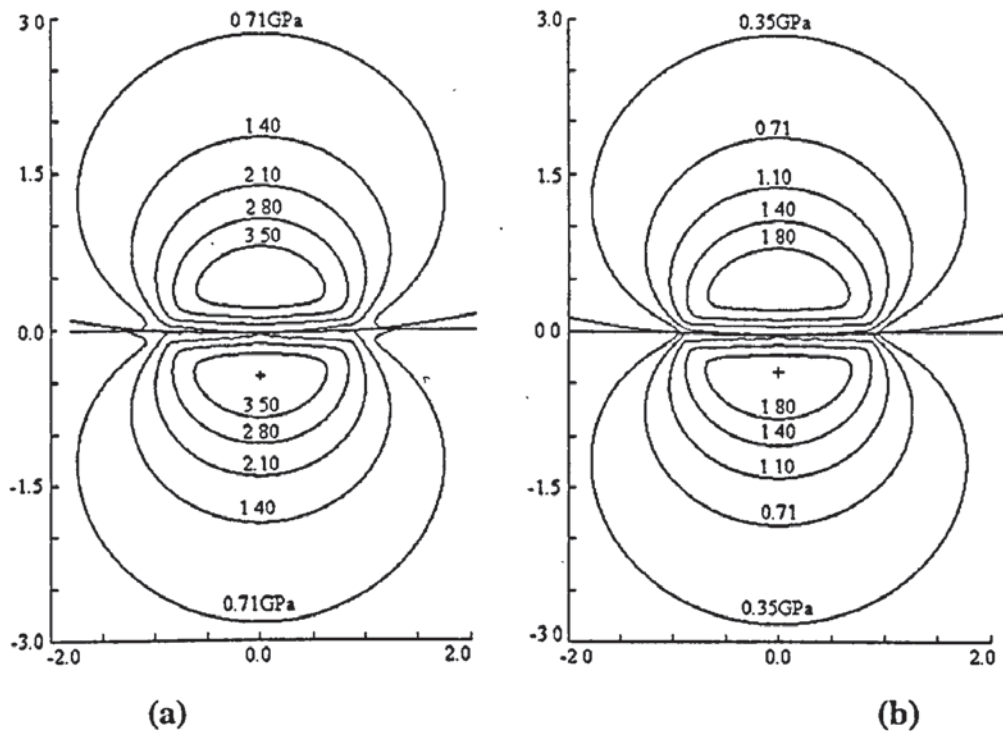


Fig. 4.15 Stress distributions inside the sphere and the half-space at the maximum compression ($t = 2.5\text{ns}$) during the impact at $V_{ni} = 5.0\text{m/s}$: (a) the effective stress; (b) the maximum shear stress.

4.3.3 Evolution of impact parameters

Figures 4.16 and 4.17 present the evolutions of impact parameters for the impact of an elastic sphere with an elastic half-space at $V_{ni} = 5.0\text{m/s}$. Figure 4.16a shows the time histories of displacements at four distinct nodes: node A (the top); B (the bottom); C (the centre) and D (the initial contact point of the substrate), see Fig. 3.4. The time histories of corresponding velocities are shown in Fig. 4.16b. Figure 4.17a shows the time history of the kinetic energy and the time history of the contact force is presented in Fig. 4.17b. It can

be seen that, for the whole process of impact, two distinct phases can again be clearly distinguished: compression and restitution. When the nodal displacements and the contact force reach their maximum values, and the nodal velocities and the kinetic energy approach zero, the compression phase is terminated and the restitution phase begins. The restitution ends as the nodal displacements and the contact force reduce to zero. After the separation, the kinetic energy remains unchanged at a constant value close to the initial one, which implies that the energy loss due to stress wave propagation can be neglected and the coefficient of restitution is very close to unity, according to Eq.(4.6).

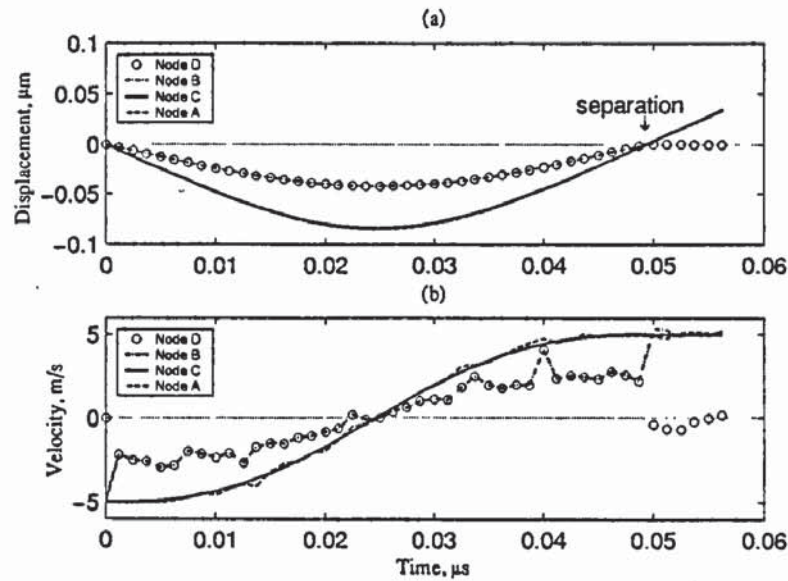


Fig. 4.16 Time histories of (a) nodal displacements and (b) velocities during the impact of an elastic sphere with an elastic half-space at $V_{ni} = 5.0\text{m/s}$.

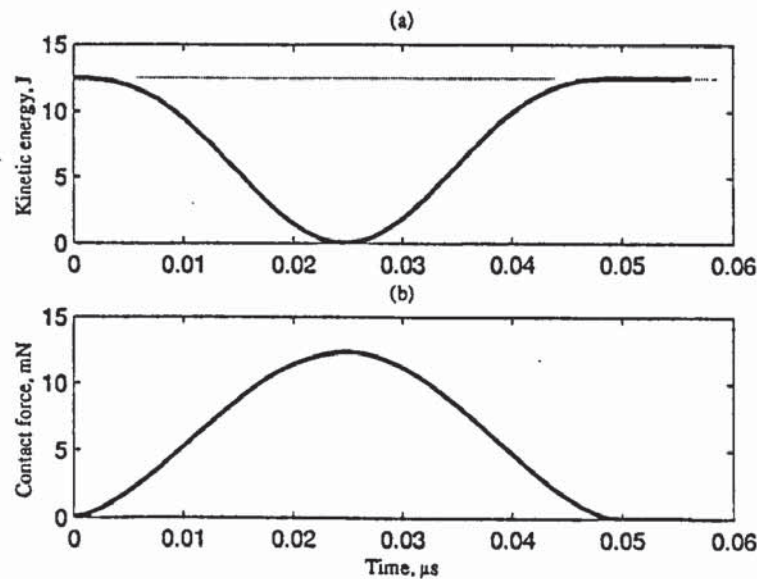


Fig. 4.17 Time histories of (a) kinetic energy and (b) impact force during the impact of an elastic sphere with an elastic half-space at $V_{ni} = 5.0\text{m/s}$.

It is also clear that during the impact the deformation of the sphere is mainly concentrated in the bottom semi-sphere since the nodal displacements at the top (A) and the centre (C) of the sphere are essentially identical. The displacement at the initial contact point of the substrate (node D) remains zero and its velocity fluctuates around zero after separation. This indicates that the deformation of the substrate has been completely recovered. Once the sphere rebounds from the substrate, the displacements at the three different nodes (A, B, C) coalesce and the overall velocities are similar. This implies that the sphere behaves like a rigid body, provided that we omit the fluctuations of the nodal velocities which are mainly due to the stress wave propagation.

4.3.4 Force-displacement relationship

It has been shown that the energy loss due to the stress wave propagation is negligible for the impact at $V_{ni} = 5.0m/s$. Thus the deformation of the sphere and the substrate is essentially quasi-static and can be analysed by Hertz theory. The force-displacement relationship is shown in Fig. 4.18, in which the prediction given by Hertz theory is also superimposed. It is clear that the FEA results are in excellent agreement with Hertz theory. The variations of the contact force with the contact radius and the variation of the contact area with displacement are shown in Fig. 4.19, in which the predictions given by Hertz theory are superimposed. It can be seen that the FEA results again agree very well with Hertz theory.

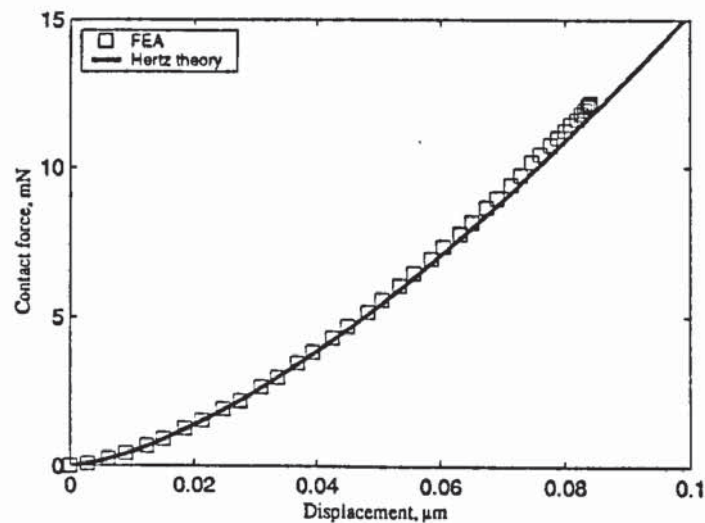


Fig. 4.18 The force-displacement relationship for the impact of an elastic sphere with an elastic half-space at $V_{ni} = 5.0m/s$.

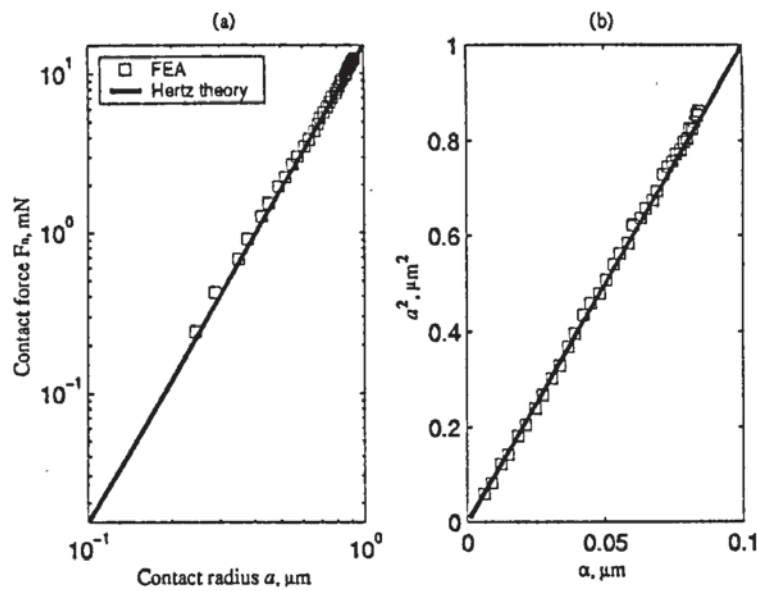


Fig. 4.19 (a) The variation of F_n with a ; (b) the variation of a^2 with α for the impact of an elastic sphere with an elastic half-space at $V_{ni} = 5.0 \text{ m/s}$.

4.4 Summary

As a preliminary study, the normal impact of elastic spheres has been investigated using FEM, for which comprehensive results have been reported and compared with theories. The reliability and accuracy of the finite element methods have been demonstrated. The effect of large deformation has also been discussed. It has been shown that:

(1) The impact behaviour of elastic spheres can be well predicted by Hertz theory provided that the initial impact velocity is so low that the deformation induced is sufficiently small and the energy loss due to stress wave propagation can be ignored. However, if the initial impact velocity is high enough, either the contact deformation or the effect of the stress wave (see appendix B) becomes significant and a proper prediction of the impact behaviour must take these factors into account.

(2) Regardless of the impact velocities, the contact deformation is mainly localised in the vicinity of the contact region. At high velocities, this localisation of the contact deformation leads to lateral expansion of the sphere, which may significantly affect the impact behaviour.

(3) Unlike static contact of elastic spheres, the impact of elastic spheres always involves the propagation of stress waves. Furthermore, the energy loss due to stress wave propagations strongly depends on how many times the longitudinal wave can reflect back to the impact point before the sphere rebounds off (see also Appendix B). It is suggested

by the present FEA study that the energy loss due to stress waves can be ignored if the longitudinal wave can reflect back to the impact point more than three times during the impact and the problem can then be regarded as a quasi-static one. For the impact of a small particle with a massive body in which no reflection of stress waves occurs, the impact velocity must be small enough to minimise the energy losses, i.e., $\lambda \leq 1\%$. For example, for material properties considered in this chapter, the initial impact velocity should be less than $1.69m/s$ for the energy loss due to stress waves to be less than one per cent.

Chapter 5 Normal Impact of Particles Involving Plastic Deformation

5.1 Introduction

Due to the localisation of stresses during the contact or impact of particles, plastic deformation is often induced. In this chapter, we consider the impact of particles involving plastic deformation, for which focus is placed on the plastic deformation that can be represented either as elastic-perfectly plastic or as elastic-plastic with work hardening. Typical stress-strain curves are shown in Figs. 2.1b and 2.1c, respectively.

For the impact of elastic-plastic particles, the particles will deform elastically if the initial impact velocity is low enough. However, yield will be initiated once the initial impact velocity reaches a certain value. Here the initial impact velocity to initiate yield is defined as the yield velocity V_{y0} . Johnson (1985) showed that, for the case of axi-symmetric contact of two spheres with Poisson's ratio $\nu = 0.3$, yield occurs when the maximum contact pressure p_0 reaches $1.6Y$ according to both the Von Mises and Tresca criteria, as given by Eq.(2.36). Assume that the effects of stress waves and the deformation are negligible when $V_{ni} \leq V_{y0}$, so that the quasi-static condition can be approached and Hertz theory is applicable. Combining Eqs.(2.9) and (2.16), we have

$$V_{ni} = \left(\frac{\pi}{2E^*} \right)^2 \left(\frac{8\pi R^{*3} p_0^5}{15m^*} \right)^{1/2} \quad (5.1)$$

Substituting Eq.(2.36) into Eq.(5.1), we obtain

$$V_{y0} = \left(\frac{\pi}{2E^*} \right)^2 \left(\frac{8\pi R^{*3} p_{y0}^5}{15m^*} \right)^{1/2} = \left(\frac{\pi}{2E^*} \right)^2 \left[\frac{8\pi R^{*3} (1.6Y)^5}{15m^*} \right]^{1/2} \quad (5.2)$$

For the impact of an elastic-plastic sphere with a rigid plane or a half-space, Eq.(5.2) can be rewritten as

$$V_{y0} = 5.052 \left(\frac{Y^5}{E^{*4} \rho} \right)^{1/2} \quad (5.3)$$

For an elastic sphere impinging against an elastic-plastic half-space with the material properties given in Table 3.2, the yield velocity is $V_{y0} = 0.29m/s$, which is much less than $1.69m/s$ above which the energy loss due to stress waves may become significant, as discussed in the preceding chapter. Note that $Y = 1.35GN/m^2$ given in Table 3.2 is the highest value assumed in this study and in reality the yield stress is generally around $1.0GN/m^2$ for most steel materials. Thus for the elastic phase of the impact of elastic-plastic particles, quasi-static conditions can normally be satisfied. On the other hand, this also implies that plastic deformation is readily induced for most impacts.

During the impact of elastic-plastic particles, the elastic deformation reaches its limits at the instant when yield initiates. According to Hertz theory, we have

$$a_{y0} = \frac{\pi R^*}{2E^*} P_{y0} \quad (5.4)$$

$$\alpha_{y0} = \frac{\pi a_{y0} P_{y0}}{2E^*} = \frac{a_{y0}^2}{R} \quad (5.5)$$

$$F_{y0} = \frac{4E^* a_{y0}^3}{3R^*} = \frac{4}{3} E^* R^{*1/2} \alpha_{y0}^{3/2} \quad (5.6)$$

where a_{y0} , α_{y0} and F_{y0} are the contact radius, the relative approach and the contact force at the onset of yield.

We shall proceed to discuss the impact behaviour of particles involving plastic deformation. Typical impact behaviour is presented in the next section, followed by discussions on parametric dependence of the rebound behaviour. In Section 5.4, a mathematical model for the normal impact of particles involving plastic deformation, which is first reported in Li *et al.* (2001), is presented. Finally, the influence of work hardening is discussed.

5.2 Typical impact behaviour of an elastic sphere with an elastic-perfectly plastic half-space

In Chapter 4, the FEA procedures have been demonstrated by the excellent agreement between the FEA results and Hertz theory for the normal impact of elastic spheres. We shall now employ the FEA procedures to investigate the normal impact of an elastic sphere with an elastic-perfectly plastic half-space. The FE model is shown in Fig. 3.5 and the

material properties are listed in Table 3.2. The impact velocity is specified to vary from $V_{ni} = 0.3m/s$ to $150m/s$. Hence it is supposed that within the specified velocities the contact deformation of the substrate would be ranging from the onset of the plastic deformation, through elastoplastic deformation until fully developed plastic deformation.

5.2.1 Pressure distribution

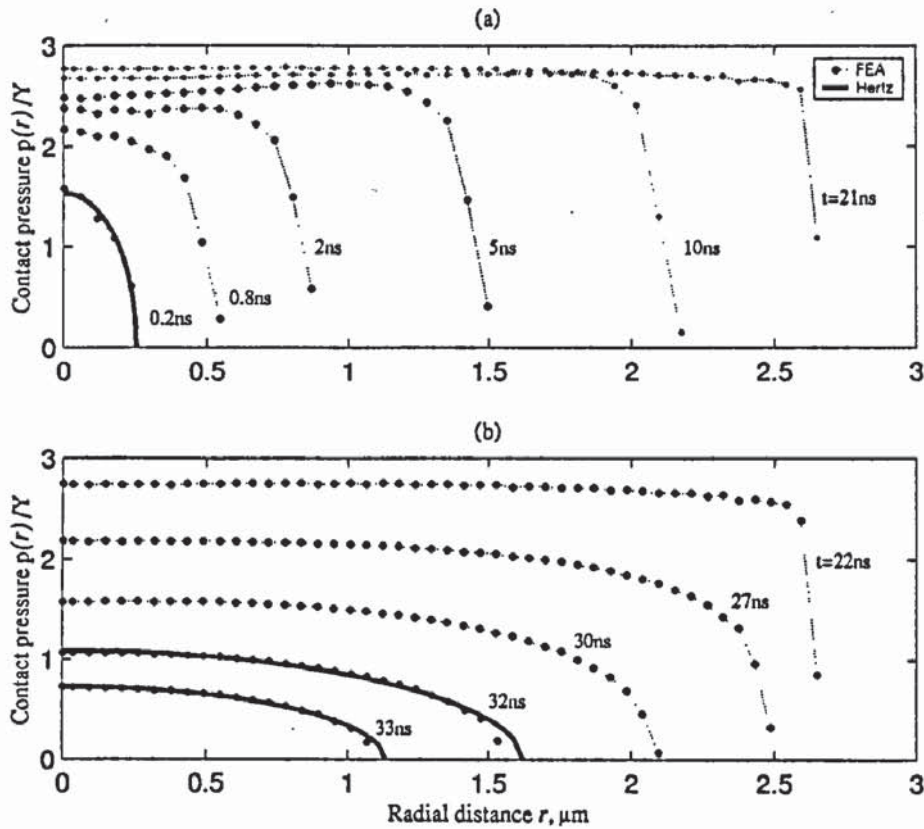


Fig. 5.1 The typical evolution of contact pressure distributions for the impact of an elastic sphere against an elastic-perfectly plastic half-space with $V_{ni} = 30m/s$ at various instants during: (a) the compression; (b) the restitution.

Since plastic deformation takes place when the maximum pressure p_0 reaches the value $1.6Y$ for axisymmetric contact of elastic-plastic bodies with $\nu = 0.3$ (Johnson 1985), for values of p_0 less than $1.6Y$, the pressure distribution should follow the elliptical distribution predicted by Hertz (1896). This is illustrated in Fig. 5.1a, which shows a typical evolution of the pressure distribution during the compression of the plastic impact at a moderate velocity ($V_{ni} = 30m/s$). It is clear that the FEA results are in good agreement with Hertz theory before the maximum pressure p_0 reaches $1.6Y$. Once p_0

exceeds $1.6Y$ yield occurs, as will be shown in Fig. 5.6b, and plastic deformation affects the pressure distribution. It can be seen from Fig. 5.1a that the pressure profile changes significantly with the evolution of plastic deformation and pronounced flattened pressure profiles are developed. This is consistent with the experimental observation of Johnson (1968) and the analysis of others (see Hardy *et al.* 1971; Sinclair *et al.* 1985; Kral *et al.* 1993). It is also clear that the flattened pressure distribution prevails during the compression. Significantly flattened pressure profiles form once the plastic zone reaches the contact surface at $t \geq 5ns$ (see Fig. 5.6d), after which the magnitude of the maximum pressure p_0 varies between 2.6 and 2.8 times the yield stress Y for the impact case considered. This is comparable with the previous results that, for fully plastic contact, the mean pressure p_m either lies between $2.7Y$ and $3.0Y$ as obtained by Tabor (1951) or is approximately equal to $2.8Y$ as obtained by others (see Johnson 1985; Sinclair *et al.* 1985; Hill *et al.* 1989).

Figure 5.1b shows the typical evolution of the pressure distribution during the restitution of the plastic impact. It is clear that at the beginning of the restitution the pressure distributions are similar to those at the end of the compression, even though the flattened pressure distribution reduces more smoothly to zero at the contact edge. It is interesting to find that the pressure distribution does follow an elliptical profile when p_0 is once more less than a value of $1.6Y$, even though the maximum pressure p_0 and the contact radius a are significantly different from those obtained during compression. This is due to the interfacial conformity induced by the permanent plastic deformation.

Note that in Fig. 5.1 the data points on the horizontal axis obtained from finite element analysis are omitted. The actual FEA results are illustrated in Fig. 5.2, in which only the pressure distribution at the maximum compression is shown. It is clear that owing to the FE approximation of the pressure distribution as discussed in Appendix A.4.4, apparent errors are introduced at the contact edge, which was also observed in Fig. 4.4 for normal impacts of elastic particles. It is also interesting to note that the flattened pressure distribution can be approximated by a Hertzian pressure distribution with a cut-off, shown by solid lines, as proposed by Thornton (1997). By this approximation the intersection of Hertzian curve with the horizontal axis represents the contact boundary, which gives the contact radius of value $a = 2.663\mu m$. While a careful measurement taken from the topography of the contact region, as shown in Fig. 5.3, shows that the contact radius is

$2.662\mu\text{m}$. It is obvious that these two approaches gives the essentially identical results for the contact radius, and it is also demonstrated that the approximation of the contact pressure distribution obtained by finite element analysis gives fairly appropriate results for the contact radius.

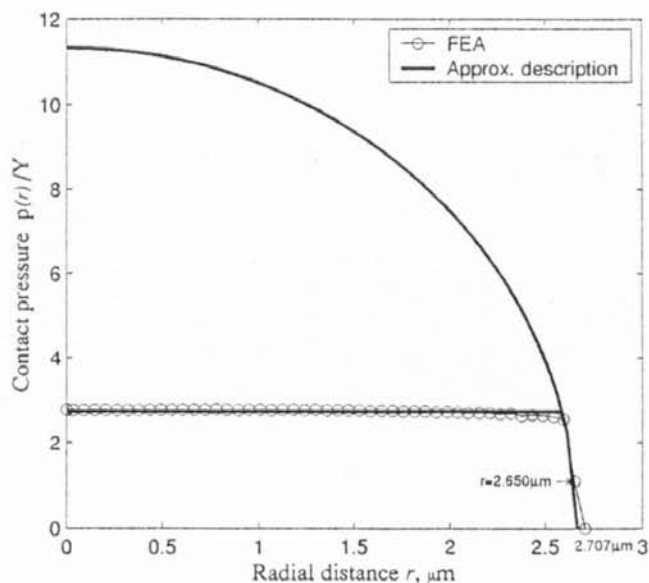


Fig. 5.2 The contact pressure distribution at the maximum compression ($t = 21\text{ns}$) during the impact of an elastic sphere with an elastic-perfectly plastic half-space at $V_{ni} = 30\text{m/s}$.

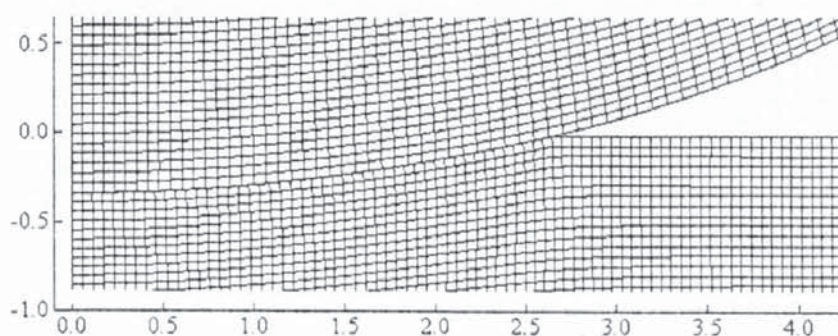
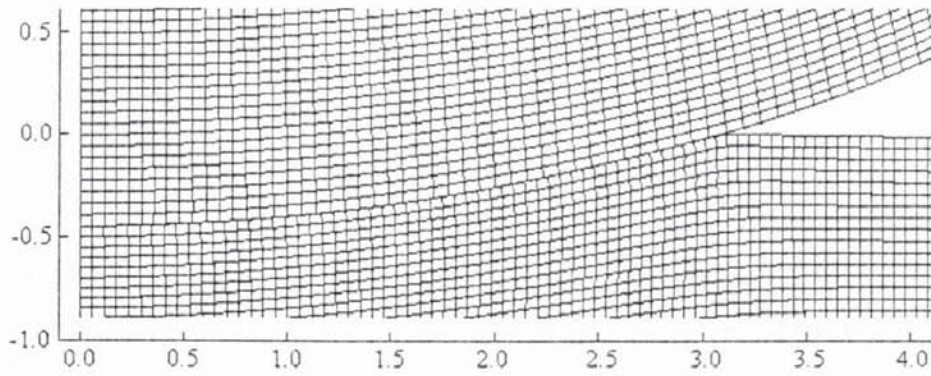


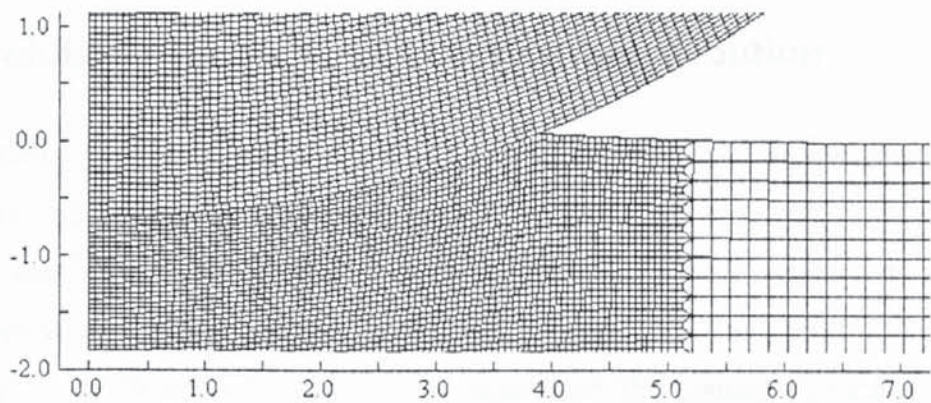
Fig. 5.3 The topography of the contact deformation at the maximum compression ($t = 21\text{ns}$) during the impact of an elastic sphere with an elastic-perfectly plastic substrate at $V_{ni} = 30\text{m/s}$ (unit: μm).

It should be noted that the pressure distributions shown in Fig. 5.1 are typical patterns only for plastic impacts at moderate velocities. As the velocity increases the plastic deformation generated during the impact could become more and more intense. Consequently, piling-up or sinking-in may occur around the periphery of the contact region, which may in turn affect the contact pressure distribution. For the present impact configuration, our FEA results show that the piling-up begins to take place during impacts with initial impact velocities higher than 40m/s , as shown in Fig. 5.4. In terms of the contact radius, it is

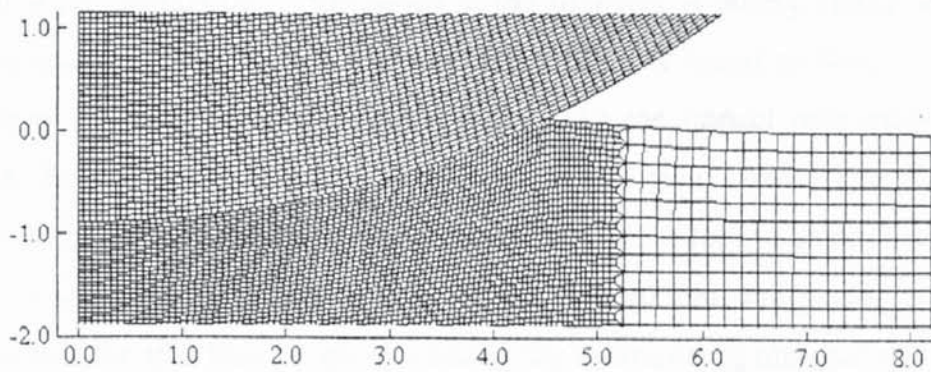
found that piling-up is initiated once the contact radius a is larger than $0.32R$. The influence of piling-up on the contact pressure distribution is illustrated in Fig. 5.5. It is clear that, with the occurrence of piling-up, the distribution of contact pressure is not flattened over the contact area, instead, the peak contact pressure is found at the contact centre and is gradually reduced towards the edge of the contact area.



(a)



(b)



(c)

Fig. 5.4 Topographies of the contact deformation at the maximum compression during the impact of an elastic sphere with a elastic-perfectly plastic half-space at (a) $V_{ni} = 40m/s$; (b) $V_{ni} = 60m/s$ and (c) $V_{ni} = 80m/s$ (unit: μm).

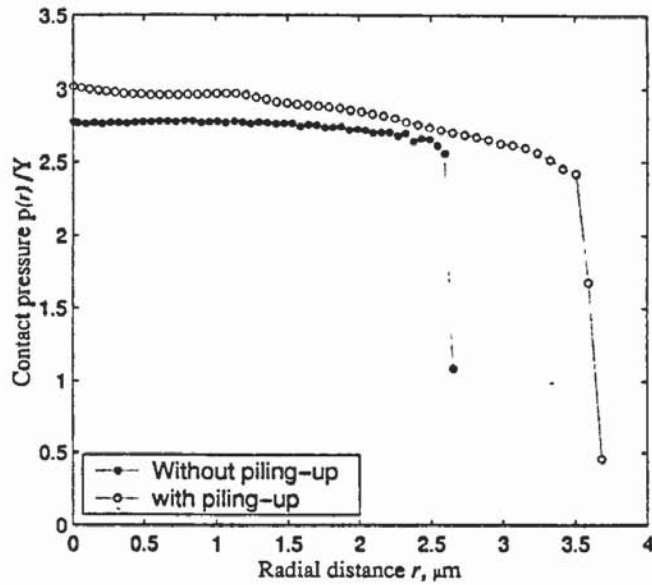


Fig. 5.5 The influence of piling-up upon the contact pressure distribution during the impact of an elastic sphere with an elastic-perfectly plastic half-space.

5.2.2 Evolution of the stress and strain distribution

The evolutions of effective stress within the substrate at various instants during the compression and restitution of the impact of an elastic sphere with an elastic-perfectly plastic half-space are shown in Figs. 5.6 and 5.7, respectively. It can be seen from Fig. 5.6 that at an early stage of the compression (see Fig. 5.6a, $t = 0.2ns$) the maximum effective stress is only $1.29GN/m^2$, which is located underneath the contact surface as indicated by “+” sign. This value is less than the yield stress $Y = 1.35GN/m^2$ as specified, which implies that at this instant the deformation of the substrate is purely elastic and no plastic deformation takes place. Thus the pressure distribution is found to follow very well the elliptical shape proposed by Hertz (see Fig. 5.1). As the impact proceeds, plastic yield occurs once the maximum effective stress reaches the yield stress. The plastic yield is expected to be initiated underneath the surface where the effective stress is the maximum (see Fig. 5.6a and Fig. 4.15). As the impact proceeds further, the plastic zone begins to expand outwards but still being encompassed by the surrounding material that is elastically deformed (Figs. 5.6b and 5.6c). At a certain instant, the plastic zone reaches the contact surface but there is still an elastic core at the contact centre as shown in Fig. 5.6d, at which instant the pressure distribution appears to be significantly flattened (Fig. 5.1). Finally, the entire contact region consists of the plastic zone that may further expand as the impact continues (see, Figs. 5.6e and 5.6f).

The evolution of effective stress during the restitution of the plastic impact is very complicated as shown in Fig. 5.7. Nevertheless it is clear that during the restitution the maximum effective stress is less than the yield stress and located in the area surrounding the contact region. Furthermore the residual effective stress is apparent after the sphere rebounds (Fig. 5.7f). The corresponding evolution of the effective plastic strain is shown in Fig. 5.8. It can be seen that the overall plastic strain distributions during the whole process of restitution are essentially identical, which qualitatively implies that the process of the restitution is essentially elastic.

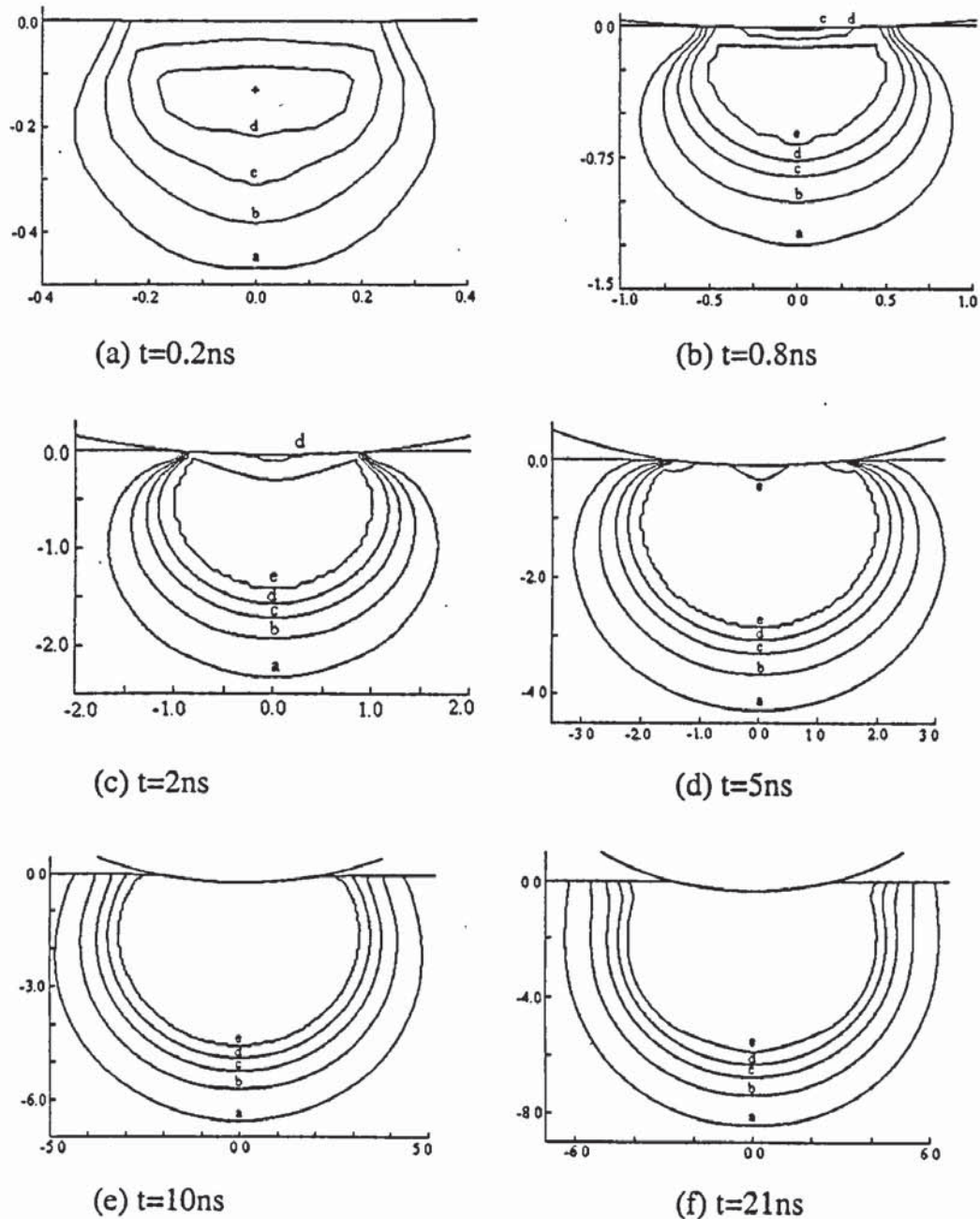


Fig. 5.6 The distributions of effective stress within the substrate at various instants during the compression of the impact of an elastic sphere with an elastic-perfectly plastic substrate at $V_{ni} = 30\text{m/s}$: a--- 0.50GN/m^2 ; b--- 0.71GN/m^2 ; c--- 0.93GN/m^2 ; d--- 1.14GN/m^2 ; e--- 1.35GN/m^2 ; "+"--- 1.29GN/m^2 .

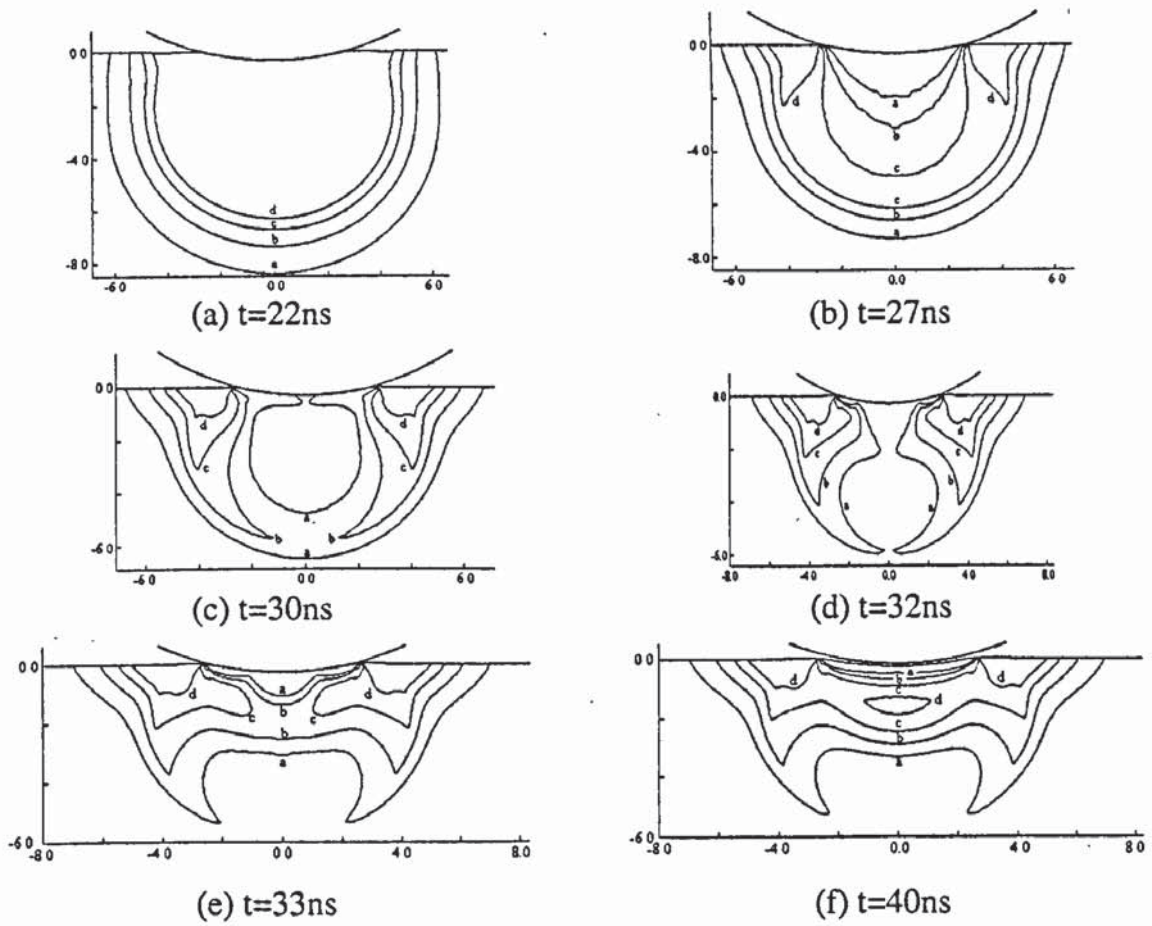


Fig. 5.7 The distributions of effective stress within the substrate at various instants during the restitution of the impact of an elastic sphere with an elastic-perfectly plastic substrate at $V_{ni} = 30\text{m/s}$: a--- 0.50GN/m^2 ; b--- 0.71GN/m^2 ; c--- 0.93GN/m^2 ; d--- 1.14GN/m^2 ; e--- 1.35GN/m^2 .

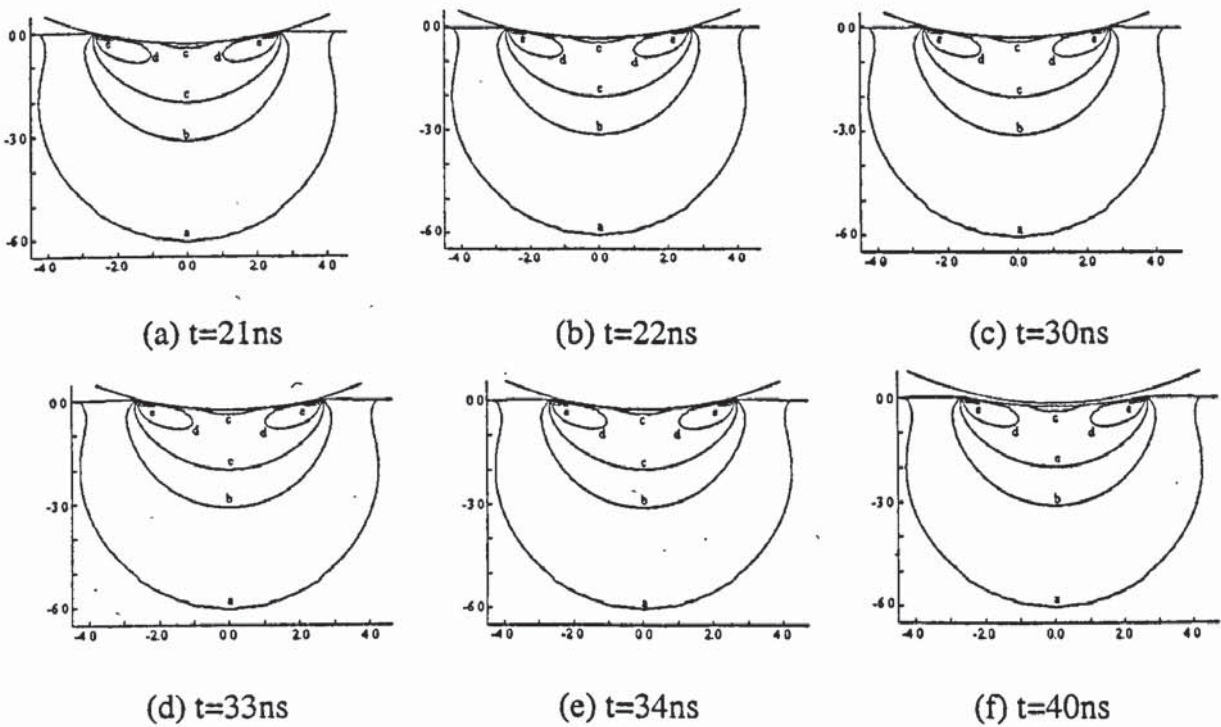


Fig. 5.8 The evolution of effective plastic strain within the substrate at various instants during the restitution of the impact of an elastic sphere with an elastic-perfectly plastic substrate at $V_{ni} = 30\text{m/s}$: a--- 0.0 ; b--- 0.038 ; c--- 0.075 ; d--- 0.11 ; e--- 0.15 .

5.2.3 Evolution of impact parameters

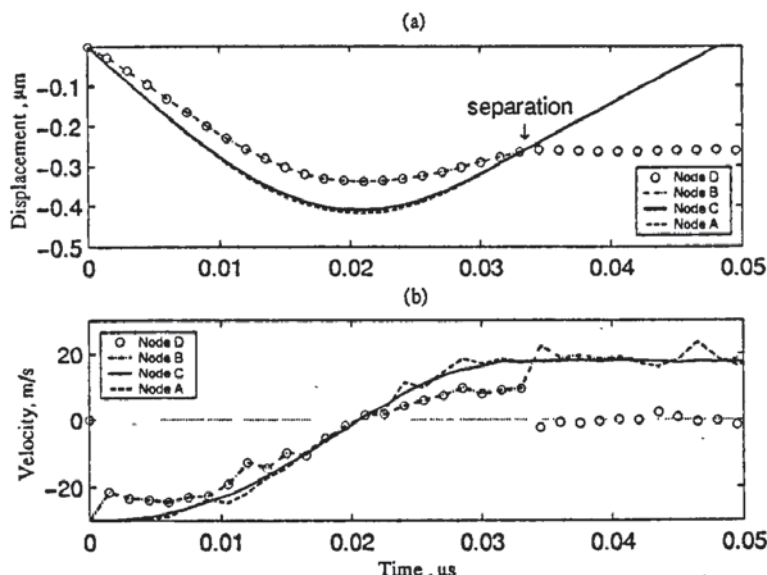


Fig. 5.9 Time histories of (a) nodal displacement and (b) nodal velocity for the impact of an elastic sphere with an elastic-perfectly plastic substrate at $V_{ni} = 30m/s$.

Figure 5.9 shows the time histories of nodal displacement and nodal velocity during the impact at $V_{ni} = 30m/s$. Results for four distinct nodes, which are at the top (A), centre (C) and bottom (B) of the sphere and the initial contact point of the half-space (D), are given. It can be seen from Fig. 5.9a that, similar to the elastic impacts discussed in Chapter 4, the difference between the displacements at the top and at the centre of the sphere is much smaller than the gap between displacements at the centre and the bottom of the sphere, which again implies that during the impact the deformation is mainly localised in the bottom half of the sphere. In contrast to the impact of an elastic sphere with an elastic half-space, the nodal displacement at the initial contact point of the half-space does not completely recover back to zero after the separation of the sphere from the plastically deformed half-space. This indicates that permanent plastic indentation occurs in the substrate, which can also be observed from Figs. 5.7f and 5.8f. Once the sphere separates from the substrate, the displacements at the three different nodes on the sphere coalesce, which implies that the sphere behaves like a rigid one after it rebounds off.

The corresponding time histories of nodal velocities are shown in Fig. 5.9b. It is clear that the velocity fluctuations are quite significant although they vary from time to time and from node to node. Furthermore the velocity is found to be oscillating and stronger oscillations are found at surface nodes than at the centre of the sphere. The velocity oscillation is due to the effect of stress wave motions. After the separation of the sphere

from the substrate, the nodal velocity at the initial contact point of the substrate is fluctuating around zero owing to the stress wave effect. The overall nodal velocities of the sphere are found to be less than the initial values. This implies that significant energy loss is induced during the impact.

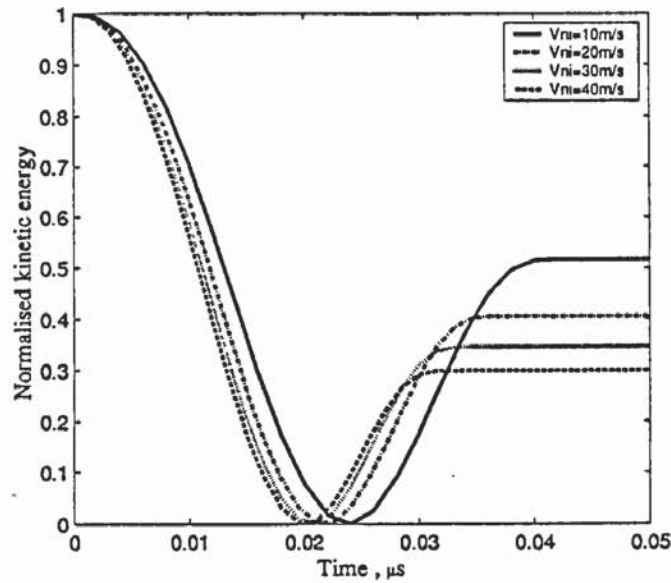


Fig. 5.10 Time histories of normalised kinetic energy during the impact of an elastic sphere with an elastic-perfectly plastic substrate at various impact velocities.

The evolutions of the normalised kinetic energy are shown in Fig. 5.10 for the impacts at various impact velocities. Unlike the impact of an elastic sphere with either a rigid wall or an elastic half-space (see Figs. 4.7 and 4.17a), for the impact of an elastic sphere with an elastic-perfectly plastic half-space at all impact velocities considered the rebound kinetic energies are much less than the initial kinetic energies. In addition, the higher the impact velocity, the smaller the normalised rebound kinetic energy. This implies that the energy loss due to plastic deformation becomes significant during the impact and more kinetic energy is dissipated by the plastic deformation at high velocities than at low velocities.

Figure 5.11 shows the typical evolutions of the contact force during the impacts at various impact velocities. It is clear that greater maximum contact forces are generated during the impact at higher impact velocities. It is also evident that the duration of impact decreases as the impact velocity increases, which is primarily due to the faster unloading at high impact velocity, as illustrated in Table 5.1 in which the corresponding durations of impact, the compression and the restitution are presented. As can be seen, the duration of compression slightly reduces as the increase of the impact velocity owing to the decrease of the duration for the elastic compression at higher impact velocity since the fully plastic

loading period is independent of the impact velocity (Johnson 1985). At higher velocities the durations of restitution are generally shorter than those at lower velocity. This is because the restitution phase is essentially elastic and the duration for elastic unloading decreases with the increasing impact velocity as given by Eq.(2.18). Compared with Fig. 2.5a, it is clear that present FEA results are in qualitative agreement with experimental results of Goldsmith (1960).

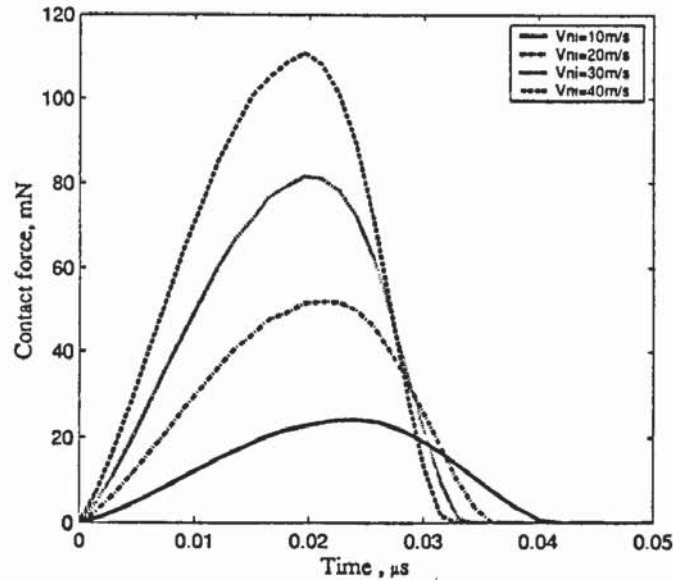


Fig. 5.11 Time histories of contact force during the impact of an elastic sphere with an elastic-perfectly plastic substrate at various impact velocities.

Table 5.1 The duration of impact at various impact velocities

Impact velocity (m/s)	Duration of impact (μs)	Duration of compression (μs)	Duration of restitution (μs)
10	0.0420	0.0235	0.0185
20	0.0374	0.0210	0.0164
30	0.0345	0.0200	0.0145
40	0.0330	0.0198	0.0132

5.2.4 Force-displacement relationship

The typical force-displacement relationships are illustrated in Fig. 5.12, in which the results for the impacts at four impact velocities are presented. We also superimpose the results for the elastic impact given by Hertz theory. It is evident that the loading curves obtained for impacts at different velocities using FEM follow on the same curve and agree very well with the Hertz theory at small displacements. But, they begin to diverge from Hertz theory when the displacement becomes large. The loading curves exhibit an upward curvature at low values of displacement following by a nearly constant slope at large

displacements, which is consistent with the experimental observations of Goldsmith and Lyman (1960), see Fig. 2.5b. The pattern of loading curves indicates that the deformation is primarily elastic at low values of the displacement and plastic deformation is initiated at a certain value of displacement. Once plastic deformation occurs, the force-displacement relationship begins to differ from Hertzian predictions. The unloading curves are not parallel to each other and the slope of unloading curve at the transition point from loading to unloading appears to become stiffer with the increasing impact velocity. Since the unloading is essentially elastic as discussed before, the change in the slope of the unloading curve at the transition point is believed to be due to the increase of the contact curvature induced by more significant plastic deformation at high impact velocities.

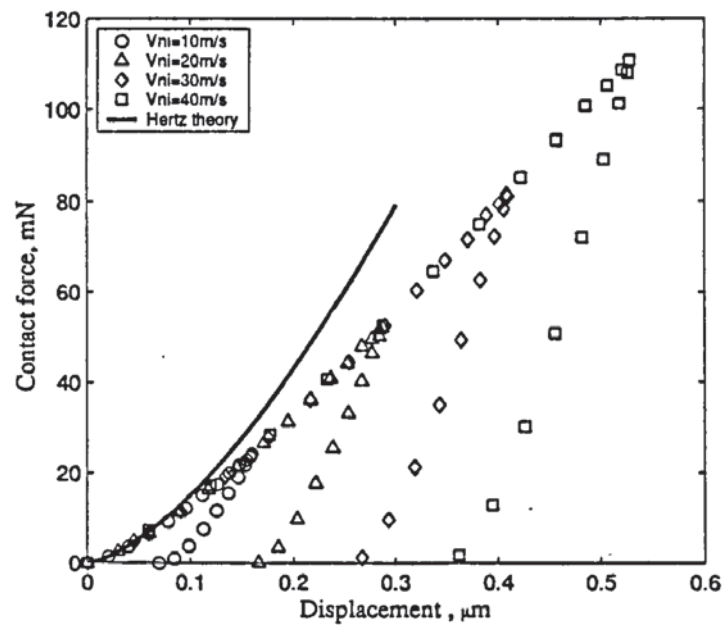


Fig. 5.12 Contact force-displacement relationships for the impact of an elastic sphere with an elastic-perfectly plastic substrate at various impact velocities.

5.2.5 Energy dissipation and coefficients of restitution

It is understood that, during the impact of an elastic sphere with an elastic-perfectly plastic half-space, portions of the kinetic energy would be dissipated by two means: one is the stress wave propagation and the other is unrecoverable plastic deformation. It has been shown in Appendix B that, for the impact of an elastic sphere with an elastic-perfectly plastic half-space, the energy loss due to the stress wave propagation is generally negligible. Thus the energy dissipation during the plastic impact is mainly due to plastic deformation.

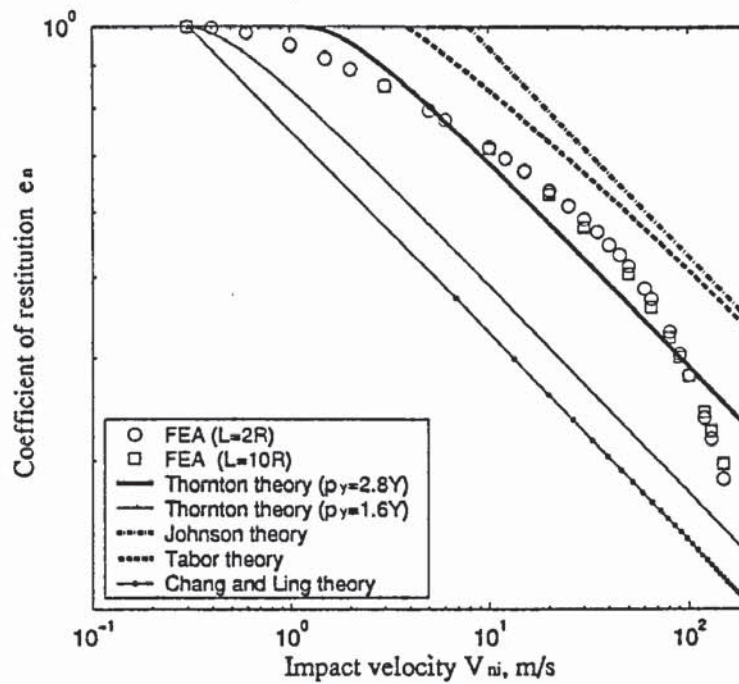


Fig. 5.13 Coefficient of restitution for the impact of an elastic sphere with an elastic-perfectly plastic half-space.

The coefficients of restitution given in Table B.3 are plotted against the initial impact velocity in Fig. 5.13 for the impact of an elastic sphere with an elastic-perfectly plastic half-space. In this figure we also superimpose the theoretical predictions of Thornton (1997), Johnson (1985), Tabor (1951) and Chang and Ling (1992). It can be seen that the FEA results obtained with two substrates of different sizes are very close and the coefficient of restitution reduces from unity as the impact velocity increases. In addition, at higher impact velocities (say $V_{ni} > 40\text{m/s}$), the coefficient of restitution begins to drop rapidly with the increasing impact velocity. This is due to the occurrence of piling-up around the perimeter of the contact area, as shown in Fig. 5.4, and the additional work that has to be done to move the material relocated around the contact region. We describe impacts in the high velocity range, where the coefficient of restitution drops rapidly with increasing impact velocity, as finite deformation plastic impacts. One of the distinct characteristics of finite deformation plastic impacts is piling-up or sinking-in occurring around the perimeter of the contact area for the impact of a sphere with a half-space, as illustrated in Fig. 5.4. Detailed discussion of finite deformation impacts will be presented in Section 5.3.

It is also clear from Fig. 5.13 that both the Johnson and Tabor theories overestimate the coefficient of restitution. This is mainly due to the fully plastic contact assumptions introduced, which is only suitable for impacts at very high velocity. Figure 5.13 also shows

that the Chang and Ling theory underestimates the coefficient of restitution. This is mainly because the volume of the deformed sphere was assumed to be conservative after the onset of plastic deformation. This is not true since immediately after plastic yield is initiated the magnitude of elastic deformation is normally of the same order as the plastic deformation and the elastic deformation is not volume conservative. Hence, by assuming that the volume is conservative after the onset of plastic deformation, it overestimates the work that needs to produce the permanent plastic deformation. As a result, it predicts more energy being dissipated by plastic deformation and gives a low coefficient of restitution.

It is recognised that the coefficient of restitution given by Thornton theory depends strongly upon the value of p_y (see Thornton 1997, Li *et al.* 2000 and Thornton *et al.* 2001). Since it was assumed that p_y remains constant during loading, it is necessary to choose a representative value of p_y for the impact at a certain impact velocity. In Fig. 5.13, p_y is assigned two values: $p_y = 1.6Y$ and $p_y = 2.8Y$. It can be seen that by using $p_y = 1.6Y$ Thornton's theory agrees with the FEA results for impacts at velocities close to the yield velocity, while using $p_y = 2.8Y$ the theory predicts similar values of coefficient of restitution to the FEA results at intermediate impact velocities. This suggests that adopting a variable p_y in Thornton's theory may be more applicable. This will be discussed further in Section 5.4.

5.3 Parametric dependence of the rebound behaviour

In the preceding section, we discussed the typical impact behaviour of an elastic sphere with an elastic-perfectly plastic half-space. It is of fundamental importance to understand whether or how the impact behaviour depends on the material and geometric properties. The dependence of contact parameters on the material and geometric properties of contacting bodies during the indentation has been investigated by many researchers (see Johnson 1985; Mesarovic and Fleck 1999, 2000; *etc.*). However little attention has been paid to the parametric dependence of the rebound behaviour of particles involving plastic deformation from the point of views of impact dynamics. This issue will be discussed in this section.

5.3.1 Impact cases considered

In order to study the parametric dependence of the rebound behaviour, two special combinations are considered: one is the impact of an elastic sphere with an elastic-perfectly plastic half-space; the other is the impact of an elastic-perfectly plastic sphere with a rigid wall. For each combination, we consider several different cases by either changing the material properties, such as Young's Modulus, Poisson's ratio, the yield stress, or changing the size of the sphere. For the combination of an elastic sphere with an elastic-perfectly plastic half-space, the FE model shown in Fig. 3.5 is used. The analysis model presented in Section 3.2.1 with the refined FE meshes, as shown in Fig. 3.3b, is used to simulate the impact of an elastic-perfectly plastic sphere with a rigid wall. All impact cases considered are listed in Table 5.2. The results for Case R2 were first reported in Li *et al.* (2000), while the impact Case 1 was chosen as an example in Section 5.2 and the results are reproduced here. The corresponding values of E^*/Y and V_{y0} are also given in the table. It is clear that for all impact cases considered the yield velocity is relatively small, which means that the plastic deformation is readily initiated for most impact cases.

5.3.2 The parametric dependence of the coefficient of restitution

For each impact case considered, simulations at various impact velocities are carried out and the coefficients of restitution for all tests are determined from Eq.(4.6). The coefficient of restitution is plotted against the impact velocity in Fig. 5.14, in which the solid symbols represent the results for the impact of an elastic-perfectly plastic sphere with a rigid wall, and the others for the impact of an elastic sphere with an elastic-perfectly plastic half-space. It can be seen that the curves apparently shift leftwards as E^*/Y increases for all impact cases. Attention is drawn to Case 7 (\square) and Case R4 (\blacktriangleright), which have the same value of E^*/Y but the values of V_{y0} are different. The coefficient of restitution obtained for these two cases are close to each other. However, careful examination reveals that at small impact velocities Case 7 generally gives slightly smaller coefficients of restitution than Case R4, which has a higher value of V_{y0} . But the situation is reversed at high impact velocities. Since for all others cases a larger value of E^*/Y corresponds to higher value of V_{y0} , it may be implied that the coefficient of restitution is mainly related to V_{y0} when the

Table 5.2 Material and geometric properties for various impact cases considered

Case No.	Sphere					Substrate					$\frac{E^*}{Y}$	V_{y0} (mm/s)	Onset of finite deformation impacts	
	E_1 (GN/m ²)	ν_1	Y (GN/m ²)	ρ_1 (Mg/m ³)	R_1 (μm)	E_2 (GN/m ²)	ν_2	Y (GN/m ²)	ρ_2 (Mg/m ³)	\bar{V}_{ni} (m/s)			$\frac{a_-^*}{R}$ (#)	$\frac{a_+^*}{R}$ (#)
1	208	0.3	---	7.85	10	208	0.3	1.35	7.85	41.94	0.32 (40)	0.34 (45)		
2	210	0.29	---	7.8	6350	204.1	0.29	0.938	7.8	35.05	0.35 (35)	0.38 (40)		
3	208	0.01	---	7.85	10	208	0.01	0.37	7.85	21.97	0.33 (20)	0.41 (30)		
4	208	0.3	---	7.85	10	208	0.3	0.37	7.85	21.95	0.29 (15)	0.37 (25)		
5	208	0.49	---	7.85	10	208	0.49	0.37	7.85	21.89	0.29 (15)	0.38 (25)		
6	208	0.3	---	7.85	10	208	0.3	0.25	7.85	17.89	0.32 (15)	0.37 (20)		
7	208	0.3	---	7.85	10	208	0.3	0.05	7.85	8.05	0.35 (8)	0.40 (12)		
R1	208	0.3	1.0	7.85	10	Rigid wall					34.5	0.19 (12)	0.22 (16)	
R2	208	0.3	0.37	7.85	10	Rigid wall					2.9	0.20 (7.5)	0.25 (12)	
R3	273	0.3	0.3	7.85	10	Rigid wall					0.988	0.19 (6.0)	0.22 (8.0)	
R4	208	0.3	0.1	7.85	10	Rigid wall					0.109	0.21 (4.0)	0.25 (6.0)	
R5	273	0.3	0.06	7.85	10	Rigid wall					0.017	0.21 (3.0)	0.23 (4.0)	
R6	273	0.3	0.03	7.85	10	Rigid wall					0.003	0.20 (2.0)	0.23 (2.5)	

\$ $P_{y0} = 1.6Y$ is assumed to be applicable at the onset of plastic yield.

The data in the parentheses indicate the impact velocity V_{ni} (m/s) at which the maximum contact radius is estimated.

impact velocity is below a certain value, above which the coefficient of restitution is related to not only V_{y0} but also E^*/Y .

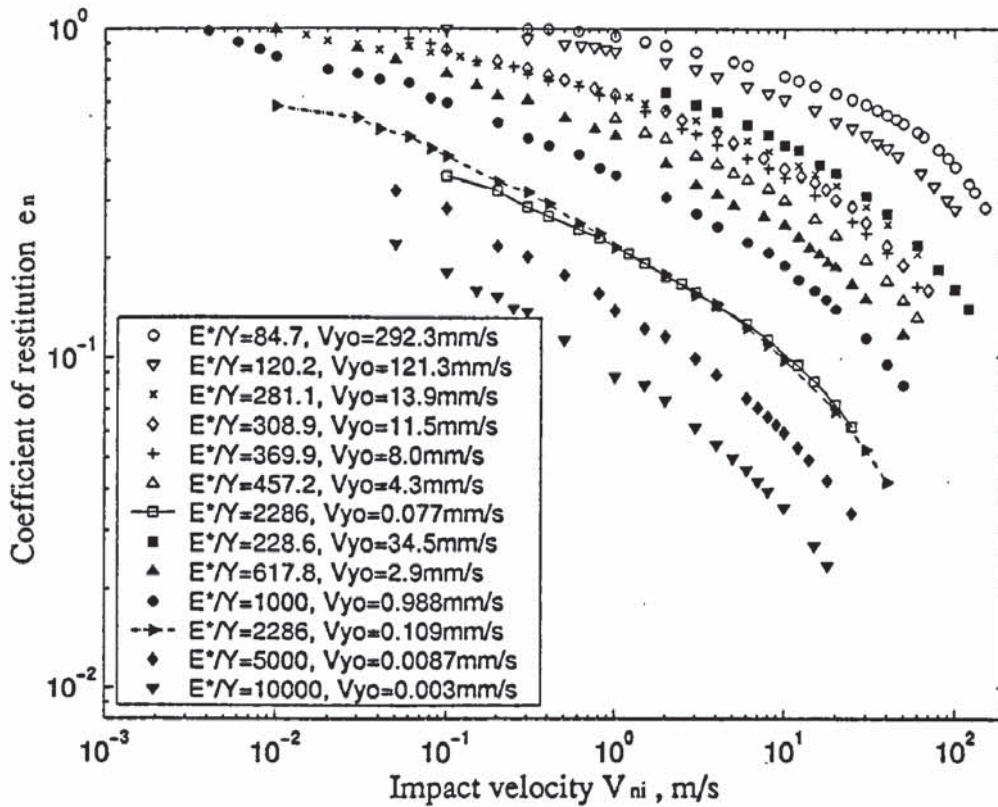
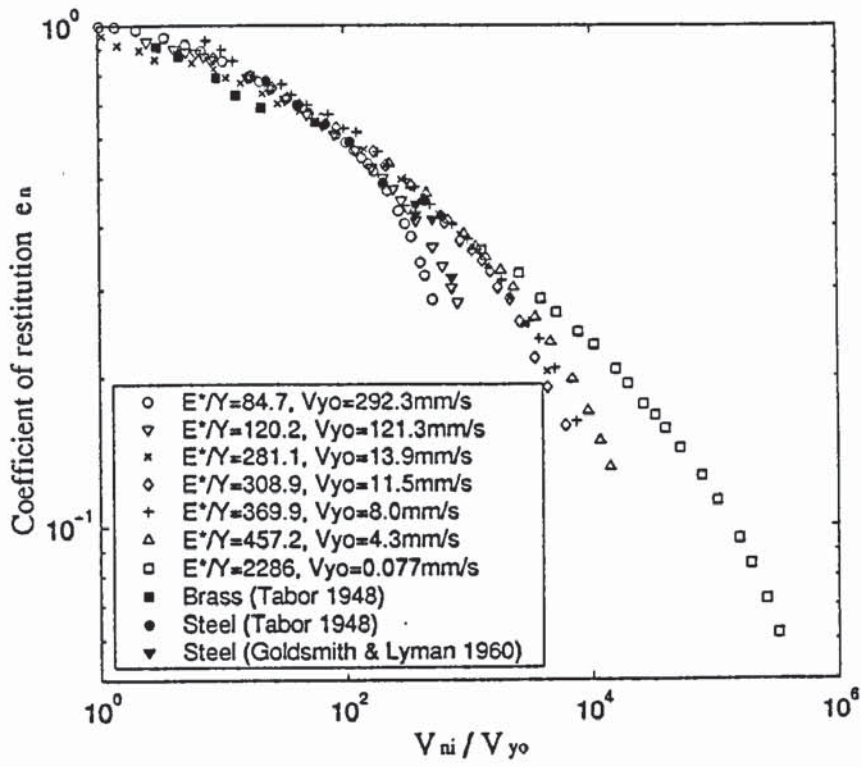
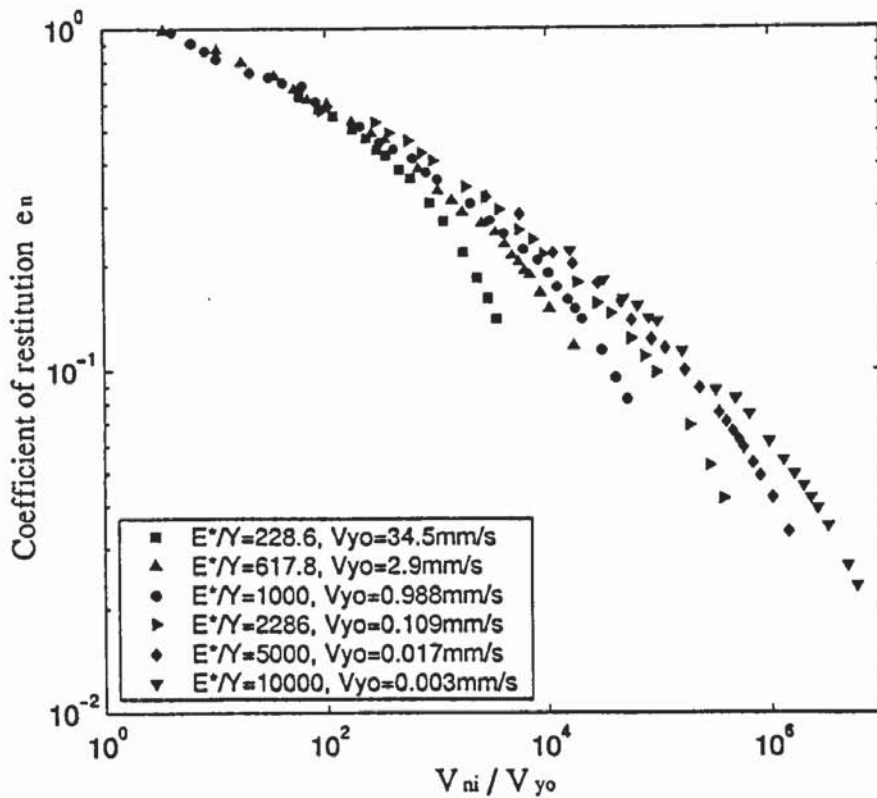


Fig. 5.14 Coefficient of restitution as a function of impact velocity V_{ni} for all impact cases considered.

The coefficients of restitution e_n are plotted against V_{ni}/V_{y0} in Fig. 5.15 for all impact cases considered. For clarity; the results for the impact of an elastic sphere with an elastic-perfectly plastic half-space are shown in Fig. 5.15a while those for the impact of an elastic-perfectly plastic sphere with a rigid wall are provided in Fig. 5.15b. In Fig. 5.15a, the experimental results of Tabor (1948) and Goldsmith and Lyman (1960) are also superimposed. The experimental results of Tabor (1948) are normalised in the same manner as used by Levy and Parry (1980), that is, a yield velocity of 100mm/s for the cast steel and 7mm/s for the brass are used. These correspond to a yield stress of 0.8GN/m^2 and 0.2GN/m^2 for the steel and brass, respectively. In addition, for these two groups of results, the indenters are assumed to be spherical bodies of steel. Material and geometric properties of Case 2 (▽), for which $V_{y0} = 123\text{mm/s}$, are used to normalise the experimental results of Goldsmith and Lyman (1960) since the material and geometric properties are essentially identical.



(a)



(b)

Fig. 5.15 Coefficient of restitution as a function of the normalised impact velocity V_{ni} / V_{y0} for all impact cases considered: (a) the impact of an elastic sphere with an elastic-perfectly plastic substrate; (b) the impact of an elastic-perfectly plastic sphere with a rigid wall.

It can be seen from Fig. 5.15a that the FEA results are in excellent agreement with experimental results obtained by Tabor (1948) and Goldsmith and Lyman (1960). The coefficients of restitution for various impact cases shown in Fig. 5.15 decrease from nearly unity with increasing V_{ni}/V_{y0} and follow a common trajectory until certain values of V_{ni}/V_{y0} are reached for the individual impact cases. Afterwards, the individual curves depart from the common trajectory and the coefficient of restitution drops rapidly as V_{ni}/V_{y0} is increased further. The divergence is due to the finite deformation of the contacting bodies. For an elastic sphere impinging against an elastic-perfectly plastic half-space, the effect of finite deformation is significant piling-up or sinking-in occurring around the perimeter of the contact area, which can be readily observed from the topographies of the contact region as illustrated in Fig. 5.4. However, for the impact of an elastic-perfectly plastic sphere with a rigid wall, the finite deformation leads to lateral expansion of the sphere near the contact region, which is difficult to be identified. Nevertheless, the onset of finite deformation of the contacting bodies requires more work done to move the displaced materials, which leads to more kinetic energy dissipated by the irrecoverable plastic strain energy required for moving the displaced materials. As a result, a lower coefficient of restitution is obtained for the impact involving finite deformations.

It is noting that in Fig. 5.15a the impact Case 3 (\times), which involves bodies with a low Poisson's ratio of $\nu = 0.01$, appears to give a slightly lower coefficient of restitution, compared to case 5 (+), for which the bodies have a high Poisson's ratio of $\nu = 0.49$, which produces a slightly higher coefficient of restitution. This is mainly due to the fact that the same value of $p_{y0} = 1.6Y$, which is valid only for $\nu = 0.3$ (Johnson 1985, p155), is assumed in the calculation of the yield velocity V_{y0} for both cases. This suggests that a lower maximum contact pressure for initial yield is expected for a smaller Poisson's ratio, and vice versa. Nevertheless, the effect of Poisson's ratio is not very significant. It is worth noting that in Fig. 5.15b the coefficient of restitution appears to reduce from unity at $V_{ni}/V_{y0} > 1$. This is attributed to numerical errors. As discussed in Appendix A, the accuracy of FEA depends strongly upon the accurate determination of the contacting boundary. Since the yield velocity for the impact of an elastic-perfectly plastic sphere with a rigid wall is generally of an order of several millimetres per second, at such low velocities the contact area is relatively small and normally only a few elements are involved in the actual contact. The error induced is therefore slightly higher.

As discussed above, the finite deformation of the impacting bodies significantly affects the rebound behaviour. The plastic impact can therefore be categorised into two groups according to the deformation mechanism involved: elastic-plastic impacts in which no finite deformation is involved and finite deformation plastic impacts in which the finite deformation becomes significant. It is of interest to define the demarcation between these two groups. It has been seen from Fig. 5.15 that when the normalised impact velocity is less than a certain value the variation of e_n with V_{ni}/V_{y0} follows the same curve for all impact cases but the curves begins to separate significantly at higher values of V_{ni}/V_{y0} . This implies that e_n depends primarily on V_{ni}/V_{y0} at lower impact velocities. It is also apparent that the lower the value of E^*/Y , the smaller the value of V_{ni}/V_{y0} at which the curves begin to depart from the common trajectory. This indicates that the onset of finite deformation plastic impact depends not only on V_{ni}/V_{y0} but also on E^*/Y . A re-plot of Fig. 5.15 is shown in Fig. 5.16, in which $e_n(E^*/Y)^{1/2}$ is plotted against $(V_{ni}/V_{y0})/(E^*/Y)^2$. For clarity, Fig. 5.16a shows the results for the impact of an elastic sphere with an elastic-perfectly plastic half-space and Fig. 5.16b shows the results for the impact of an elastic-perfectly plastic sphere with a rigid wall. It is interesting to note that in the finite deformation regime the results coalesce into a single curve in Fig. 5.16 when $(V_{ni}/V_{y0})/(E^*/Y)^2$ is above a certain values. The FEA results show that the individual curves begin to merge together when

$$(V_{ni}/V_{y0})/(E^*/Y)^2 \geq 0.02 \quad (5.7)$$

for impacts of an elastic sphere with an elastic-perfectly plastic half-space and

$$(V_{ni}/V_{y0})/(E^*/Y)^2 \geq 0.008 \quad (5.8)$$

for impacts of an elastic-perfectly plastic sphere with a rigid wall. Equations (5.7) and (5.8) provide the criteria for the onset of finite deformation. According to these criteria the corresponding values of \bar{V}_{ni} and the normalised maximum contact radii a_-^*/R and a_+^*/R are shown in the last column of Table 5.2, where a_-^*/R and a_+^*/R are estimated from the current tests at a velocity just below and above the critical velocity \bar{V}_{ni} , respectively. It can

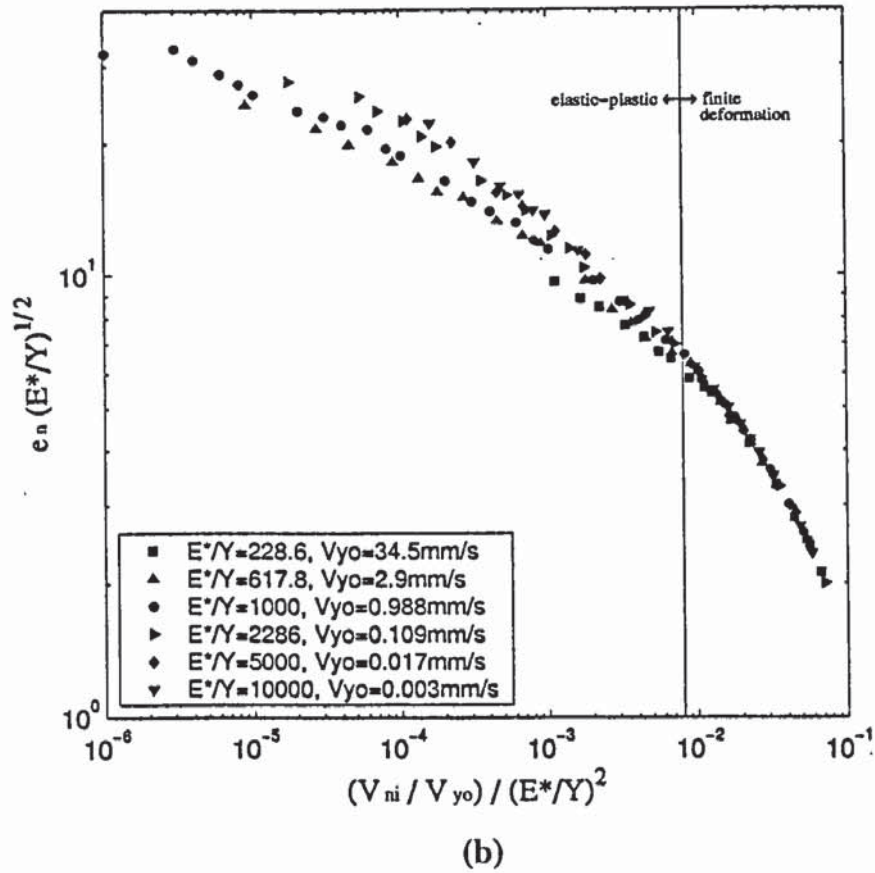
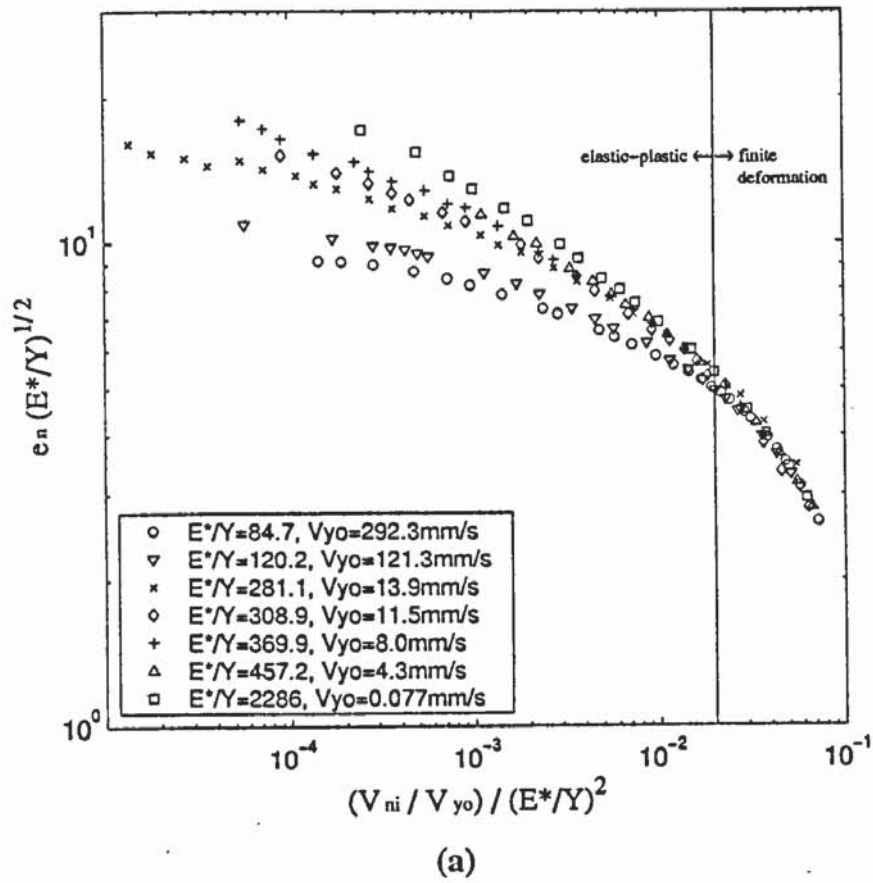


Fig. 5.16 $e_n(E^*/Y)^{1/2}$ versus $(V_{ni}/V_{yo})/(E^*/Y)^2$ for all impact cases considered: (a) the impact of an elastic sphere with an elastic-perfectly plastic half-space; (b) the impact of an elastic-perfectly plastic sphere with a rigid wall.

be seen that the maximum contact radius is *ca.* $0.35R$ for the initiation of the finite-deformation for impacts of an elastic sphere with an elastic-perfectly plastic half-space and *ca.* $0.22R$ for the combination of an elastic-perfectly plastic sphere with a rigid wall. This is comparable to the analysis of Mesarovic and Fleck (2000) who showed that for an elastic-perfectly plastic sphere with E^*/Y in the range from 250 to 10,000, when indented by a rigid half-space, both the mean contact pressure and the radius of contact curvature begins to reduce with increasing a/R when a/R is larger than *ca.* 0.2.

According to the criteria given by Eqs.(5.7) and (5.8), the results for various impact cases at velocities lower than the critical velocity \bar{V}_{ni} are plotted in Fig. 5.17, and those at velocities higher than the critical velocity are shown in Fig. 5.18. In Fig. 5.17, the coefficient of restitution is plotted against the normalised impact velocity V_{ni}/V_{y0} . The solid symbols represent the results for the impact of an elastic-perfectly plastic sphere with a rigid wall; the remaining symbols denote the results for the impact of an elastic sphere with an elastic-perfectly plastic half-space. It can be seen that the curves of the coefficient of restitution e_n versus V_{ni}/V_{y0} coalesce to form a single master curve, which indicates that, for impacts at a velocity lower than the critical velocity \bar{V}_{ni} , the effect of plastic deformation on the coefficient of restitution depends primarily upon V_{ni}/V_{y0} ; *i.e.*, the normalised impact velocity V_{ni}/V_{y0} satisfactorily accounts for the dependence of the coefficient of restitution on material and geometric properties until finite deformation occurs. A better fit to the data for $V_{ni}/V_{y0} \geq 100$ gives the following empirical expression:

$$e_n = 2.10(V_{ni}/V_{y0})^{-1/4} \quad (5.9)$$

as shown by solid line in Fig. 5.17. This is consistent with the prediction of Johnson (1985) that the coefficient of restitution is proportional to $V_{ni}^{-1/4}$.

In Fig. 5.18, the coefficient of restitution e_n is shown as a function of $(V_{ni}/V_{y0})/(E^*/Y)$ for various impact cases at velocities higher than the critical velocity. Again, the solid symbols represent the results for the impact of an elastic-perfectly plastic sphere with a rigid wall; the remaining symbols denote the results for the impact of an elastic sphere with an elastic-perfectly plastic half-space. It is interesting to find that the curves of the coefficient of restitution e_n versus $(V_{ni}/V_{y0})/(E^*/Y)$ for a variety of impact cases merge

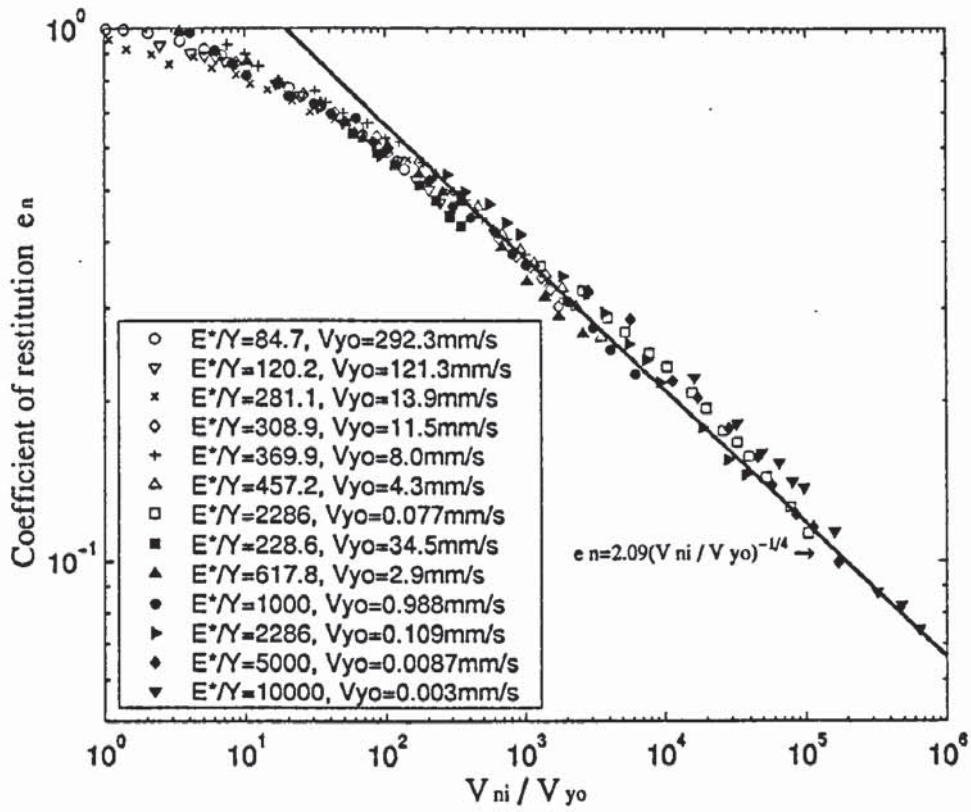


Fig. 5.17 Coefficient of restitution as a function of V_{ni} / V_{y0} for all impacts at velocities less than the critical velocity \bar{V}_{ni} for the onset of finite-deformation plastic impact.

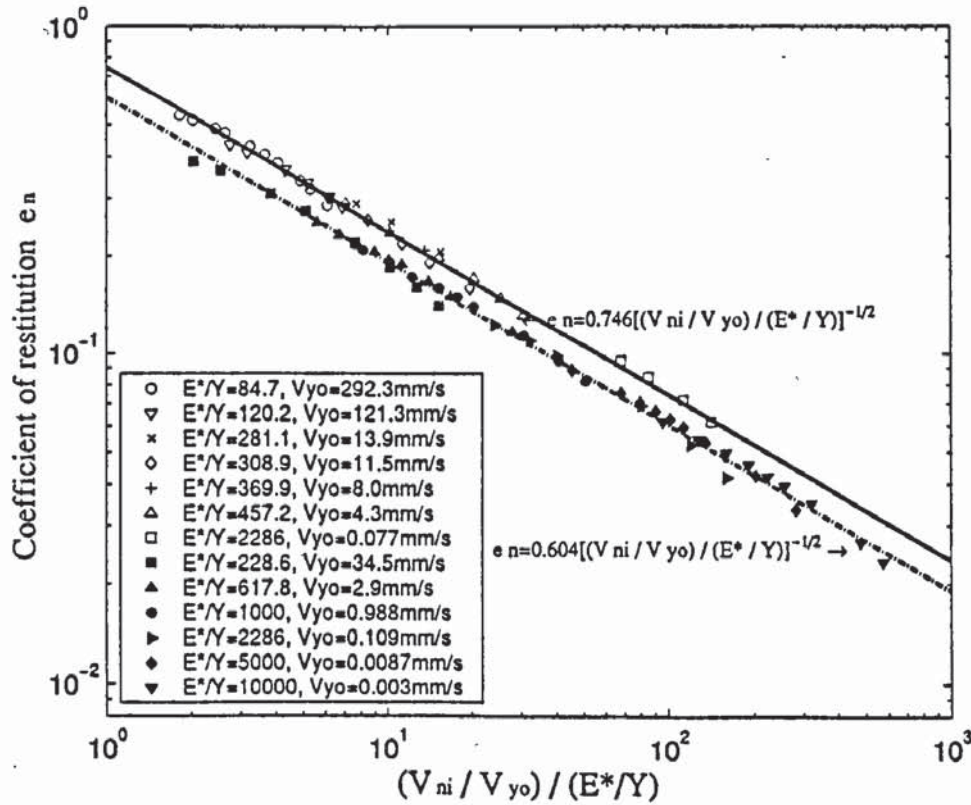


Fig. 5.18 Coefficient of restitution as a function of $(V_{ni} / V_{y0}) / (E^* / Y)$ within finite-deformation range for all impact cases considered.

into two main clusters: one for the combinations of an elastic-perfectly plastic sphere with a rigid wall, the other for the combinations of an elastic sphere with an elastic-perfectly plastic half-space. The coefficient of restitution for the former is found to be below that for the latter at the same value of $(V_{ni}/V_{y0})/(E^*/Y)$. This indicates that during an impact involving finite plastic deformation more energy is dissipated by the plastic deformation of the sphere than by the plastically deformed half-space. In other words, the sphere undergoes more plastic deformation than the substrate does for the same value of $(V_{ni}/V_{y0})/(E^*/Y)$, which is in agreement with the analysis of Mesarovic and Fleck (2000). A least-median-square regression fit of the theoretical formula to the FEA results leads to the following empirical equations:

$$e_n = 0.583 \left(\frac{V_{ni}/V_{y0}}{E^*/Y} \right)^{-0.490} \quad (5.10)$$

for the impacts of an elastic-perfectly plastic sphere with a rigid wall, and

$$e_n = 0.722 \left(\frac{V_{ni}/V_{y0}}{E^*/Y} \right)^{-0.485} \quad (5.11)$$

for the impacts of an elastic sphere with an elastic-perfectly plastic half-space. Equations (5.10) and (5.11) indicate that the coefficient of restitution e_n is approximately proportional to $[(V_{ni}/V_{y0})/(E^*/Y)]^{-1/2}$. Hence, by making use of this proportional dependence, a better fit to the FEA results of the finite-deformation plastic impacts is given by the approximate expressions:

$$e_n = 0.604 \left(\frac{V_{ni}/V_{y0}}{E^*/Y} \right)^{-1/2} \quad (5.12)$$

for the impacts of an elastic-perfectly plastic sphere with a rigid wall, and

$$e_n = 0.746 \left(\frac{V_{ni}/V_{y0}}{E^*/Y} \right)^{-1/2} \quad (5.13)$$

for the impacts of an elastic sphere with an elastic-perfectly plastic half-space. Equations (5.12) and (5.13) are shown in Fig. 5.18 by dashed and solid lines, respectively.

5.4 Mathematical modelling of the impact of elastic-perfectly plastic particles---LWT model (Li *et al.* 2001)

In this section, a theoretical model for the impact of elastic-perfectly plastic particles is presented. This theoretical model was first reported in Li *et al.* (2001) and shall be referred to as the LWT model.

It is assumed in the LWT model that the pressure distribution during the plastic loading stage is similar to the suggestion of Thornton (1997), i.e., the pressure distribution is described by a truncated Hertzian pressure distribution with a limited contact pressure p_0 . But, in contrast to Thornton's theory in which p_0 was assumed to be constant during the impact, p_0 is allowed to vary with the contact radius. The contact pressure distribution is defined by

$$p(r) = p_0 \quad 0 \leq r \leq a_p \quad (5.14a)$$

$$p(r) = \frac{3F_e}{2\pi a^2} \left[1 - \left(\frac{r}{a} \right)^2 \right]^{1/2} \quad a_p \leq r \leq a \quad (5.14b)$$

in which,

$$F_e = \frac{4E^* a^3}{3R^*} \quad (5.14c)$$

is the equivalent elastic contact force required to produce the same contact area, and

$$\left(\frac{a_p}{a} \right)^2 = 1 - \left(\frac{2\pi a^2 p_0}{3F_e} \right) = 1 - \left(\frac{\pi p_0 R^*}{2E^* a} \right)^2 \quad (5.14d)$$

where a_p is the radius of the contact over which a uniform pressure is assumed. The applied contact force is obtained by the integration of the pressure over the whole contact area as follows,

$$F_n = 2\pi \int_0^a p(r) r dr = \pi a_p^2 p_0 + F_e \left[1 - \left(\frac{a_p}{a} \right)^2 \right]^{3/2} \quad (5.15)$$

Substituting Eq.(5.14) into (5.15) yields

$$F_n = \pi R^{*2} p_0 \left[\left(\frac{a}{R^*} \right)^2 - \frac{1}{3} \left(\frac{\pi p_0}{2E^*} \right)^2 \right] \quad (5.16)$$

It is clear that Eqs.(5.14)-(5.16) will reproduce the Hertz theory for a purely elastic contact if a_p is set to zero. For elastic-plastic impacts, it is, however, necessary to determine how p_0 varies with contact radius.

As mentioned previously, the contact interaction involves three stages: elastic, elastoplastic and fully plastic. It is commonly recognised that the Hertz theory applies during the elastic stage, which is terminated by the onset of plastic deformation when $p_0 = p_{y0}$. The fully plastic stage commences when $p_0 = \lambda Y$ where λ is a constant between 2.8 and 3.0 (Goldsmith 1960; Johnson 1985; Hardy *et al.* 1971; Bhushan 1996). During the elastoplastic stage p_0 increases from $1.6Y$ to λY and the contact radius increases from a_{y0} to εa_{y0} , where ε is a constant in the range from 16 to 20 as suggested by Johnson (1985) and Sinclair *et al.* (1985). The exact values for both λ and ε appear to depend on material properties and interpretation of experimental data. In this study, λ and ε are determined from the FEA results for which $\lambda = 2.85$ and $\varepsilon = 20$ are obtained.

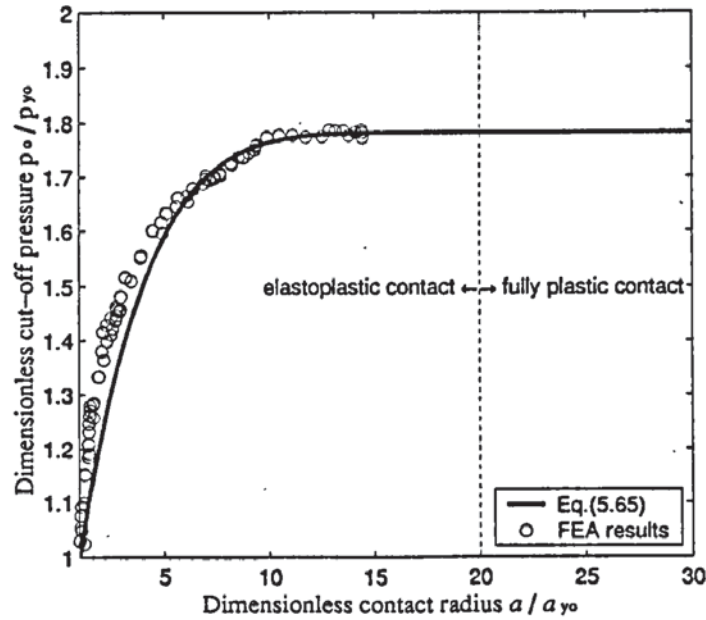


Fig. 5.19 The dimensionless cut-off pressure as a function of the dimensionless contact radius.

Johnson (1985) indicates how the mean contact pressure varies with the contact radius (see also Fig. 2.3). However the exact relationship between the maximum contact pressure p_0 and a in the elastoplastic contact regime has not been reported in the literature. Here the following relationship is assumed:

$$\frac{\lambda Y - p_0}{\lambda Y - p_{y0}} = \left[\frac{\varepsilon a_{y0} - a}{(\varepsilon - 1)a_{y0}} \right]^n \quad \text{for elastoplastic contact } \left(1 \leq \frac{a}{a_{y0}} \leq \varepsilon \right) \quad (5.17)$$

where n is an empirical constant and from the FEA results we take $n = 6$. Figure 5.19 shows how the contact pressure at the centre of the contact area varies with contact radius

according to Eq.(5.17) with the FEA results superimposed. It can be seen that the predictions given by Eq.(5.17) are in reasonable agreement with the FEA results.

Another significant effect of plastic deformation, which has not been fully addressed in the literature, is the change in the contact curvature due to irrecoverable plastic deformation during loading. Consequently, we rewrite Eq.(2.11) in the form

$$\alpha = a^2/R_p^* \quad (5.18)$$

where $R_p^* > R^*$ accounts for the effect of plastic deformation. In order to accommodate this phenomenon we assume that, during the elastoplastic stage, the relative approach may be defined as:

$$\alpha = a^2/R_p^* = a^2/R^* - k\alpha_p \quad (5.19)$$

where α_p is the permanent relative compression and k is a constant to be determined. If the contact interaction is purely elastic $\alpha_p = 0$ and $R_p^* = R^*$, as given by Hertz theory.

If we further assume that, during elastoplastic contact interaction, there is no piling-up or sinking-in in adjacent to the perimeter of the contact area then, according to Johnson (1985) fully plastic interaction occurs when $R_p^* = 2R^*$. Therefore, from Eq.(5.19) we obtain the following expression for the constant k

$$k = \alpha^* / \alpha_p^* \quad (5.20)$$

where α^* and α_p^* are the total displacement and plastic displacement of the sphere centre, respectively, when the contact radius $a = \epsilon a_{y0}$. As will be demonstrated later, analysis shows that $k = 1.23$. The plastic displacement α_p can be calculated from the unloading data assuming that the force-displacement behaviour is elastic and is provided by Hertzian equations but with a curvature $1/R_p^*$ corresponding to the point of maximum compression, viz:

$$F_n = \frac{4}{3} E^* R_p^{*1/2} \alpha^{3/2} - \frac{4}{3} E^* R_p^{*1/2} \alpha_p^{3/2} \quad (5.21)$$

Substituting Eq.(5.21) into Eq.(5.19) yields,

$$\frac{\alpha}{R^*} = \left(\frac{a}{R^*}\right)^2 - k \left[\left(\frac{\alpha}{R^*}\right)^{3/2} - \left(\frac{R^*}{R_p^*}\right)^{1/2} \left(\frac{3F_n}{4R^{*2}E^*}\right) \right]^{2/3}$$

$$\begin{aligned}
&= \left(\frac{a}{R^*}\right)^2 - k \left[\left(\frac{\alpha}{R^*}\right)^{3/2} - \left(\frac{\alpha}{R^*}\right)^{1/2} \left(\frac{R^*}{a}\right) \left(\frac{3F_n}{4R^{*2}E^*}\right) \right]^{2/3} \\
&= \left(\frac{a}{R^*}\right)^2 - k \left(\frac{\alpha}{R^*}\right) \left[1 - \left(\frac{\alpha}{R^*}\right)^{-1} \left(\frac{R^*}{a}\right) \left(\frac{3F_n}{4R^{*2}E^*}\right) \right]^{2/3}
\end{aligned} \tag{5.22}$$

Equation (5.22) can be rewritten as

$$\frac{\alpha}{R^*} = \frac{\left(\frac{a}{R^*}\right)^2}{1 + k \left[1 - \left(\frac{R^{*2}}{\alpha a}\right) \left(\frac{3F_n}{4R^{*2}E^*}\right) \right]^{2/3}} \tag{5.23}$$

For convenience, Eq.(5.23) is rewritten in dimensionless form

$$\frac{\alpha}{\alpha_{y0}} = \frac{\left(\frac{a}{a_{y0}}\right)^2}{1 + k \left[1 - \left(\frac{\alpha_{y0}}{\alpha}\right) \left(\frac{a_{y0}}{a}\right) \left(\frac{F_n}{F_{y0}}\right) \right]^{2/3}} \tag{5.24}$$

The contact force given by Eq.(5.16) can also be rewritten in dimensionless form

$$\frac{F_n}{F_{y0}} = \frac{3}{2} \left(\frac{a}{a_{y0}}\right)^2 \left(\frac{p_0}{p_{y0}}\right) - \frac{1}{2} \left(\frac{p_0}{p_{y0}}\right)^3 \tag{5.25}$$

Here a_{y0} , α_{y0} and F_{y0} are given by Eqs.(5.4)-(5.6), and p_{y0} is defined in Eq.(2.36) for contacting bodies with $\nu = 0.3$. The ratio of p_0 / p_{y0} can be expressed as:

$$\frac{p_0}{p_{y0}} = \frac{a}{a_{y0}} \quad \frac{a}{a_{y0}} \leq 1 \text{ for elastic contact} \tag{5.26a}$$

$$\frac{p_0}{p_{y0}} = \frac{\lambda}{1.6} - \frac{\lambda - 1.6}{1.6} \left(\frac{\varepsilon - a/a_{y0}}{\varepsilon - 1}\right)^n \quad 1 \leq \frac{a}{a_{y0}} \leq \varepsilon \text{ for elastoplastic contact} \tag{5.26b}$$

$$\frac{p_0}{p_{y0}} = \frac{\lambda}{1.6} \quad \frac{a}{a_{y0}} \geq \varepsilon \text{ for fully plastic contact} \tag{5.26c}$$

The contact force and displacement at the transition from elastoplastic to fully plastic regimes can be determined in terms of Eqs.(5.25) and (5.18). For $\lambda = 2.85$ and $\varepsilon = 20$ we find $F^p = 1066F_{y0}$ and $\alpha^p = 200\alpha_{y0}$, where F^p and α^p are the contact force and relative approach at the onset of fully plastic deformation. Substituting F^p and α^p into Eq.(5.24) we obtained $k = 1.23$.

The variation of the radius of curvature of the contact surface with the contact radius and the displacement are shown in Fig. 5.20. It can be seen that the radius of curvature increases at a decreasing rate with an asymptotic value of $R_p^*/R^* = 2.15$ for $k = 1.23$. This is comparable with the suggestions of Johnson (1985) that $R_p^*/R^* = 2.0$. It is noted that Hill *et al.* (1989) and Mesarovic and Fleck (1999, 2000) report that the relative radius of curvature could reach 2.8, in which case pronounced piling-up is observed at the edge of the contact. This is clearly beyond the range where the theory can be applied (Johnson 1985).

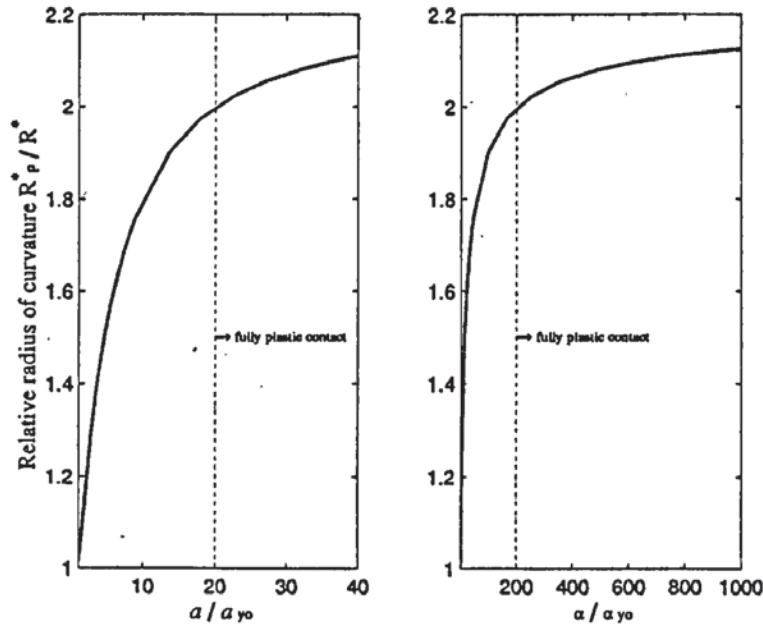


Fig. 5.20 Variation of the radius of curvature with the contact radius and displacement.

The unloading curve from a point $(\bar{\alpha}, \bar{F}_n)$ is assumed to be elastic and obtained by Hertzian equations but with a curvature $1/\bar{R}_p$ at the transition point from loading to unloading, corresponding to the point of maximum compression. Thus the force-displacement relationship for the unloading curve can be expressed by:

$$F_n = \frac{4}{3} E^* \bar{R}_p^{1/2} \alpha^{3/2} - \left(\frac{4}{3} E^* \bar{R}_p^{1/2} \bar{\alpha}^{3/2} - \bar{F}_n \right) = \bar{F}_n - \frac{4}{3} E^* \bar{R}_p^{1/2} (\bar{\alpha}^{3/2} - \alpha^{3/2}) \quad (5.27)$$

The dimensionless form of Eq.(5.27) is given by:

$$\frac{F_n}{F_{y0}} = \frac{\bar{F}_n}{F_{y0}} - \left(\frac{\bar{R}_p}{R^*} \right)^{1/2} \left[\left(\frac{\bar{\alpha}}{\alpha_{y0}} \right)^{3/2} - \left(\frac{\alpha}{\alpha_{y0}} \right)^{3/2} \right] \quad (5.28)$$

Equations (5.24)-(5.26) and (5.28) present the relationships between the dimensionless maximum pressure, dimensionless contact radius, dimensionless displacement and dimensionless contact force. The dimensionless contact force-displacement relationship can be determined numerically. For example, for a given dimensionless contact radius one can calculate the dimensionless maximum contact pressure from Eq.(5.26), dimensionless contact force from Eq.(5.25), and dimensionless displacement from Eq.(5.24). For the unloading curve, one can calculate the dimensionless contact force or displacement using Eq.(5.28).

The rebound kinetic energy is equal to the work done during elastic recovery and using Eq.(5.27) we obtain

$$W_r = \frac{1}{2}mV_{nr}^2 = \int_{\bar{\alpha}_p}^{\bar{\alpha}} F_n d\alpha = \frac{8}{15}E^* \bar{R}_p^{1/2} (\bar{\alpha}^{5/2} - \bar{\alpha}_p^{5/2}) + \left(\bar{F}_n - \frac{4}{3}E^* \bar{R}_p^{1/2} \bar{\alpha}^{3/2} \right) (\bar{\alpha} - \bar{\alpha}_p) \quad (5.29)$$

in which

$$\frac{\bar{\alpha}_p}{\alpha_{y0}} = \left[\left(\frac{\bar{\alpha}}{\alpha_{y0}} \right)^{3/2} - \left(\frac{R^*}{\bar{R}_p} \right)^{1/2} \left(\frac{\bar{F}_n}{F_{y0}} \right) \right]^{2/3} \quad (5.30)$$

Using Eq.(2.16), the initial kinetic energy, which is just sufficient to initiate plastic yield, can be obtained as follows:

$$W_{y0} = \frac{1}{2}mV_{y0}^2 = \int_0^{\alpha_{y0}} F_n d\alpha = \frac{8}{15}E^* R^{*1/2} \alpha_{y0}^{5/2} = \frac{2}{5}F_{y0} \alpha_{y0} \quad (5.31)$$

Then Eq.(5.29) can be rewritten in the following dimensionless form:

$$\frac{W_r}{W_{y0}} = \left(\frac{\bar{R}_p}{R} \right)^{1/2} \left[\left(\frac{\bar{\alpha}}{\alpha_{y0}} \right)^{5/2} - \left(\frac{\bar{\alpha}_p}{\alpha_{y0}} \right)^{5/2} \right] + \frac{5}{2} \left[\frac{\bar{F}_n}{F_{y0}} - \left(\frac{\bar{R}_p}{R^*} \right)^{1/2} \left(\frac{\bar{\alpha}}{\alpha_{y0}} \right)^{3/2} \right] \left(\frac{\bar{\alpha}}{\alpha_{y0}} - \frac{\bar{\alpha}_p}{\alpha_{y0}} \right) \quad (5.32)$$

The initial kinetic energy is equal to the work done during deceleration of the sphere, which is expressed as

$$W_i = \frac{1}{2}mV_i^2 = \int_0^{\bar{\alpha}} F_n d\alpha = W_{y0} + \int_{\alpha_{y0}}^{\bar{\alpha}} \tilde{F}_n d\alpha \quad (5.33)$$

where \tilde{F}_n can be obtained from Eq.(5.25) for $a \geq \alpha_{y0}$. The dimensionless form of Eq.(5.33) is

$$\frac{W_i}{W_{y0}} = 1 + \frac{5}{2} \sqrt{\frac{\bar{\alpha}}{\alpha_{y0}}} \frac{F_n}{F_{y0}} d \left(\frac{\alpha}{\alpha_{y0}} \right) \quad (5.34)$$

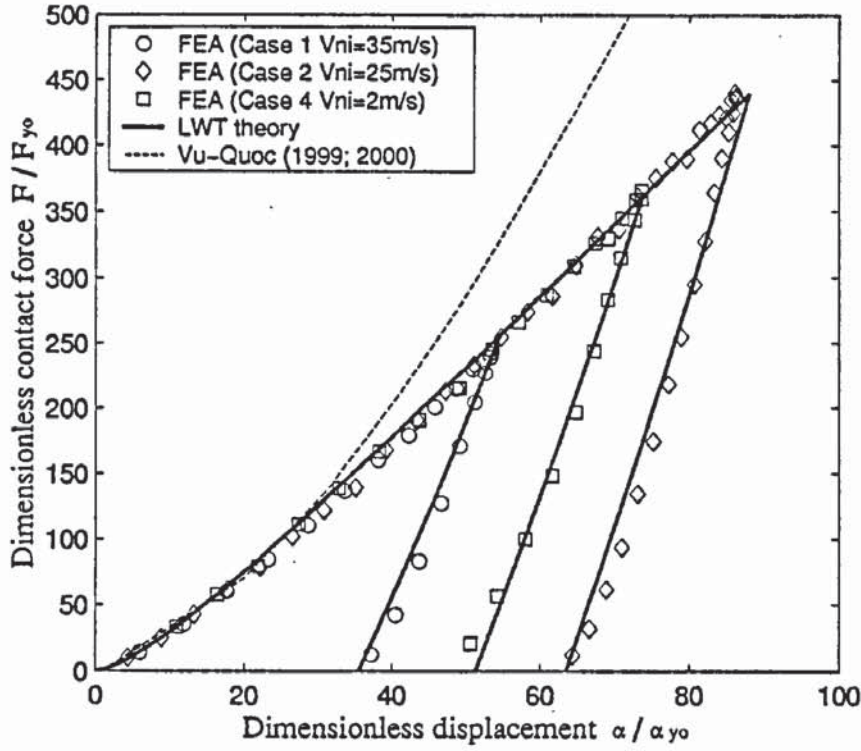
Integration of Eq.(5.34) can be done numerically, using the obtained numerical results of the dimensionless contact force and displacement as described above. Based on the calculated initial and rebound velocities one can obtain the coefficient of restitution as follows:

$$e_n = \frac{V_{nr}}{V_{ni}} = \sqrt{\frac{W_r}{W_i}} = \sqrt{\frac{W_r/W_{y0}}{W_i/W_{y0}}} \quad (5.35)$$

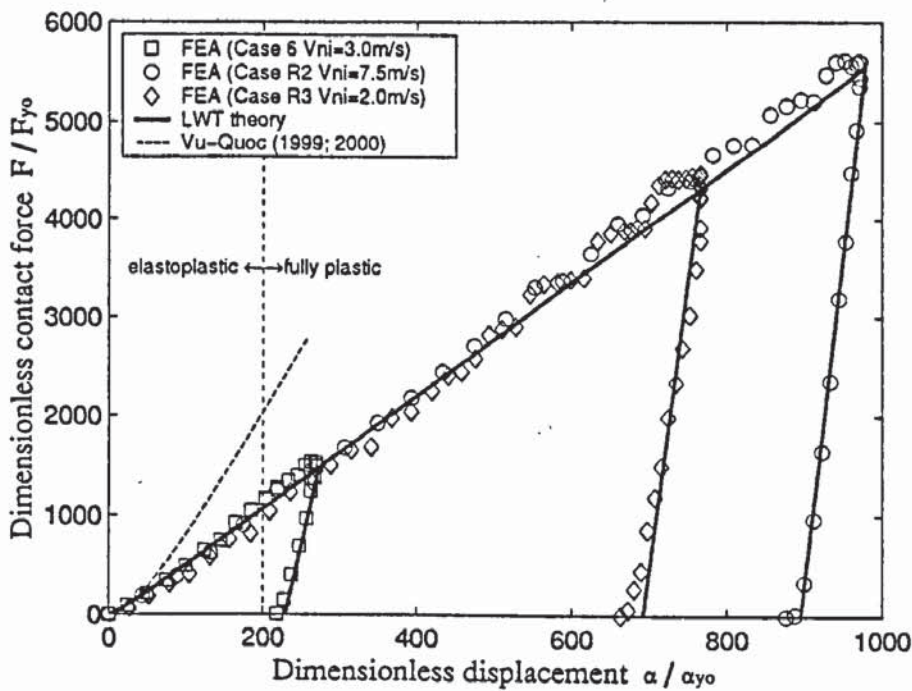
In order to validate the theoretical model described above, comparisons of the contact force-displacement relationships and of the coefficients of restitution obtained from the FE analysis with the theoretical predictions have been made; and are presented in Figs. 5.21 and 5.22 respectively. We also superimpose the results given by Vu-Quoc *et al.* (1999, 2000) in both figures. It is clear from Fig. 5.21 that for both loading and unloading the predictions of the LWT model are in good agreement with the FEA results obtained for different impact cases and over a wide deformation range. This clarifies that the assumptions made in the model are reasonable. In contrast, the loading curve provided by Vu-Quoc *et al.* (1999, 2000) is acceptable only for a very narrow region where the plastic deformation is very small. When significant plastic deformation is involved the results given by Vu-Quoc *et al.* (1999, 2000) do not agree with the finite element analysis even qualitatively. The reason for this is that two unreasonable assumptions were made in the model presented by Vu-Quoc *et al.* (1999, 2000): one was for the plastic contact radius and the other was for the adjustment coefficient of contact curvature, both of which were assumed to vary linearly with the contact force. These two assumptions were based purely on their FEA results that were obtained for very limited conditions involving only a small degree of plastic deformation.

Figure 5.22 shows the variation of coefficient of restitution with the normalised impact velocity V_{ni}/V_{y0} . The FEA results for various impact cases in the elastic-plastic deformation regime shown in Fig. 5.17 are reproduced here together with the experimental results of Tabor (1948) and Goldsmith and Lyman (1960). It can be seen that the LWT model agrees well with both FEA and experimental results, whereas the model presented by Vu-Quoc *et al.* (1999, 2000) fits the FEA and experimental results only in a very

narrow region. It is also interesting to note that the curve given by the LWT model coincides with the line given by the equation (5.9) when $V_{ni}/V_{y0} > 200$. This not only demonstrates the validity of the LWT model but also indicates that at high impact velocities the LWT model predicts a $-1/4$ power law, which is in agreement with Johnson (1985).



(a)



(b)

Fig. 5.21 Force-displacement relationships for the impact of elastic-perfectly plastic particles.

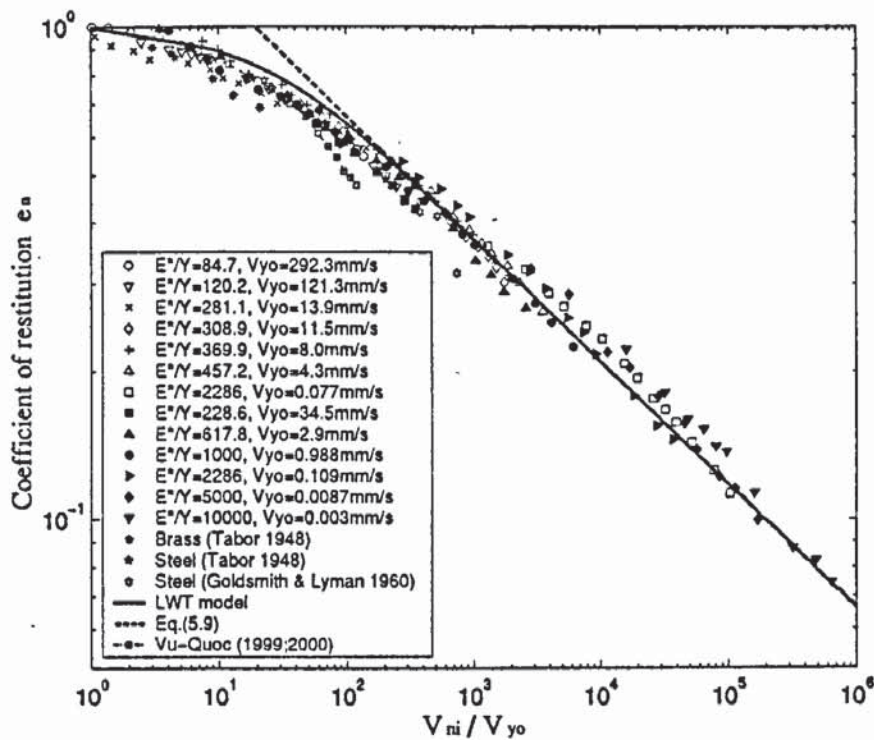


Fig. 5.22 Variation of coefficient of restitution with normalised impact velocity.

5.5 The influence of work hardening

So far we have discussed the normal impact behaviour of particles involving elastic-perfectly plastic deformation. However, in reality, most materials exhibit some degree of work hardening, for which the constitutive law is generally simplified by a curve shown in Fig. 2.1c. We shall consider the effect of work hardening on the normal impact behaviour with the bilinear constitutive law in this section.

Impacts of an elastic sphere with an elastic-plastic work hardening half-space are simulated using the same FEA procedure as discussed in Section 3.2.2. The material properties considered are given in Table 3.2. Some typical results are reported in the following sections and the effect of work hardening on the impact behaviour is also discussed.

5.5.1 Pressure distribution

The typical contact pressure distributions for the impact of an elastic sphere onto an elastic-plastic work hardening half-space are shown in Fig. 5.23. Comparing with the results shown in Fig. 5.1, which shows the contact pressure distribution for an impact with

an elastic-perfectly plastic half-space, the distinct features of the contact pressure distribution for an impact involving work hardening are that (1) the peak contact pressure occurs near the edge of the contact region and the contact pressure distributions have a dip in the centre of the contact area; (2) the overall magnitude of the contact pressure increases as the contact area increases and neither the mean contact pressure nor the maximum value remain below $3.0Y$. This is obviously due to the effect of strain hardening of the material as indicated in Fig. 2.1c. The same phenomenon was observed by Kral *et al.* (1993).

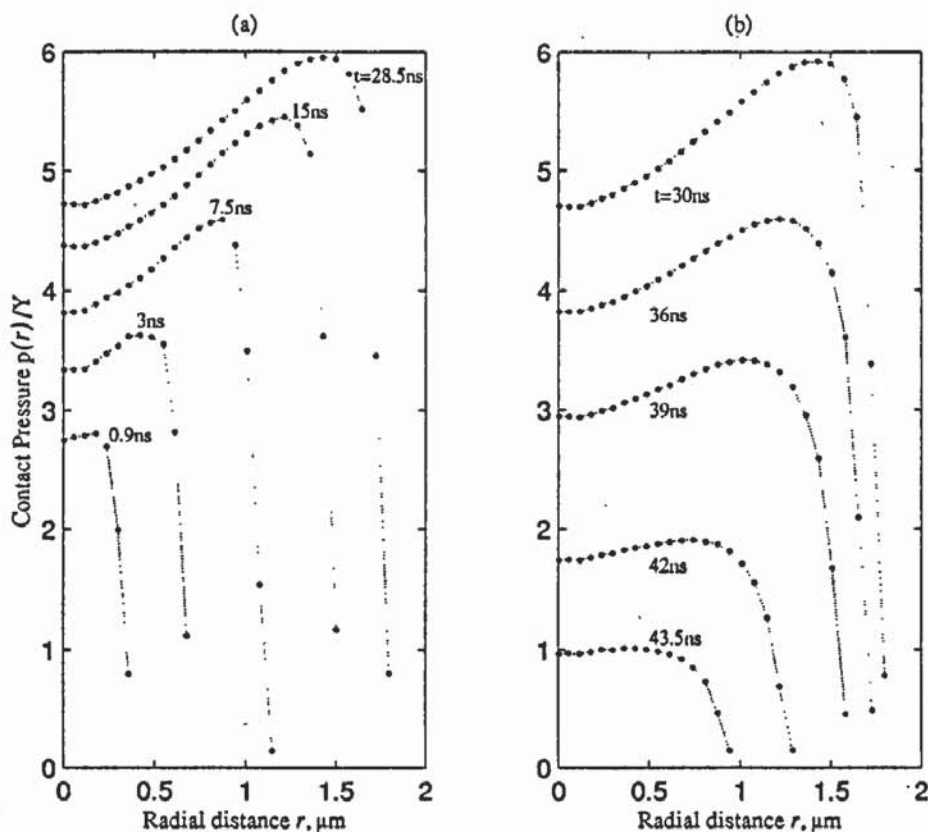


Fig. 5.23 The typical evolution of contact pressure distributions for the impact of an elastic sphere with an elastic-plastic work hardening half-space at $V_{ni} = 10\text{m/s}$: (a) during compression; (b) during restitution.

5.5.2 Evolution of kinetic energy

Figure 5.24 shows the comparison of time evolutions of normalised kinetic energy between impacts of an elastic sphere onto an elastic-plastic work hardening half-space and impacts of an elastic sphere with an elastic-perfectly plastic half-space at various impact velocities. Similar to an impact with an elastic-perfectly plastic half-space, no oscillations are found in the time histories of kinetic energy for an impact of an elastic sphere with an elastic-plastic work hardening half-space. After the sphere has separated from the substrate, the kinetic energy remains unchanged. It is clear that an impact with an elastic-plastic work

hardening half-space generally produces higher rebound kinetic energy than an impact with elastic-perfectly plastic half-space, for all the velocities considered. This implies that more energy is dissipated by plastic deformation in impacts with a perfectly plastic half-space than in impacts with an elastic-plastic work hardening half-space for a given impact velocity. Consequently, lower coefficients of restitution are expected to be obtained for impacts with an elastic-perfectly plastic half-space, as will be discussed in Section 5.5.5.

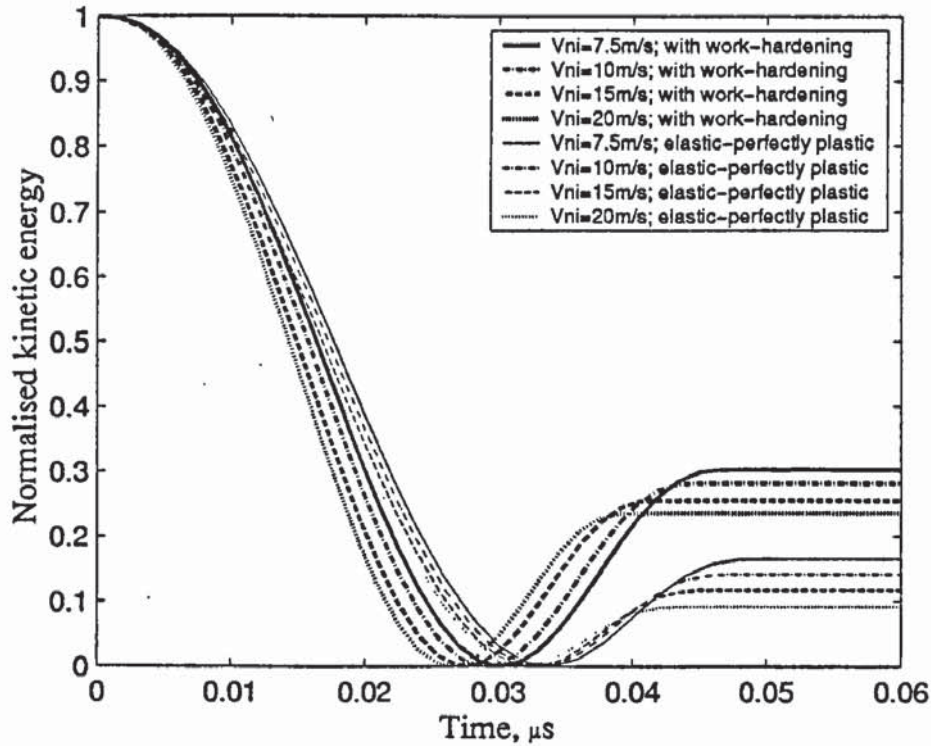


Fig. 5.24 Time evolution of the normalised kinetic energy for impacts of an elastic sphere with an elastic-plastic half-space with and without work hardening at various impact velocities.

5.5.3 Evolution of contact force

As the kinetic energy decreases during deceleration of the sphere the contact force increases and then decreases as the kinetic energy increases. Figure 5.25 shows comparisons of the time evolution of the contact force between impacts of an elastic sphere onto an elastic-plastic work hardening half-space and impacts of an elastic sphere with an elastic-perfectly plastic substrate at various impact velocities. It can be seen that work hardening results in a higher contact force being developed and shorter impact duration, although the two cases produce the similar patterns for the time evolution of contact force.

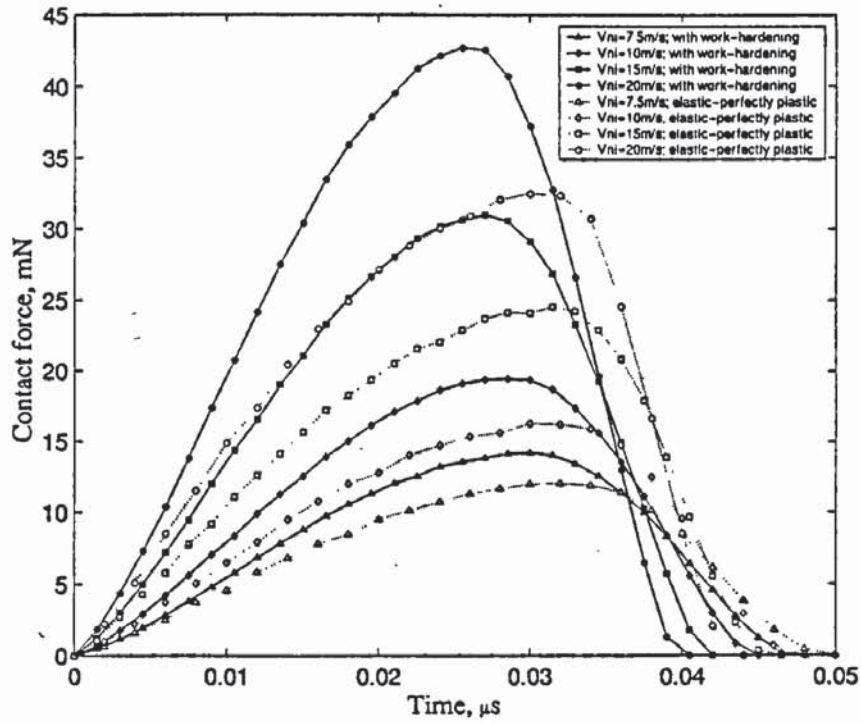


Fig. 5.25 Time evolution of the contact force for impacts of an elastic sphere with an elastic-plastic half-space with and without work hardening at various impact velocities.

5.5.4 Contact force-displacement relationship

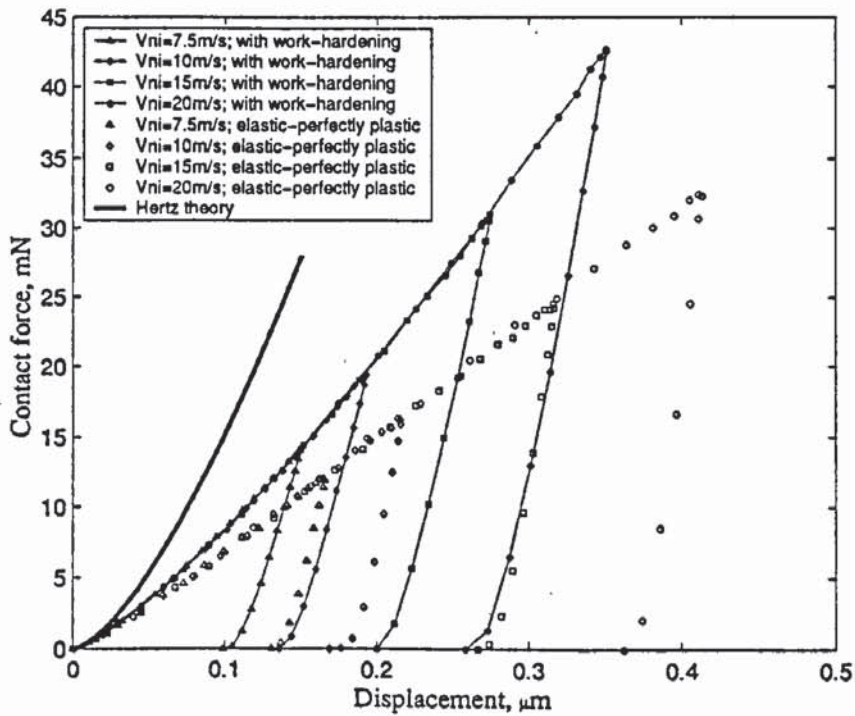


Fig. 5.26 Force-displacement relationships for impacts of an elastic sphere with an elastic-plastic half-space with and without work hardening at various impact velocities.

Figure 5.26 shows the relationships between the contact force and the displacement at the centre of the sphere for impacts of an elastic sphere onto an elastic-plastic work hardening half-space and for impacts of an elastic sphere with an elastic-perfectly plastic half-space at various impact velocities. Also superimposed is elastic prediction given by Hertz theory. As would be expected, the force-displacement curve obtained for the impact with elastic-plastic work hardening half-space lies between those obtained for elastic and elastic-perfectly plastic impacts. Unlike the impact of an elastic sphere with an elastic-perfectly plastic half-space, for which the loading curves exhibit an upward curvature at low values of displacement followed by a nearly constant slope at large displacements, the impacts with an elastic-plastic work hardening half-space do not exhibit a completely or partly linear relationship between the contact force and displacement. This is consistent with the experimental observations of Goldsmith and Lyman (1960).

5.5.5 Coefficient of restitution

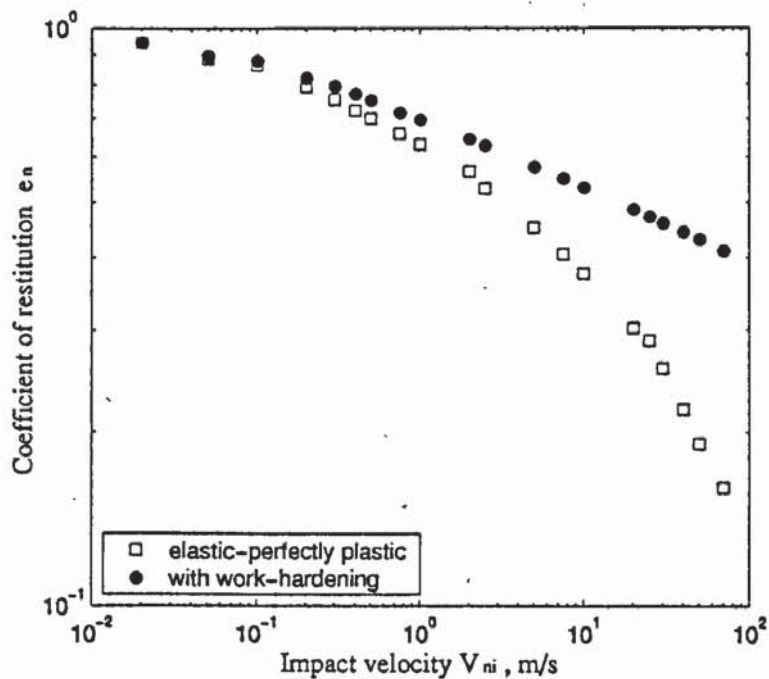


Fig. 5.27 Coefficient of restitution for the impact of an elastic sphere with an elastic-plastic half-space with and without work hardening.

The variation of the coefficient of restitution with impact velocity for the impact of an elastic sphere onto an elastic-plastic half-space with and without work hardening is shown in Fig. 5.27. Here for both cases the coefficient of restitution is calculated using Eq.(4.6). It has been discussed in Section 5.3.2 that owing to the piling-up taking place around the periphery of the contact region the coefficient of restitution begins to reduce markedly

when the impact velocity is larger than 21.95m/s (see Table 5.2) for the impact of an elastic sphere with an elastic-perfectly plastic half-space, as was shown in Fig. 5.13. For the impact of an elastic sphere onto an elastic-plastic work hardening half-space, the coefficient of restitution is also found to decrease with impact velocity but the rate is much lower than that for the impact with an elastic-perfectly plastic half-space, and the rate does not change significantly for the impact velocities considered. A higher coefficient of restitution is generally obtained for the impact of an elastic sphere onto an elastic-plastic work hardening half-space than the impact with an elastic-perfectly plastic substrate at the same velocity. This indicates that work hardening significantly affects the impact behaviour, which is consistent with observations of Kharaz and Gorham (2000) for the impacts of aluminium oxide spheres of 5mm diameter with thick plates of mild steel and aluminium alloy.

5.6 Summary

In this chapter, the normal impact of particles involving plastic deformation has been extensively investigated. The normal impact behaviour of particles involving elastic-perfectly plastic deformation has been discussed in detail, including the description of typical impact behaviour of an elastic sphere with an elastic-perfectly plastic half-space, the investigation of the parametric dependence of the rebound behaviour and establishment of a mathematical model for the normal impact of elastic-perfectly plastic particles. The finite-deformation plastic impact has also been addressed. Finally, the influence of work hardening has been discussed.

In summary, it has been shown that, according to the degree of contact deformation, the impact can generally be categorised into three groups: elastic impact, elastic-plastic impact (including elastoplastic impact and fully plastic impact) and finite-deformation plastic impact. For most elastic-plastic solid spherical particles, the impact can be regarded as elastic only when the impact velocity is very low (say V_{ni} is less than only a few centimetres per second for most steel materials). At such low velocities, the effect of stress waves can be neglected and the impact can be analysed using Hertzian theory.

Elastic-plastic impacts are common in engineering application. It has been shown that, for an elastic-plastic impact without work hardening, significantly flattened contact pressure

distributions are induced, which can be approximated by a Hertzian pressure distribution with a cut-off with the maximum contact pressure in the range from $2.6Y$ to $3.0Y$. In the case of work hardening plastic materials, the maximum contact pressure moves towards the contact edge and the contact pressure distributions have a dip in the centre of the contact area. For the impact of particles involving elastic-perfectly plastic deformation, the contact force-displacement relationship begins to differ from Hertz theory with the onset of plastic deformation and the loading curves exhibit an upward curvature at low value of displacement followed by a nearly constant slope at large displacements. However, for the impact of particles with elastic-plastic work hardening, neither a completely nor a partly linear relationship between the contact force and displacement is obtained. The coefficient of restitution is found to decrease with increasing impact velocity for both impacts of elastic-plastic particles with and without work hardening. The coefficient of restitution is found to depend mainly upon V_{ni}/V_{y0} for the impact of elastic-perfectly plastic particles and to be proportional to $(V_{ni}/V_{y0})^{-1/4}$ at high velocities. The impact of elastic-plastic particles with work hardening generally produces a higher coefficient of restitution than the elastic-plastic impact without work hardening at the same velocity, due to the effect of work hardening.

Finite-deformation plastic impact is addressed in this chapter. The appearance of finite-deformation plastic impact is the onset of piling-up or sinking-in around the periphery of the contact region for the impact of an elastic sphere with an elastic-perfectly plastic substrate and the lateral expansion of the sphere near the contact region for the impact of an elastic-perfectly plastic sphere with a rigid wall. The criteria for the onset of finite-deformation plastic impact have been established in terms of the impact velocity and material properties and given in Eqs.(5.7) and (5.8). For finite-deformation plastic impacts, the coefficient of restitution is found to be proportional to $[(V_{ni}/V_{y0})/(E^*/Y)]^{-1/2}$.

Chapter 6 Frictional Contacts under Tangential Loading

6.1 Introduction

So far, we have discussed the normal impact of particles. Before we proceed to investigate the oblique impact of particles, let us first consider frictional contacts under tangential loading. Our attention will focus on the contact traction distributions since accurate predictions of traction distributions over the interface are crucial to an exact analysis of the contact/impact problems. The aim of this chapter is two-fold: firstly, frictional contact of elastic spherical bodies under tangential loading is investigated using FEM and the results are compared with previous theories in order to demonstrate the reliability and accuracy of the FEA procedures for modelling oblique impacts of particles; secondly, the FEA procedures are extended to simulate the frictional contacts of plastic bodies under tangential loading, for which traction distributions are provided. This issue has never been addressed in literature.

The FEA procedures for modelling frictional contacts with tangential loading were discussed in Section 3.3. The modelling parameters were given in Table 3.3. The traction distributions for elastic and plastic contacts will be discussed in the following sections.

6.2 Elastic contact

According to equilibrium, it is expected that the contact force generated during the contact would be equal to the external loading exerted on the indenter as specified and in the opposite directions. This is demonstrated in Fig. 6.1, which shows the evolution of contact forces during the frictional contact of a rigid indenter with an elastic substrate under the loading condition specified in Fig. 3.8. It can be seen that at the early stage of loading in the normal direction, there are some oscillations on the normal contact force curve. However, the oscillations are quickly damped out by the mass proportional damping and a stable solution is obtained. No oscillation is found for both the evolution of the normal force and that of tangential contact force during the period when the applied normal force \bar{F}_n is constant.

Now we shall look at the contact pressure distributions at various instants during the period when the normal force is constant but the tangential force monotonically increases and then remains constant. At any instant the contact pressures are obtained from the nodal forces over the interface using the tributary method. The corresponding results at instants A-E marked in Fig. 6.1 are shown in Figs. 6.2-6.6.

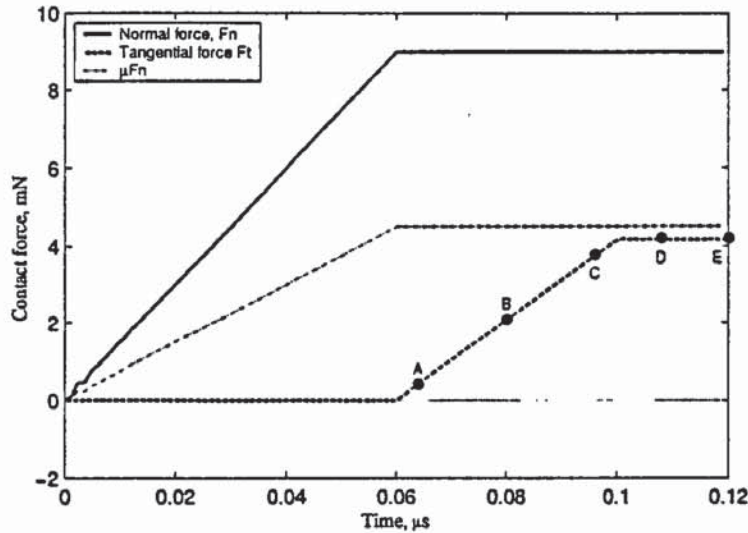


Fig. 6.1 The evolution of contact forces during the frictional contact of a rigid indenter with an elastic substrate.

6.2.1 Normal contact pressure distribution

Figure 6.2 shows the normal contact pressure distributions at various instants for the frictional contact of a rigid indenter with an elastic substrate. In the figure, the graphs shown in the left side are 3D views of the normal contact pressure distribution, and those shown in the right side are the contours of the normal contact pressure distribution, in which the outer curves represent the boundary of the contact area with $p = 0$. It can be seen that the normal contact pressure is of ellipsoidal shape and the contact area is essentially circular.

The normal contact pressure distributions within the symmetry plane ($y-z$ plane) at various instants are shown in Fig. 6.3. It is clear that the normal contact pressure distributions at various instants are similar and only marginal differences are obtained between the normal contact pressure distributions at different instants with different degree of the tangential loading. In addition, it is found that the differences mainly lie near the edge of the contact

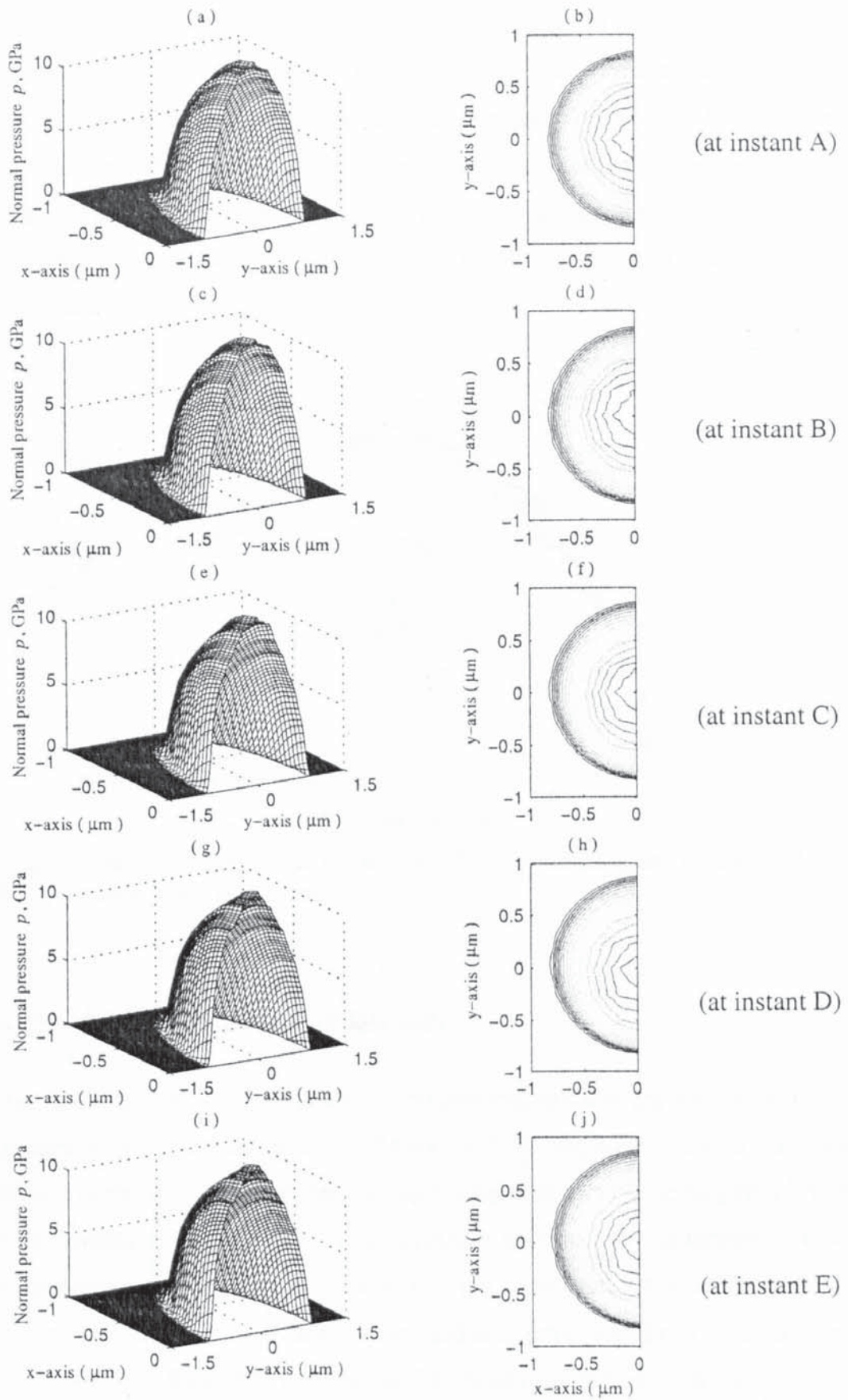


Fig. 6.2 Normal contact pressure distributions at various instants for the frictional contact of a rigid indenter with an elastic substrate.

area and the normal contact pressures at a certain central region are identical for different tangential force applied. As to be shown later, within this certain central region, no sliding occurs during the entire loading history. Therefore, the change in normal contact pressure with the tangential force mainly occurs in the slip region. This is mainly due to the effect of the tangential interaction. In present analysis, the material constants for the indenter and substrate are different. This difference in material constants results in the normal contact pressure distribution slightly tilting towards the trailing edge for the sliding of a indenter over a plane surface, as discussed by Johnson (1985) (see also Fig. 2.7). Nevertheless, this influence is insignificant.

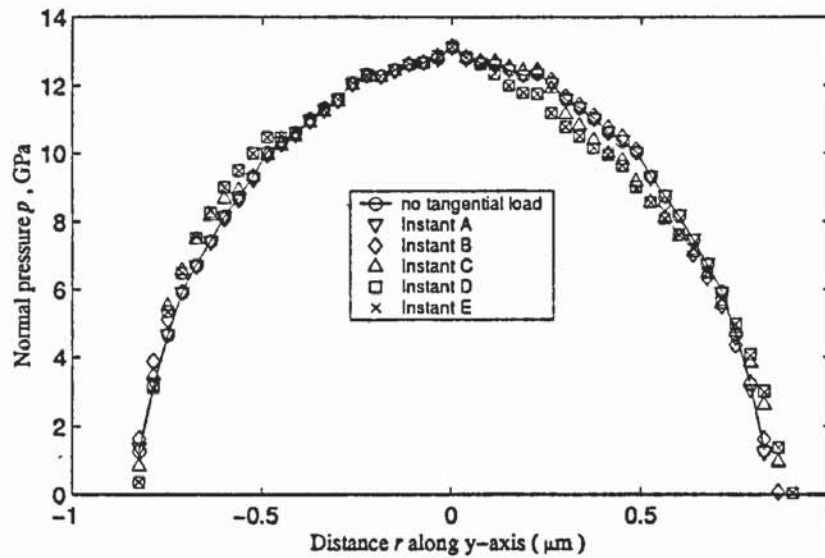


Fig. 6.3 Influence of tangential traction on the normal pressure distribution in the symmetry plane (y-z plane).

6.2.2 Tangential traction distribution

The tangential traction distributions at the corresponding instants are shown in Fig. 6.4. Again, the graphs shown in the left side are 3D views of the tangential traction distribution, and those shown in the right side are the corresponding contours of the tangential traction distribution. In contrast to the normal contact pressure distribution, the tangential traction distribution apparently has a concave part within the inner area. According to Mindlin (1949), this area is referred to as a stick region, and the remaining area is the slip region. The boundaries between these two regions can be clearly identified from the plots of the contours of the tangential traction and are marked by thick lines.

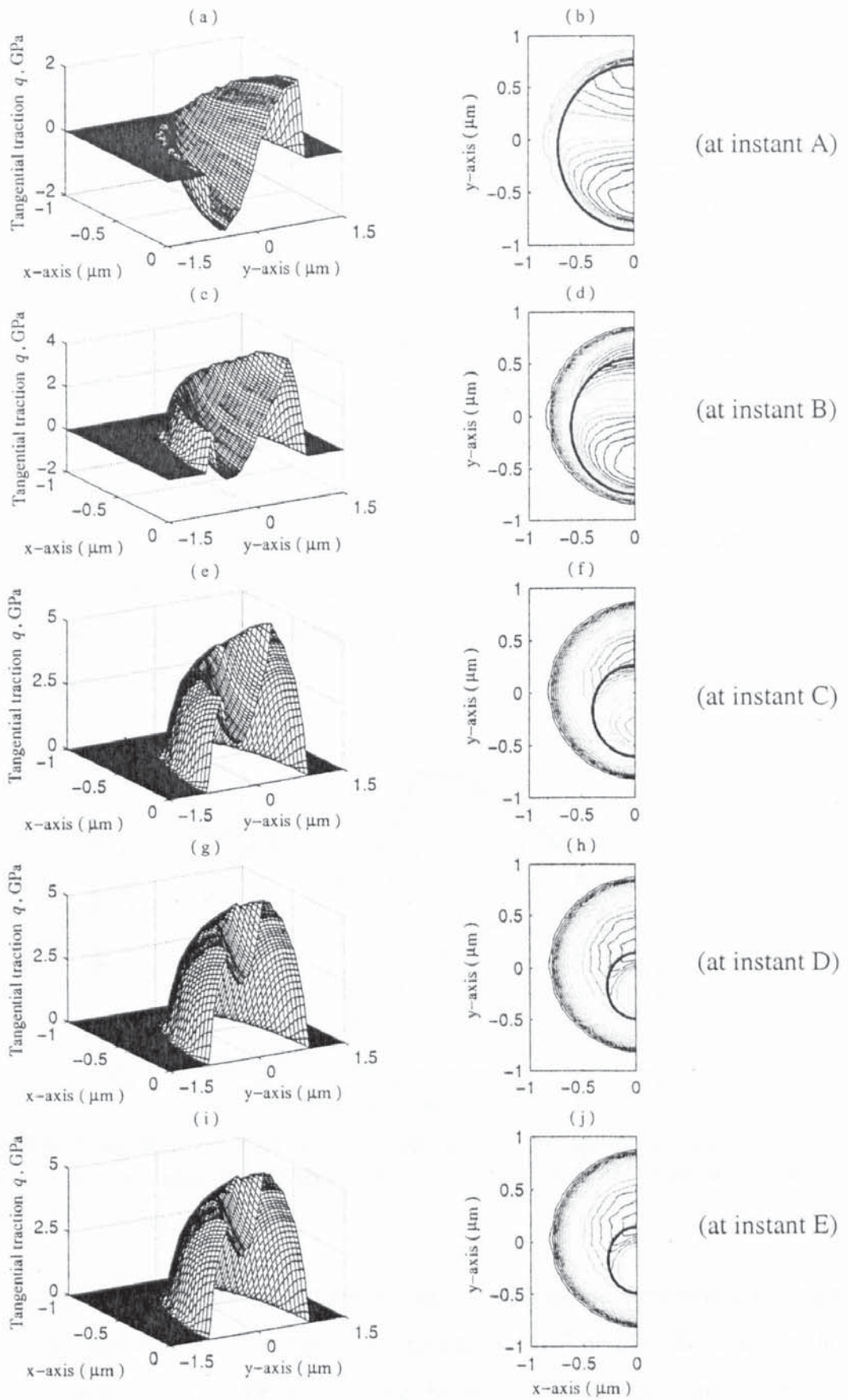


Fig. 6.4 Tangential traction distributions at various instants for the frictional contact of a rigid indenter with an elastic substrate.

It is interesting to note from Fig. 6.4 that the stick region is essentially circular but not centrally located. Instead, it is found that at the beginning of the tangential loading the boundary of the stick region is coincident with the trailing edge of the contact area. With the increase of the tangential force, the stick region shrinks inwards, but its centre slightly moves towards the trailing edge of the contact area. It is also found that the results at instants D and E that have the same loading condition are identical (see Figs. 6.4g-6.4j), which demonstrate that the present solutions are convergent and stable. Figure 6.5 shows the tangential traction distributions within the symmetry plane (y - z plane) at various instants. It is clear that the tangential traction distribution is not symmetrical, and the overall distribution is slightly tilted towards the trailing edge of the contact area. This is due to the effect of the difference in elastic constants of the indenter and the substrate. We have $\beta = 0.286$ from Eq.(2.75) for present case. It is expected that unsymmetrical traction distributions be obtained for such a dissimilar combination of the material properties, as pointed out by Johnson (1985, 2001) and Hills *et al.* (1993). It is interesting to find that the patterns shown in Fig. 6.5 are very similar to those obtained by Hills *et al.* (1993), see Fig. 2.7b, which implies that the difference in elastic constants is responsible for the unsymmetrical traction distributions.

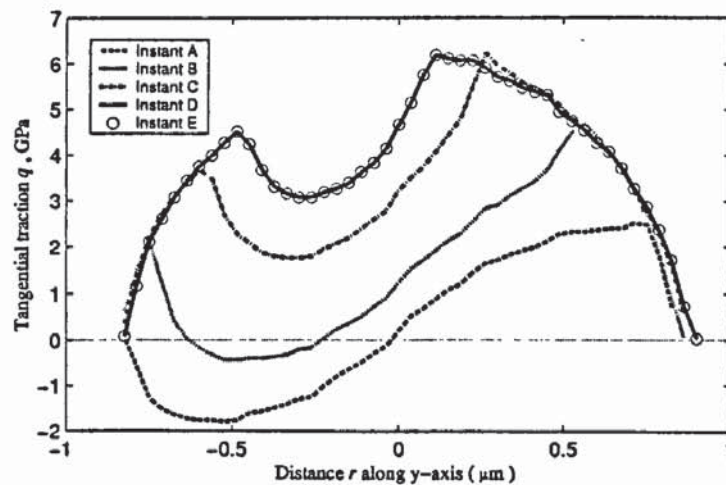


Fig. 6.5 Tangential traction distributions within the symmetry plane (y - z plane) at various instants for the contact of a rigid indenter with an elastic substrate.

Figure 6.6 shows the corresponding distributions of the normal pressure and tangential traction in the symmetry plane (y - z plane) at instants A, B, C and D, respectively. In this figure, the squares represent the FEA results for the normal contact pressure p , the circles denote the FEA results for the tangential traction q , and the diamonds give the FEA results obtained by $q' = q - \mu p$ within the stick region. The dashed and chain lines are obtained by

the better fit of the FEA results p and q' with theoretical formula and are denoted by \bar{p} and \bar{q}' , respectively, and the solid lines are given by $\bar{q} = \mu\bar{p} - \bar{q}'$ within the stick region and $\bar{q} = \mu\bar{p}$ within the surrounding slip region. It is clear that the tangential traction obtained by FE analysis can be approximated by the same manner as proposed by Mindlin (1949), except that the centre of the stick region is offset a distance due to the effect of the difference in material properties. It also shows that negative tangential tractions were produced at the beginning of tangential loading. This is due to the dissimilarity of elastic material properties which results in a negative tangential traction being produced by the normal force even though there is no tangential loading, as obtained by Hill *et al.* (1993) and shown in Fig. 2.7b.

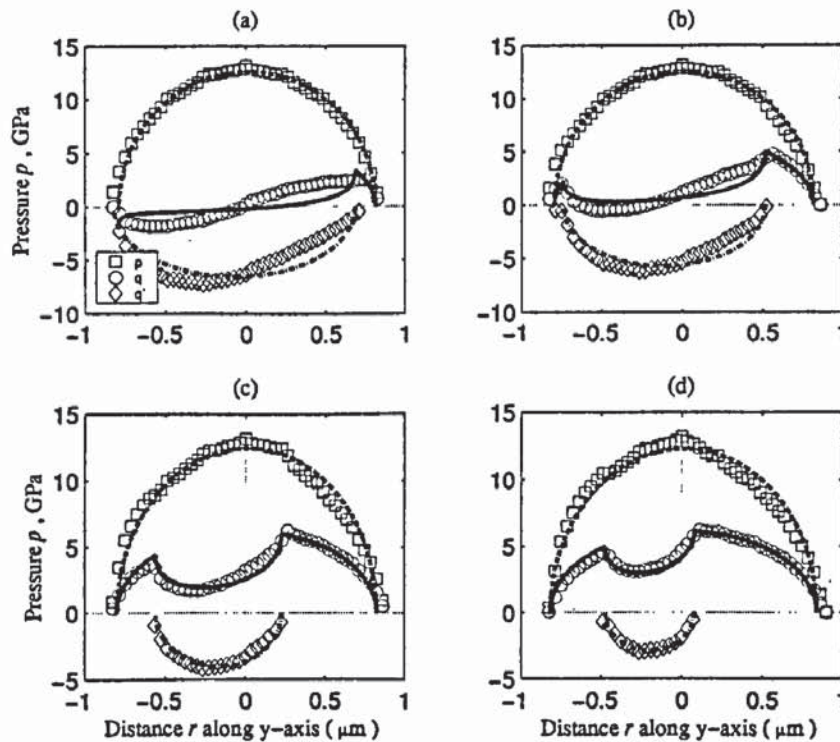


Fig. 6.6 The distributions of the normal pressure and tangential traction in the symmetry plane (y-z plane) at various instants: (a) at instant A; (b) at instant B; (c) at instant C and (d) at instant D.

6.3 Plastic contact

The evolution of contact forces for the frictional contact of a rigid indenter and an elastic-perfectly plastic substrate subjected to the loadings conditions specified in Fig. 3.8 is shown in Fig. 6.7. It is clear that only at the early stage, after the normal force has first been applied, there are some oscillations on the normal contact force curve. Damping quickly releases oscillations thereafter and convergent solutions are obtained. No oscillation is observed for the evolution of the normal and tangential contact forces during

the period when the applied normal force becomes constant. During this period, the contact pressure distributions at various instants are again obtained from the nodal forces over the interface using the tributary method. The corresponding results at instants A-E marked in Fig. 6.8 are shown in Figs. 6.8-6.11.

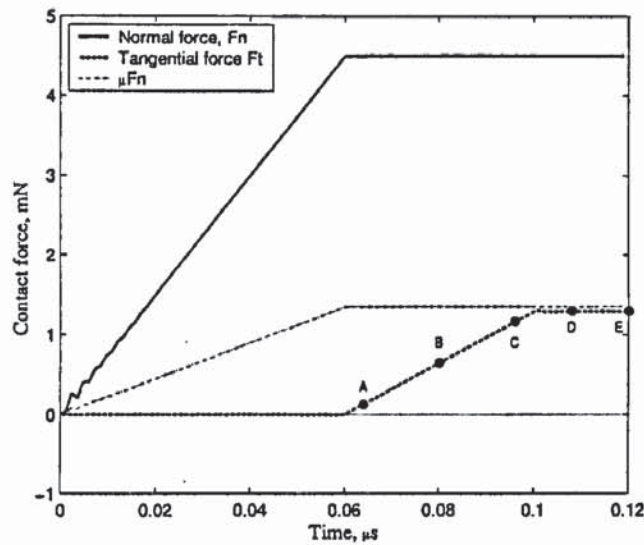


Fig. 6.7 The evolution of contact forces during the frictional contact of a rigid indenter and an elastic-perfectly plastic substrate.

6.3.1 Normal contact pressure distribution

Figure 6.8 shows the normal contact pressure distributions at various instants for the frictional contact of a rigid indenter with an elastic-perfectly plastic substrate. Again, in this figure, the graphs shown in the left side are 3D views of the normal contact pressure distribution, and those shown in the right side are the contours of the normal contact pressure distribution, in which the outer curves represent the boundary of the contact area with $p = 0$. Similar to the results of the normal impact of elastic-perfectly plastic bodies shown in Chapter 5, the normal contact pressure distribution is not elliptical in shape. Instead, significant flattening appears in the centre of the contact. The contact area is found to be essentially circular. Additionally, at the beginning of tangential loading, the normal contact pressure is centrally located (See Fig. 6.8b), but with the increase of the tangential force, the normal contact pressure distribution become skewed towards the trailing edge of the contact area. This is due to the effect of the dissimilarity of material properties. For clarity, normal contact pressure distributions within the symmetry plane (y - z plane) at various instants are plotted in Fig. 6.9. It is clear that, with no tangential load, the normal pressure distribution is symmetric. As the tangential force increases, the normal contact

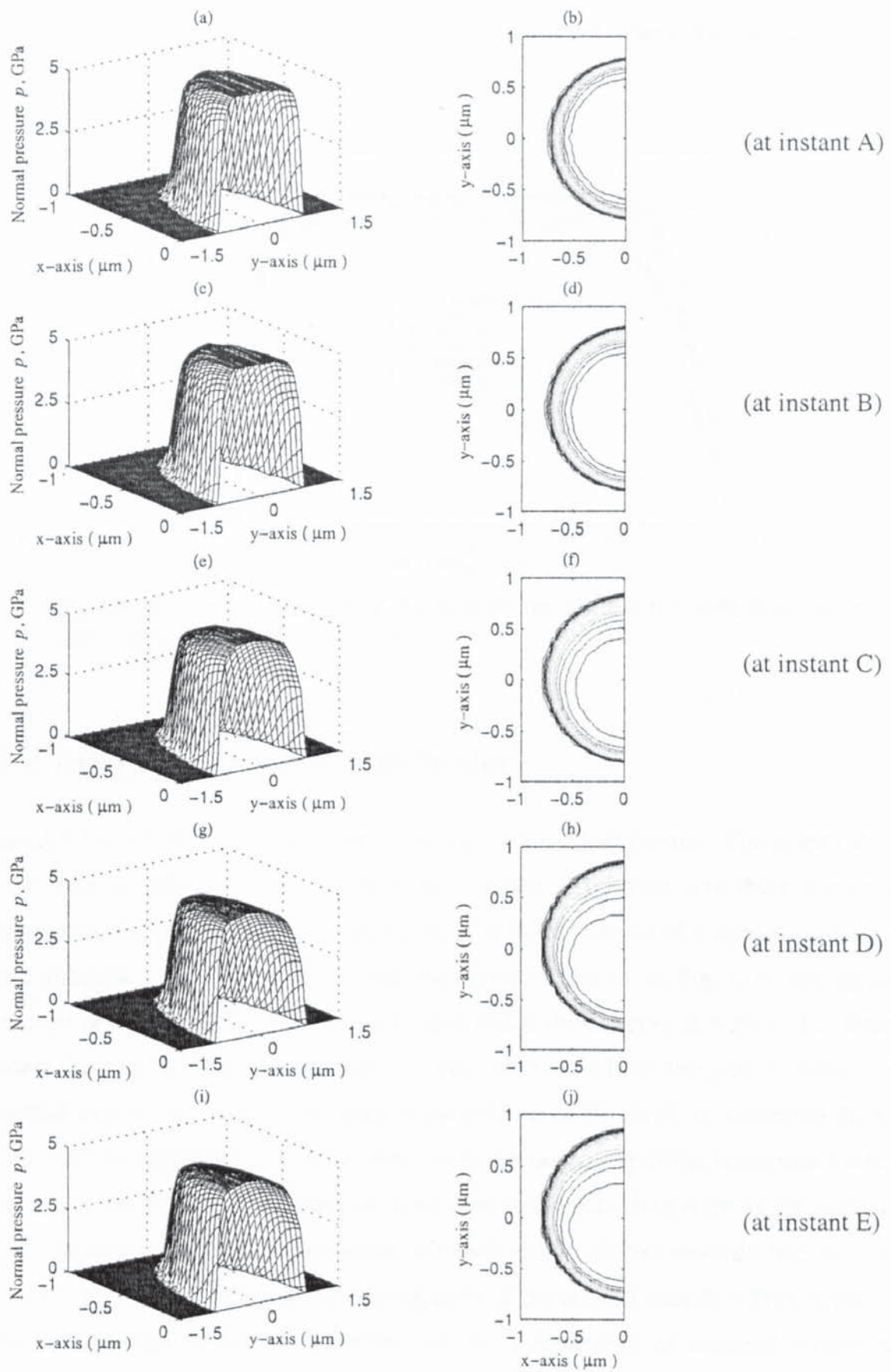


Fig. 6.8 Normal contact pressure distributions at various instants for the frictional contact of a rigid indenter with an elastic-perfectly plastic substrate.

pressure distribution becomes asymmetric with a decrease in the maximum contact pressure and a slight increase in the contact area. Figure 6.9 clearly demonstrates that, for frictional contact of elastic-plastic bodies, the tangential interaction affects the normal contact pressure distribution.

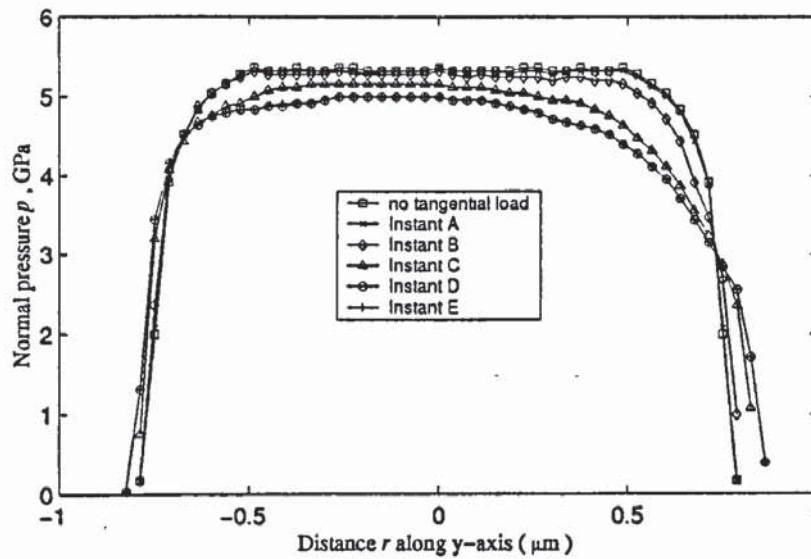


Fig. 6.9 Influence of tangential traction on the normal pressure distribution in the symmetry plane (y-z plane).

6.3.2 Tangential traction distribution

Figure 6.10 shows the corresponding tangential traction distributions. The graphs shown in the left side are 3D views of the tangential traction distribution and those shown in the right side are the corresponding contours. Similar to the contact of a rigid indenter with an elastic substrate, the tangential traction distributions shown in Fig. 6.10 are apparently composed of two regions: an inner stick zone and a surrounding slip zone. The boundary between the stick and slip regions can be clearly identified from the plot of contours of the tangential traction as shown in the right-hand column of Fig. 6.10, in which the thick solid curves mark the boundary. It can be seen that at the beginning of the tangential loading the boundary of the stick region is almost coincident with the trailing edge of the contact area. As the tangential force further increases, the stick region shrinks inwards, but the centre of the stick region moves towards the trailing edge of the contact area (see Figs. 6.10d, 6.10f, 6.10h, 6.10j). This is due to the effect of the dissimilarity of material properties. As expected, the results at instants E and F that have the same loading conditions are identical (see Figs. 6.10g-6.10j), which demonstrate that the present solutions are convergent and stable.

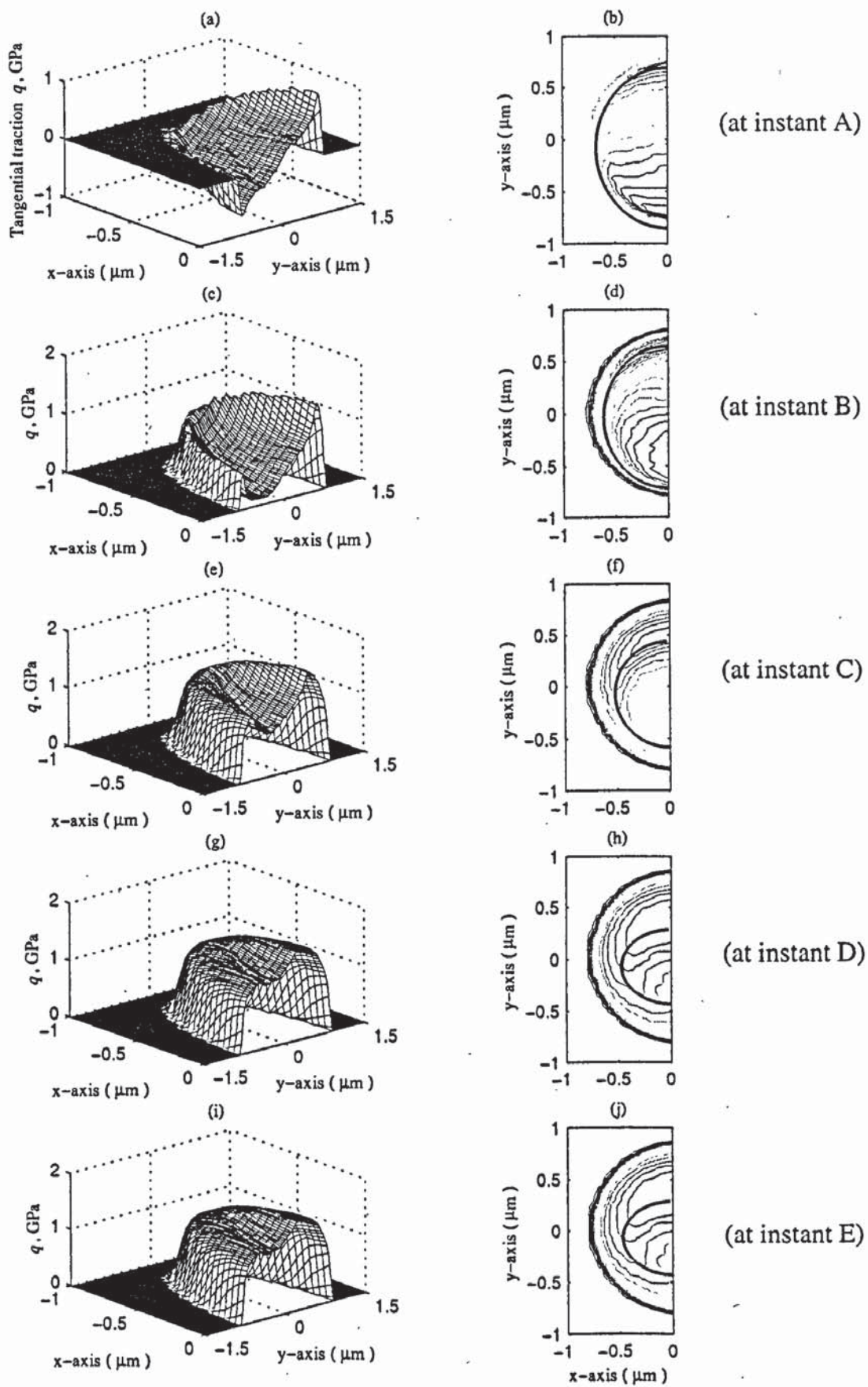


Fig. 6.10 Tangential traction distributions at various instants for the frictional contact of a rigid indenter with an elastic-perfectly plastic substrate.

Figure 6.11 shows the corresponding distributions of the normal pressure and tangential traction in the symmetry plane (y - z plane), respectively. In the figure, the squares represent the FEA results for the normal contact pressure and the circles the FEA results for the tangential traction. It is clear that the tangential traction obtained by FEA can be approximated by the same manner as used for the contact of a rigid indenter with an elastic substrate, that is, the tangential traction can be estimated by the multiplication of the friction coefficient with the normal contact pressure, with a negative traction superimposed in the stick region. This approximation is illustrated in Fig. 6.11 with thick lines. It can be seen from Fig. 6.11 that the tangential traction distributions at higher tangential loadings are well estimated by the above approximation (see Figs. 6.11c and 6.11d). However, at lower tangential loading, significant deviation is observed (see Fig. 6.11a and Fig. 6.11b). This is due to the negative tangential traction produced near the trailing edge of the contact area by the normal force when dissimilar materials are involved in the impact, as discussed in Section 6.2.2.

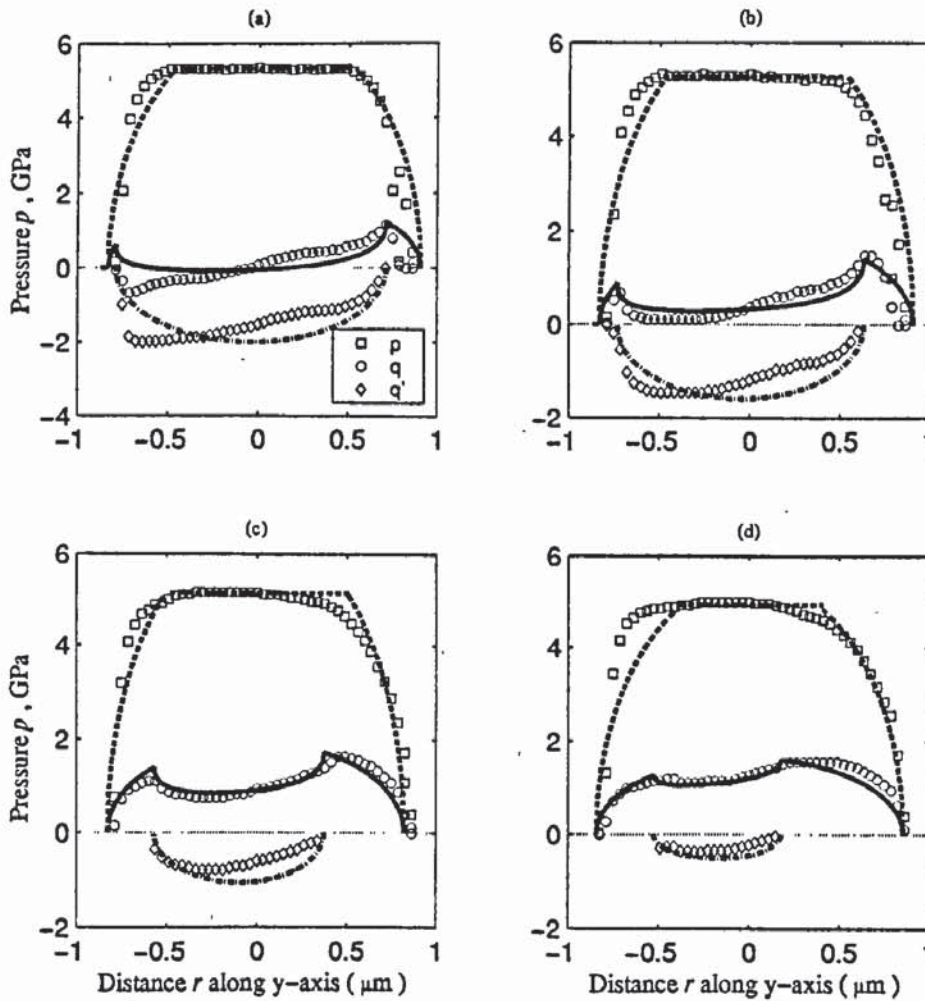


Fig. 6.11 The distributions of the normal pressure and tangential traction in the symmetry plane (y - z plane) at various instants: (a) at instant A; (b) at instant B; (c) at instant C and (d) at instant D.

6.4 Summary

In this chapter, the frictional contact of a rigid indenter with either an elastic or an elastic-perfectly plastic substrate has been investigated using FEM. For a simple loading history as shown in Fig. 3.8, the evolution of tangential traction has been presented and the effect of plastic deformation on tangential and normal interaction has been discussed.

The tangential traction for the frictional contact of elastic bodies obtained from the FE analysis is in good agreement with theoretical predictions (Mindlin 1949; Johnson 1985; Hills *et al.* 1993). It has shown that, due to the dissimilarity of material properties, the traction distributions become asymmetric and skew towards the trailing edge of the contact area. Nevertheless, the tangential tractions for both the elastic and plastic contacts are found to be composed of two regions: a stick region and a slip region. Furthermore, it is found that, even for contacts involving plastic deformation, the tangential traction distributions can be approximated by the product of the friction coefficient and the normal pressure distribution in the slip region and by superimposing a negative traction over the stick region. In addition, the normal contact pressure for plastic contact can be approximated by a Hertzian pressure distribution with a cut-off, as discussed in Chapter 5.

It is also found that the influence of tangential traction on the normal contact pressure is insignificant for the contact of a rigid indenter and an elastic substrate, but it is significant for the contact of a rigid indenter with an elastic-perfectly plastic substrate. It is hence suggested that the two-way coupling of the normal and tangential responses is not insignificant for the oblique plastic impact problems.

7.1 Introduction

The investigation of tangential loading with frictional contacts presented in the preceding chapter has demonstrated the ability of FEM for investigating oblique interactions of solid bodies. We shall advance our study into the oblique impact of particles, since in the most common impact cases the particles hit each other or a target at an inclined angle, in which the tangential response is induced due to the interface friction. The oblique impact of particles has recently become one of the most interesting research topics. However, our understanding of the oblique impact behaviour of particles is far from complete, since the problem becomes more complicated owing to the presence of friction. Further investigation is hence necessary to provide a better understanding of the problem.

In this chapter, the oblique impact of elastic particles is investigated using FEM. The theoretical consideration is first presented. The effects of impact angle, initial velocity, friction and Poisson's ratio on the impact behaviour are then explored.

7.2 Theoretical aspects

When a particle collides with a fixed target, the motion of the particle is governed by the contact force. To accurately predict the rebound behaviour of a particle during the oblique impact, the contact force must be known *a priori*. In this section, the correlation between the rebound parameters and the initial impact condition is presented by introducing some classical parameters, such as the normal coefficient of restitution e_n and the impulse ratio f , and on the basis of the conservation of impulse and momentum.

The oblique impact of a sphere with a plane surface is illustrated in Fig. 3.9. The normal coefficient of restitution e_n can be defined by Eq.(2.67). Analogously, a tangential coefficient of restitution e_t can be defined as

$$e_t = \frac{V_{tr}}{V_{ti}} \quad (7.1)$$

the coefficients e_n and e_t can be used to represent the recovery of translational kinetic energy in the normal and tangential directions, respectively. The recovery of total kinetic energy during the impact can be estimated by defining a total coefficient of restitution e as follows,

$$e = \frac{V_r}{V_i} = \frac{\sqrt{V_{nr}^2 + V_{tr}^2}}{V_i} \quad (7.2)$$

$$= \sqrt{\frac{V_{nr}^2}{V_{ni}^2 / \cos^2 \theta} + \frac{V_{tr}^2}{V_{ti}^2 / \sin^2 \theta}} = \sqrt{e_n^2 \cos^2 \theta + e_t^2 \sin^2 \theta}$$

It is clear that e is related to e_n , e_t and the impact angle θ , and it is dominated by e_n at small impact angles ($\theta \rightarrow 0^\circ$) and by e_t at large impact angles ($\theta \rightarrow 90^\circ$).

The impulse ratio defined in Eq.(2.69) can be estimated by

$$f = \frac{P_t}{P_n} = \frac{\int F_t dt}{\int F_n dt} \quad (7.3)$$

where F_n and F_t are the normal and tangential components of the contact force, respectively. It is clear that the impulse ratio f is different from the friction coefficient μ ; it may or may not equal μ (see also Brach 1988).

According to Newton's second law, P_n and P_t are expressed in term of the incident and rebound velocities in Eq.(2.65) and can be rewritten as

$$P_n = m(V_{nr} - V_{ni}) \quad (7.4a)$$

$$P_t = m(V_{tr} - V_{ti}) \quad (7.4b)$$

where m is the mass of the sphere. Substituting Eqs.(7.4) into Eq.(7.3) and using Eqs.(2.67) and (7.1), we obtain

$$e_t = 1 - \frac{f(1 + e_n)}{\tan \theta} \quad (7.5)$$

Similarly, the rotational impulse P_ω is defined by

$$P_\omega = I(\omega_r - \omega_i) = I\omega_r \quad (7.6)$$

where I is the inertia moment of the sphere, $\omega_i (= 0)$ and ω_r are the initial and rebound rotational angular velocities, respectively. According to the conservation of angular momentum about point C (see Fig. 3.9), we have

$$P_\omega = RP_t \quad (7.7)$$

where R is the radius of the sphere.

Substituting Eqs.(7.4b) and (7.6) into Eq.(7.7) yields,

$$\omega_r = \frac{-mR(V_{ii} - V_{ir})}{I} \quad (7.8)$$

For a solid sphere,

$$I = \frac{2}{5}mR^2 \quad (7.9)$$

Hence

$$\omega_r = \frac{-5(V_{ii} - V_{ir})}{2R} = \frac{5V_{ii}(e_t - 1)}{2R} \quad (7.10)$$

Substituting Eq.(7.5) into Eq.(7.10), we obtain

$$\omega_r = -\frac{5f(1 + e_n)V_{ni}}{2R} \quad (7.11)$$

The tangential component of rebound velocity at the contact patch, v_{ir} , can be expressed as

$$v_{ir} = V_{ir} + R\omega_r \quad (7.12)$$

Substituting Eq.(7.11) into Eq.(7.12), we have

$$v_{ir} = V_{ir} - \frac{5}{2}f(1 + e_n)V_{ni} \quad (7.13)$$

rearranging Eq.(7.5) and then substituting into Eq.(7.13). We have,

$$v_{ir} = V_{ii} - \frac{7}{2}f(1 + e_n)V_{ni} \quad (7.14a)$$

$$\text{or } v_{ir} = V_{ii} - \frac{7}{2}f(1 - e_t)V_{ii} \quad (7.14b)$$

Eq.(7.14b) can be rewritten as

$$e_t = \frac{5}{7} + \frac{2v_{ir}}{7V_{ii}} \quad (7.15)$$

Introducing a dimensionless impact angle φ_i and a dimensionless reflection angle at the contact patch φ_r as

$$\varphi_i = \frac{V_{ii}}{\mu V_{ni}} \quad (7.16a)$$

$$\varphi_r = \frac{v_{ir}}{\mu V_{ni}} \quad (7.16b)$$

Eq.(7.15) can be rewritten as

$$e_t = \frac{5}{7} + \frac{2\varphi_r}{7\varphi_i} \quad (7.17)$$

It can be seen that the dimensionless reflection angle of the contact patch φ_r , will be positive if $e_n > 5/7$, otherwise, negative reflection angle will be obtained, regardless of the normal coefficient of restitution e_n .

Using Eq.(7.16), Eq.(7.14) can be rewritten in the dimensionless form as

$$\varphi_r = \varphi_i - \frac{7(1+e_n)}{2} \frac{f}{\mu} \quad (7.18)$$

It is clear that once the contact force during the oblique impact is known *a priori*, the impulse ratio f can be determined from Eq.(7.3), and the rebound behaviour of the particle can hence be well predicted from Eqs.(7.5)-(7.18). However, accurate description of the contact force during the oblique impact is a complicated topic since it depends on the initial impact condition, the frictional condition and material properties. Some attempts have been made to predict the rebound behaviour as discussed in Section 2.3. Among those, the simplest model to describe the rebound behaviour is the classical rigid body dynamics.

7.2.1 The classical rigid body dynamics

According to the predictions of the classical rigid body dynamics, the tangential rebound velocity at the contact patch v_{tr} is either positive if sliding occurs throughout the impact, or zero if sliding does not persist throughout the impact. This implies that there is a critical impact angle θ_{rigid}^* above which sliding occurs throughout the impact and below which $\dot{v}_{tr} = 0$, see Eq.(2.68). Combining Eqs.(2.68) and (7.3), we have

$$v_{tr} = 0 \quad (\theta \leq \theta_{rigid}^*) \quad (7.19a)$$

$$f = \mu \quad (\theta > \theta_{rigid}^*) \quad (7.19b)$$

Using Eq.(7.14), we have

$$\theta_{rigid}^* = \tan^{-1} \left(\frac{7\mu}{2} (1+e_n) \right) \quad (7.20)$$

For the impact with $e_n = 1$, Eq.(7.20) reduces to

$$\theta_{rigid}^* = \tan^{-1}(7\mu) \quad (7.21)$$

Substituting Eq.(7.19) into Eqs.(7.15) and (7.5) yields,

$$e_t = \begin{cases} 5/7 & \theta \leq \theta_{rigid}^* \\ 1 - 2\mu/\tan \theta & \theta > \theta_{rigid}^* \end{cases} \quad (7.22)$$

Replacing e_t in Eq.(7.10) by Eq.(7.22), we have

$$\omega_r = \begin{cases} -\frac{5V_{ti}}{7R} = -\frac{5V_{ni} \tan \theta}{7R} & \theta \leq \theta_{rigid}^* \\ -\frac{5\mu V_{ni}}{R} & \theta > \theta_{rigid}^* \end{cases} \quad (7.23)$$

Combining Eqs.(7.14) and (7.19), we obtain

$$v_{tr} = \begin{cases} 0 & \theta \leq \theta_{rigid}^* \\ V_{ti} - 7\mu V_{ni} & \theta > \theta_{rigid}^* \end{cases} \quad (7.24)$$

Eq.(7.24) can be rewritten in terms of dimensionless impact angle φ_i and dimensionless reflection angle at the contact patch φ_r as

$$\varphi_r = \begin{cases} 0 & \theta \leq \theta_{rigid}^* \\ \varphi_i - 7 & \theta > \theta_{rigid}^* \end{cases} \quad (7.25)$$

According to the classical rigid body dynamics, Eqs.(7.19)-(7.25) can be used to predict the rebound behaviour of rigid spherical particles if the contact deformation is not dominant. Note that Eqs.(7.22)-(7.25) are only appropriate for the case in which $e_n = 1$, since all these parameters depends on e_n , as shown in the preceding section.

7.2.2 Model of elastic bodies (Maw *et al.* 1976; 1981)

Since the classical rigid body dynamics uses the idealised “rigid body” and ignores the contact deformation that is inevitable in practice, the accuracy and the application range of this theory are limited. Although the classical rigid body dynamics has been modified and advanced by many researchers as discussed in Section 2.3.1, accurate prediction of the oblique impact behaviour of elastic bodies must take the contact deformation into account. Based on the theory of Hertz (1896) and Mindlin and Deresiewicz (1953), Maw *et al.* (1976, 1981) developed a numerical model for the oblique impact of elastic bodies (see Section 2.3.3). It was shown that when

$$\psi_i \geq (4\chi - 1) \quad (7.26)$$

sliding occurs throughout the whole duration of impact and the magnitude of the tangential force F_t is equal to μF_n at all times (see Fig. 2.10). For the impact of a solid sphere with an elastic half-space, using Eqs.(2.79)-(2.82), Eq.(7.26) can be rewritten as

$$\theta \geq \theta_{elastic}^* = \tan^{-1} \left[\frac{\mu(7\kappa - 1)}{\kappa} \right] \quad (7.27)$$

where $\theta_{elastic}^*$ is the critical impact angle above which sliding occurs throughout the impact, according to the analysis of Maw *et al.* (1976, 1981). Therefore, from Eq.(7.3), we have

$$f = \mu \quad (7.28)$$

Replacing f by μ in Eqs.(7.5), (7.11) and (7.14) yields

$$e_t = 1 - \frac{(1 + e_n)\mu}{\tan \theta} \quad (7.29)$$

$$\omega_r = -\frac{5\mu(1 + e_n)V_{ni}}{2R} \quad (7.30)$$

$$v_{tr} = V_{ti} - \frac{7}{2}\mu(1 + e_n)V_{ni} \quad (7.31)$$

Again, Eq.(7.31) can be rewritten in terms of dimensionless impact angle φ_i and dimensionless reflection angle at the contact patch φ_r as

$$\varphi_r = \varphi_i - \frac{7}{2}(1 + e_n) \quad (7.32)$$

It is clear that, for the impact throughout which sliding occurs, the rebound parameters of the sphere can be determined from Eqs.(7.29)-(7.32).

It was also shown that the contact deformation significantly affects the oblique impact behaviour for impacts that sliding does not persist the whole impact duration (see Fig. 2.11). For this case, it is still impossible to completely understand the impact behaviour in a simple and solvable analytical manner by avoiding the intensive numerical computation, although the tangential rebound velocity of the contact patch was obtained with complex numerical implementation by Maw *et al.* (1976, 1981).

In order to provide a better understanding of the oblique impact behaviour of deformable particles, finite element methods are employed here to investigate oblique impacts of elastic particles. The FE model used here was presented in Section 3.4 and the material properties were given in Table 3.5. The influence of plastic deformation will be discussed in next chapter. In this chapter, we focus on the impact of a rigid sphere with an elastic half-space, since, as discussed in Appendix D, the overall impact behaviour between the impact of the same substrate by a rigid and by an elastic sphere are similar, but the computing cost is significantly reduced if a rigid sphere is used. The influence of initial velocity conditions, friction coefficient and Poisson's ratio are investigated and detailed results are reported in the following sections.

7.3 Typical time evolutions of the impact parameters

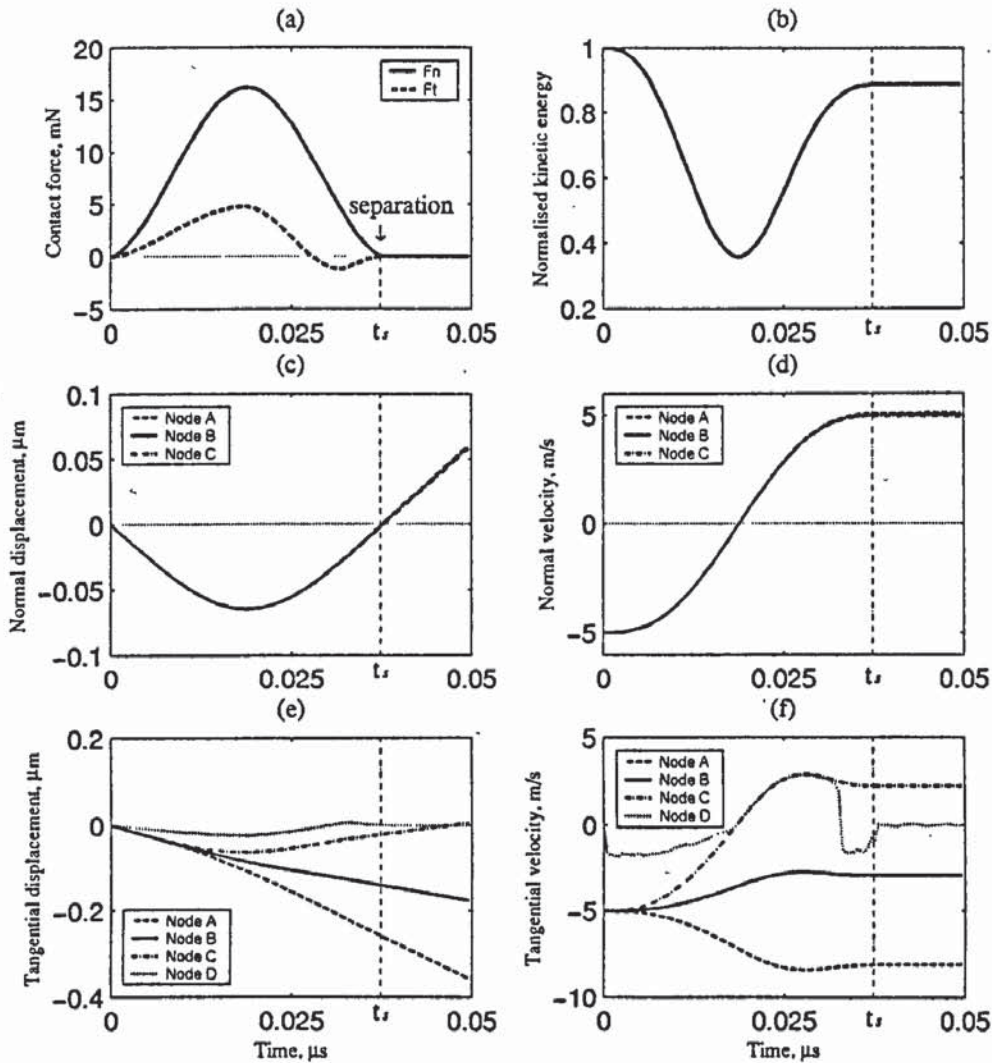


Fig. 7.1 Typical time evolutions of the impact parameters during the impact of a rigid sphere against an elastic substrate with $V_{ni} = 5.0\text{ m/s}$ at $\theta = 45^\circ$: (a) the contact forces; (b) the total kinetic energy; (c) Nodal displacements in normal direction; (d) nodal velocities in normal direction; (e) Nodal displacements in tangential direction and (f) nodal velocities in tangential direction.

The typical time evolutions of the impact parameters are shown in Fig. 7.1 for a rigid sphere impacting against an elastic substrate with an initial normal velocity of $V_{ni} = 5.0\text{ m/s}$ at an impact angle $\theta = 45^\circ$. It can be seen from Fig. 7.1a that the normal and tangential forces start with a value of zero at the beginning of the impact ($t=0.0\mu\text{s}$) and are simultaneously retarded to zero again at the end of the impact. Hence the interaction can be readily asserted to terminate at time $t = t_s$, where t_s is the instant when the sphere just separates from the substrate and the normal and tangential force just reach zero, as marked

in the figure. It is clear that the normal force completes a half cycle only whereas the tangential force nearly goes through a full cycle. This is owing to the difference of the tangential and normal contact stiffness (Johnson 1985). For a solid sphere with $\nu = 0.3$, the ratio of the tangential to normal frequencies of the contact resonance is 1.7 (Johnson 1985). This implies that if sliding does not occur throughout the impact the tangential force will complete almost a full cycle during the period when normal force finishes a half cycle; noting that this is true only for the impact during which sliding does not occur throughout the whole duration. Once sliding persists for the whole duration of impact, the tangential force F_t is always of magnitude μF_n (see Fig. 7.5).

Figure 7.1b shows the time history of the normalised kinetic energy $W(t)/W_i$, where $W(t)$ and W_i represent the total kinetic energy at arbitrary time t and at the beginning of the impact, respectively. It can be seen that the kinetic energy decreases to a minimum greater than zero during compression, then it increases due to the release of the strain energy stored in the elastic substrate during restitution. After the separation, the kinetic energy remains unaltered. It is clear that the kinetic energy is not recovered completely, which indicates some of the kinetic energy is dissipated. As will be shown later, the energy loss in the normal direction is negligible and the kinetic energy is mainly dissipated by friction over the contact interface.

Figures 7.1c and 7.1d present the time history of the normal displacements and velocities at nodes A (at top), B (at centre) and C (at bottom) of the sphere, respectively. As expected, no oscillation is observed for all curves and the curves are essentially merged together, because of the use of the rigid model for the sphere. At separation, the nodal displacements return to zero and the nodal velocity at the sphere centre is of the same absolute value as the initial normal velocity. This implies that there is no permanent displacement of the substrate and the initial kinetic energy in the normal direction is completely recovered. Small deviations between displacements and velocities at different nodes can be found at the end of the impact and after the rebound of the sphere, which is due to the rotation of the sphere.

Figures 7.1e and 7.1f show the time evolution of the tangential displacements and velocities at nodes A (at top), B (at centre) and C (at bottom) of the sphere, and node D, the initial contact point of the substrate, respectively. It is clear that the tangential response of different nodes within the sphere appears to deviate from each other. This is purely due to

the rotation of the sphere. In addition, the curves of displacement at nodes C and D do not coalesce, which implies that there are relative displacements between these two nodes and the sliding between the sphere and the substrate occurs during the impact. Furthermore, it is interesting to find that the curves of the nodal velocity at these two nodes (C and D) merge together within a certain period during the impact, which implies that, in this period, there is no sliding between the sphere and the substrate. In other words, the sphere slides over the substrate at the beginning of the impact, after a certain time, they stick together and finally it slides again. It is also clear that the tangential velocities of different nodes remain unchanged once the sphere separates from the substrate and the gap between node A and B is found to be equal to that between B and C, as expected. This implies that the sphere rotates with a constant rebound rotational (angular) velocity after the separation. The rebound rotational (angular) speed ω_r can hence be determined by

$$\omega_r = \frac{V_{ts}^A - V_{ts}^B}{R} \equiv \frac{V_{ts}^B - V_{ts}^C}{R} \quad (7.33)$$

where subscribe *ts* denotes the tangential velocity component at the separation and the superscripts A, B, C refer to nodes A, B, C, respectively. During the impact, the tangential velocity at the centre of the sphere (Node B) is not constant but significantly reduces. This illustrates that portions of the translational kinetic energy in the tangential direction are transformed, as will be discussed further in Section 7.7.

Typical evolutions of the relative displacements between nodes C and D are shown in Fig. 7.2 for impacts of a rigid sphere against an elastic substrate with a fixed initial normal velocity $V_{ni} = 5.0m/s$ at different angles. It can be seen that, for the impact at a small impact angle (15°), the relative displacement essentially remains unchanged at zero until the very end of the impact. This implies that there is no sliding between the sphere and the substrate at the beginning of the impact, but sliding occurs before the sphere bounds off from the substrate. For the impact at a large impact angle (65°), the relative displacement keeps increasing, which indicates that the sliding takes place throughout the impact. For the impact at an intermediate impact angle (45°), the relative displacement increases at the initial period of the impact, and then it remains unaltered over a certain period, finally decreases at the end of the impact. This illustrates that sliding occurs only at the beginning and end of the impact, and the directions of the sliding over these two periods are opposite.

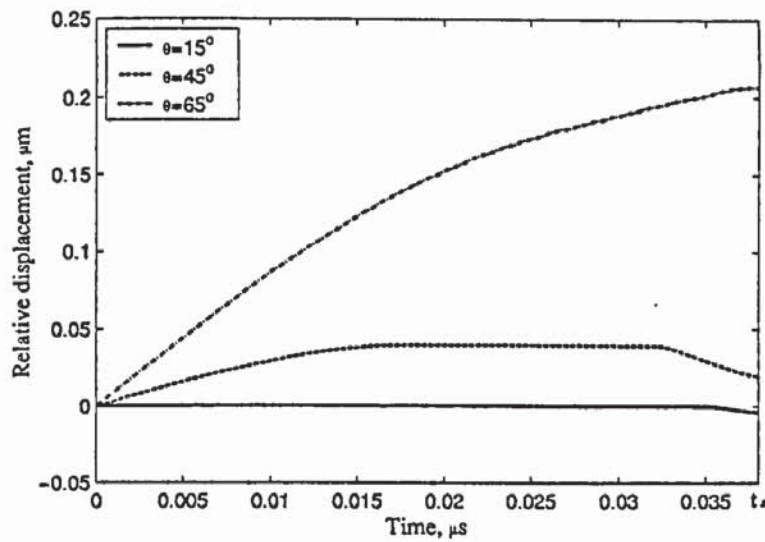


Fig. 7.2 The typical evolutions of the relative displacement between nodes C and D for the impacts of a rigid sphere against an elastic substrate at different angles with a fixed initial normal velocity $V_{ni} = 5.0m/s$.

7.4 Typical features of the interaction during oblique impact of elastic particles

Now let us consider the typical characteristics of the interaction during impact of a rigid sphere with an elastic substrate. Figure 7.3 shows the time evolutions of the normal contact force for impacts at various incident angles with a fixed initial normal velocity $V_{ni} = 5.0m/s$. It can be seen that the normal force responses are identical for different impact angles, which implies that the tangential response does not affect the response of the normal contact force. The corresponding normal force-displacement relationships are shown in Fig. 7.4, in which the result given by Hertz theory is also superimposed. It is clear that the force-displacement curves for the impacts at different impact angles merge together and FEA results are in good agreements with Hertz theory. This again indicates that the tangential response does not interfere with the normal impact behaviour.

Figure 7.5 presents the typical time histories of the tangential force for impacts at various incident angles with a fixed initial normal velocity $V_{ni} = 5.0m/s$, in which the solid thin lines represent the limiting condition $F_t = |\mu F_n|$. It can be seen that most of the evolution curves have two regions: one is the positive tangential force and the other is the negative tangential force. It is found that the negative tangential force region decreases with the increasing impact angle. When the incident angle is greater than 65° , the second period

disappears. The period of sliding, during which $F_t = |\mu F_n|$, is found to increase with the impact angle. For impacts at low impact angles ($<15^\circ$), sliding occurs only at the very end of the impact. For impacts at high impact angles ($>65^\circ$), sliding occurs during all the period. Similar results were obtained by Maw *et al.* (1976, 1981) and Thornton and Yin (1991).

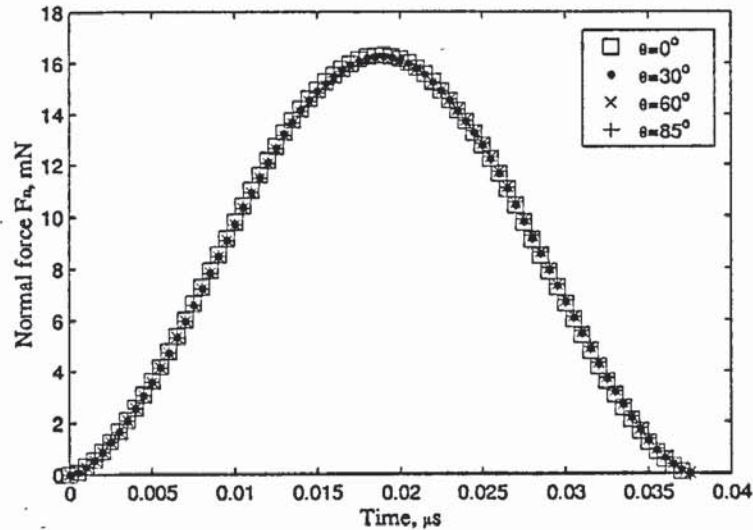


Fig. 7.3 The time evolutions of the normal contact force for the impacts of a rigid sphere against an elastic substrate at various impact angles with a fixed initial normal velocity $V_{ni} = 5.0\text{m/s}$.

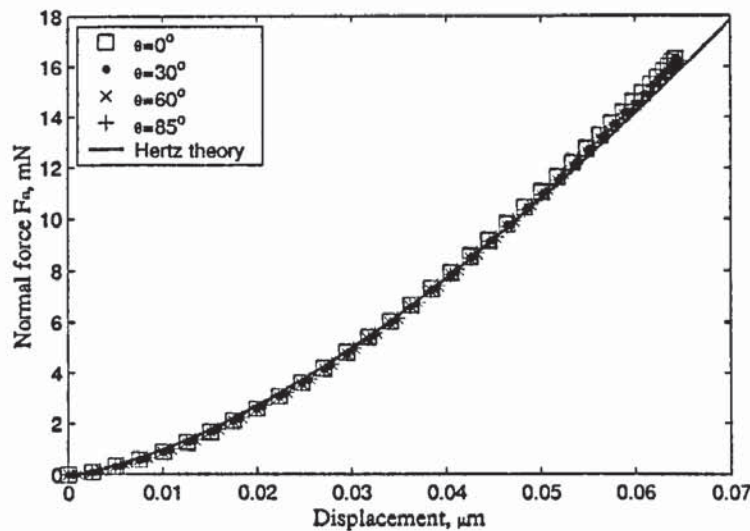


Fig. 7.4 Normal force-displacement relationships for the impacts of a rigid sphere against an elastic substrate at various angles with a fixed initial normal velocity $V_{ni} = 5.0\text{m/s}$.

Figure 7.6 shows the variation of tangential force with normal force for the impacts at various incident angles with a fixed initial normal velocity $V_{ni} = 5.0\text{m/s}$. It is clear that, at large impact angles ($>65^\circ$), the entire curve coincides with the line given by $F_t = \mu F_n$; at small impact angles, the curve does not reach the line $F_t = |\mu F_n|$ except at the very end of

the impact; and at intermediate impact angles, the curve coincides with the lines of $F_t = |\mu F_n|$ at both the beginning and the end of the impact. This implies that sliding takes place throughout the impact at large impact angles, while it occurs only at the very end of the impact at small impact angles and at both the beginning and the end of the impact at intermediate impact angles. These features are in good agreements with the observations of Maw *et al.* (1976; 1981) and Thornton and Yin (1991).

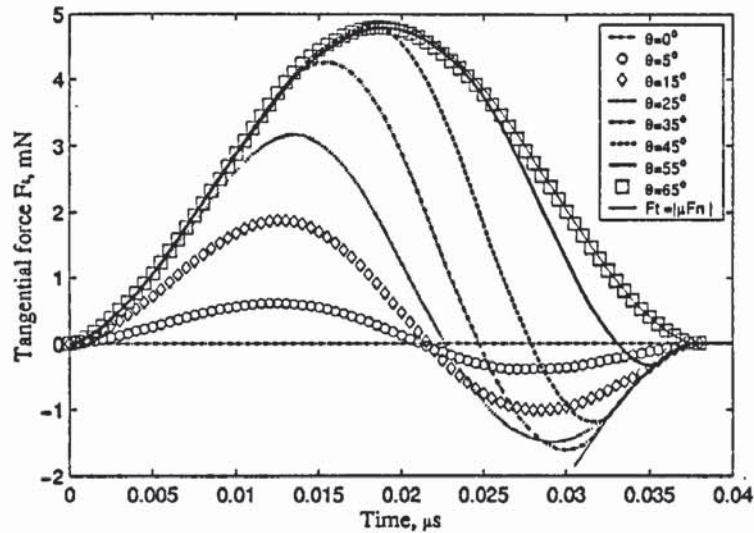


Fig. 7.5 The typical time histories of the tangential force for impacts of a rigid sphere with an elastic substrate at various impact angles with a fixed initial normal velocity $V_{ni} = 5.0m/s$.

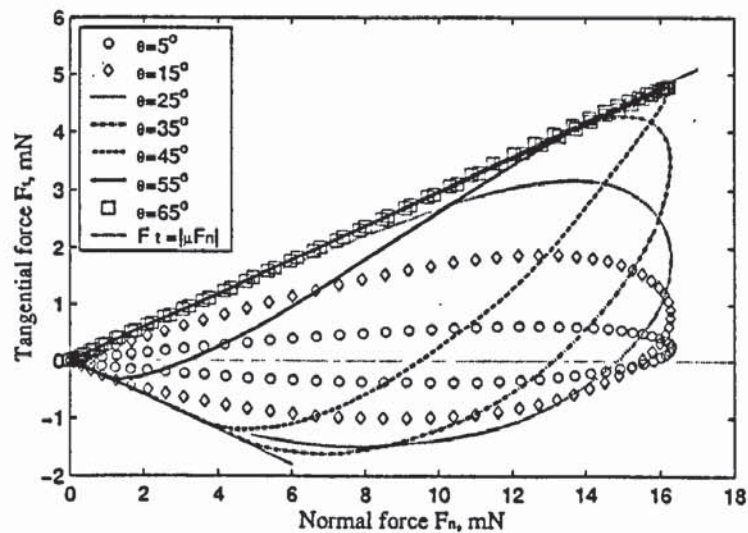


Fig. 7.6 The variation of tangential force with normal force for impacts of a rigid sphere with an elastic substrate at various impact angles with a fixed initial normal velocity $V_{ni} = 5.0m/s$.

The typical tangential force-displacement relationships for the impacts at various incident angles with a fixed initial normal velocity $V_{ni} = 5.0m/s$ are shown in Fig. 7.7. It is clear that when the impact angle is large enough (say, $>65^\circ$), the tangential force-displacement

curve never reverses, since sliding occurs throughout the impact. At small and intermediate impact angles, reversal of the tangential displacement with change in sign of the tangential force is a common phenomenon, as observed by Thornton and Yin (1991).

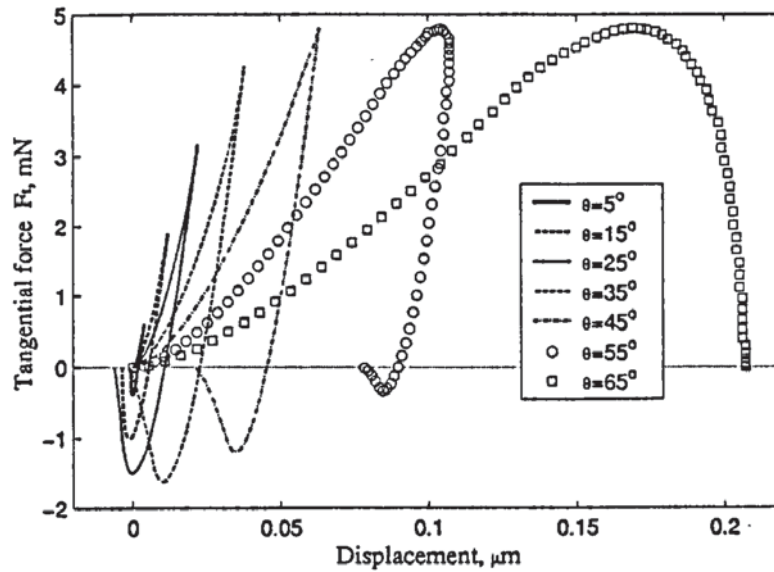


Fig. 7.7 The typical tangential force-displacement relationships for impacts of a rigid sphere with an elastic substrate at various impact angles with a fixed initial normal velocity $V_{ni} = 5.0\text{ m/s}$.

7.5 The peak tangential force

It is of general interest in engineering applications to determine the peak tangential force which varies with the impact angle, not only because wear rate of steel tubes is closely correlated with maximum tangential force (Ko 1985), but also because the resultant stress and strain distributions within the contacting body is dominated by both peak normal and peak tangential force. In this section, we shall consider the dependence of the peak tangential force upon the initial velocity conditions, the friction coefficient and Poisson's ratio.

7.5.1 The influence of initial velocity conditions

In order to investigate the peak tangential force at various initial velocity conditions, four groups of tests have been carried out with different initial velocity conditions prescribed either by keeping the initial speed constant at $V_i = 2.0\text{ m/s}$ and $V_i = 5.0\text{ m/s}$ or by fixing the initial normal velocity at $V_{ni} = 2.0\text{ m/s}$ and $V_{ni} = 5.0\text{ m/s}$.

Figure 7.8 shows the variation of the peak tangential force $F_{t,max}$ with impact angle for various impact cases, where the peak tangential force $F_{t,max}$ is determined by

$$F_{t,max} = \max(|F_t(t)|) \quad 0 \leq t \leq t_s \quad (7.34)$$

It is clear that two different trends are obtained with different approaches to specify the initial velocity. For the impacts with fixed initial speeds, the peak tangential force increases with increasing impact angle until a certain angle is reached; afterwards it reduces towards zero as the impact angle further increases. The critical impact angle for the peak tangential force reaching its maximum value is around 40° for two tests with different initial speeds, which implies that the critical impact angle is independent of the magnitude of the initial speed. This is in agreement with the experimental observations of Lewis and Rogers (1988). However, for the impacts with fixed initial normal velocities, the peak tangential force increases as the impact angle increases until it reaches a maximum value when the impact angle is around 45° , and remains essentially constant for larger impact angles. The decrease of the peak tangential force for the impacts with a fixed initial speed at high impact angles is due to the decrease in normal contact force.

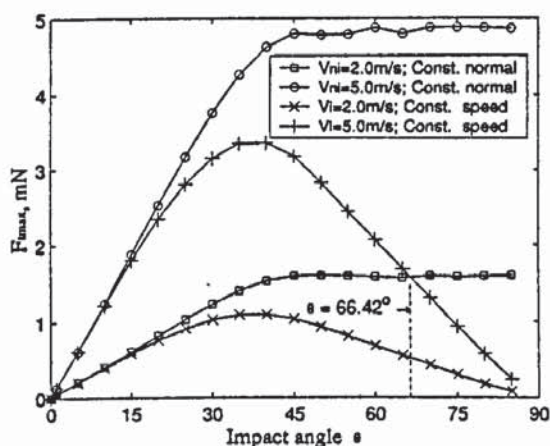


Fig. 7.8 The variation of the peak tangential force $F_{t,max}$ with impact angle θ for various impact cases.

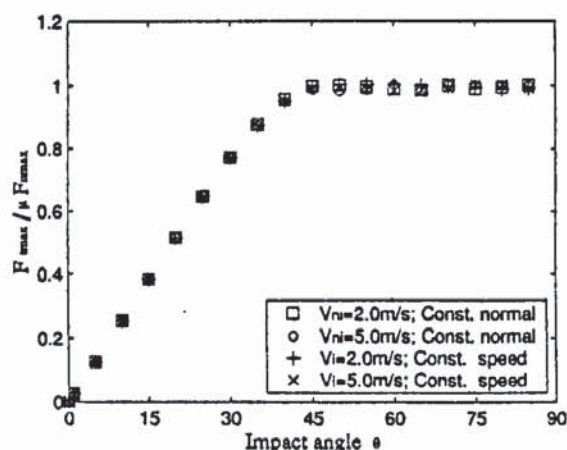


Fig. 7.9 The variation of $F_{t,max} / \mu F_{n,max}$ with impact angle θ for various impact cases.

In Fig. 7.8, consider the intersection of the curves for impacts at a fixed initial speed $V_i = 5.0m/s$ and those at a fixed initial normal velocity $V_{ni} = 2.0m/s$. For these two impact cases, the initial velocity conditions are identical when

$$\cos \theta = \frac{V_{ni}}{V_i} = \frac{2}{5} \quad (7.35)$$

which gives $\theta = 66.4^\circ$. Finite element analysis shows that the intersection occurs at the same impact angle as predicted by Eq.(7.35), which demonstrates the repeatability of the finite element analysis.

Figure 7.9 shows the variation of normalised peak tangential force $F_{t\max} / \mu F_{n\max}$ with impact angle for various impact cases considered, where the peak normal force $F_{n\max}$ is determined by

$$F_{n\max} = \max(|F_n(t)|) = F_n(t = t_c) \quad 0 \leq t \leq t_s \quad (7.36)$$

It is interesting to find that the results for the different impact cases coalesce. This implies that, at the same impact angle, the value of $F_{t\max} / \mu F_{n\max}$ is identical regardless of which approach being used to specify the initial velocity conditions and the magnitude of the initial velocity. Therefore, the peak tangential force relies on the peak normal contact force developed. It is also found that, when the impact angle is larger than around 45° , the value of $F_{t\max} / \mu F_{n\max}$ is constant at a value of unity. This is because, when the impact angle is larger than around 45° , the peak tangential force $F_{t\max}$ occurs simultaneously with the peak normal force $F_{n\max}$ and $F_{t\max} = \mu F_{n\max}$, as shown in Fig. 7.5.

7.5.2 The influence of friction

The effect of friction on the peak tangential force is considered in this section. It has been shown in the preceding section that the dependence of the peak tangential force upon the initial velocity conditions can be generalised by the normalised peak tangential force $F_{t\max} / \mu F_{n\max}$. Hence, only impacts with a fixed initial normal velocity of $V_{ni} = 5.0\text{m/s}$ are simulated to investigate the effect of friction. The material properties are given in Table 3.5, and the friction coefficient over the interface is assumed to be $\mu = 0.3, 0.5$ and 0.8 , respectively. For each test, the peak tangential and normal forces are determined from Eqs.(7.34) and (7.36), respectively.

Figure 7.10 shows the variation of $F_{t\max} / \mu F_{n\max}$ with the impact angle for impacts with different friction coefficients. It can be seen that, for all impact cases considered here, the value of $F_{t\max} / \mu F_{n\max}$ increases as the impact angle increases, until a certain impact angle is reached, then $F_{t\max} / \mu F_{n\max}$ remains constant at unity. It is found that the critical impact

angle increases as the friction coefficient increases. In Fig. 7.11 $F_{t \max} / \mu F_{n \max}$ is plotted against $\tan \theta / \mu$. It is clear that the curves for different coefficients of friction coalesce to form a master curve. In addition, when $\tan \theta / \mu \geq (7\kappa - 3) / \kappa$, $F_{t \max} / \mu F_{n \max}$ is essentially unity for all impacts with different friction coefficients. Hence, the critical angle $\bar{\theta}$ above which the peak tangential force $F_{t \max}$ will be equal to $\mu F_{n \max}$ is given by

$$\bar{\theta} = \tan^{-1} \left[\frac{\mu(7\kappa - 3)}{\kappa} \right] \quad (7.37)$$

The corresponding critical angles given by Eq.(7.37) for the impacts with different friction coefficients are listed in the third column of Table 7.1.

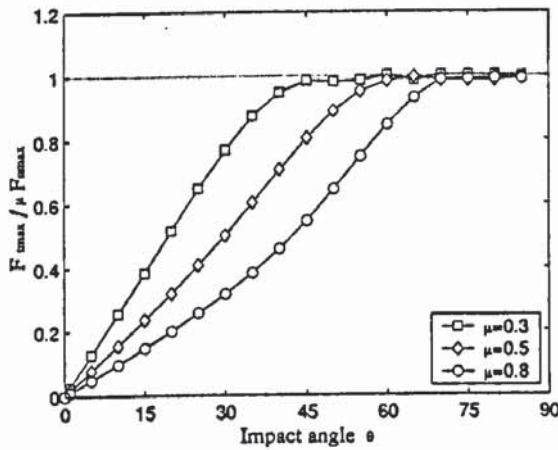


Fig. 7.10 The variation of $F_{t \max} / \mu F_{n \max}$ with the impact angle for impacts with different coefficients of friction.

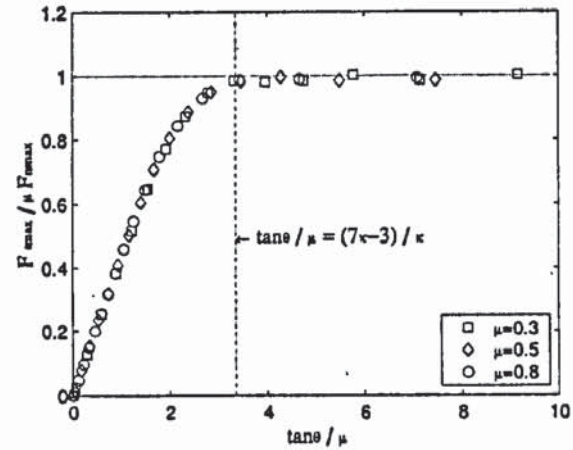


Fig. 7.11 The variation of $F_{t \max} / \mu F_{n \max}$ with $\tan \theta / \mu$ for impacts with different coefficients of friction.

Table 7.1 Critical angles for the impacts with different friction coefficients

Friction coefficient μ	κ	Critical impact angle for peak tangential force		Critical impact angle over which sliding occurs throughout the impact	
		$\bar{\theta}$ Eq.(7.37)	$\bar{\theta}_s$ Eq.(7.40)	$\theta_{elastic}^*$ Eq.(7.27)	θ_{rigid}^* Eq.(7.21)
0.3	0.8235	45.2°	46.4°	60.0°	64.5°
0.5	0.8235	59.2°	60.3°	70.9°	74.1°
0.8	0.8235	69.6°	70.3°	77.8°	79.9°

7.5.3 The influence of Poisson's ratio

It was shown by Johnson (1985) and Maw *et al.* (1976, 1981) that, during oblique impacts of elastic bodies, the impact behaviour is dependent on the initial ratio of the tangential to normal stiffness κ as defined in Eq.(2.82). For the impact of a rigid sphere with an elastic

substrate, κ depends on Poisson's ratio. It is hence necessary to study the effect of Poisson's ratio on the impact behaviour, for which different impact cases are considered with the material properties shown in Table 3.5 except that the Poisson's ratios are varied to be $\nu = 0.0, 0.3$ and 0.49 . Table 7.2 shows the corresponding values of κ for the Poisson's ratios considered. The initial velocity conditions for various impact angles are prescribed with a fixed initial normal velocity of $V_{ni} = 5.0 \text{ m/s}$.

Table 7.2 Critical angles for the impacts with different Poisson's ratios

Poisson's ratio ν	κ	Critical impact angle for peak tangential force		Critical impact angle over which sliding occurs throughout the impact	
		$\bar{\theta}$ Eq.(7.37)	$\bar{\theta}_s$ Eq.(7.40)	$\theta_{elastic}^*$ Eq.(7.27)	θ_{rigid}^* Eq.(7.21)
0.0	1.0	50.2°	46.4°	60.95°	64.54°
0.3	0.8235	45.2°	46.4°	60.02°	64.54°
0.49	0.6755	37.5°	46.4°	58.87°	64.54°

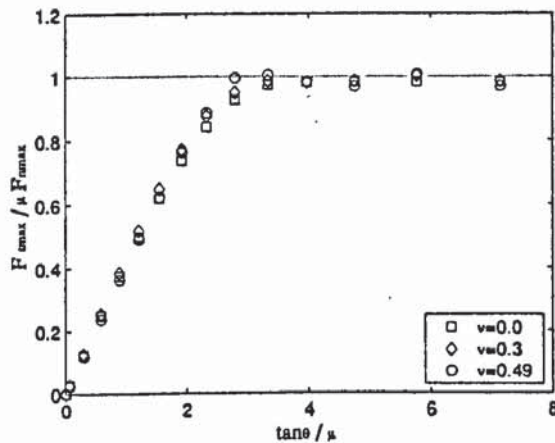


Fig. 7.12 The variation of $F_{t,max} / \mu F_{n,max}$ with $\tan \theta / \mu$ for the impacts with different Poisson's ratios.

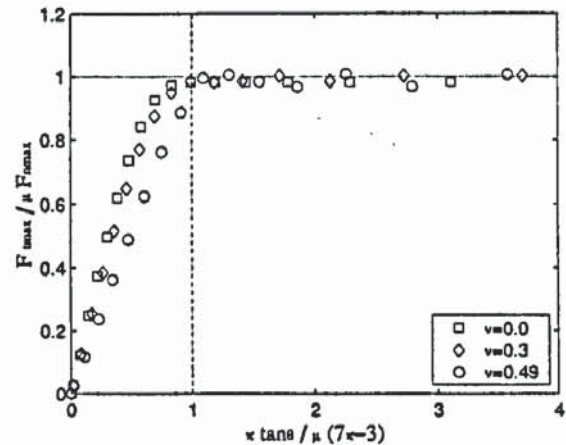


Fig. 7.13 The variation of $F_{t,max} / \mu F_{n,max}$ with $\kappa \tan \theta / \mu (7\kappa - 3)$ for the impacts with different Poisson's ratios.

Figure 7.12 shows the variation of $F_{t,max} / \mu F_{n,max}$ with normalised impact angle $\tan \theta / \mu$ for the impacts with various Poisson's ratios. It can be seen that the results of all the tests are similar. Nevertheless $F_{t,max} / \mu F_{n,max}$ appears to reach unity at a slightly smaller normalised impact angle $\tan \theta / \mu$ if Poisson's ratio is increased. A plot of $F_{t,max} / \mu F_{n,max}$ versus $\kappa \tan \theta / \mu (7\kappa - 3)$ shown in Fig. 7.13 reveals that, for impacts with different Poisson's ratios, $F_{t,max} / \mu F_{n,max}$ reaches unity when $\kappa \tan \bar{\theta} / \mu (7\kappa - 3) = 1$ as given by Eq.(7.37). This confirms the observations from the tests for the impacts with different friction coefficients as shown in Fig. 7.11. Note that in Fig. 7.13 $F_{t,max} / \mu F_{n,max} = 1$ does not occur at exactly $\kappa \tan \theta / \mu (7\kappa - 3) = 1$ for $\nu = 0.49$, this is due to numerical error when

Poisson's ratio approaches 0.5. It is concluded that the peak tangential force reaches its limit of $\mu F_{n \max}$ when Eq.(7.37) is satisfied. Furthermore, referring to Fig. 7.5, the peak tangential force will first reach this limit only when both the peak tangential and normal forces occur simultaneously at the instant of maximum compression, in which case sliding occurs throughout the whole period of compression. Stronge (1994) suggested that $F_{t \max} / \mu F_{n \max}$ could only be as large as unity if the peak tangential and normal forces occur simultaneously at

$$\tan \bar{\theta}_c \geq \mu m / m_t \quad (7.38)$$

where m is the mass of the sphere and m_t is given by Eq.(2.91). Using Eq.(2.91), Eq.(7.38) can be rewritten as

$$\tan \bar{\theta}_c \geq \mu \left(1 + \frac{1}{K^2} \right) \quad (7.39)$$

which indicates that the critical impact angle is independent of material properties. Since $K^2 = 2/5$ for a solid sphere, Eq.(7.39) becomes

$$\tan \bar{\theta}_c \geq \frac{7}{2} \mu \quad (7.40)$$

The critical impact angles given by Eq.(7.40) are listed in Tables.7.1 and 7.2 for different friction coefficients and Poisson's ratios, respectively. It is clear that Eq.(7.37) gives the similar results to Eq.(7.40) for the impacts with different values of μ . But Eq.(7.40) does not take account of the dependence of the critical impact angle on the material properties for impacts with different Poisson's ratios. Therefore, it suggests that Eq.(7.38) gives more representative criteria.

7.6 Impulse ratio

As discussed in section 7.2.1, the rebound behaviour of the particle during the elastic oblique impact can be well predicted as long as the impulse ratio is known. Therefore, it is instructive to investigate the dependence of the impulse ratio upon the impact angle, friction and material properties. For all tests reported in Section 7.5, the normal and tangential impulses are determined by integrating the normal and tangential forces over the duration of impact, respectively, and the impulse ratio is then determined from Eq.(7.3). The corresponding results are reported in this section.

7.6.1 The influence of initial velocity conditions

The variation of impulse ratio f with impact angle is shown in Fig. 7.14 for the four series of tests with different initial velocity conditions and the same friction coefficient of $\mu = 0.3$. It is clear that, at a same impact angle, the impulse ratios are identical for all tests considered. This indicates that the impulse ratio is independent of the magnitude of initial velocity for a certain impact angle. The impulse ratio is found to increase as the impact angle increases when the impact angle is less than around 60° , and is constant at a value equal to μ when the impact angle is larger than 60° . Referring to Fig. 7.5, the impulse ratio can only be as large as the friction coefficient μ when sliding occurs throughout the impact, for which $F_t = \mu F_n$ at any instant during the impact. This implies that sliding occurs throughout the impact when the impact angle is larger than 60° for all four series of tests considered here. This is consistent with the analysis of Maw *et al.* (1976, 1981), who showed that sliding occurs throughout the impact when the impact angle is larger than $\theta_{elastic}^* (= \arctan[\mu(7\kappa - 1)/\kappa])$. For the four series of tests considered here, $\theta_{elastic}^* = 60.02^\circ$.

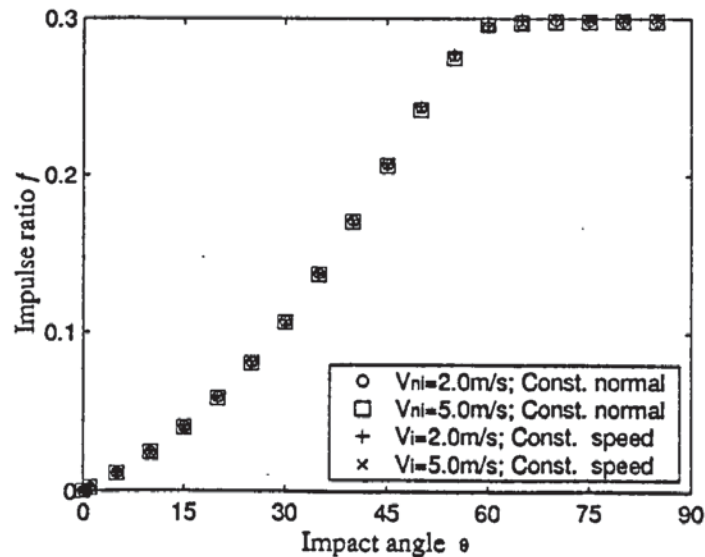


Fig. 7.14 The variation of impulse ratio f with impact angle θ for impacts with different initial velocity conditions

7.6.2 The influence of friction

The impulse ratios for impacts with different friction coefficients are shown in Fig. 7.15, in which the normalised impulse ratio f/μ is plotted against normalised impact angle

$\tan \theta / \mu$. It can be seen that the individual curves coalesce into a single curve. This implies that the dependence of impulse ratio upon the friction is governed by the normalised impact angle $\tan \theta / \mu$. It is also found from Fig. 7.15 that when $\tan \theta / \mu \geq (7\kappa - 1) / \kappa$, the impulse ratio is equal to the friction coefficient μ and sliding occurs throughout the impact. This is again in excellent agreement with the prediction of Maw *et al.* (1976, 1981).

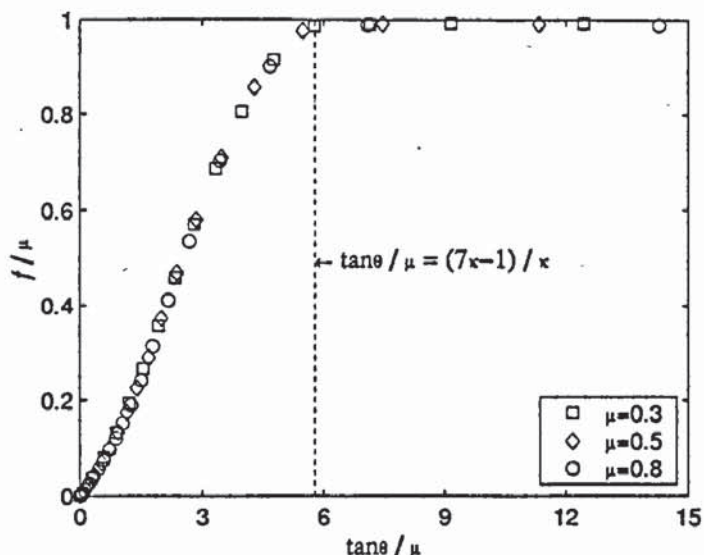


Fig. 7.15 The variation of f / μ with normalised impact angle $\tan \theta / \mu$ for impacts with different friction coefficients.

7.6.3 The influence of Poisson's ratio

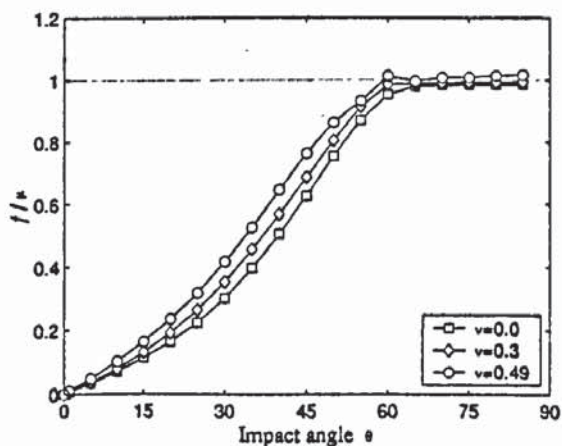


Fig. 7.16 The variation of f / μ with normalised impact angle $\tan \theta / \mu$ for impacts with different Poisson's ratios ($\mu = 0.3$).

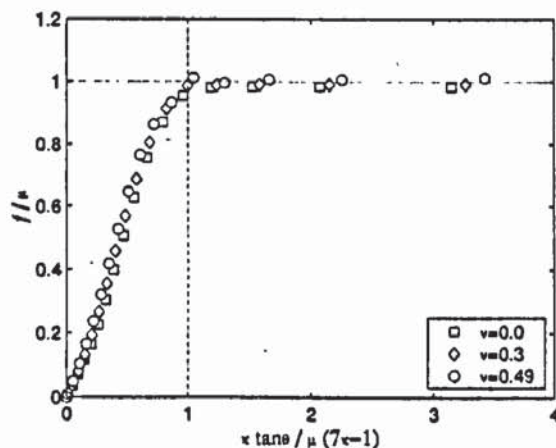


Fig. 7.17 The variation of f / μ with $\kappa \tan \theta / \mu (7\kappa - 1)$ for impacts with different Poisson's ratios ($\mu = 0.3$).

Figure 7.16 shows the normalised impulse ratio f / μ at various impact angles for impacts

with different Poisson's ratios ($\nu = 0.0; 0.3; 0.49$). It is clear that the impulse ratio increases with impact angle until a critical angle is reached, above which f/μ essentially equals to unity. This indicates that sliding persists during the whole duration of the impact. At the same impact angle, a higher value of f/μ is obtained for the impact with a higher Poisson's ratio. Nevertheless, a plot of f/μ against $\kappa \tan\theta/\mu(7\kappa-1)$ shown in Fig. 7.17 reveals that, for impacts with different Poisson's ratios, f/μ is essentially close to unity when $\kappa \tan\theta/\mu(7\kappa-1)$ is larger than unity. Since $f = \mu$ means that sliding occurs throughout the impact by definition (see Eq.(7.3)), Figure 7.17 also indicates that sliding will occur throughout the impact for impacts with different Poisson's ratios if the impact angle satisfies $\tan\theta/\mu \geq (7\kappa-1)/\kappa$, as suggested by Maw *et al.* (1976, 1981).

7.7 Coefficient of restitution and kinetic energy loss

Coefficients of restitution are commonly used to describe the change in velocities before and after the impact, and account for the change in kinetic energies during the impact. For oblique impact of particles, three coefficients of restitution are defined: (1) a normal coefficient of restitution e_n defined by Eq.(2.17) which denotes the change in normal velocity of the velocities at the end and beginning of the impact; (2) a tangential coefficient of restitution defined in Eq.(7.1), which represents the change of the velocity of the centroid of the particle in the tangential direction; and (3) a total coefficient of restitution that is defined in Eq.(7.2). It has been shown in Eq.(7.2) that the total coefficient of restitution is actually a function of the normal and tangential coefficients of restitution and the impact angle. According to these three coefficients of restitution, the change in kinetic energies can be estimated in the normal direction, tangential direction and as a whole, respectively.

In this section, the FEA results for the coefficients of restitution during impacts with different initial velocity conditions, friction coefficients and Poisson's ratios are reported. For the impact of a rigid sphere with an elastic substrate, both the normal and tangential components of the velocity of the sphere centre remain constant once the sphere bounds off (see Fig. 7.1). Therefore, the normal and tangential coefficients of restitution are calculated from Eqs.(2.17) and (7.1) in terms of the corresponding velocity components of the sphere centre. The total coefficient of restitution is determined from the square root of the ratio of

total linear rebound kinetic energy to the initial kinetic energy, i.e.,

$$e = \sqrt{\frac{W_r}{W_i}} \quad (7.41)$$

Since the kinetic energy is also constant once the sphere rebounds (see Fig. 7.1b), the value of kinetic energy at the separation is used to calculate the total coefficient of restitution.

7.7.1 The influence of initial velocity conditions

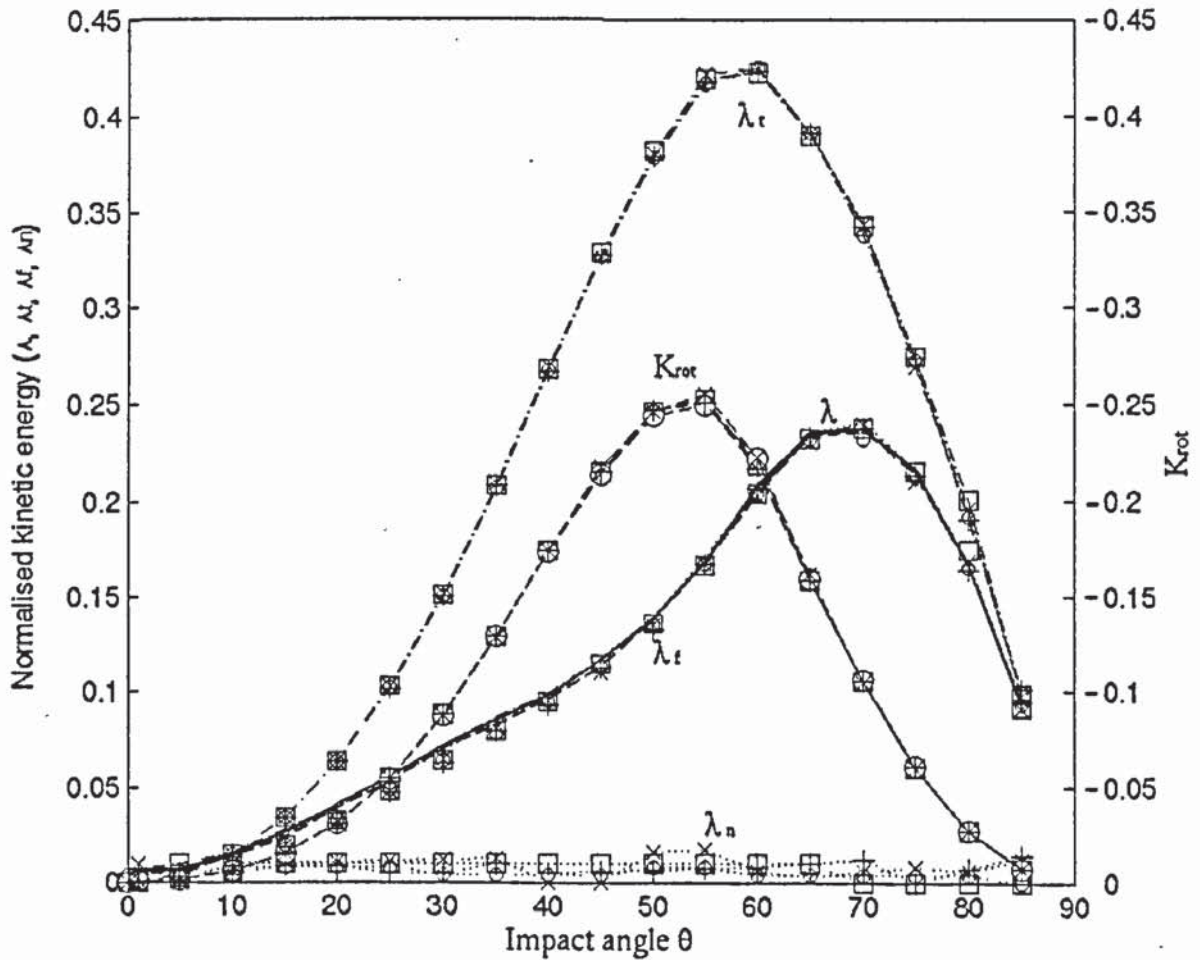


Fig. 7.18 The change in normalised kinetic energies at various impact angles for impacts with different initial velocity conditions.

Figure 7.18 shows the change in the normalised kinetic energies at various impact angles for impacts with different initial velocity conditions, in which all kinetic energies are normalised by the initial kinetic energy $W_i (=0.5mV_i^2)$, where m is the mass of the sphere. The total normalised kinetic energy loss λ is defined by Eq.(B.1) and is represented by lines only. The normalised linear kinetic energy losses in normal and tangential directions, λ_n and λ_t , are defined by

$$\lambda_n = \frac{W_{ni} - W_{nr}}{W_i} = \frac{\frac{1}{2}mV_{ni}^2 - \frac{1}{2}mV_{nr}^2}{\frac{1}{2}mV_i^2} = \frac{V_{ni}^2 - V_{nr}^2}{V_{ni}^2 / \cos^2 \theta} = \left(1 - \frac{V_{nr}^2}{V_{ni}^2}\right) \cos^2 \theta = (1 - e_n^2) \cos^2 \theta \quad (7.42)$$

$$\lambda_t = \frac{W_{ti} - W_{tr}}{W_i} = \frac{\frac{1}{2}mV_{ti}^2 - \frac{1}{2}mV_{tr}^2}{\frac{1}{2}mV_i^2} = \frac{V_{ti}^2 - V_{tr}^2}{V_{ti}^2 / \sin^2 \theta} = \left(1 - \frac{V_{tr}^2}{V_{ti}^2}\right) \sin^2 \theta = (1 - e_t^2) \cos^2 \theta \quad (7.43)$$

and are denoted by symbols with superimposed dotted lines and dashed dot lines, respectively. In Eqs.(7.42) and (7.43), W denotes the kinetic energy, the first subscripts n and t denote the normal and tangential components, and the second subscripts i and r denote the corresponding initial and rebound values, respectively. The normalised rotational kinetic energy K_{rot} is defined as

$$K_{rot} = \frac{W_{ri} - W_{rr}}{W_i} = \frac{\frac{1}{2}I\omega_i^2 - \frac{1}{2}I\omega_r^2}{\frac{1}{2}mV_i^2} \quad (7.44)$$

Since $\omega_i = 0$ is prescribed in all the simulations, Eq.(7.44) reduces to

$$K_{rot} = -\frac{I\omega_r^2}{mV_i^2} \quad (7.45)$$

The normalised rotational kinetic energy K_{rot} is represented by symbols with dashed lines in Fig. 7.18.

It can be seen from Fig. 7.18 that the impacts with different initial velocity conditions produce essentially identical results for the variations of normalised kinetic energies with impact angle. The normalised total kinetic energy loss increases with increasing impact angle and reaches its maximum at about 70° and then decreases with further increase in impact angles. The kinetic energy losses in the normal direction at various impact angles are very small (less than 1%) and can be ignored. The change in normalised tangential kinetic energy are more significant and it is generally higher than the total normalised kinetic energy losses, which is not only due to some kinetic energies being dissipated by friction but also due to a portion of tangential kinetic energy being transformed into rotational kinetic energy. In addition, as the impact angle increases, the change in tangential kinetic energy increases, and reaches its maximum at around 60° ; then it decreases as the impact angle increases further. The rotational kinetic energy is also found to increase with the increase of impact angle and the maximum value of rotation kinetic energy is reached at around 55° ; afterwards, it decreases as the impact angle decreases. The

difference between the change in tangential kinetic energy λ_t and the gained rotational kinetic energy W_{rot} is the energy dissipated by friction. Hence, we may define

$$\lambda_f = \lambda_t - K_{rot} \quad (7.46)$$

which is presented by symbols only in Fig. 7.18. It is clear that λ_f is very close to the total kinetic energy loss λ . Therefore, it may be concluded that, during elastic oblique impacts, the kinetic energy is mainly dissipated by friction (only a very small amount is dissipated by stress wave propagation). Furthermore, the linear kinetic energy in tangential direction is significantly reduced due to the friction force, which not only does frictional work but also transfers the kinetic energy into the rotational kinetic energy. The transformation of kinetic energy during oblique impacts of elastic particles is illustrated in Fig. 7.19.

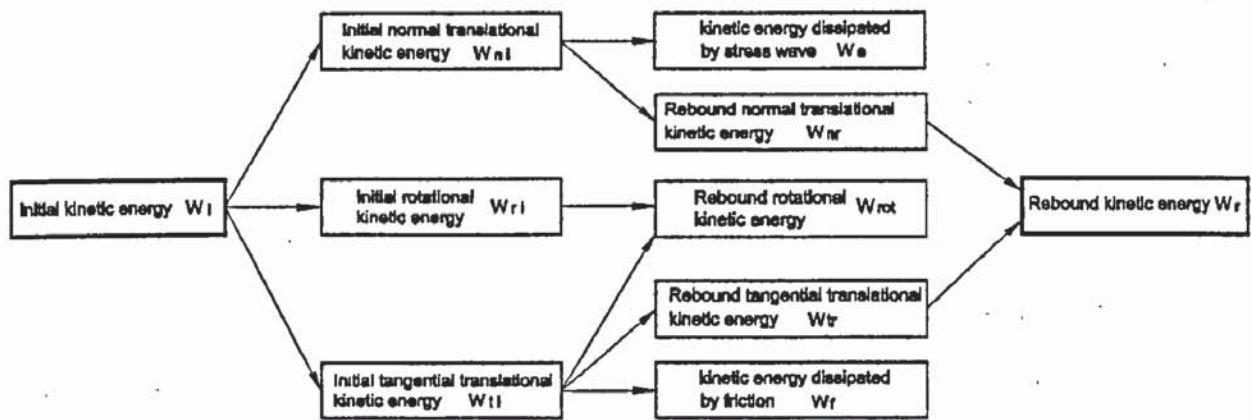


Fig. 7.19 Transformation of kinetic energy during the oblique impact of elastic particles.

Since the frictional force developed during the oblique impact is mainly responsible for the transformation of kinetic energy and the energy loss in the normal direction is generally negligible, it is necessary to investigate how the kinetic energy in tangential direction is transformed. Figure 7.20 shows the transformation of initial tangential kinetic energy at various impact angles during the impact of a rigid sphere against an elastic substrate with a fixed initial normal velocity of $V_{ni} = 5.0m/s$, and the corresponding results for the impacts with a fixed initial speed of $V_i = 5.0m/s$ is shown in Fig. 7.21. For both cases, the increase of the impact angle is accompanied by the increase of the tangential velocity and the initial linear kinetic energy in the tangential direction.

For the impacts at high impact angles, in which sliding occurs throughout the impact, the tangential impulse is proportional to the normal impulse. Furthermore, the rebound angular velocity depends proportionally upon the normal initial velocity (see Eq.(7.11)). Therefore,

for impacts with a fixed initial normal velocity, the rotational kinetic energy remains constant and only the friction work increases with incident angle. Moreover, the initial tangential translational kinetic energy, which is proportional to $\tan^2 \theta$, increases much faster with impact angle than the friction work that is proportional to $\tan \theta$. Thus, the

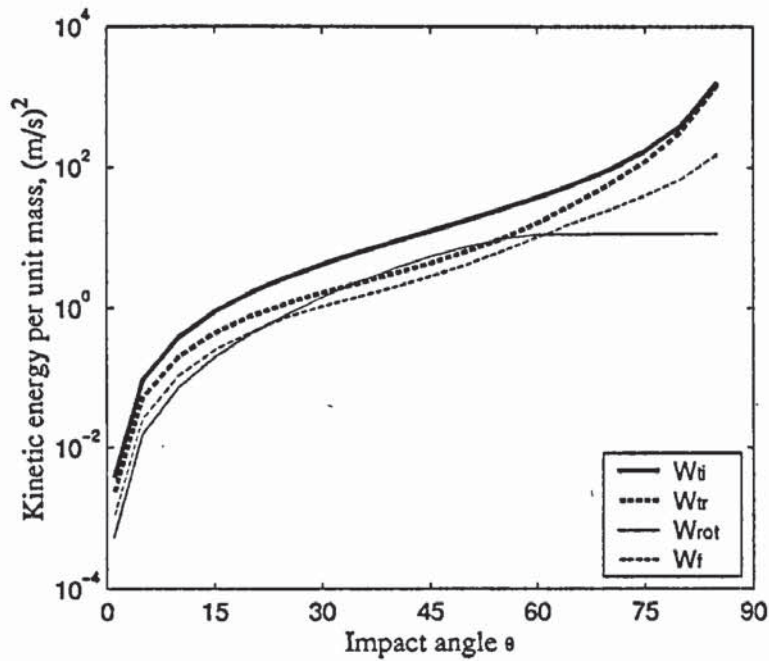


Fig. 7.20 Transformation of initial linear kinetic energy in the tangential direction at various impact angles during the impact of a rigid sphere against an elastic substrate with a fixed initial normal velocity of $V_{ni} = 5.0 \text{ m/s}$ ($\mu = 0.3$).

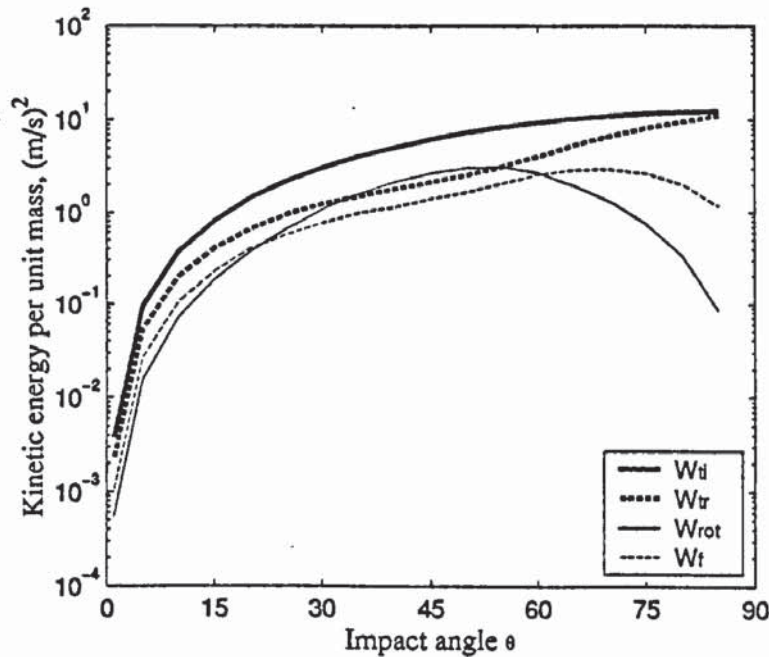


Fig. 7.21 Transformation of initial linear kinetic energy in the tangential direction at various impact angles during the impact of a rigid sphere against an elastic substrate with a fixed initial speed of $V_i = 5.0 \text{ m/s}$ ($\mu = 0.3$).

increase of the initial tangential translational kinetic energy is much greater than the increase of the kinetic energy transformed (including the rotational kinetic energy gained and the friction work dissipated). When the impact angle is close to 90° , the loss in tangential translational kinetic energy is negligible compared to the very high initial tangential translational kinetic energy and it is expected that the tangential coefficient of restitution would be almost equal to unity. For the impacts with a fixed initial speed, the normal velocity decreases with the increasing impact angle. Hence, the rotational kinetic energy, which is proportional to $\cos^2 \theta$, significantly reduces as the impact angle approaches 90° . In addition, the frictional work also decreases with the impact angle as a result of the decrease in the frictional force. The total kinetic energies transformed decrease with the increase of impact angle, although the initial tangential translational kinetic energy increases as the impact angle increases. As a result, the ratio of the rebound tangential translational kinetic energy to the initial one increases with the impact angle. Again, when the impact angle is close to 90° , the loss in tangential translational kinetic energy is negligible compared to the very large initial tangential translational kinetic energy and hence the tangential coefficient of restitution tends to unity.

For the impacts at low and intermediate impact angles, with either a fixed initial speed or a fixed initial normal velocity, in which sliding does not occur throughout the impact, the maximum friction force increases with the incident angle (see Fig. 7.8) and the corresponding frictional work and rotational kinetic energy also increase with impact angle. It is shown in Figs. 7.20 and 7.21 that the increasing rate of rotational kinetic energy with impact angle is higher than the increasing rate of initial tangential translational kinetic energy when the impact angle is less than 45° . This implies that the tangential coefficient of restitution would decrease with the increase of the impact angle and it would reach its minimum at around 45° for $\mu = 0.3$.

Figure 7.22 shows the change in normalised tangential kinetic energy at various impact angles for impacts with different initial velocity conditions, in which all kinetic energies are normalised by the initial tangential translational kinetic energy W_{ii} . The normalised total tangential translational kinetic energy loss is

$$\lambda'_t = \frac{W_{ii} - W_{tr}}{W_{ii}} = 1 - \frac{W_{tr}}{W_{ii}} = 1 - \frac{V_{tr}^2}{V_{ii}^2} \quad (7.47)$$

and the normalised rotational kinetic energy is given by

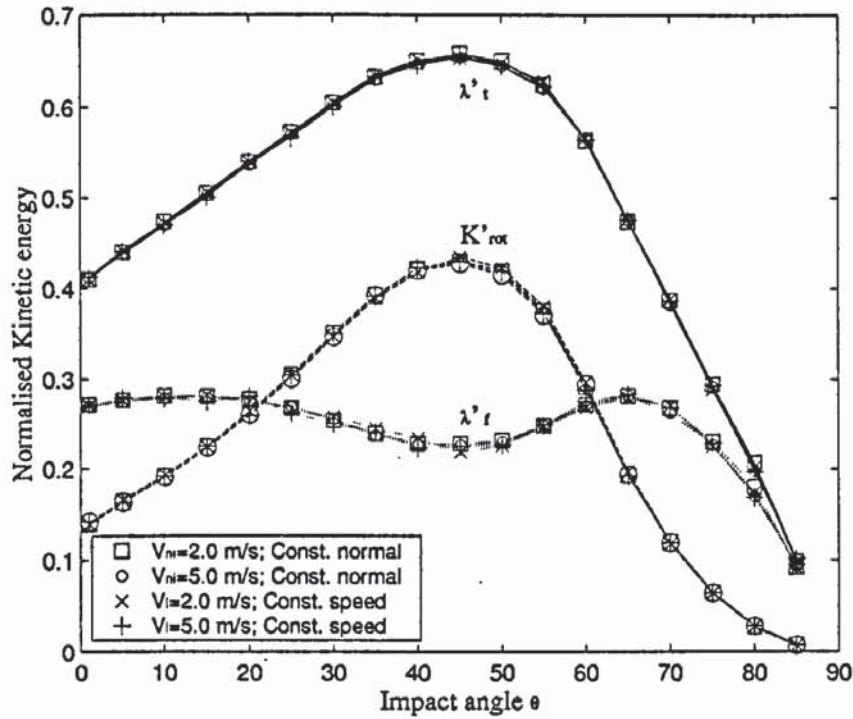


Fig. 7.22 The change in tangential kinetic energies at various impact angle for the impacts with different initial velocity conditions.

$$K'_{rot} = \frac{W_{rr}}{W_{ii}} = -\frac{\frac{1}{2}I\omega_r^2}{\frac{1}{2}mV_{ii}^2} \quad (7.48)$$

and the normalised kinetic energy dissipated by friction is obtained from

$$\lambda'_f = \frac{W_f}{W_{ii}} = \frac{W_{ii} - W_{ir} - W_{rr}}{W_{ii}} = \bar{\lambda}_t - \bar{K}_{rot} \quad (7.49)$$

It can be seen from Fig. 7.22 that the same results are obtained for impacts with different initial velocity conditions. Moreover, even at very small impact angles (say $\theta = 1^\circ$), a certain amount of rotational kinetic energy is gained and a certain portion of kinetic energy is dissipated by friction, which leads to a significant reduction in tangential translational kinetic energy. It is found that, when the impact angle is less than the critical angle for the sliding occurring throughout the impact (*c.a.* 60°), the normalised translational kinetic energy dissipated by friction is essentially unchanged at around 0.27. If sliding occurs throughout the impact, the normalised translational kinetic energy dissipated by friction decreases towards zero as the impact angle approaches 90° . The normalised rotational kinetic energy gained during the impact is found to increase as the impact angle increases, and reaches its maximum value at around 45° , then it reduces to zero when the impact angle approaches 90° . It is clear that at small impact angles (say $\theta \leq 20^\circ$), the kinetic energy dissipated by friction is more than the gained rotational kinetic energy, and this also occurs at high impact angles (say $\theta \geq 60^\circ$). However, in between, more tangential kinetic

energy is transformed into the rotational kinetic energy than dissipated by friction. Consequently, the change in tangential translational kinetic energy is found to increase from a certain value at small impact angle to its maximum at around 45° , then decreases towards zero as the impact angle approaches 90° .

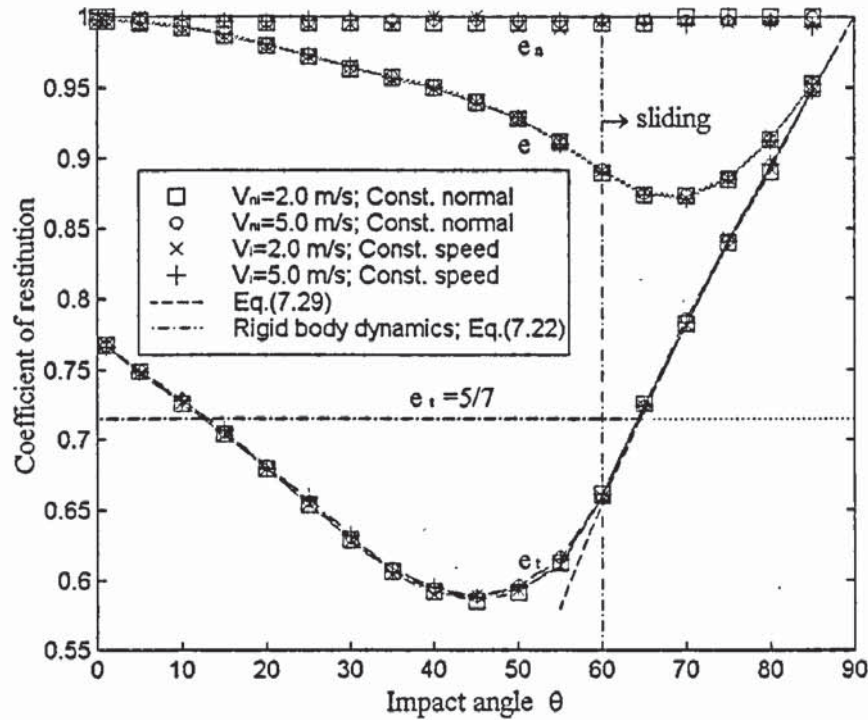


Fig. 7.23 The coefficients of restitution at various impact angle for the impacts with different initial velocity conditions.

Figure 7.23 shows the coefficients of restitution at various impact angles for the impacts with different initial velocity conditions. We also superimpose the results for the tangential coefficient of restitution given by Eqs.(7.22) and (7.29). It is clear that, for impacts in which sliding occurs throughout the impact, the FEA results are in excellent agreement with the results predicted by Maw *et al.* (1976, 1981). Classical rigid body dynamics overestimates the critical impact angle, above which sliding persists for the whole impact duration, and cannot accurately predict the tangential coefficient of restitution for impacts that sliding does not occur throughout the impact. This is primarily due to neglect of the contact deformation in classical rigid body dynamics. At large impact angles, the whole contact region slides throughout the impact and the effect of tangential stiffness on the rebound kinematics becomes negligible. Therefore, classical rigid body dynamics gives the same results as those given by both the elastic model and present finite element analysis. It is also demonstrated in Fig. 7.23 that the total coefficient of restitution e is dominated by the normal coefficient of restitution e_n at small impact angles; but by the tangential coefficient of restitution e_t at large impact angles (see Eq.(7.2)).

7.7.2 The influence of friction

Figure 7.24 shows the effect of friction on the coefficients of restitution. It can be seen that the values of e_n are close to unity for all cases. This indicates that neither the energy loss due to stress wave propagation and friction nor the effect of tangential response on the normal coefficient of restitution is significant. The tangential coefficient of restitution e_t shifts rightwards with increasing friction coefficient. When the impact angle approaches zero, the tangential coefficients of restitution for impacts with different friction coefficients are found to lie between 0.75 and 0.80. In addition, the minimum values of the tangential coefficient of restitution occur at higher impact angles when the friction coefficient increases. The minimum tangential coefficients of restitution at different impact angles are all very close to a value of 0.58. The tangential coefficients of restitution in Fig. 7.24 are re-plotted against the normalised impact angle $\tan\theta/\mu$ in Fig. 7.25, which shows that the curves coalesce to form a single curve with a minimum of 0.58 at $\tan\theta/\mu = (7\kappa - 3)/\kappa$, as observed by Ning (1995).

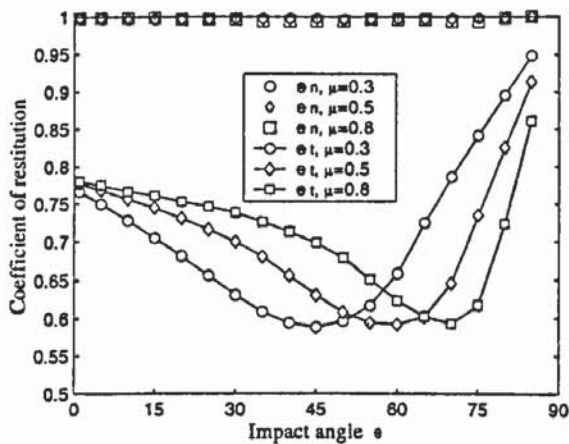


Fig. 7.24 The coefficients of restitution at various impact angles for impacts with different friction coefficients.

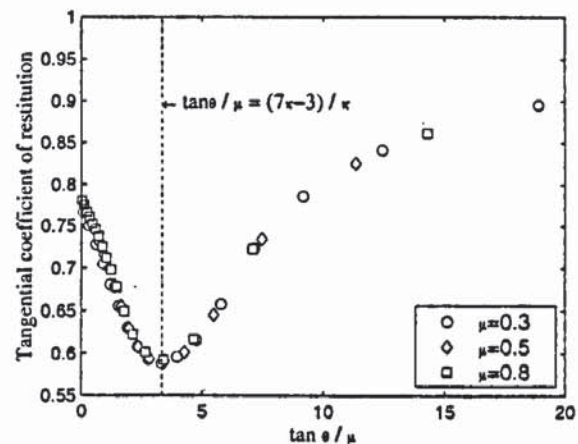


Fig. 7.25 The variation of tangential coefficients of restitution with normalised impact angle $\tan\theta/\mu$ for impacts with different friction coefficients.

7.7.3 The influence of Poisson's ratio

Figure 7.26 shows the effect of Poisson's ratio on the coefficients of restitution. It is clear that the normal coefficients of restitution e_n are again close to unity. The tangential coefficients of restitution for impacts with different Poisson's ratios merge together at large impact angles, while at small impact angles, the higher the Poisson's ratio, the smaller the

tangential coefficient of restitution. This corresponds to the analysis in Section 7.6.3. It has been shown that sliding occurs throughout the impact and $f = \mu$ if the impact angle satisfies $\kappa \tan \theta / \mu(7\kappa - 1) \geq 1$ (see Fig. 7.17). In this case, the tangential coefficient of restitution is only dependent on the impact angle (see Eq.(7.5)). At small impact angles, a slightly higher impulse ratio is produced during the impact with a higher Poisson's ratio owing to larger lateral (tangential) expansion. Consequently, a smaller tangential coefficient of restitution is given for impacts at the same impact angle with $e_n = 1$, according to Eq.(7.5). This clearly demonstrates that the effect of tangential stiffness is negligible for impacts at large impact angles during sliding occurs throughout the impact; but the tangential stiffness plays an important role in impacts at small impact angles.

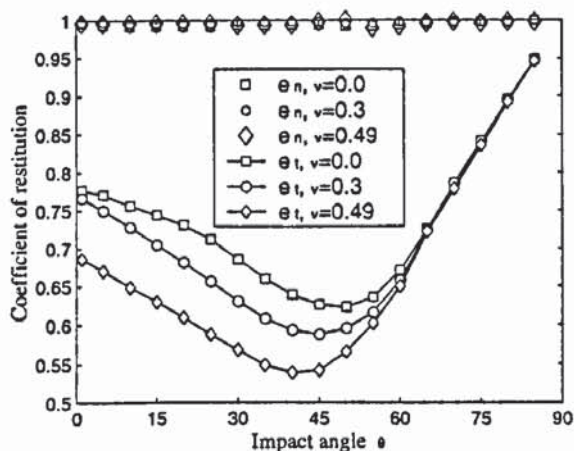


Fig. 7.26 The coefficients of restitution at various impact angles for impacts with different Poisson's ratios.

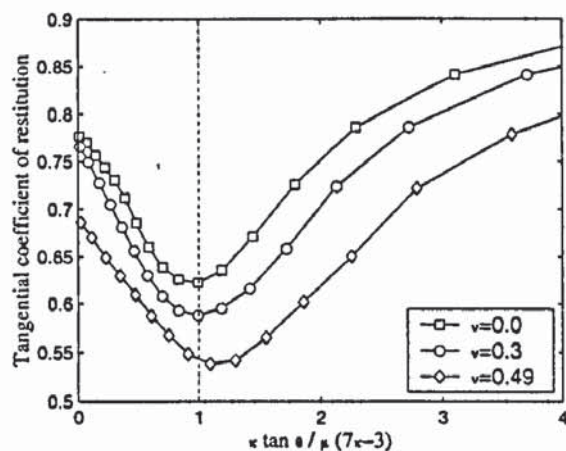


Fig. 7.27 The variation of the tangential coefficients of restitution with $\kappa \tan \theta / \mu(7\kappa - 3)$ for impacts with different friction coefficients.

It can also be seen from Fig. 7.26 that the impact angle at which the tangential coefficient of restitution has a minimum value increases as the Poisson's ratio decreases, so does the minimum value of the tangential coefficient of restitution. The tangential coefficients of restitution are plotted against $\kappa \tan \theta / \mu(7\kappa - 3)$ in Fig. 7.27. It is found that the tangential coefficient of restitution reaches its minimum value when $\kappa \tan \theta / \mu(7\kappa - 3) = 1$. This corresponds to the results obtained from the impacts with different friction coefficients (see Fig. 7.25) and the analysis of Ning (1995). It is hence concluded that the tangential coefficient of restitution reaches its minimum value at $\kappa \tan \theta / \mu(7\kappa - 3) = 1$. Comparing with Figs. 7.11 and 7.13, we find that the tangential coefficient of restitution reaches its minimum value at the same impact angle as the peak tangential force first reaches its limit μF_n .

7.8 Reflection angle of the contact patch

It has been shown in the preceding section that the tangential stiffness has a significant influence on the oblique impact behaviour at small impact angles for which sliding does not occur throughout the impact; but is negligible when the impact angle is so large that sliding occurs throughout the impact. To further study the effect of tangential stiffness on the rebound behaviour of the particles, it is worth looking at the reflection angle at the contact patch. In this section, the effects of initial velocity conditions, friction and Poisson's ratio on the reflection angle of the contact patch are investigated.

7.8.1 The influence of initial velocity conditions

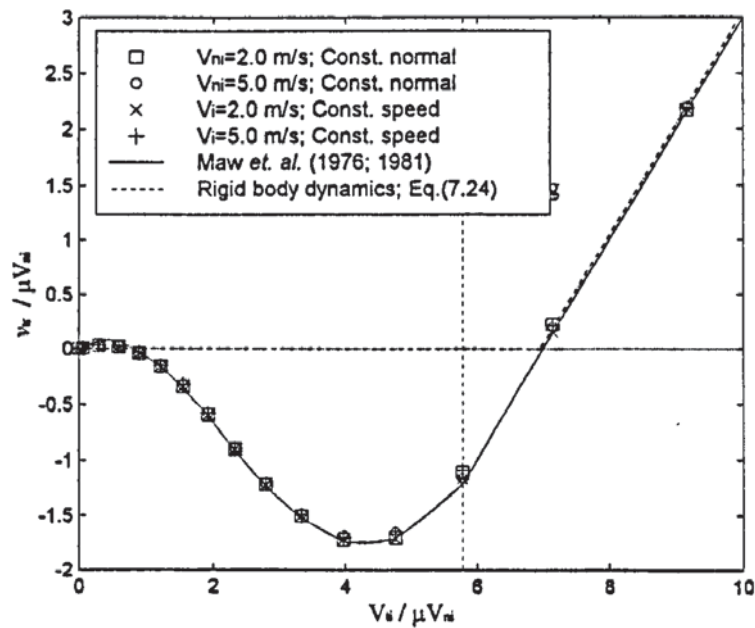


Fig. 7.28 The variation of normalised reflection angle of the contact patch $v_{tr} / \mu V_{ni}$ with normalised impact angle $V_{ti} / \mu V_{ni}$ for impacts with different initial velocity conditions.

Figure 7.28 shows the variation of the normalised reflection angle of the contact patch ϕ_r with normalised impact angle ϕ_i for impacts with different initial velocity conditions. The predictions of classical rigid body dynamics (Eq.(7.24)) and Maw *et al.* (1976) are also shown in the figure. It can be seen that the FEA results are independent of the magnitude of the initial velocity for a given impact angle. The FEA results are in good agreement with those predicted by Maw *et al.* (1976). Although rigid body dynamics predicts the same

expression for gross sliding, it cannot accurately predict the reflection angle of the contact patch for regions where sliding does not occur throughout the impact, since it ignores the effect of contact deformation. Owing to the contact deformation, the recovery of elastic strain energy stored by the deformation of contacting bodies in the tangential direction is responsible for the reversal of the initial tangential velocity at the contact patch for the impacts at intermediate impact angles.

7.8.2 The influence of friction

The effect of friction on the reflection angle of the contact patch is shown in Fig. 7.29. It can be seen that the results for impacts with different friction coefficients follow the same trace and are in good agreement with the results given by Maw *et al.* (1976, 1981). This implies that the effect of friction on the reflection angle of the contact patch is governed by the normalised impact angle $V_{ii} / \mu V_{ni}$.

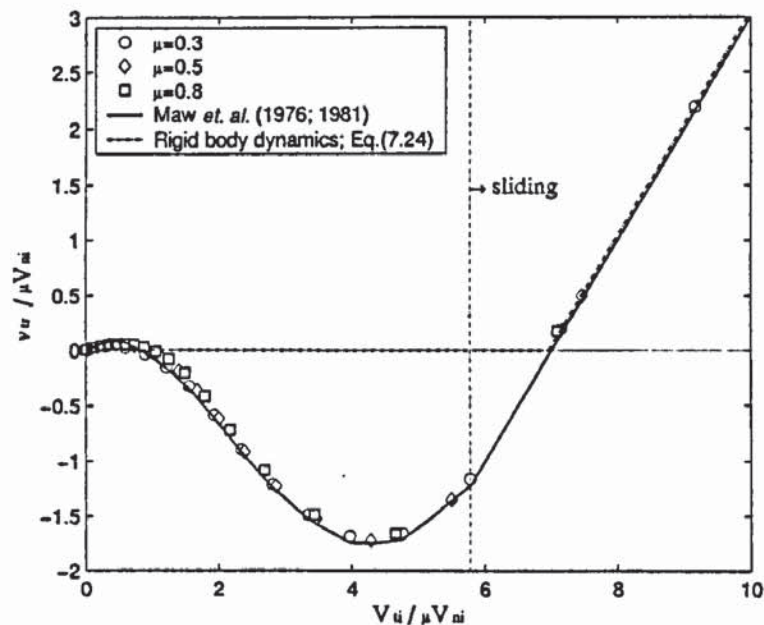


Fig. 7.29 The variation of normalised reflection angle of the contact patch $v_{ir} / \mu V_{ni}$ with normalised impact angle $V_{ii} / \mu V_{ni}$ for impacts with different friction coefficients.

7.8.3 The influence of Poisson's ratio

Figure 7.30 shows the effect of Poisson's ratio on the reflection angle of the contact patch. The experimental results obtained by Johnson (1983) for a rubber sphere (Poisson's ratio $\nu = 0.5$) are also plotted in this figure. It can be seen that FEA results for $\nu = 0.49$ are in

good agreement with the experimental results obtained by Johnson (1983). It is also clear that at large impact angles the results for different Poisson's ratios merge together. This implies that for impacts at large impact angles, in which sliding occurs throughout the impact, the effect of Poisson's ratio is negligible. However, at small impact angles, the curves diverge from each other and the curve moves leftwards and downwards as the Poisson's ratio increases, indicating that the reflection angle of the contact patch depends significantly upon the value of Poisson's ratio. The results are in qualitative agreement with the DEM analysis of Ning (1995) and Thornton *et al.* (2001). The dimensionless reflection angle of the contact patch is plotted against dimensionless impact angle in Fig. 7.31 for the impacts with different Poisson's ratios. It is clear that the curves do not merge together, which demonstrates that ψ is not a normalising parameter, as pointed out by Ning (1995) (see also Fig. 2.11). It is interesting to find that the maximum values of reversed (negative) dimensionless reflection angles of the contact patch are essentially identical of *c.a.* -1.4 for impacts with different impact Poisson's ratios. This is consistent with the analysis of Maw *et al.* (1976, 1981), as shown in Fig. 2.11, (see also, Johnson 1985, p358).

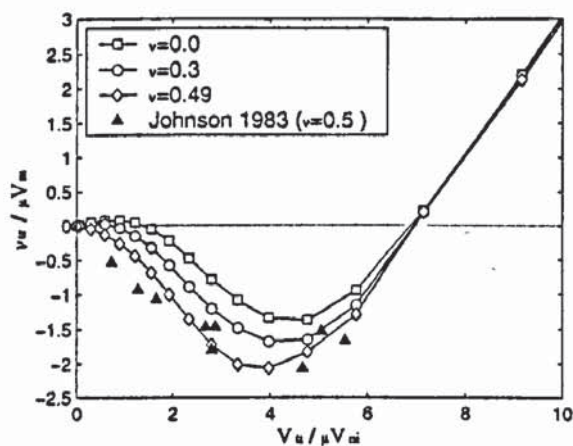


Fig. 7.30 The variation of the normalised reflection angle of the contact patch $v_{ir} / \mu V_{ni}$ with normalised impact angle $V_{ii} / \mu V_{ni}$ for impacts with different Poisson's ratios.

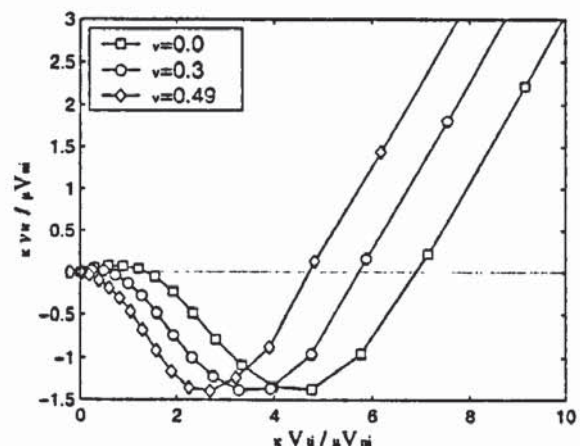


Fig. 7.31 The variation of the dimensionless reflection angle of the contact patch $\kappa v_{ir} / \mu V_{ni}$ with dimensionless impact angle $\kappa V_{ii} / \mu V_{ni}$ for impacts with different Poisson's ratios.

7.9 Rebound angular velocity

During the oblique impact of a spherical particle with a substrate, the particle rotates because of the tangential interaction. This leads to a portion of the initial tangential kinetic energy being transformed into rotational kinetic energy of the particle. The rotational

kinetic energy gained by the particle is a function of the angular rotational velocity. In this section, we shall consider the effects of initial velocity conditions, friction and Poisson's ratio on the rebound angular velocity, which is determined from Eq.(7.33) for all tests reported.

7.9.1 The influence of initial velocity conditions

The rebound angular rotational velocities at various impact angles are shown in Fig. 7.32 for impacts with different initial velocity conditions. It is clear that there are two different trends. For impacts at a fixed initial speed, the rebound angular velocity increases with increasing impact angle until a certain angle is reached; afterwards it reduces towards zero as the impact angle further increases. The critical impact angle for the rebound angular velocity reaching its maximum value is around 55° for the two series of tests with different magnitudes of initial speed. However, for impacts with a fixed initial normal velocity, the rebound angular velocity increases with impact angle until it reaches the maximum value at a certain angle (about 60°).

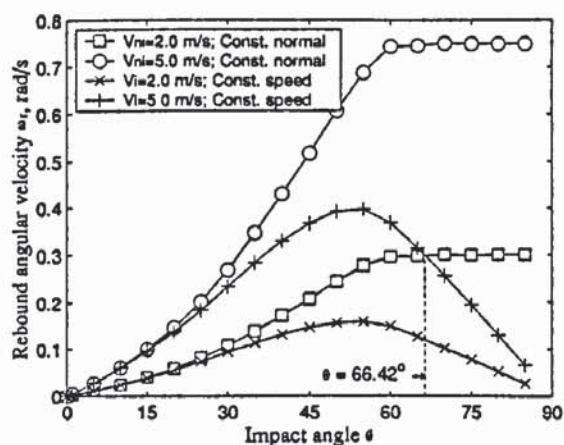


Fig. 7.32 The rebound angular velocity at various impact angles for impacts with different initial velocity conditions.

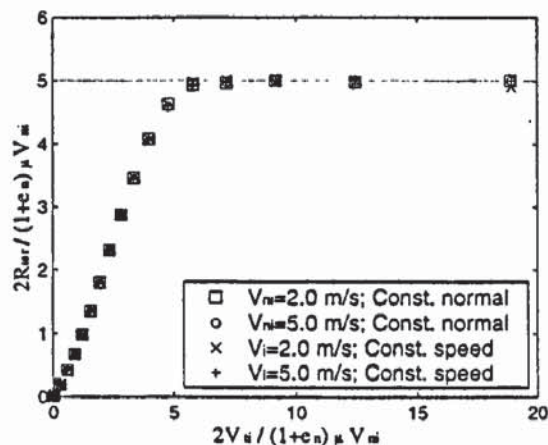


Fig. 7.33 The normalised rebound angular velocity versus the normalised impact angle for impacts with different initial velocity conditions.

For impacts at a given impact angle with different initial velocity conditions, it is found that the higher the initial normal velocity, the higher the rebound rotational speed. This corresponds to the prediction of Eq.(7.11). According to Eq.(7.11), for all impact cases considered here, the rebound angular velocity is dependent only on the initial normal velocity V_{ni} , since the normal coefficient of restitution e_n is essentially equal to unity, and the impulse ratio is independent of the initial velocity condition at a given impact angle, as

shown in Fig. 7.14. Again, it is noted that the curve for the impact with a fixed initial speed of $V_i = 5.0m/s$ intersects with the curve for the impact with a fixed initial normal velocity of $V_{ni} = 2.0m/s$ at $\theta = 66.42^\circ$, when the initial velocity conditions are identical.

Fig. 7.33 shows the corresponding normalised rebound angular velocity versus the normalised impact angle for impacts with different initial velocity conditions. It is clear that all the curves merge together. Moreover, once the impact angle reaches the critical angle for sliding occurring throughout the impact, the normalised rebound angular velocity remains constant and is equal to 5. This is consistent with Eq.(7.11).

7.9.2 The influence of friction

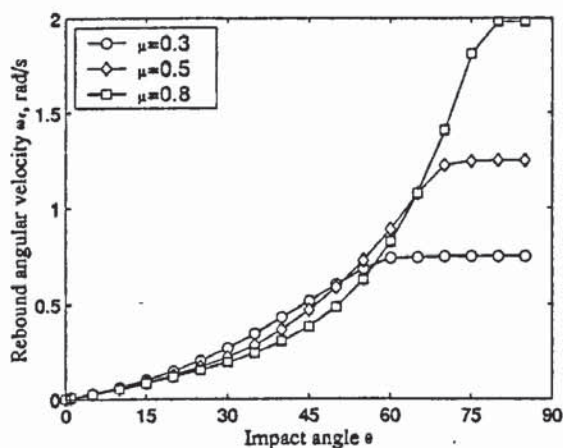


Fig. 7.34 The rebound angular velocity at various impact angles for impacts with different friction coefficients.

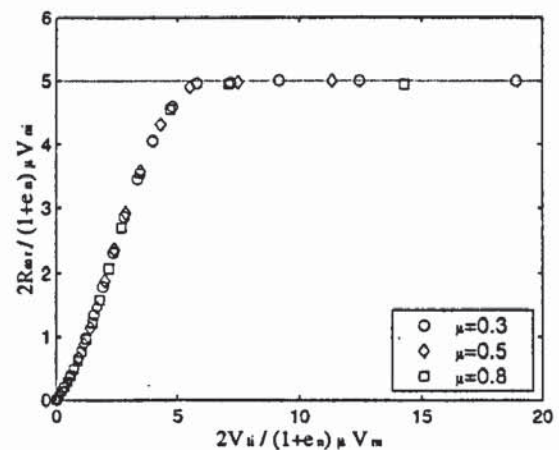


Fig. 7.35 The normalised rebound angular velocity versus the normalised impact angle for impacts with different friction coefficients.

Since the critical impact angle for sliding occurring throughout the impact increases with the increasing friction coefficient, an increase in friction coefficient should result in the rebound angular velocity that reaches the limiting value at a larger impact angle if the different impact angles are specified by keeping the initial normal velocity constant. This is confirmed in Fig. 7.34, which shows the effect of friction on the rebound angular velocity. The corresponding normalised rebound angular velocity is plotted against the normalised impact angle in Fig. 7.35. It is clear that the three curves coalesce to form a master curve with a constant maximum value of 5 for the region in which sliding occurs throughout the impact, as predicted by Eq.(7.11).

7.9.3 The influence of Poisson's ratio

Figure 7.36 shows the effect of Poisson's ratio on the rebound angular velocity. It can be seen that the rebound angular velocity for different Poisson's ratios are essentially identical at large impact angles where sliding occurs throughout the impact. This again implies that the effect of Poisson's ratio becomes negligible once sliding occurs throughout the impact. However, the effect of Poisson's ratio becomes significant at small impact angles, and the higher the Poisson's ratio, the larger the rebound angular velocity. It has been shown from Fig. 7.16 that the higher the Poisson's ratio, the higher the impulse ratio. Hence, it is implied that the rotation of the sphere is associated with the impulse ratio. The corresponding normalised rebound angular velocity is plotted against normalised impact angle in Fig. 7.37. It is apparent that the normalised rebound angular velocity reaches a limiting value of 5 when sliding occurs throughout the impact, as predicted by Eq.(7.11). When sliding does not occur, a higher normalised rebound angular velocity is obtained for impacts with a higher Poisson's ratio.

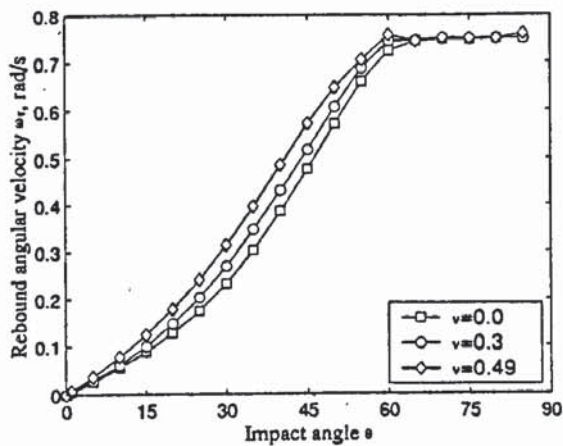


Fig. 7.36 The rebound angular velocity at various impact angles for impacts with different Poisson's ratios.

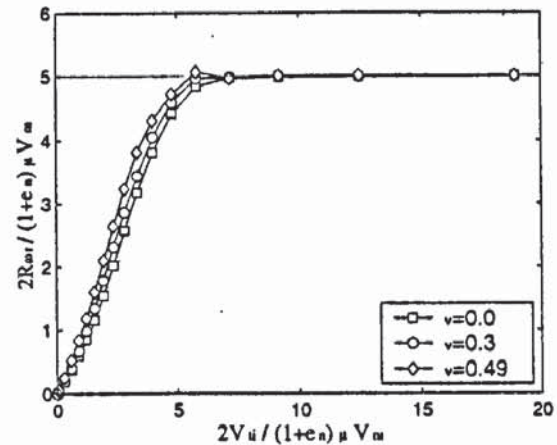


Fig. 7.37 The normalised rebound angular velocity versus the normalised impact angle for impacts with different Poisson's ratios.

7.10 Summary

The impact of a rigid sphere with an elastic substrate has been intensively investigated using FEM in this chapter. Simulations have been performed for impacts at various impact angles that are specified by two different approaches: keeping the initial speed constant and keeping the initial normal velocity constant. The effects of initial velocity conditions, impact angle, friction and Poisson's ratio on the oblique impact behaviour have been

discussed. Comparisons of FEA results with theoretical predictions and experimental results have also been made. As a summary, it has been shown that

1) For the tests of oblique impact of elastic particles, the choice of the approach used to specify the impact angle is not important because the results obtained from the impacts with different initial velocity conditions specified by the two different approaches can be generalised by the same scaling law (See Figs. 7.9, 7.14, 7.18, 7.22, 7.28 and 7.33). However, as will be shown in the next chapter, keeping the initial normal velocity constant has the advantage that it can isolate the dependence of plastic deformation on the normal component of the initial impact velocity.

2) The finite element analysis has reproduced the results of the analysis of Maw *et al.* (1976, 1981) and Ning (1995), and is in good agreement with experimental results of Johnson (1983) and Lewis and Rogers (1988).

3) The dependence of the impact behaviour on the friction coefficient is governed by the normalised impact angle $\tan\theta/\mu$. The dependence of the impact behaviour on the Poisson's ratio is complicated and is not governed by a single simple parameter. Since the value of Poisson's ratio affects the ratio of tangential stiffness to normal stiffness, the effect of Poisson's ratio at large impact angles where sliding occurs throughout the impact, is negligible, but it becomes significant once sliding does not occur. This demonstrates that the contact deformation plays an important role for impacts in which sliding does not occur throughout the impact. Hence, the classical rigid body dynamics, which ignores the contact deformation, can only predict the rebound behaviour at large impact angles, at which sliding occurs throughout the impact.

4) The peak tangential force $F_{t,max}$ is found to first reach its limit value of $\mu F_{n,max}$ at the same critical impact angle

$$\theta = \arctan\left[\frac{\mu(7\kappa - 3)}{\kappa}\right] \quad (7.37)$$

as the tangential coefficient of restitution reaches its minimum. At this critical impact angle, sliding persists during the whole of compression.

5) During the oblique impact of elastic particles, the main energy loss is due to friction. The tangential force not only does frictional work, but also transfers some translational kinetic energy into rotational kinetic energy. As a result, a portion of the initial kinetic energy is dissipated by friction.

Chapter 8 Oblique Impact of Plastic Particles

8.1 Introduction

In the preceding chapter, we discussed the oblique impact of elastic particles, for which no plastic deformation was involved. However, plastic deformation is usually involved in engineering applications. Once plastic deformation takes place, the impact process becomes more complicated. The key issue in the oblique impact of plastic particles is that a portion of the initial kinetic energy is dissipated due to plastic deformation and local profiles of the contact surface change in time because of the unrecoverable plastic deformation, which in turn may affect the impact behaviour of the particle.

In this chapter, the oblique impact of plastic particles is investigated using FEM. Since the validity of the FE model shown in Fig. 3.10 has been demonstrated in the preceding chapter for reliably simulating the oblique impact of elastic particles, the same model is used to investigate the plastic oblique impact of a sphere with a substrate by assuming one of the bodies to be elastic-perfectly plastic and the other to be either rigid or elastic. Four combinations considered for plastic oblique impact were shown in Table 3.4, and the material properties were given in Table 3.5. We consider a variety of impact cases with either different friction coefficients or different magnitudes of the initial velocity so that the effect of friction and plastic deformation can be explored. The detailed analysis results are presented in the subsequent sections.

8.2 Contact deformation

Physically, different combinations of the contact bodies lead to different patterns of contact deformation. In this section, we shall examine the difference between the contact deformation for four impact combinations, since it is considered that the impact behaviour depends on the contact deformation pattern.

Figure 8.1 shows the typical profiles of contact deformation at various instants for a PR impact at $\theta = 85^\circ$ with $V_n = 5.0\text{m/s}$ and $\mu = 0.3$. Since the substrate is rigid, it is un-

deformable and the deformation only takes place within the sphere. Pronounced deformation of the sphere can be observed and the contact plane always remains horizontal. The sphere is significantly flattened because of the unrecoverable plastic deformation (see Figs. 8.1c and 8.1d). Inclination of the flattened sphere surface indicates the rotation of the sphere. Figure 8.2 gives the corresponding profiles of contact deformation for a PE impact at the same angle with the same velocity and friction conditions. Since the substrate is elastic, it deforms during the impact. However, the deformation of the substrate is recovered at the end of the impact. At the instant of separation, the contact plane is identical to the initial one, i.e., horizontal. The sphere is slightly flattened due to plastic deformation. Comparing Fig. 8.1 with Fig. 8.2, the overall contact deformation patterns for PE impact are similar to those of the PR impact, except that elastic deformation occurs in the substrate during the impact.

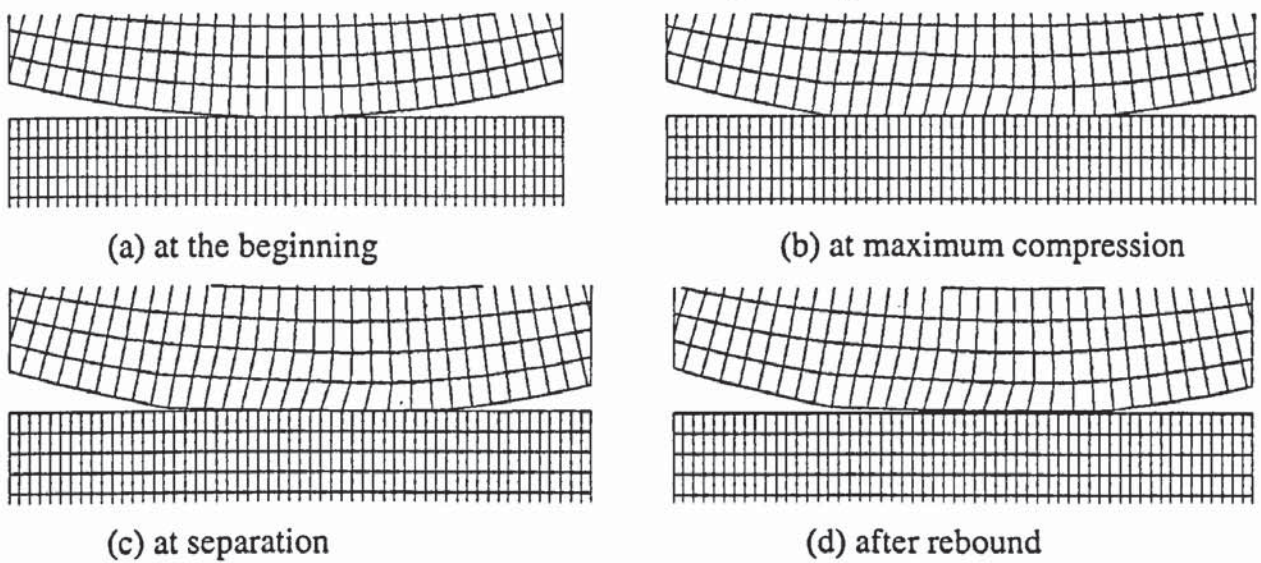


Fig. 8.1 Profiles of the contact deformation over the interface for PR impact at $\theta = 85^\circ$ with $V_{ni} = 5.0m/s$ and $\mu = 0.3$.

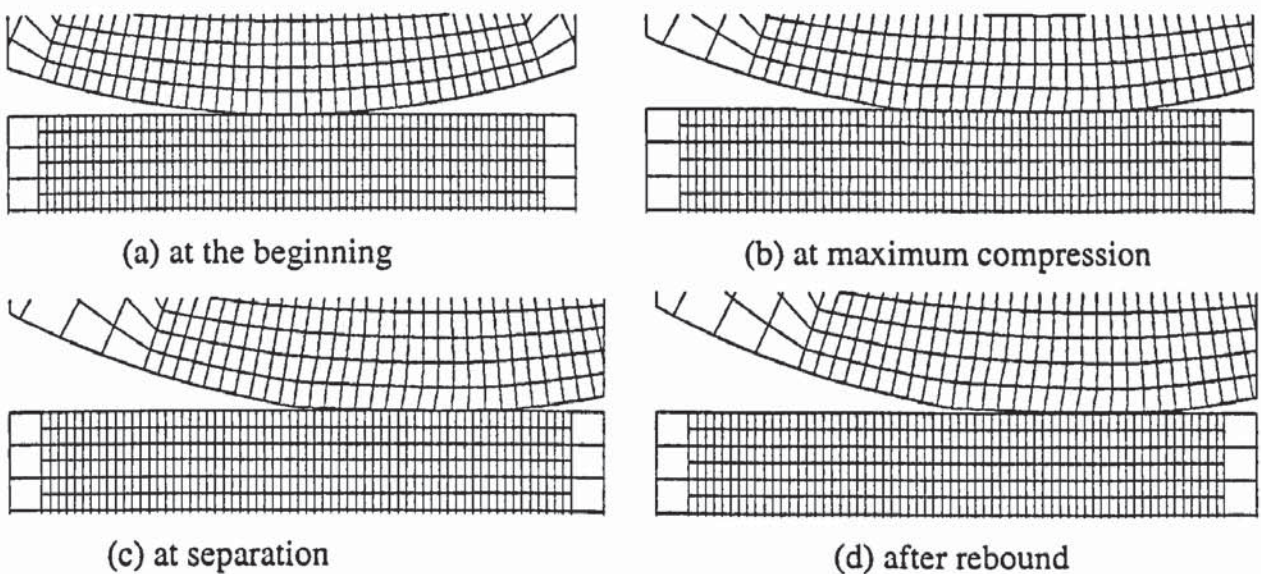


Fig. 8.2 Profiles of the contact deformation over the interface for PE impact at $\theta = 85^\circ$ with $V_{ni} = 5.0m/s$ and $\mu = 0.3$.

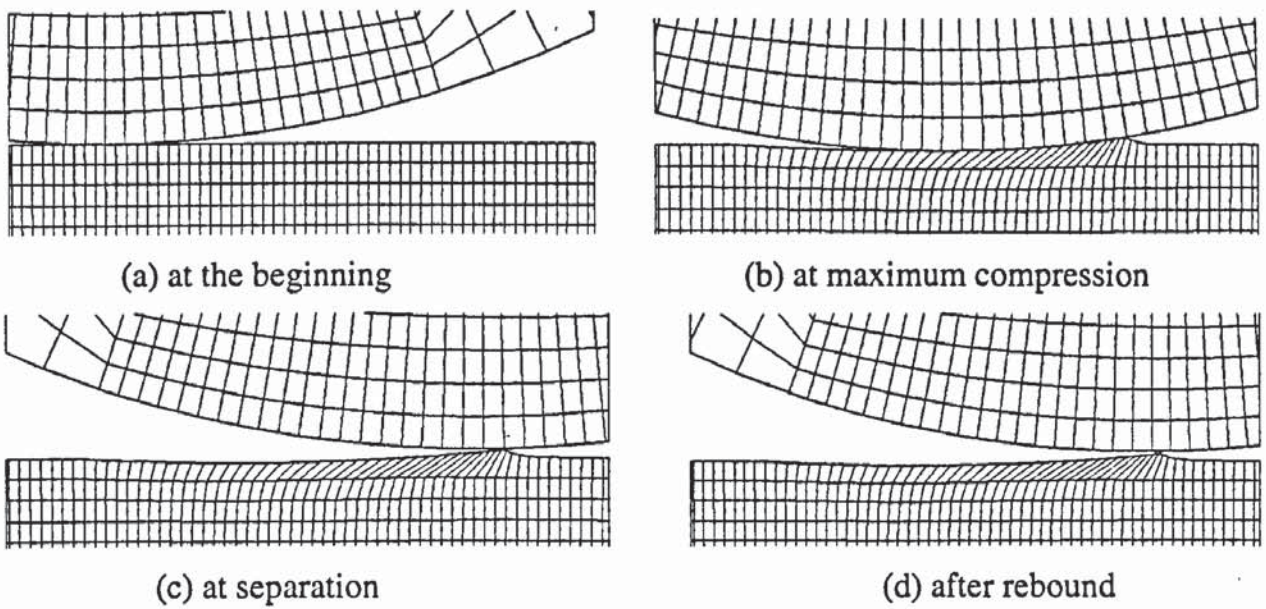


Fig. 8.3 Profiles of the contact deformation over the interface for RP impact at $\theta = 85^\circ$ with $V_{ni} = 5.0m/s$ and $\mu = 0.3$.

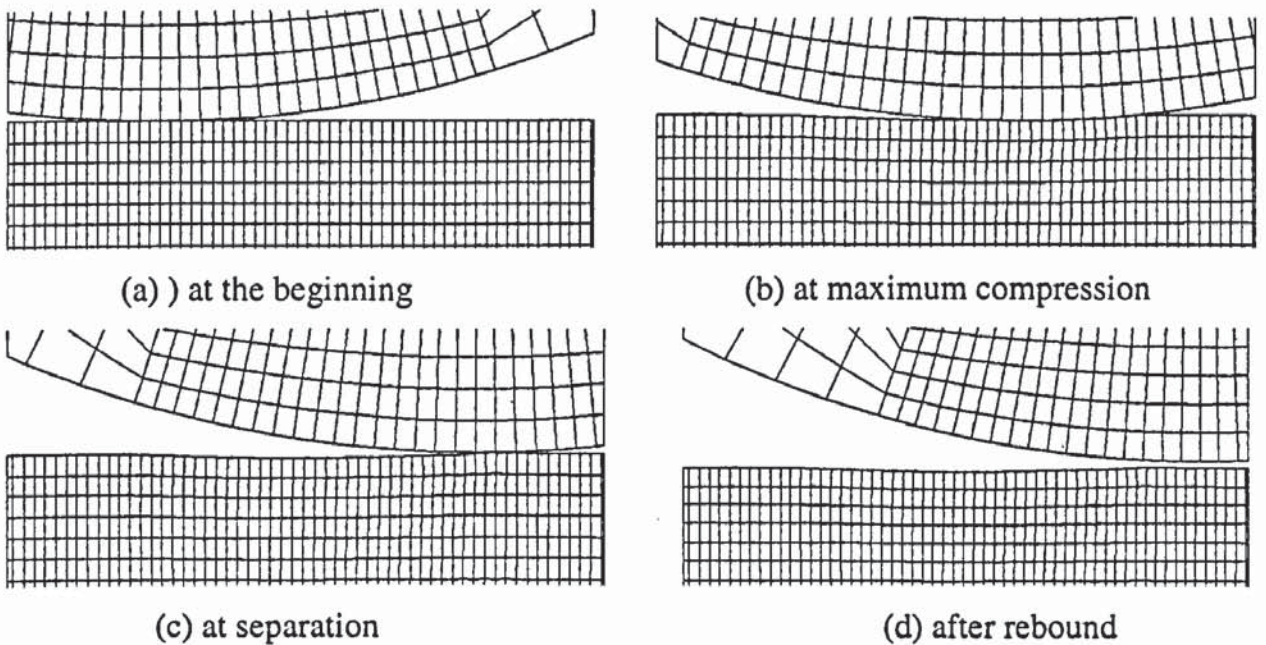


Fig. 8.4 Profiles of the contact deformation over the interface for RP impact at $\theta = 85^\circ$ with $V_{ni} = 5.0m/s$ and $\mu = 0.0$.

When the material types are reversed, i.e., if the substrate is specified as plastic, different patterns for the contact deformation are obtained, as shown in Figs. 8.3-8.5. Figure 8.3 shows the typical profiles of contact deformation for a RP impact at $\theta = 85^\circ$ with $V_{ni} = 5.0m/s$ and $\mu = 0.3$. It illustrates that the rigid (un-deformable) sphere ploughs into the plastic substrate and the materials at the interface are displaced to form a lip at the front of the contact area. This is generally referred to as a prow. After the sphere bounds off, a crater is left in the substrate. Examination of the process at all impact angles reveals that craters are commonly produced for RP impacts even for frictionless impacts (see Fig. 8.4). The impact angle at which the prow begins to appear depends upon the friction coefficient

and initial velocity conditions. For frictionless RP impacts, a prow only forms when the impact angle is larger than 80° . However, for frictional RP impacts with $\mu = 0.3$, the prow begins to appear at around 60° . The contact deformation patterns for EP impacts are similar to those for RP impacts, as shown in Fig. 8.5. It is clear that a prow is also produced during the EP impact. The phenomena of indentation and prow formation have also been observed in real experiments by many other researchers (see, for example, Hutchings *et al.* 1976; Sheldon and Kanhere 1972; Rickerby and Macmillan 1980; *etc.*).

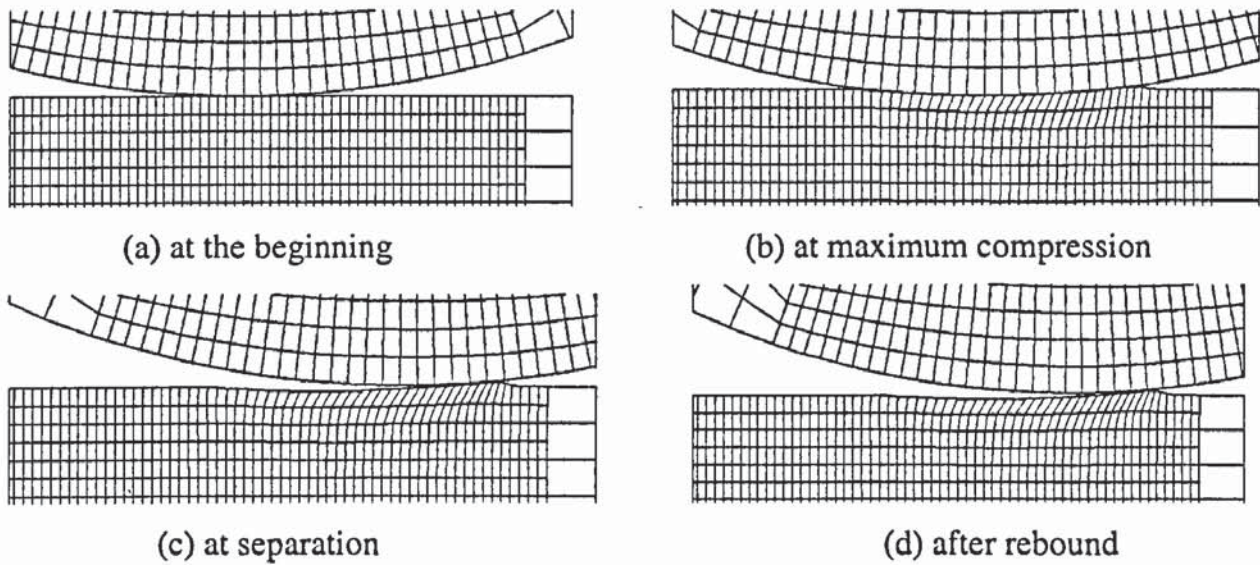


Fig. 8.5 Profiles of the contact deformation over the interface for EP impact at $\theta = 85^\circ$ with $V_{ni} = 5.0\text{m/s}$ and $\mu = 0.3$.

8.3 Yield and residual plastic strain distribution

8.3.1 Yield

The onset of material yield for sliding contacts was studied by Johnson and Jefferis (1963), who showed that the yield depends upon the friction coefficient. For low values of the friction coefficient ($\mu \leq 0.25$ assuming the Tresca criterion and $\mu \leq 0.3$ assuming von Mises criterion), yield is first initiated at a point beneath the contact surface, similar to normal contacts. However, for large values of friction, yield first occurs at the interface, rather than at the subsurface. The FEA of sliding of a rigid cylinder over a surface by Tengena and Hurkx (1985) confirmed the analysis of Johnson and Jefferis (1963). The onset of plastic yield for the oblique impact of a sphere with a substrate is considered in this section.

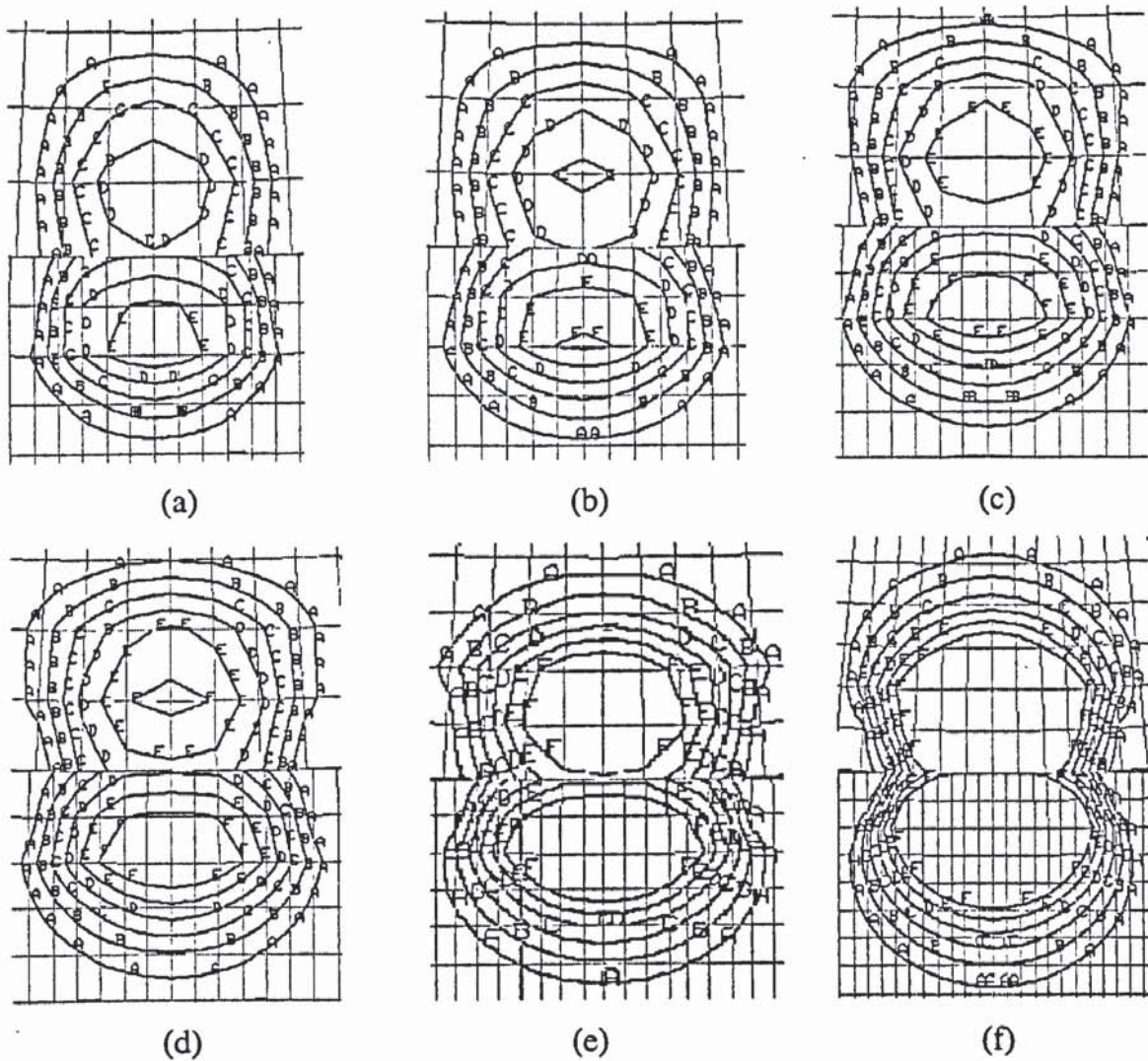


Fig. 8.6 The evolution of von Mises stress distribution during the impact of an elastic sphere with a plastic substrate at $\theta = 0^\circ$ with $V_{ni} = 5.0\text{m/s}$. Contour levels (GPa): A-1.0; B-1.17; C-1.34; D-1.51; E-1.68; F-1.85.

Figures 8.6 and 8.7 show the evolution of the von Mises stress distribution during impacts of an elastic sphere with a plastic substrate with $V_{ni} = 5.0\text{m/s}$ at $\theta = 0^\circ$ and $\theta = 85^\circ$, respectively. The friction coefficient is $\mu = 0.3$. The contour level F denotes the yield stress and represents the boundary between the elastic and plastic zones. It is clear that yield is initiated at a point below the contact surface for both the normal impact ($\theta = 0^\circ$) (see Fig. 8.6b) and the oblique impact at a very large impact angle ($\theta = 85^\circ$) (see Fig. 8.7b). Comparing Figs. 8.6b and 8.7b, the onset of yield is found to occur at a point closer to the contact surface for the impact at $\theta = 85^\circ$ than for $\theta = 0^\circ$. This implies that the tangential force (friction force) brings the yield point closer to the contact surface, which is consistent with the analysis of Johnson and Jefferis (1963), Hamilton and Goodman (1966), Bryant and Keer (1982) and Sackfield and Hills (1983). It can also be seen from Figs. 8.6 and 8.7 that the plastic zone gradually expands. The plastic zone reaches the

contact surface at a certain instant (see Figs. 8.6f and 8.7e) and then fully plastic contact begins.

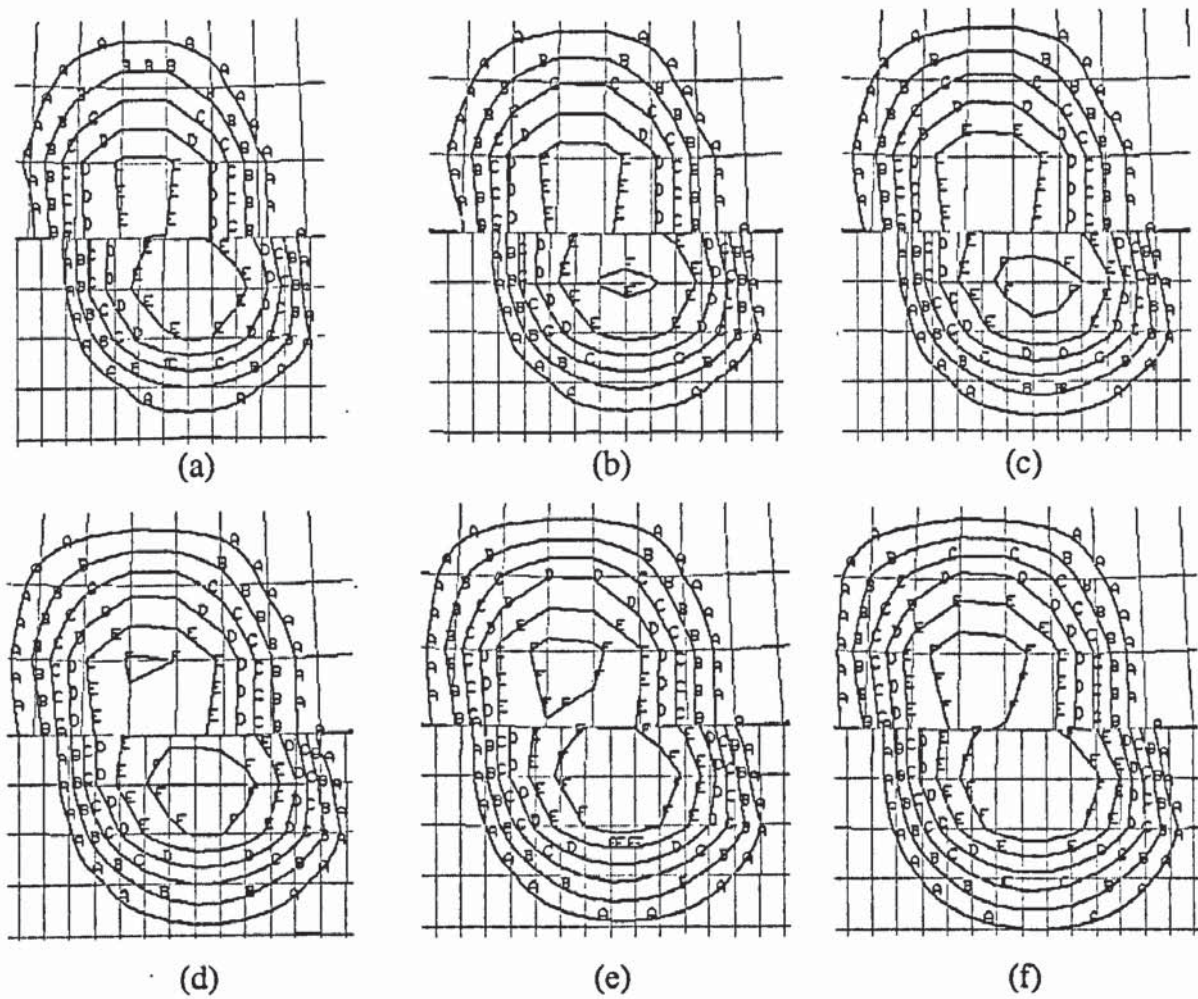


Fig. 8.7 The evolution of von Mises stress distribution during the impact of an elastic sphere with a plastic substrate at $\theta = 85^\circ$ with $V_{ni} = 5.0m/s$ Contour levels (GPa): A-1.0; B-1.17; C-1.34; D-1.51; E-1.68; F-1.85.

8.3.2 Residual plastic strain distribution

For plastic impacts, the energy dissipated by plastic deformation W_p can be qualitatively estimated by the following expressions:

$$W_p = \int_p \sigma^* \varepsilon_r dV \quad (8.1)$$

where σ^* is the effective stress at the maximum compression, ε_r is the residual effective plastic strain which is identical to that at maximum compression because the unloading process is essentially elastic (see Section 5.2.2), and V_p the volume of the plastic zone. Since for elastic-perfectly plastic materials the effective stresses within the plastic zone at maximum compression are identical and equal to the yield stress Y , Eq.(8.1) may be rewritten as

$$W_p = Y \int_p \epsilon_r dV \quad (8.2)$$

It is clear that the energy dissipated by plastic deformation depends on the residual effective plastic strain distribution and the size of the plastic zone. The larger the plastic zone and the more intense the residual plastic strain, the more energy is dissipated by plastic deformation. Hence, it is instructive to investigate the distribution of the residual effective plastic strain.

The distributions of residual effective plastic strain for PR impacts at different impact angles with a fixed initial normal velocity of $V_{ni} = 5.0m/s$ and $\mu = 0.3$ are shown in Fig. 8.8. It can be seen that the residual effective plastic strain for the normal impact is symmetrically distributed with the most intense plastic strain concentrating inside the sphere. With the increase of the impact angle, the most intense plastic strain move towards the front of the contact patch. It is interesting to find that when the impact angle is larger than 50° , the distributions of residual plastic deformation are almost identical. This implies that the nearly same amount of energy is dissipated by plastic deformation when $\theta \geq 50^\circ$. Similar features are obtained for PE impacts as shown in Fig. 8.9. Compared to Fig. 8.8, it can be seen that, when $\theta \geq 50^\circ$, the overall residual plastic strain for PE impacts is greater than for PR impacts.

Figures 8.10 and 8.11 show the distributions of residual plastic strain at various impact angles for RP and EP impacts with a fixed initial normal velocity of $V_{ni} = 5.0m/s$ and $\mu = 0.3$, respectively. It is clear that as the impact angle increases the most intense plastic strain moves towards the rear of the contact patch from the symmetrical distributions during normal impact. In contrast to PR and PE impacts, at large impact angles, the overall residual effective plastic strain still increases as the impact angle increases, which indicates that the amount of energy dissipated by plastic deformation increases as the impact angle increases.

It also can be seen from Figs. 8.8-8.11 that the residual plastic strain distribution depends on the combination of contacting bodies. Under the same velocity and friction condition, the overall residual plastic strain is greater for impacts with a plastic substrate than those with a plastic sphere; while the effect of impact angle on the residual plastic strain is greater for impacts with a plastic substrate than those with a plastic sphere. It is also clear that, when the sphere is plastic, intense plastic deformation occurs at the rear of the contact

patch; while intense plastic deformation occurs at the front of the contact patch when the substrate is plastic.

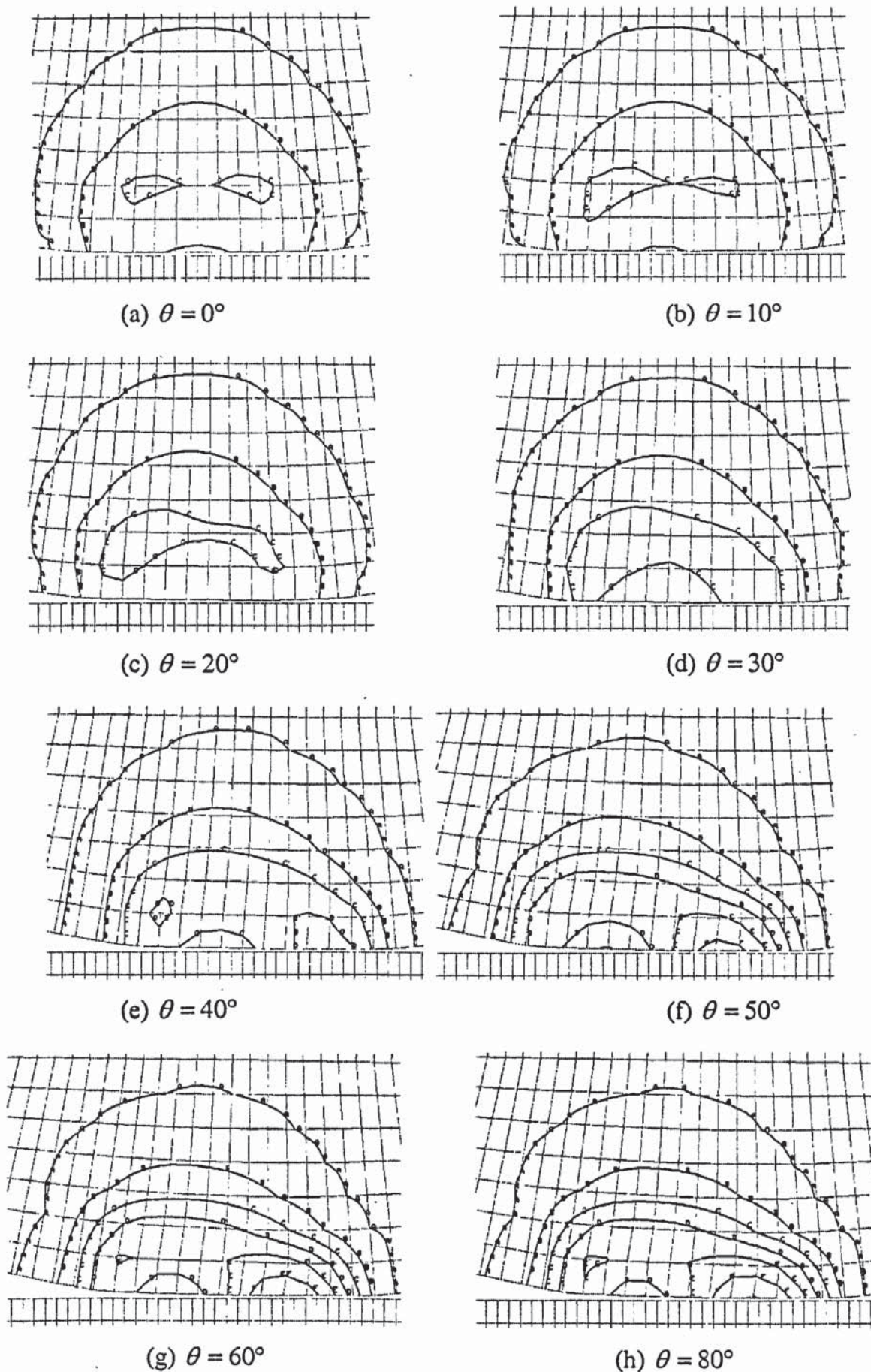


Fig. 8.8 Residual effective plastic strain distribution for PR impacts with $V_{ni} = 5.0m/s$ and $\mu = 0.3$. Contour level: A-0.0001; B-0.0175; C-0.0340; D-0.0505; E-0.0670; F-0.0835; G-0.1000

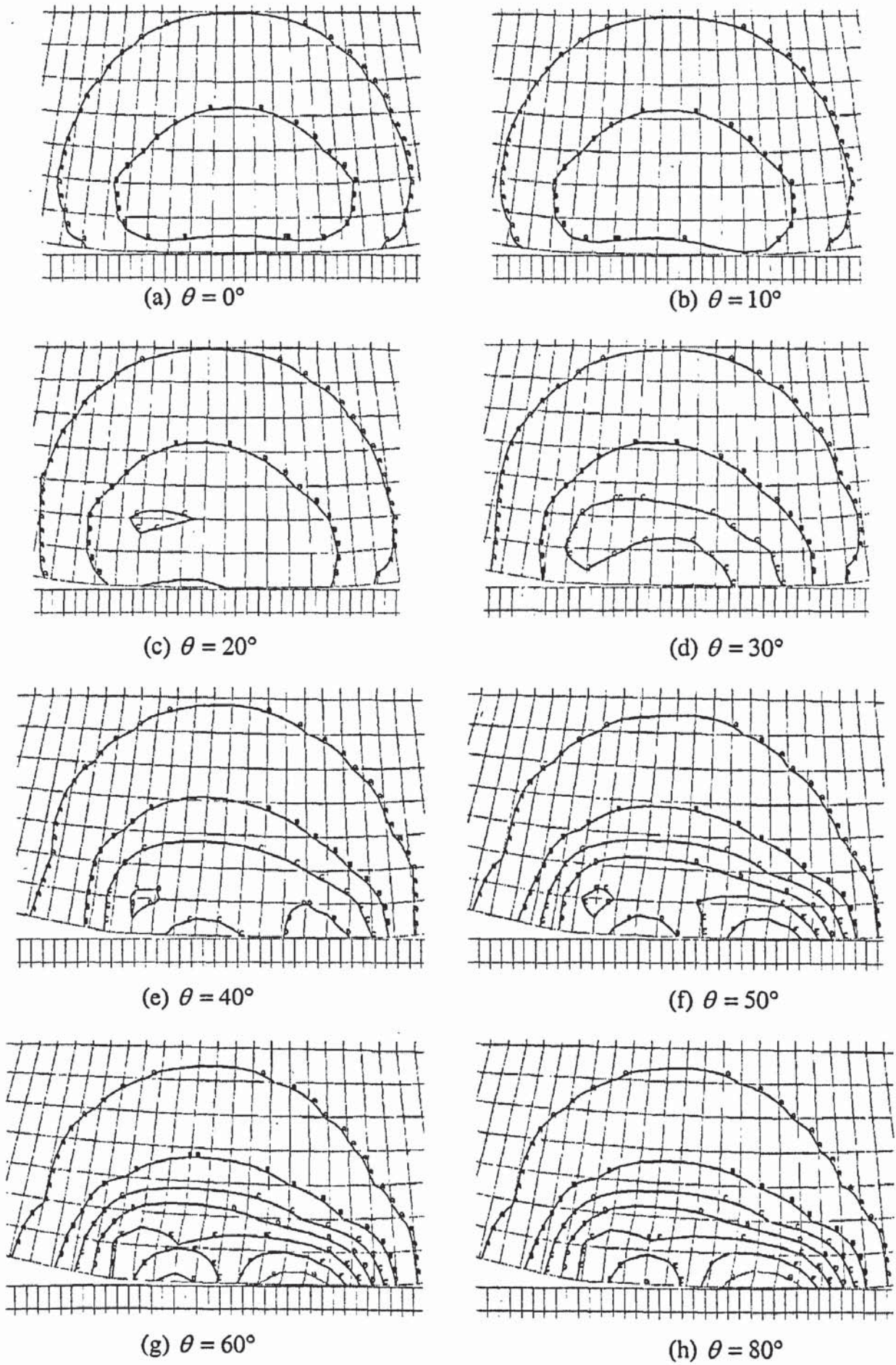
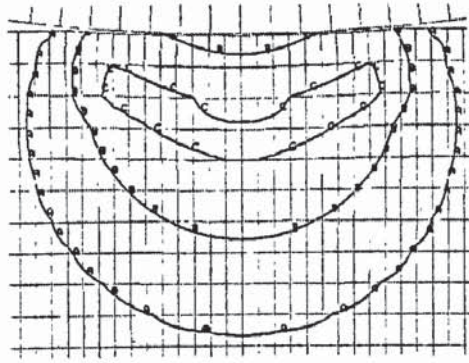
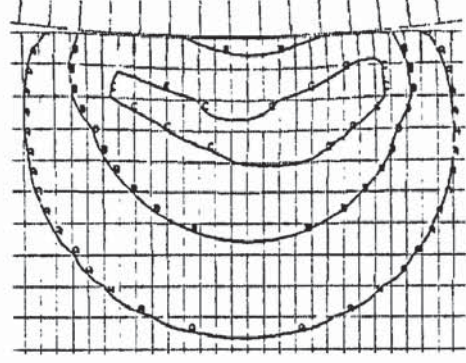


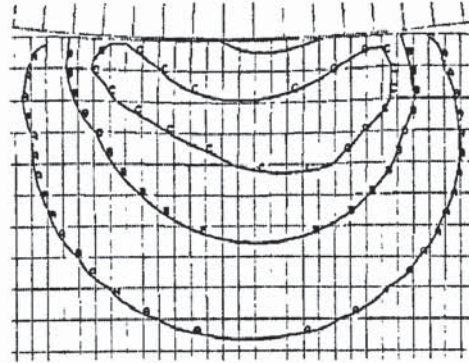
Fig. 8.9 Residual effective plastic strain distribution for PE impacts with $V_{ni} = 5.0m/s$ and $\mu = 0.3$. Contour level: A-0.0001; B-0.0175; C-0.0340; D-0.0505; E-0.0670; F-0.0835; G-0.1000



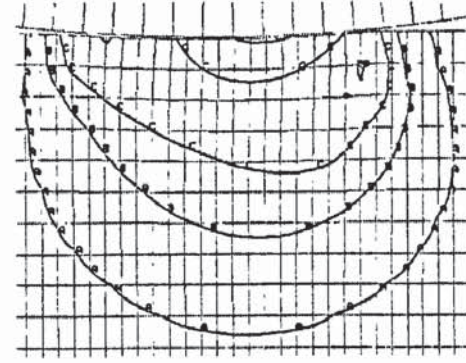
(a) $\theta = 0^\circ$



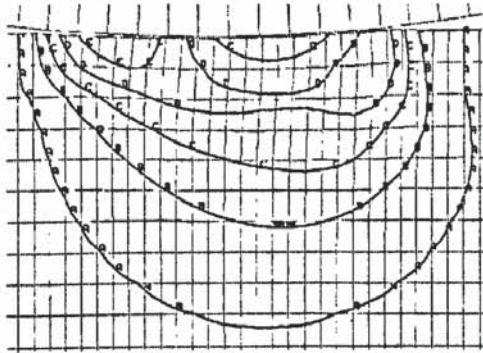
(b) $\theta = 10^\circ$



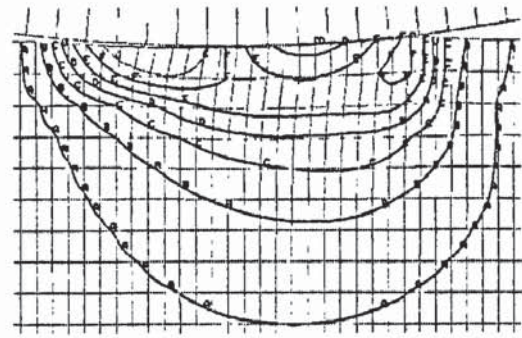
(c) $\theta = 20^\circ$



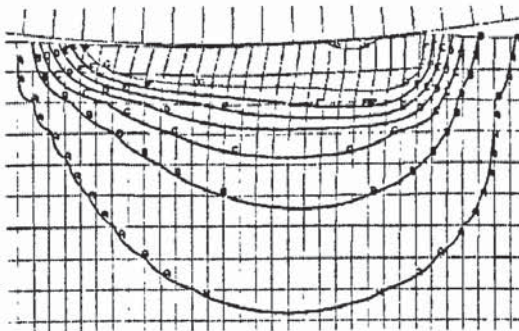
(d) $\theta = 30^\circ$



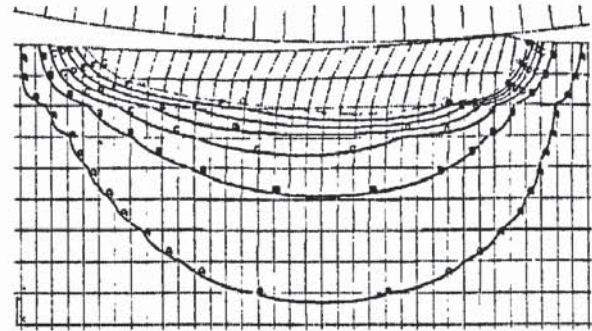
(e) $\theta = 40^\circ$



(f) $\theta = 50^\circ$

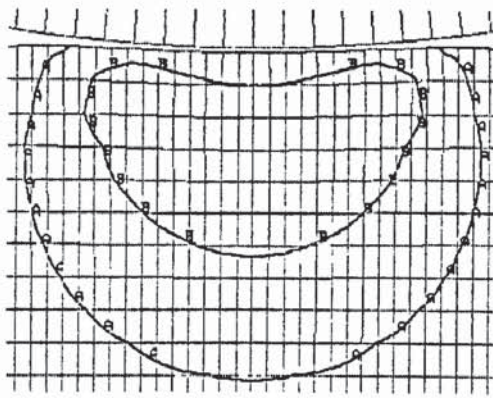


(g) $\theta = 60^\circ$

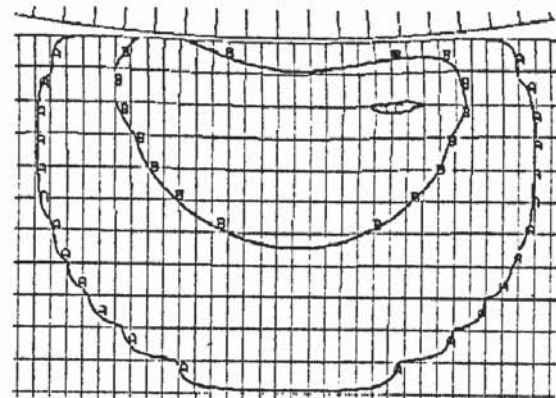


(h) $\theta = 80^\circ$

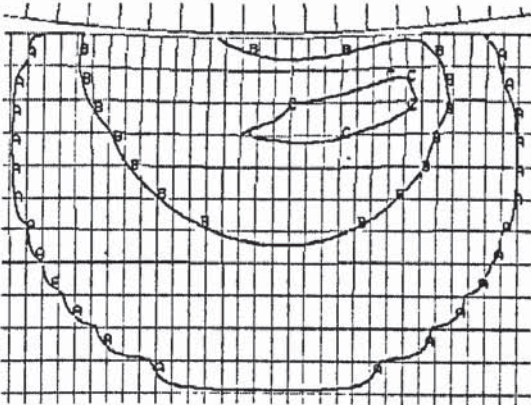
Fig. 8.10 Residual effective plastic strain distribution for RP impacts with $V_{ni} = 5.0m/s$ and $\mu = 0.3$. Contour level: A-0.0001; B-0.0175; C-0.0340; D-0.0505; E-0.0670; F-0.0835; G-0.1000



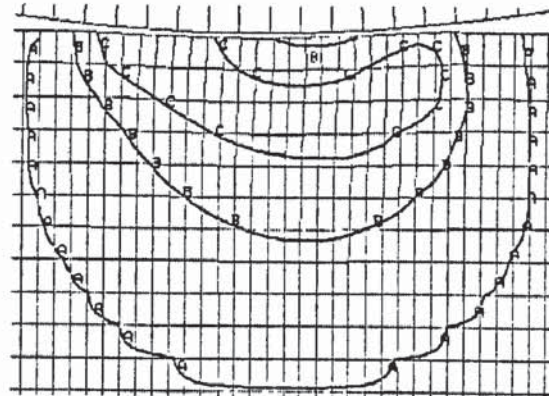
(a) $\theta = 0^\circ$



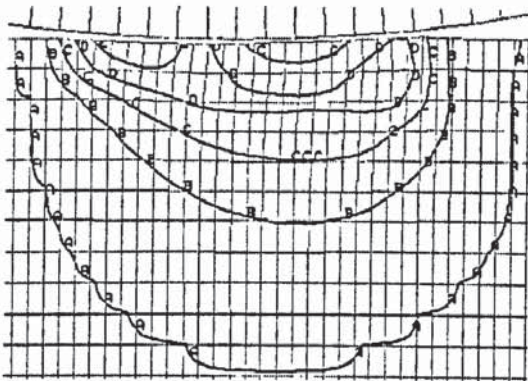
(b) $\theta = 10^\circ$



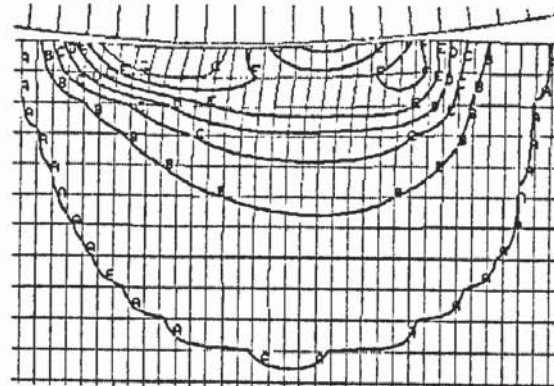
(c) $\theta = 20^\circ$



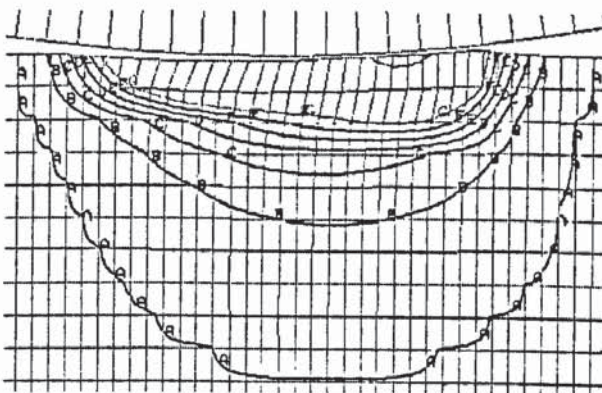
(d) $\theta = 30^\circ$



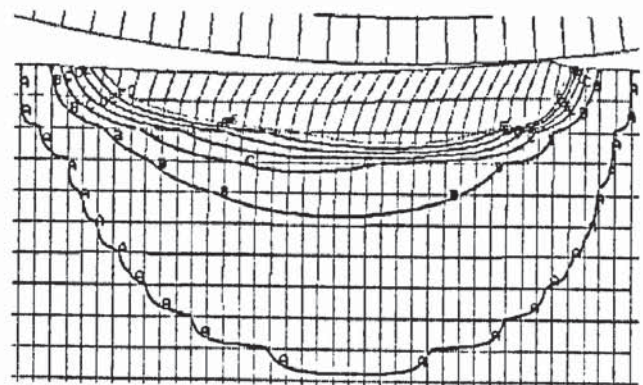
(e) $\theta = 40^\circ$



(f) $\theta = 50^\circ$



(g) $\theta = 60^\circ$



(h) $\theta = 80^\circ$

Fig. 8.11 Residual effective plastic strain distribution for EP impacts with $V_{ni} = 5.0\text{m/s}$ and $\mu = 0.3$. Contour level: A-0.0001; B-0.0175; C-0.0340; D-0.0505; E-0.0670; F-0.0835; G-0.1000

8.4 Typical interaction behaviour

In this section, the time evolution of the normal contact force, normal force-displacement relationship, time evolution of the tangential force and normal-tangential force relationship are presented for PR, PE, RP and EP impacts with a fixed initial normal velocity $V_{ni} = 5.0\text{m/s}$ at various impact angles. The effect of friction and plastic deformation are discussed.

8.4.1 Time evolution of normal contact force

Figure 8.12 shows the time histories of the normal contact force for PR impacts at various impact angles for $\mu = 0.3$. It is clear that the curves are similar to those obtained for the oblique impact of elastic particles (see Fig. 7.3), but two distinct features can be observed: 1) For PR impacts, the period of restitution is shorter than the loading period, whereas they are equal in the oblique impact of elastic particles; 2) the curves are found to deviate from each other for PR impacts at various impact angles, whereas they merged together for all impact angles in the oblique impact of elastic particles, as shown in Fig. 7.3. Furthermore, it can be seen that the evolutions of normal contact force are essentially identical when the impact angle is less than 20° , and when the impact angle is larger than 50° , the curves merge together again. The deviations hence occur at intermediate impact angles. The tangential force is relatively small compared to the normal force at small impact angles so that its effect on normal force is negligible. The tangential force increases with the impact angle. When the impact angle is larger than 50° , the tangential force is saturated during compression and the effects of tangential force on the normal response at different impact angles are equal. That is why the evolutions of the normal contact force are close to each other again at large impact angles. A similar feature is also observed for PE impacts as shown in Fig. 8.13. In addition, it is interesting to note that the difference between the normal force evolutions occurs in the middle period of the impact duration, when the peak tangential force is developed, as will be shown later.

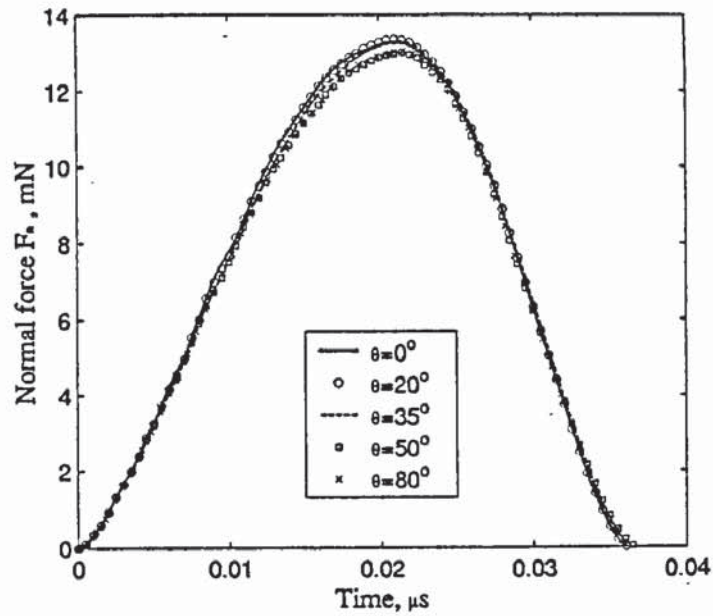


Fig. 8.12 The time histories of the normal contact force at various impact angles for PR impacts with $V_{ni} = 5.0m/s$ and $\mu = 0.3$.

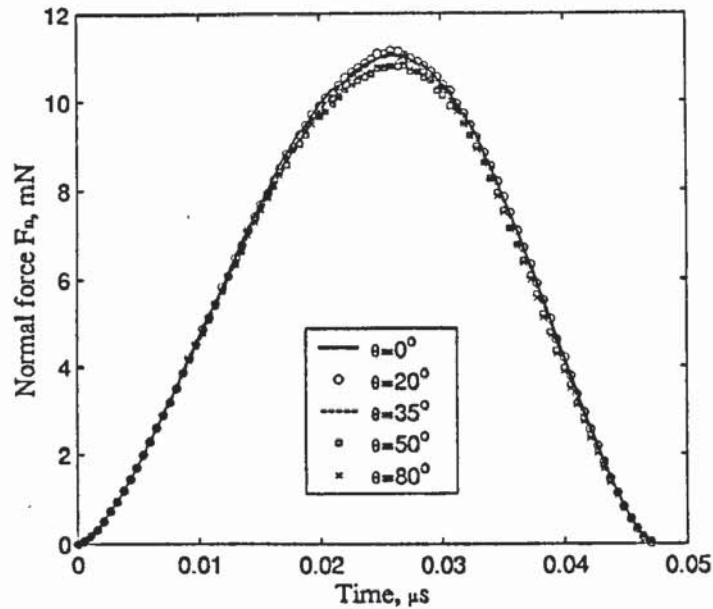


Fig. 8.13 The time histories of the normal contact force at various impact angles for PE impacts with $V_{ni} = 5.0m/s$ and $\mu = 0.3$.

Figures 8.14 and 8.15 shows the time evolution of the apparent normal contact force (vertical component of the contact force) at various impact angles for RP and EP impacts, respectively. It is clear that the apparent normal force evolutions for RP and EP impacts are similar. At the beginning of the impact the curves coalesce for different impact angles, thereafter they (say $>50^\circ$) begin to diverge remarkably. A lower peak value of the apparent normal force and a longer duration of impact are obtained for impacts at large impact angles. Moreover, the larger the impact angle, the lower the peak apparent normal force and the longer the duration of the impact. It appears to take a longer time for the apparent

normal force to unload at large impact angles, but the period of loading is essentially identical for different impact angles.

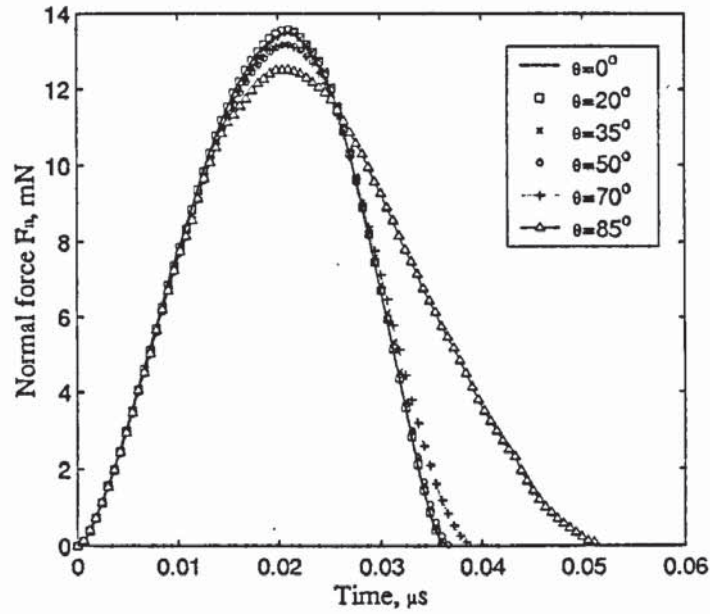


Fig. 8.14 The time histories of apparent normal contact force at various impact angles for RP impacts with $V_{ni} = 5.0m/s$ and $\mu = 0.3$.

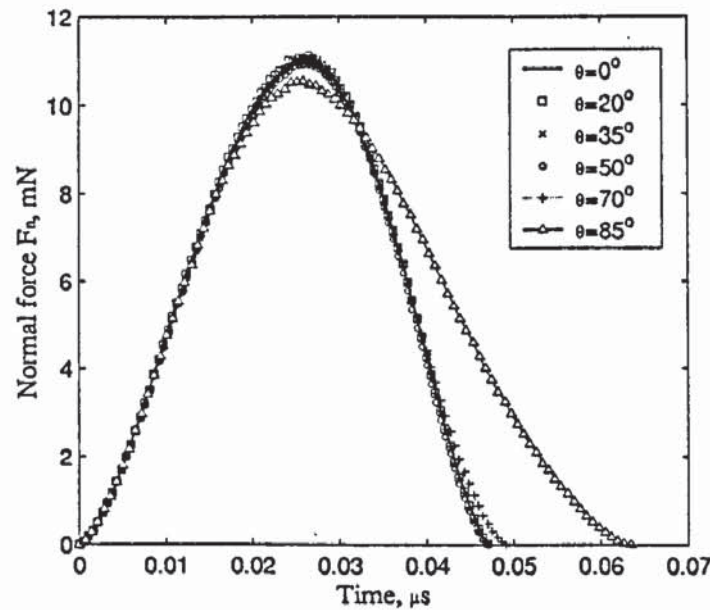


Fig. 8.15 The time histories of apparent normal contact force at various impact angles for EP impacts with $V_{ni} = 5.0m/s$ and $\mu = 0.3$.

An additional test, in which the coefficient of friction was set to zero, has been carried out to isolate the effect of friction. In theory, if there is no friction over the interface the tangential interaction is absent. Therefore, the normal contact force should be same for different impact angles if the initial normal component of the initial velocity is fixed. However, as shown in Fig. 8.16, the deviation of the normal contact force evolution at large impact angles ($>70^\circ$) is apparent. This deviation is due to the effect of the unrecoverable plastic deformation, as shown in Figs. 8.3 and 8.4. Even for frictionless RP

impact, the residual deformation of the substrate is apparent (see Fig. 8.4d). Once friction is involved, the residual deformation of the substrate becomes more significant (see Fig. 8.3d), as a prow is observed at the front of the crater.

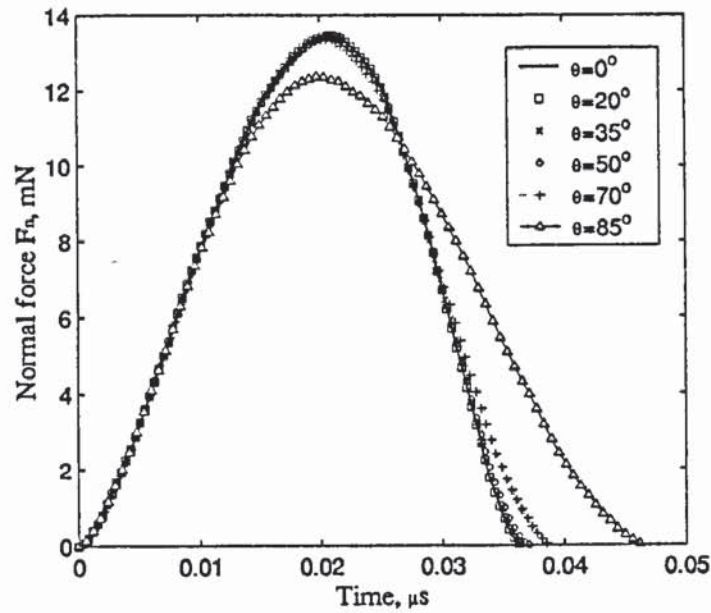


Fig. 8.16 The time histories of apparent normal contact force at various impact angles for frictionless RP impacts with $V_{ni} = 5.0 \text{ m/s}$ ($\mu = 0.0$).

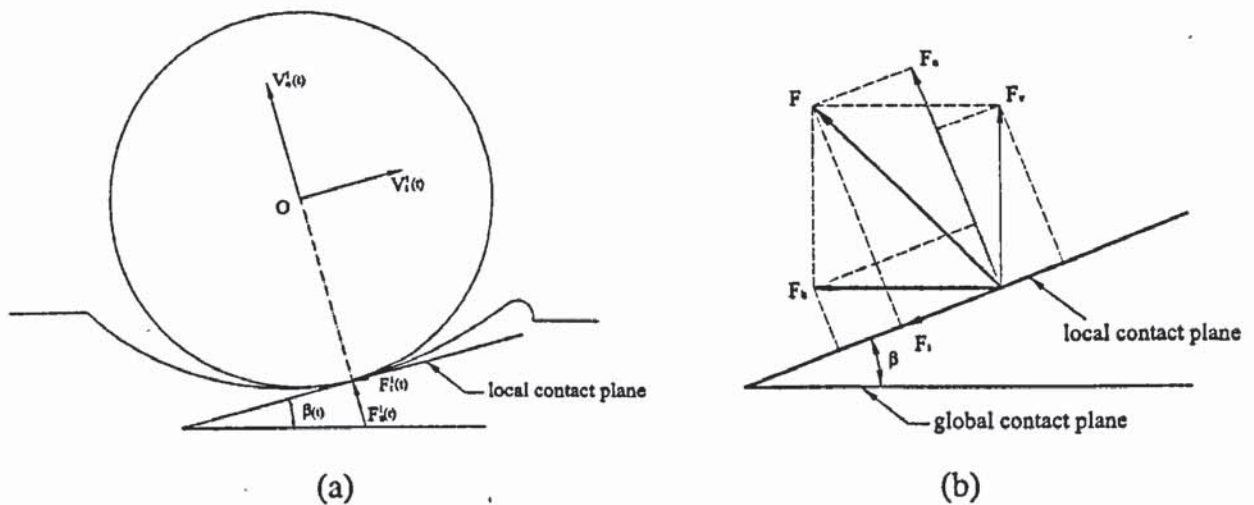


Fig. 8.17 The effect of indentation and prow.

The influence of the crater induced by plastic deformation of the substrate is twofold:

1. Owing to the crater induced in the substrate, the large tangential component of initial velocity (for impacts with a fixed initial normal component) forces the sphere to remain in contact with the substrate, until the sphere moves to the edge of the crater; from which the sphere bounces off, see Figs. 8.3c, 8.4c and 8.5c. This results in a longer duration of impact.

2. Since the sphere is forced to move in the crater that apparently has a curved surface rather than on the original horizontal surface, the orientation of the local contact plane changes during the impact. Due to the change in orientation of the local contact plane, the normal component of contact force with respect to the local contact plane does not act in vertical direction, but acts at an inclined angle β , as illustrated in Fig. 8.17.

From Fig. 8.17b, the normal contact force F_n and the tangential contact force F_t are related to the vertical and tangential forces (F_v , F_h) as follows

$$F_n = F_h \sin \beta + F_v \cos \beta \quad (F_n > F_v \text{ for } \beta > 0) \quad (8.3a)$$

$$F_t = F_h \cos \beta - F_v \sin \beta \quad (F_t < F_h \text{ for } \beta > 0) \quad (8.3b)$$

In the FEA, the vertical and horizontal contact forces were calculated, ignoring any change in contact orientation, and F_v and F_h are plotted in the figures in this chapter. Consequently, when considering high speed glancing impacts against a plastic substrate (as in the case of the constant normal velocity series of impacts) it should be noted that the normal and tangential forces are apparent forces that would be measured by an experimentalist.

In the case of frictionless impacts, it follows from Eqs.(8.3) that

$$F_v = F_n \cos \beta \text{ and } F_h = F_n \sin \beta \quad (8.4)$$

indicating that an apparent tangential force (F_h) may be observed due to the inclination of the contact plane, Fig.8.4. It should also be noted that the angle β is not constant but varies with time during the impact.

8.4.2 Normal force-displacement relationships

The corresponding normal force-displacement relationships for PR, PE, RP and EP impacts at various impact angles are shown in Figs. 8.18-8.22. The static and dynamic friction coefficients are identical ($\mu = 0.3$). Note that in Figs. 8.20-8.22 the force and displacement are given as the apparent values in the vertical direction.

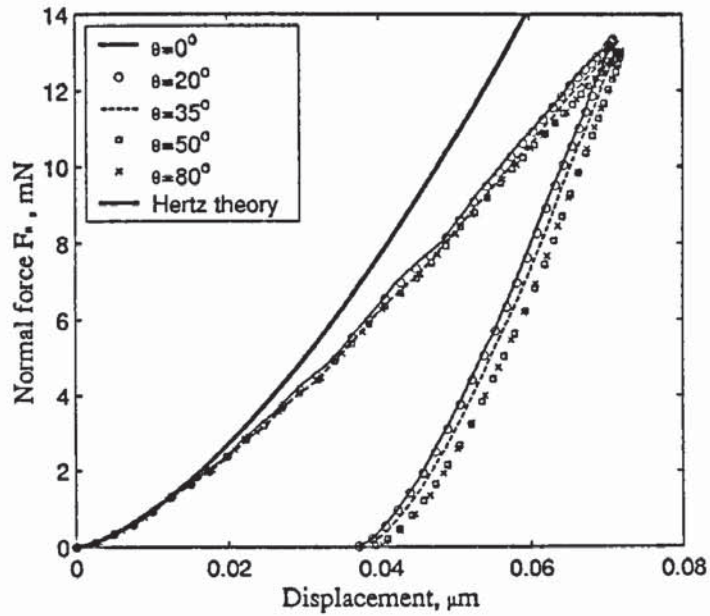


Fig. 8.18 The normal force-displacement relationships for PR impacts at various impact angles with $V_{ni} = 5.0\text{m/s}$ and $\mu = 0.3$.

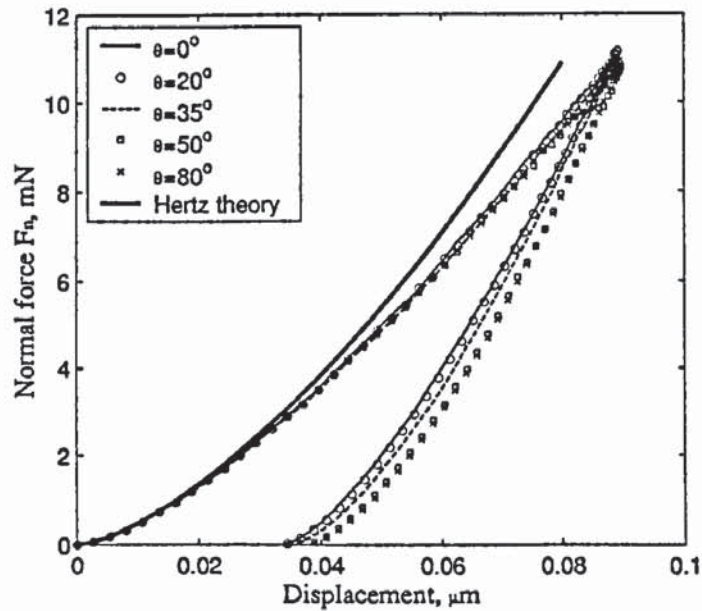


Fig. 8.19 The normal force-displacement relationships for PE impacts at various impact angles with $V_{ni} = 5.0\text{m/s}$ and $\mu = 0.3$.

It can be seen from Figs. 8.18 and 8.19 that, during the initial period of loading, the force-displacement curves for all impact angles follow the curve given by Hertz theory. With the increase of displacement, the curves begin to diverge from Hertz theory. This is due to the effect of plastic deformation. The divergence of the force-displacement curves is mainly found for impacts with intermediate angles. This is because for low impact angles, the friction does not have much influence; while for high impact angles, the tangential response becomes dominant and the friction effect therefore becomes almost identical.

When unrecoverable plastic deformation occurs in the substrate, the force-displacement relationship becomes more complicated. This is because the formation of a permanent crater and a prow affect the normal interaction, as discussed in the previous section. The effect of plastic deformation within the substrate is shown in Figs. 8.20-8.22, which show the normal force-displacement relationships for RP, EP and frictionless RP impacts, respectively. Again, similar results are obtained for RP and EP impacts.

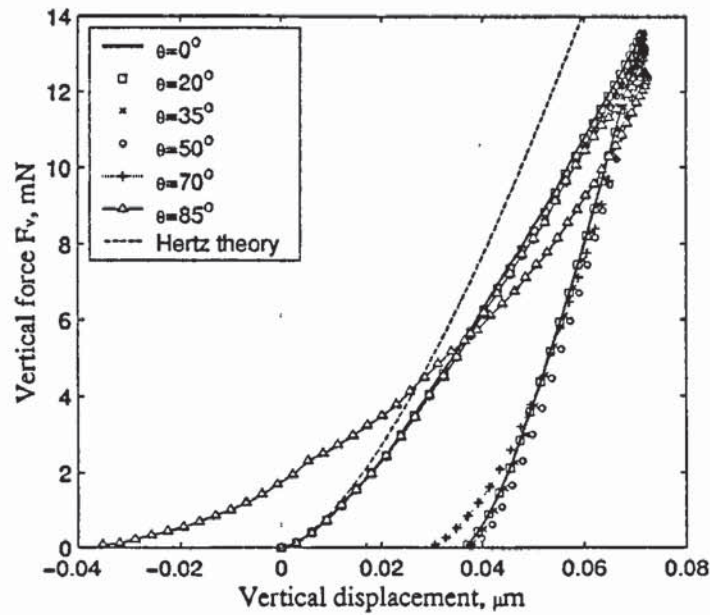


Fig. 8.20 The apparent normal force-displacement relationships for RP impacts at various impact angles with $V_{ni} = 5.0\text{m/s}$ and $\mu = 0.3$.

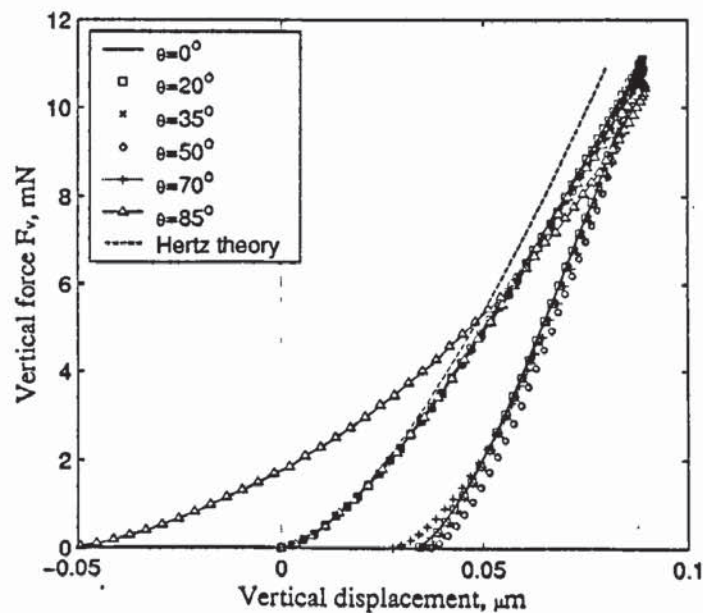


Fig. 8.21 The apparent normal force-displacement relationships for EP impacts at various impact angles with $V_{ni} = 5.0\text{m/s}$ and $\mu = 0.3$.

It is noticed that, for the very high impact angle case ($\theta = 85^\circ$), negative normal displacements are obtained, which indicates that the position of the sphere at separation is

higher than the initial position. This is clearly illustrated by the fact that the value of the contact force is not zero when the normal displacement returns to zero. As expected, the magnitude of the negative displacement is higher for the frictional RP impact than the frictionless RP impact at the same impact angle, since a more significant prow has been formed in the frictional RP impact, as shown in Figs. 8.3 and 8.4.

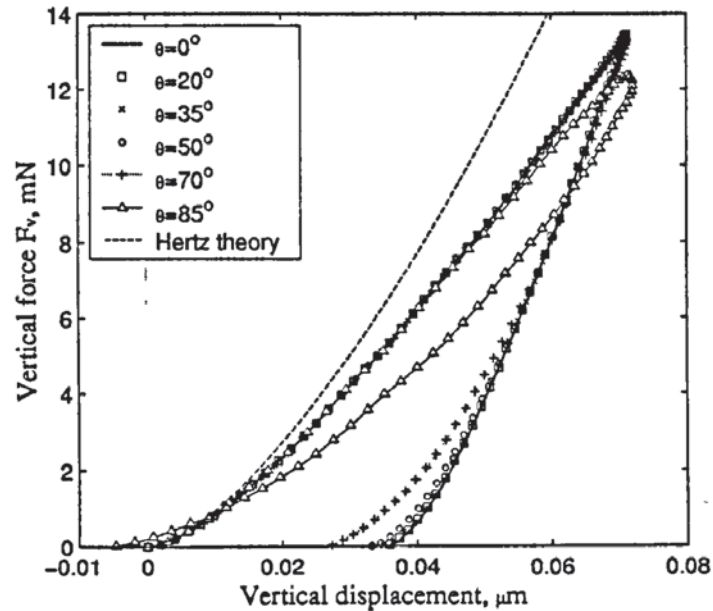


Fig. 8.22 The apparent normal force-displacement relationships for frictionless RP impacts at various impact angles with $V_{ni} = 5.0\text{m/s}$ ($\mu = 0.0$).

8.4.3 Tangential force evolution

Figures 8.23-8.26 present the time evolutions of the tangential force during PR, PE, RP and EP impacts at various impact angles for $\mu = 0.3$. Note that the tangential force shown in Figs. 8.25 and 8.26 is the horizontal component of the contact force. In Figs. 8.23 and 8.24, the solid lines denote the results given by $F_t = |\mu F_n|$, where F_n is determined from the impact at large impact angles (say $\theta > 50^\circ$), because the normal force evolutionary curves are not identical for different impact angles but are substantially the same when the impact angle is larger than 50° , as shown in Figs. 8.12 and 8.13.

The results for PR and PE impacts presented in Figs 8.23 and 8.24 are similar to those for the oblique impacts of elastic particles (see Fig. 7.5). For RP and EP impacts (see Figs.8.25 and 8.26), when the impact angle is small, the apparent tangential force evolution is similar to those for PR and PE impacts. However, when the impact angle is sufficiently high (say

$>60^\circ$), quite different evolution are produced. Furthermore, the impacts appear to persist longer and higher tangential forces than those given by the limit condition are developed. This is due to the change in local contact orientation. As discussed in Section 8.4.1, the longer duration of impact is induced by the formation of a prow and high value of initial tangential velocity. At high impact angles, sliding occurs throughout the impact and the local tangential force F_t is always equal to μF_n . Therefore, from Eq.(8.3), we have

$$\frac{F_h}{F_v} = \frac{\mu \cos \beta + \sin \beta}{\cos \beta - \mu \sin \beta} \geq \mu \quad (8.5)$$

at any instant for any inclined angle $\beta \geq 0$.

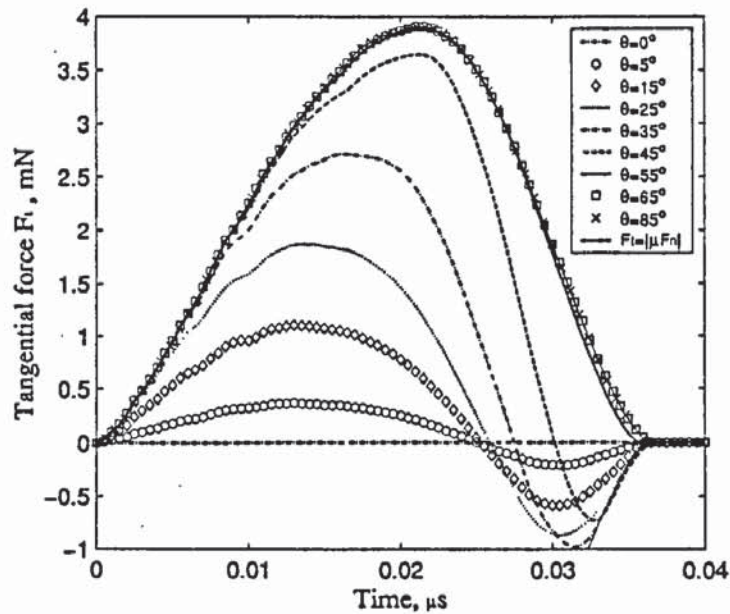


Fig. 8.23 The time evolutions of tangential force for PR impacts at various impact angles with $V_{ni} = 5.0m/s$ and $\mu = 0.3$.

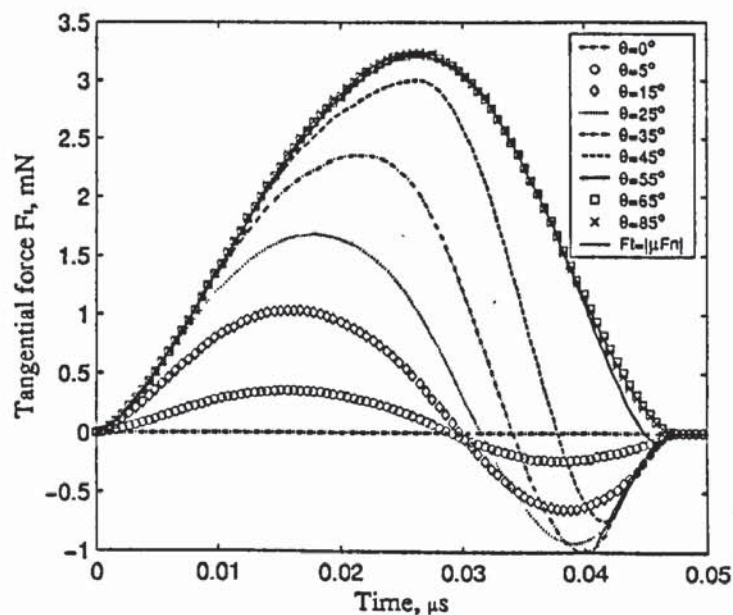


Fig. 8.24 The time evolutions of tangential force for PE impacts at various impact angles with $V_{ni} = 5.0m/s$ and $\mu = 0.3$.

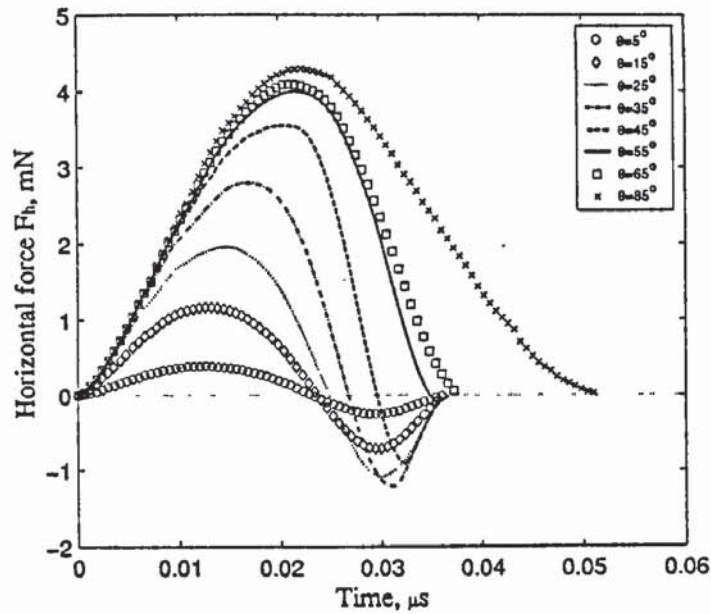


Fig. 8.25 The time evolutions of apparent tangential force for RP impacts at various impact angles with $V_{ni} = 5.0\text{ m/s}$ and $\mu = 0.3$.

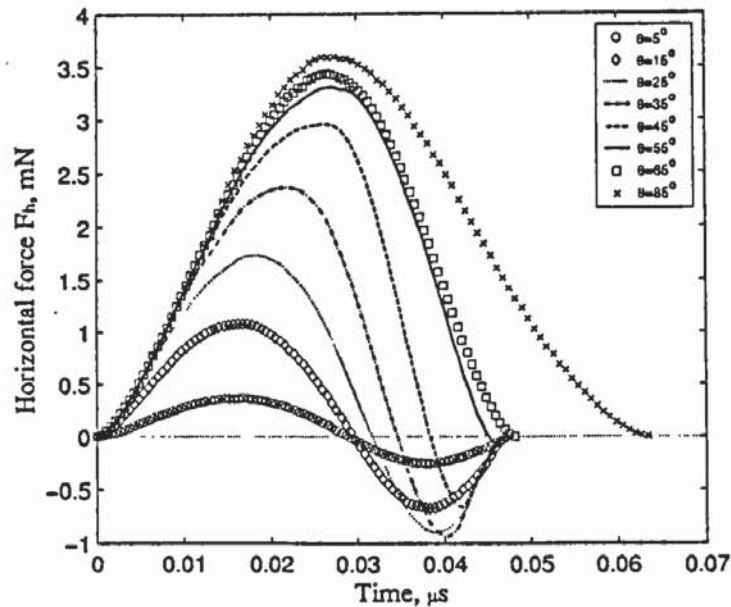


Fig. 8.26 The time evolutions of apparent tangential force for EP impacts at various impact angles with $V_{ni} = 5.0\text{ m/s}$ and $\mu = 0.3$.

8.4.4 Normal-tangential force relationship

The variations of tangential force with normal force are shown in Figs. 8.27-8.30 for PR, PE, RP and EP impacts at various impact angles for $\mu = 0.3$. The solid lines in all these figures represent the limit condition $F_t = |\mu F_n|$. Note that the normal and tangential forces shown in Figs. 8.29 and 8.30 are the normal and tangential components of the contact force with reference to the initial contact plane, *i.e.*, F_v and F_h .

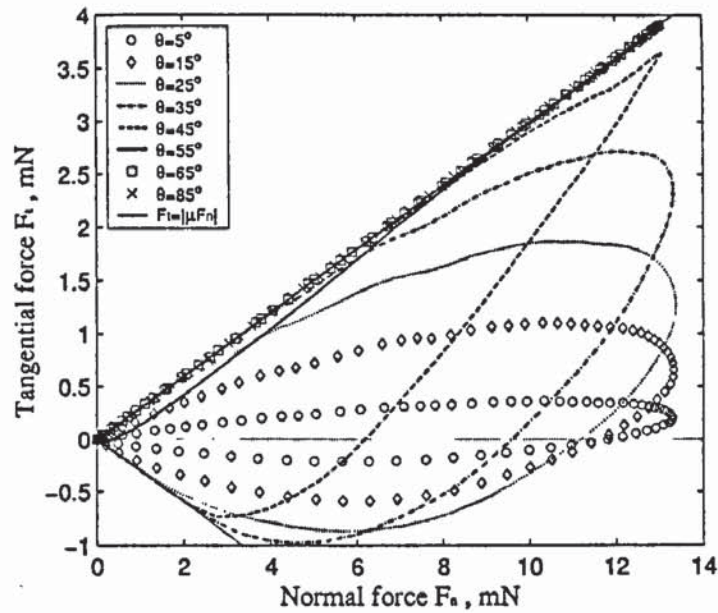


Fig. 8.27 The normal-tangential force relationships for PR impacts at various impact angles with $V_{ni} = 5.0\text{ m/s}$ and $\mu = 0.3$.

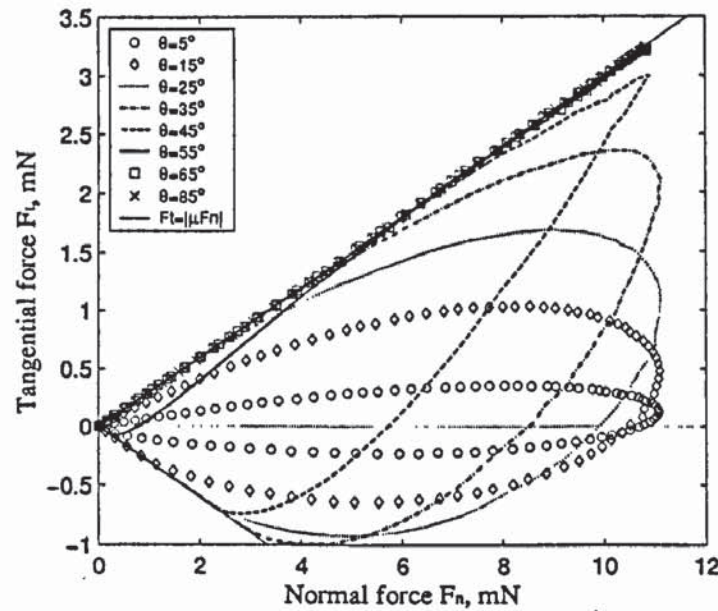


Fig. 8.28 The normal-tangential force relationships for PE impacts at various impact angles with $V_{ni} = 5.0\text{ m/s}$ and $\mu = 0.3$.

Qualitative similarity between the normal-tangential force relationships for PR impact and PE impact can be found in Figs. 8.27 and 8.28. It is clear that, for impacts at relatively large incident angles ($>65^\circ$), the curves follow the line given by $F_t = \mu F_n$. For impacts at small incident angles, the curve does not reach the curves given by $F_t = |\mu F_n|$ until at the very end of the impact. For impacts at intermediate impact angles, the curves coincide with the $F_t = |\mu F_n|$ limits at both the beginning and the end of the impact. This indicates that sliding occurs only at the very end of the impact at low impact angles ($<10^\circ$), at both the beginning and the end of the impact at intermediate impact angles, and throughout the

impact at high incident angles ($>60^\circ$). These characteristics are similar to those in the oblique impact of elastic particles (see Fig. 7.6).

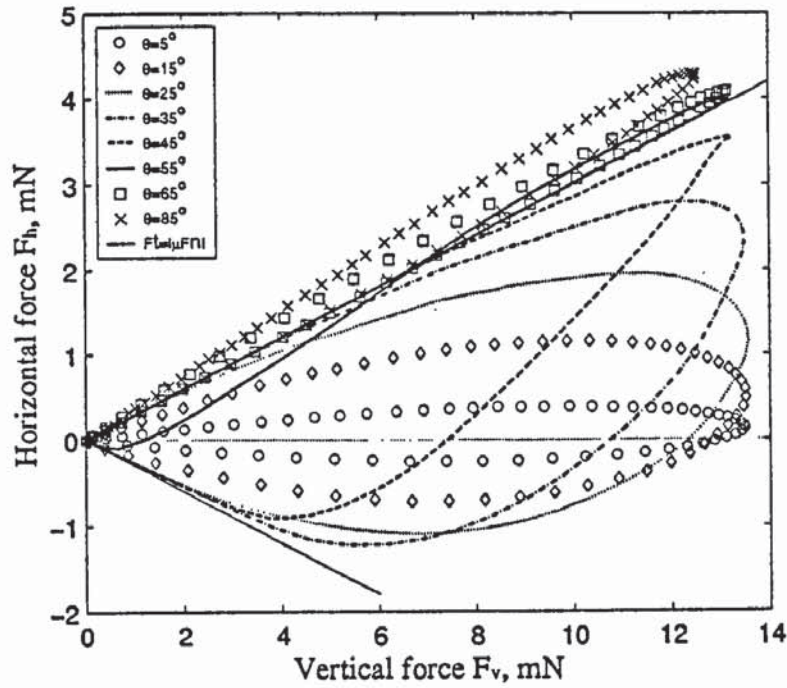


Fig. 8.29 The apparent normal-tangential force relationships for RP impacts at various impact angles with $V_{ni} = 5.0\text{m/s}$ and $\mu = 0.3$.

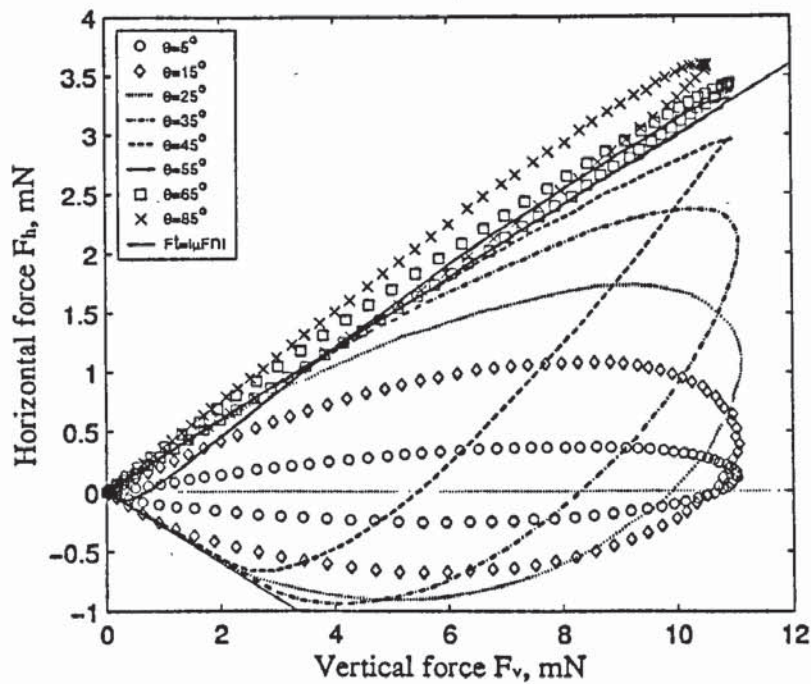


Fig. 8.30 The apparent normal-tangential force relationships for EP impacts at various impact angles with $V_{ni} = 5.0\text{m/s}$ and $\mu = 0.3$.

For RP and EP impacts, however, it is found that the change in local contact plane orientation induced by plastic deformation significantly affects the normal and tangential force evolutions, and thus also affects the apparent normal-tangential force relationships, as

shown in Figs. 8.29 and 8.30. Note that the normal and tangential forces in Figs. 8.29 and 8.30 are apparent forces with respect to vertical and horizontal directions, respectively. It can be seen that, at small impact angles, the pattern of the normal-tangential force relation for RP impacts is similar to those for PR, PE impacts. At large impact angles (say $>65^\circ$), except at the beginning of the impact, the tangential force is apparently greater than the results given by limiting condition $F_t = |\mu F_n|$. This is attributed to the effect of the change in local contact orientation, as illustrated by Eq.(8.5), in which it shows that, for any $\beta(>0)$, F_h / F_v is always larger than μ . This is why the results for large impact angles shown in Figs. 8.29 and 8.30 are apparently above the limiting condition. When the impact angle is small, the change in local contact plane orientation is negligible. Thus, the common feature observed in PR, PE impacts still holds.

8.5 Maximum tangential force

As discussed in previous sections, according to the different characteristics of contact deformation, i.e., whether the orientation of the contact plane changes during the impact, the four impact cases can be classified into two distinct groups: 1) impacts involving plastic deformation in the sphere, in which the substrate is either rigid or elastic; and 2) Impacts involving plastic deformation in the substrate, for which the orientation of the local contact plane changes due to the plastically deformed substrate. In this section, we shall consider the peak tangential force for different impact cases and the corresponding effect of plastic deformation. Here the peak forces are determined from Eqs.(7.34) and (7.36). Note that for the impact against a plastic substrate the tangential force is with reference to the initial contact plane, i.e., the horizontal component of the contact force.

8.5.1 Impacts involving plastic deformation in the sphere

Figure 8.31 shows the variation of the peak tangential force with impact angle for impacts involving plastic deformation in the sphere with $\mu = 0.3$, in which Fig. 8.31a presents the results for PR impacts and Fig. 8.31b presents the results for PE impacts. For each combination, we present the results for three series of tests with different initial velocity conditions: impacts with a fixed initial speed of $V_i = 5.0m/s$ and impacts with fixed initial

normal velocities of $V_{ni} = 2.0\text{m/s}$ and 5.0m/s . It can be seen that the overall variation of the peak tangential force with impact angle for PR impacts with different initial velocity conditions are similar to those for PE impacts. For impacts with a fixed initial speed the peak tangential force increases with the increase of impact angle until $\theta = 45^\circ$, at which the peak tangential force reaches its maximum. When the impact angles is larger than 45° , the peak tangential force decreases with the further increasing impact angle. For impacts with fixed initial normal velocity, the peak tangential force increases as the impact angle increases until the impact angle reaches a certain value (around 45° for impacts with $V_{ni} = 2.0\text{m/s}$ and around 50° for impacts with $V_{ni} = 5.0\text{m/s}$). At higher impact angles, in contrast to the impacts with a fixed initial speed, the peak tangential force remains constant.

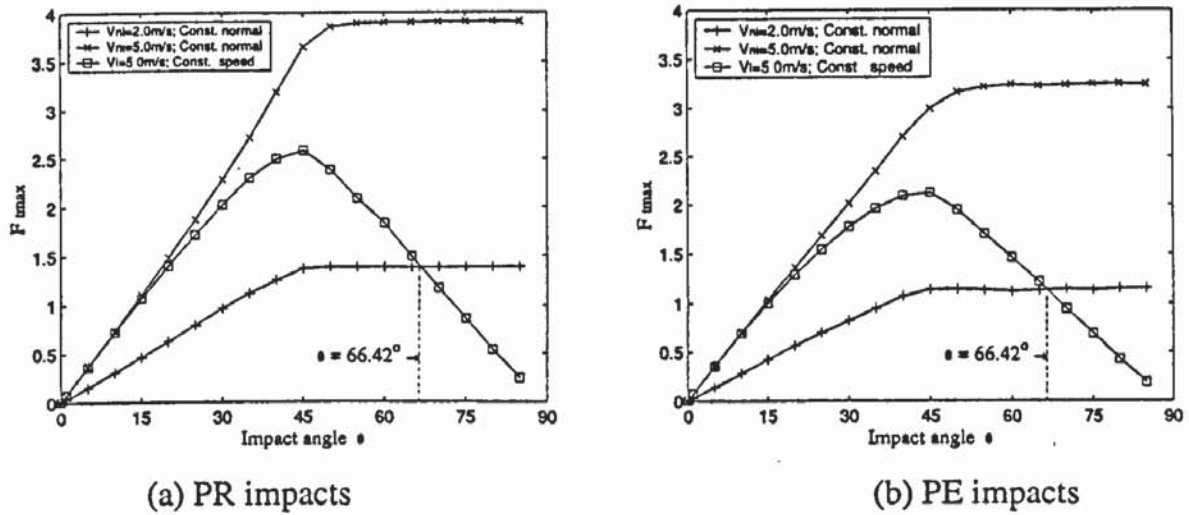


Fig. 8.31 The variation of peak tangential force with impact angle for impacts involving plastic deformation in the sphere with $\mu = 0.3$.

At large impact angles, the peak tangential force is generated simultaneously as the peak normal force is, see Figs. 8.23 and 8.24, and the peak tangential force is proportional to the peak normal force according to Coulomb's law of dry friction. Since the normal component of the initial velocity decreases as the impact angle increases if the initial speed is fixed, the peak normal contact force will decrease as the impact angle increases. As a result, the peak tangential force decreases as the impact angle increases. However, for impacts with fixed initial normal velocity, the peak normal contact force is essentially identical for impacts at large impact angles (see Figs. 8.12 and 8.13) and, therefore, the peak tangential force remains unchanged.

As can be expected from Eq.(7.38), the curve for the impact with a fixed initial speed $V_i = 5.0m/s$ intersects with that with a fixed initial normal velocity $V_{ni} = 2.0m/s$ at $\theta = 66.42^\circ$. Comparing with the results for elastic impacts shown in Fig. 7.12, we find that the critical impact angles for the peak tangential force reaching its limit is slightly increased as the extent of plastic deformation is intensified. For example, for impacts with a fixed initial speed, the critical impact angle is increased from around 40° for elastic impacts to 45° for the plastic impact. For impacts with a fixed initial normal velocity of $V_{ni} = 5.0m/s$, the critical impact angle is increased from around 45° for elastic impacts to 50° for the plastic impact.

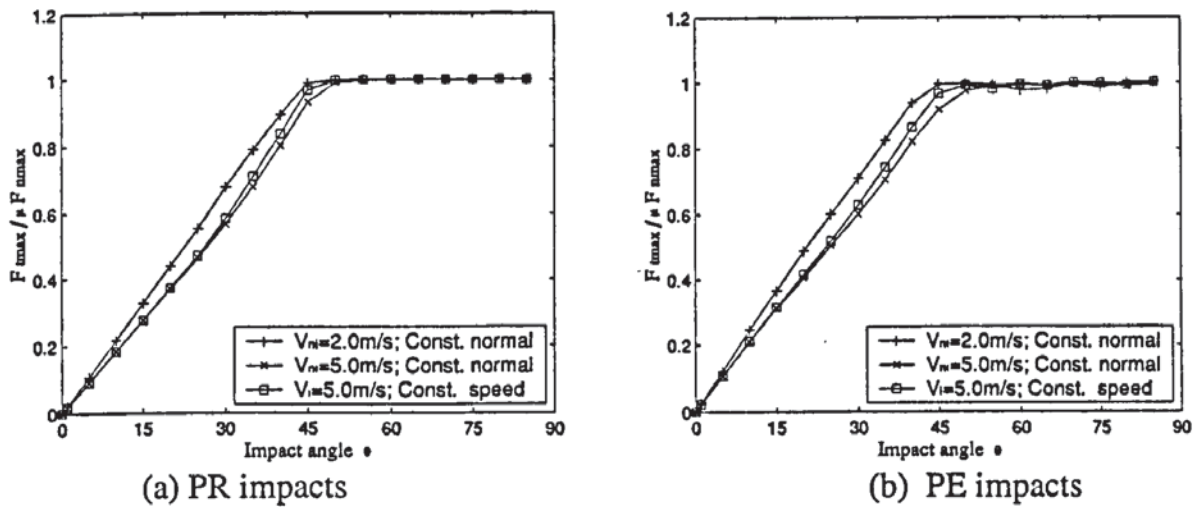


Fig. 8.32 The variation of $F_{t,max} / \mu F_{n,max}$ with impact angle for impacts involving plastic deformation in the sphere with $\mu = 0.3$.

The corresponding normalised peak tangential force $F_{t,max} / \mu F_{n,max}$ is shown in Fig. 8.32 for both PR (Fig. 8.32a) and PE impacts (Fig. 8.32b). Again, similar patterns are observed. It can be seen that, at large impact angles, the results for all impact cases merge together and are equal to unity, regardless of the initial velocity conditions. This is because at large impact angles the peak tangential force is simply equal to the peak normal force times the friction coefficient. At small impact angles, there are discrepancies between the three sets of results: the lower the initial normal velocity, the higher the peak tangential force. This implies that the peak tangential force is somehow reduced with the existence of the plastic deformation. Comparing with the results for elastic impacts shown in Fig. 7.9, the critical impact angle for the normalised peak tangential force $F_{t,max} / \mu F_{n,max}$ is found to increase slightly with the plastic deformation.

8.5.2 Impacts involving plastic deformation in the substrate

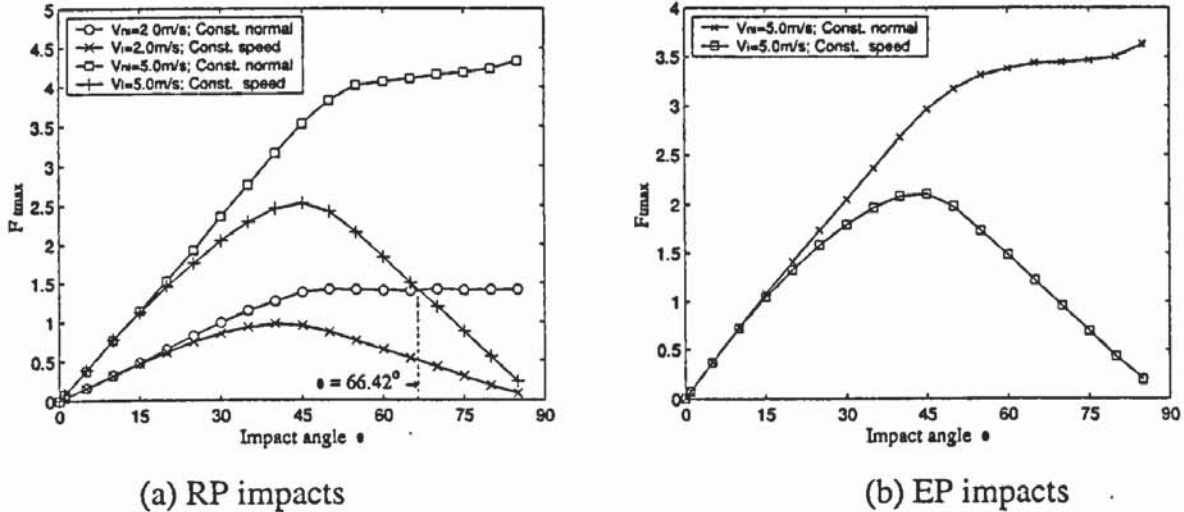


Fig. 8.33 The variation of peak tangential force with impact angle for impacts involving plastic deformation in the substrate with $\mu = 0.3$.

The variations of the peak tangential force with impact angle for impacts with plastic deformation in substrates are shown in Fig. 8.33. It is clear that similar patterns are observed for both RP and EP impacts. For impacts with a fixed initial speed, they are similar to those in PR and PE impacts. For impacts with a fixed initial normal velocity, at small impact angles, the peak tangential force increases as the impact angle increases. At large impact angles, the peak tangential force increases with impact angle although at a very slow rate, which is in contrast to the impacts with plastic spheres as shown in Fig. 8.31. In addition, the rate of increase in the peak tangential force increases as the value of the initial normal velocity increases. The increase of the peak tangential force at large impact angles is due to the change in orientation of local contact plane, which generally produces a higher apparent tangential forces as discussed before.

Figure 8.34 shows the corresponding normalised peak tangential force $F_{t \max} / \mu F_{n \max}$ for RP (Fig. 8.34a) and EP impacts (Fig. 8.34b) with different initial velocity conditions. It is clear that, at small impact angles, the normalised peak tangential force $F_{t \max} / \mu F_{n \max}$ increases as the impact angle increases. In addition, an apparent discrepancy exists between the different initial impacts conditions. When the impact angle is greater than a certain value, the peak tangential force $F_{t \max}$ essentially remains constant at $\mu F_{n \max}$ for impacts with a fixed initial speed, but increases slightly for those with fixed initial normal velocities owing to the change in the orientation of local contact plane. Furthermore, the higher the

initial normal velocity, the higher the increase in peak tangential force at large impact angles, which indicates that a more significant change in the orientation of the local contact plane takes place. Moreover, the critical angle at which the peak tangential force $F_{t\max}$ appears to reach $\mu F_{n\max}$ slightly increases as the normal component of the initial velocity increases.

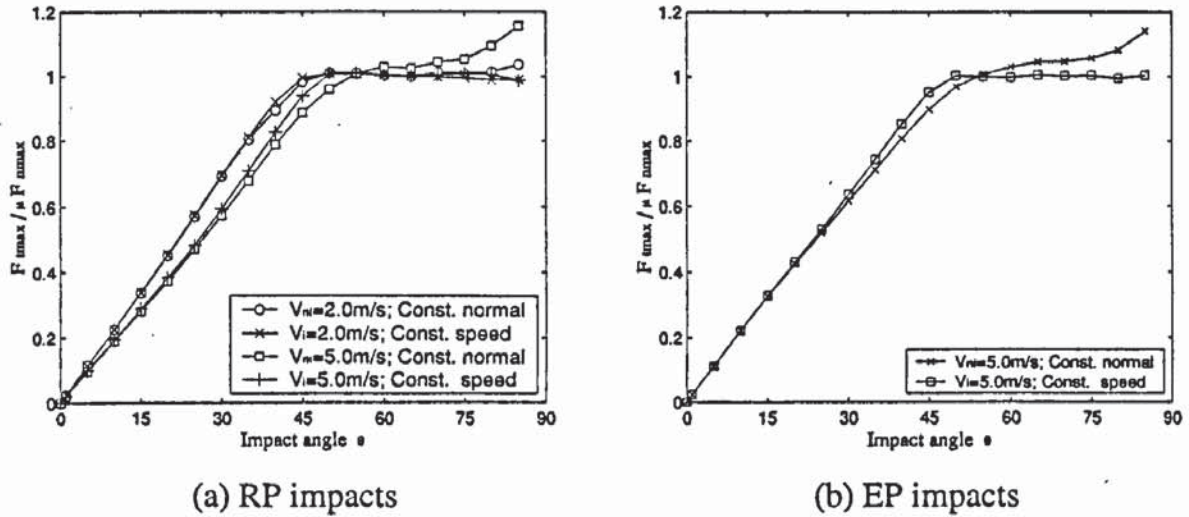


Fig. 8.34 The variation of $F_{t\max} / \mu F_{n\max}$ with impact angle for impacts involving plastic deformation in the substrate with $\mu = 0.3$.

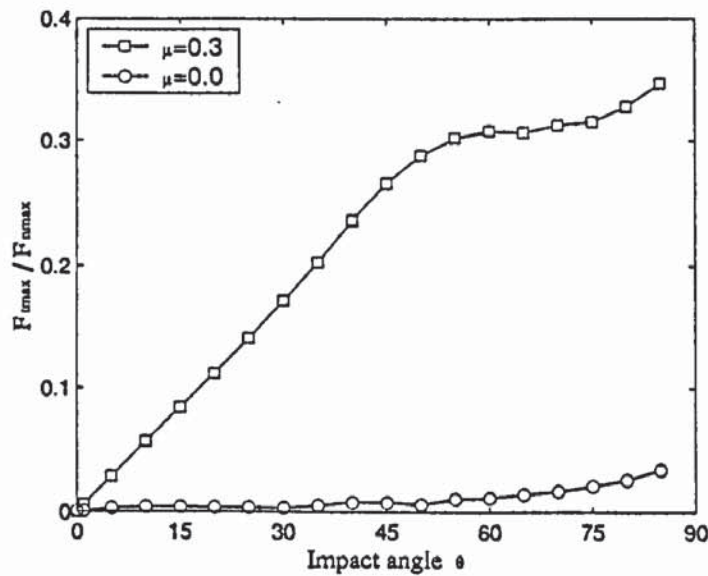


Fig. 8.35 The variation of $F_{t\max} / F_{n\max}$ with impact angle for the frictional ($\mu = 0.3$) and frictionless ($\mu = 0.0$) RP impacts with constant normal velocity $V_{ni} = 5.0\text{m/s}$.

In order to further illustrate the effect of the change in orientation of the local contact plane induced by plastic deformation of the substrate, Fig. 8.35 shows the variation of normalised peak tangential force $F_{t\max} / F_{n\max}$ with impact angle for the frictional

($\mu = 0.3$) and frictionless ($\mu = 0.0$) RP impacts with a fixed normal velocity $V_{ni} = 5.0 \text{ m/s}$. It is obvious that there should be no tangential force if no friction is present over the interface. The FEA shows that for frictionless RP impacts, the apparent peak tangential force is negligible at small impact angles, but when the impact angle is larger than 50° , it gradually increases as the impact angle increases which is similar to the frictional RP impact; and it reaches around 10% of $F_{n\max}$ at $\theta = 85^\circ$. The apparent increase of $F_{t\max}$ in frictional and frictionless RP impacts at large impact angles is due to the change in orientation of the local contact plane, which is induced by plastic deformation in the substrate (Figs. 8.3-8.5) and the high value of initial tangential velocity that forces the sphere in contact with the indentation at an inclined contact plane, see Fig. 8.17. In the presence of friction, the orientation of the local contact plane changes more significantly. It is also clear that the higher the plastic deformation of the substrate, the more significant the change in local contact plane orientation.

8.6 Impulse ratio

As mentioned in Section 7.2, the impulse ratio f is one of the key factors required to predict the rebound behaviour of particles due to oblique impacts, and it reflects the relationship between the tangential and normal interactions. In this section, we shall consider the influence of plastic deformation on the impulse ratio f for PR, PE, RP and EP impacts under different initial velocity conditions.

8.6.1 Impacts involving plastic deformation in the sphere

The variations of normalised impulse ratio f/μ with impact angle for PR and PE impacts are shown in Fig. 8.36a and Fig. 8.36b. It can be seen that the results for PR and PE impacts are very much similar. The normalised impulse ratio f/μ increases with the impact angle until the impact angle reaches a critical angle. Then as the impact angle further increases, the normalised impulse ratio remains constant at a value of unity. The range of impact angles in which the impulse ratio $f = \mu$ corresponds to impacts in which sliding occurs throughout the impact. It is clear that, for all PR and PE impacts, sliding occurs throughout the impact when the impact angle is larger than 60° , which is identical to

that for impacts of elastic particles (see Fig. 7.14). This implies that the plastic deformation does not change the criteria for sliding occurring throughout the impact.

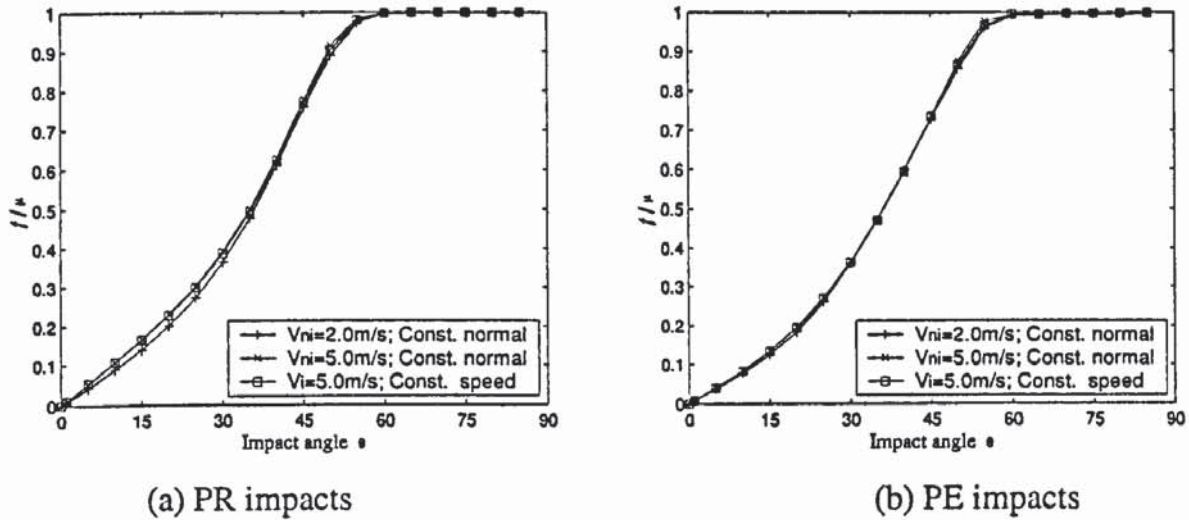
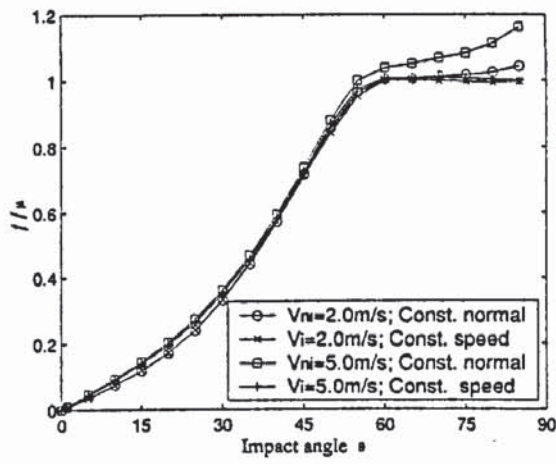


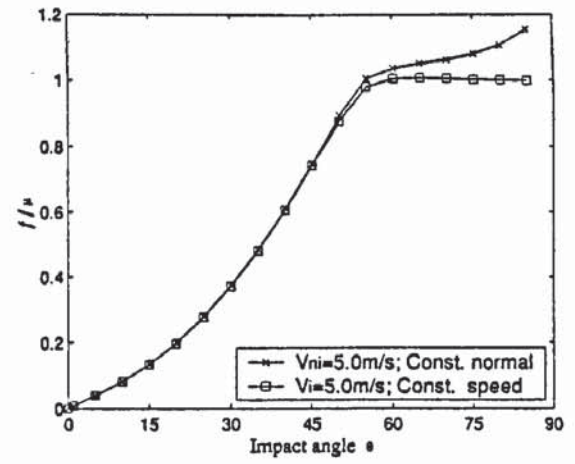
Fig. 8.36 The variation of f/μ with impact angle for impacts involving plastic deformation in the sphere with $\mu = 0.3$.

8.6.2 Impacts involving plastic deformation in the substrate

Figure 8.37 shows the apparent variation of normalised impulse ratio f/μ with impact angle for RP and EP impacts. It can be seen that at small impact angles, the normalised impulse ratio f/μ increases with impact angles. However, at large impact angles, two different trends are obtained for impacts with fixed initial speeds and with fixed initial normal velocities. The normalised impulse ratio f/μ obtained for a fixed initial speed remains equal to unity at high impact angles. However, the normalised impulse ratio f/μ for impacts with a fixed initial normal velocity apparently increases with impact angle at high impact angles, which is again due to the change in the orientation of the local contact plane. The normalised impulse ratio f/μ begins to reach a value of unity at around 60° , which is similar to impacts with plastic spheres as shown in Fig. 8.36. The apparent increase in f/μ at large impact angles becomes more significant for impacts with a higher initial normal velocity, see Fig. 8.37a. For impacts with fixed initial speeds, both the normal and tangential components of the initial velocity are small with respect to the impacts with a fixed normal velocity. Therefore, at large impact angles, the crater formed during impacts with fixed initial speeds is insignificant. Hence, the normalised impulse ratio f/μ remains constant at unity at large impact angles for impacts with a fixed initial speed.



(a) RP impacts



(b) EP impacts

Fig. 8.37 The apparent variation of f/μ with impact angle for impacts involving plastic deformation in the substrate with $\mu = 0.3$.

From Fig. 8.17b, the apparent impulse ratio, f' , can be defined as

$$f' = \frac{\int F_h dt}{\int F_v dt} = \frac{\int (F_n \sin \beta + F_t \cos \beta) dt}{\int (F_n \cos \beta - F_t \sin \beta) dt} \quad (8.6)$$

Since $F_t \equiv \mu F_n$ when sliding occurs throughout the impact, Eq.(8.6) becomes

$$f' = \frac{\int (F_n \sin \beta + \mu F_n \cos \beta) dt}{\int (F_n \cos \beta - \mu F_n \sin \beta) dt} = \frac{\int (\sin \beta + \mu \cos \beta) dt}{\int (\cos \beta - \mu \sin \beta) dt} \quad (8.7)$$

It is clear that for any inclined angle $\beta (\geq 0)$, $\int (\sin \beta + \mu \cos \beta) dt \geq \int \mu \cos \beta dt$ and $\int (\cos \beta - \mu \sin \beta) dt \leq \int \cos \beta dt$. Thus, we obtain

$$f' = \frac{\int (\sin \beta + \mu \cos \beta) dt}{\int (\cos \beta - \mu \sin \beta) dt} \geq \mu \quad (8.8)$$

For $\mu = 0$, Eq.(8.7) becomes

$$f' = \frac{\int \sin \beta dt}{\int \cos \beta dt} = \tan \beta \quad (8.9)$$

Therefore, as a consequence of the inclination of the local contact plane the apparent impulse ratio is higher than the friction coefficient μ , as shown in Fig. 8.37. It is also apparent from Eq.(8.9) that, for frictionless impact, the apparent impulse ratio f' will be non-zero if the inclination of the local contact plane is induced. This is demonstrated by finite element analysis as presented in Fig. 8.38, which shows the results for frictional and frictionless RP impacts with a fixed initial normal velocity of $V_{ni} = 5.0\text{m/s}$. In theory, the

impulse ratio for frictionless impact should be zero. This is true for frictionless RP impacts at small impact angles (say $<60^\circ$), in which the impulse ratio f is close to zero. However, when the impact angle is greater than 60° , the apparent impulse ratio is no longer negligible. Moreover, the apparent impulse ratio f' begins to increase with impact angle. This is clearly due to the change in orientation of local contact plane as discussed above.

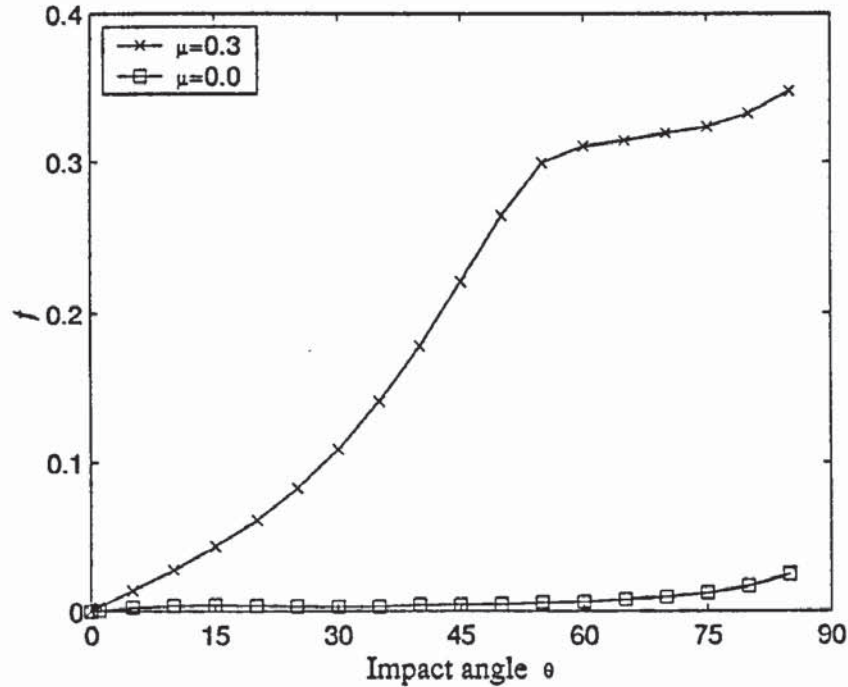


Fig. 8.38 The variation of apparent impulse ratio f with impact angle for the frictional ($\mu = 0.3$) and frictionless ($\mu = 0.0$) RP impacts with constant normal velocity $V_{ni} = 5.0m/s$.

8.7 Kinetic energy loss and coefficient of restitution

Kinetic energy loss and coefficients of restitution during oblique impact of elastic particles have been discussed in Section 7.7. It has been shown that, for the oblique impact of elastic particles, the total initial kinetic energy W_i can be considered as a summation of three parts: initial normal translational kinetic energy W_{ni} ; initial tangential translational kinetic energy W_{ti} and initial rotational kinetic energy W_{ri} . The transformation of the kinetic energy during the oblique impact of elastic particles has been illustrated in Fig. 7.19. For the oblique impact of plastic particles, the kinetic energy transformation becomes more complicated since some kinetic energy would be dissipated by plastic deformation, which will be denoted by W_p , and coupling between the normal and tangential response may become significant. Idealistically, we may assume that the

coupling between the normal and tangential response is negligible and the work done due to plastic deformation only dissipates the normal translational kinetic energy. The transformation of kinetic energy can hence be depicted by Fig. 8.39. Comparing Fig. 8.39 with Fig. 7.19, the transformation of the kinetic energy for elastic oblique impacts can be regarded as a special case of the plastic oblique impacts with $W_p = 0$. Since the kinetic energy loss can be estimated by the coefficients of restitution (e , e_n and e_t), we shall consider the effect of plastic deformation on the coefficients of restitution in this section.

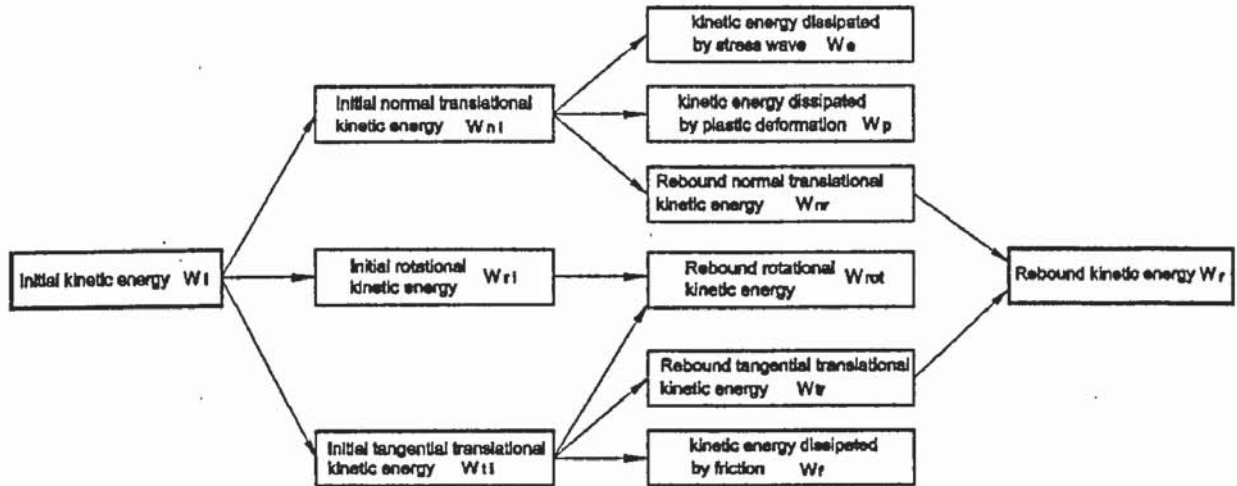


Fig. 8.39 Transformation of kinetic energy during the oblique impact of plastic particles.

8.7.1 Impacts involving plastic deformation in the sphere

Figure 8.40 shows the variation of the normal coefficient of restitution with impact angle for impacts with plastic spheres (PR and PE impacts) under different initial velocity conditions. It can be seen that, qualitatively, the results for PR impacts (Fig. 8.40a) and PE impacts (Fig. 8.40b) are similar. The intersection between the curves for the impacts with a fixed initial normal velocity $V_{ni} = 2.0m/s$ and with a fixed initial speed $V_i = 5.0m/s$ at $\theta = 66.42^\circ$ again demonstrates that the FEA gives the same results for impacts with the same initial velocity condition. Two distinct trends are obtained between impacts with a fixed initial speed and a fixed initial normal velocity: For the latter, the normal coefficient of restitution keeps essentially identical when the impact angle is small (say $<15^\circ$). As the impact angle increases the normal coefficient of restitution begins to reduce. Finally, the normal coefficient of restitution remains constant again once the impact angle is larger than a certain angle. This critical angle decreases as the initial normal velocity increases. For

example, the critical impact angle is around 45° for initial normal velocity $V_{ni} = 2.0\text{m/s}$, and around 50° for initial normal velocity $V_{ni} = 5.0\text{m/s}$.

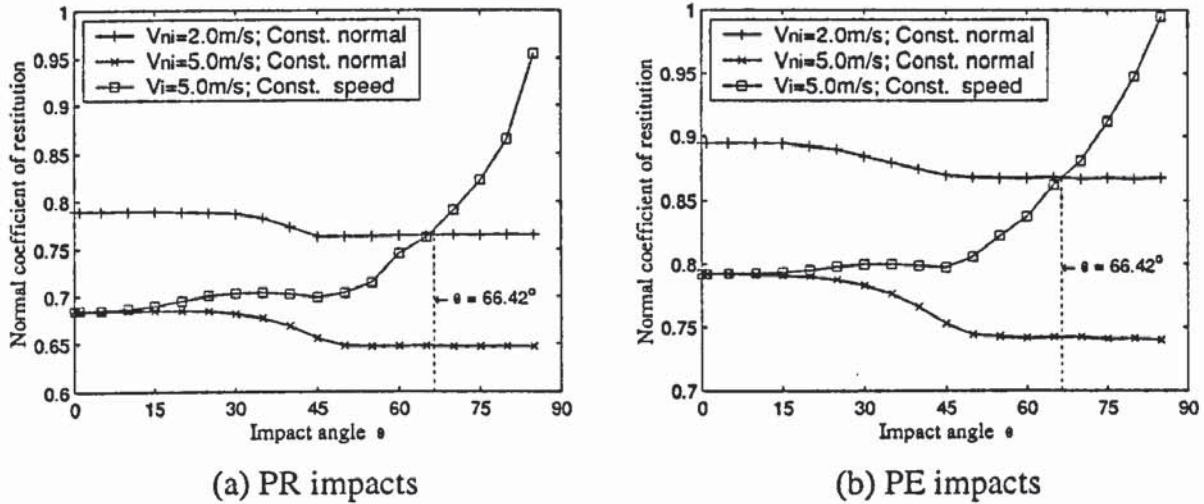


Fig. 8.40 The variation of normal coefficient of restitution with impact angle for impacts involving plastic deformation in the sphere with $\mu = 0.3$.

The reduction of the normal coefficient of restitution at the intermediate impact angles is apparently due to the effect of the frictional force (tangential force). The frictional force reduces the tangential translational kinetic energy by doing frictional work and transforming some translational kinetic energy into rotational kinetic energy. It also increases the amount of plastic deformation within the plastic sphere (See Figs. 8.8 and 8.9). This leads to more normal translational kinetic energy being dissipated by the enhanced plastic deformation (Wu *et. al.*, 2001). It is understood that both normal force and frictional (tangential) force contribute to the plastic deformation since the plastic deformation depends on the total resultant force. Thus, the maximum plastic deformation depends on the maximum resultant force. This means that, if the tangential force reaches its maximum simultaneously with the normal force, the higher the maximum tangential force, the more significant the plastic deformation, and therefore more kinetic energy is dissipated. It has been shown in Fig. 8.31 that the peak tangential forces for impacts with a fixed initial normal velocity are identical when the impact angle is larger than 45° for $V_{ni} = 2.0\text{m/s}$ and 50° for $V_{ni} = 5.0\text{m/s}$. This is why the normal coefficient of restitution remains unchanged at large impact angles.

However, for impacts with fixed initial speeds, the normal coefficient of restitution always increases with impact angle. Nevertheless, it is worth noting that there are still some dips at intermediate impact angles. This more or less indicates the effect of the tangential

responses on the normal coefficient of restitution. As discussed before, the normal velocity component decreases with impact angle if we fix the initial speed, and the normal coefficient of restitution depends strongly on the initial normal velocity component, and it increases as the initial normal velocity decreases. This means that the normal coefficient of restitution should keep increasing with impact angle if the tangential force does not affect the normal coefficient of restitution. In addition, it will reach a value of unity when the initial normal velocity component is less than the yield velocity V_{y0} as defined in Eq.(5.2).

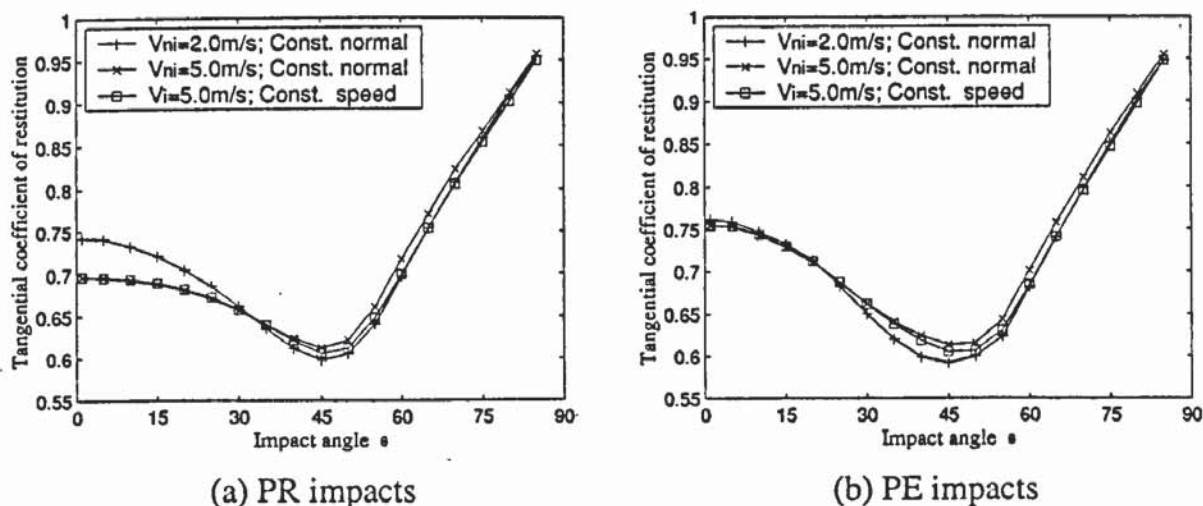


Fig. 8.41 The variation of tangential coefficient of restitution with impact angle for impacts involving plastic deformation in the sphere with $\mu = 0.3$.

The corresponding tangential coefficient of restitution is plotted against the impact angle in Fig. 8.41 for PR and PE impacts. It can be seen that the overall patterns for these two impact cases are similar. The tangential coefficient of restitution reaches its minimal at around 45° . A higher value of the minimal tangential coefficient of restitution is obtained for the impact with a higher initial normal velocity. However, when the impact angle approaches to zero, i.e., close to normal impact, the limit value of the tangential coefficient of restitution decreases with increasing initial normal velocity component. The variation of the tangential coefficient of restitution with impact angle for plastic oblique impacts is qualitatively similar to that in elastic oblique impacts. This indicates that it is the frictional force that not only does frictional work but also transforms some translational kinetic energy into the rotational kinetic energy, as discussed in Section 7.7.

8.7.2 Impacts involving plastic deformation in the substrate

The variation of the normal coefficient of restitution with impact angle for RP and EP impacts is shown in Fig. 8.42. For impacts with fixed initial speeds, the normal coefficient of restitution always increases with increasing impact angle although there are some apparent dips at intermediate impact angles, which is similar to that observed in the PR and PE impacts. For impacts with fixed initial normal velocities, the results are similar to those in PR and PE impacts only at low and intermediate impact angles, where the normal coefficient of restitution keeps essentially constant at low impact angles and decreases with the increase of impact angle at intermediate impact angles. At large impact angles, however, the normal coefficient of restitution apparently increases with impact angle. In addition, for both RP and EP impacts with a fixed initial normal velocity $V_{ni} = 5.0\text{ m/s}$ at $\theta = 85^\circ$, the apparent normal coefficients of restitution are found to be larger than unity, which is unexpected. This is due to the change in orientation of the local contact plane (see Figs. 8.3-8.5).

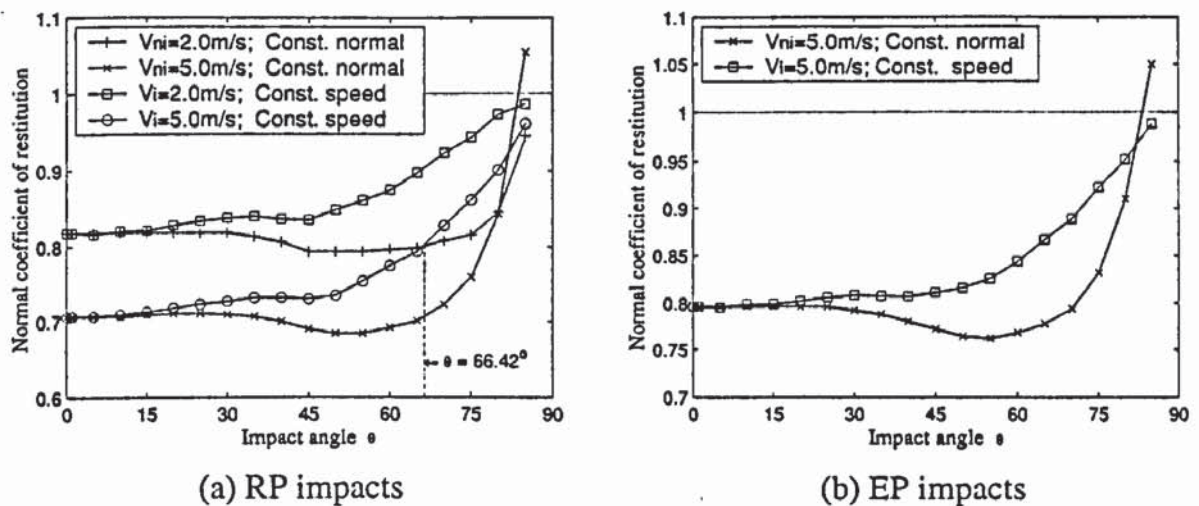


Fig. 8.42 The variation of the normal coefficient of restitution with impact angle for impacts involving plastic deformation in the substrate with $\mu = 0.3$.

The coefficients of restitution presented are referenced to the initial contact plane. However, if the normal coefficient of restitution is calculated by using the velocity normal to the deformed contact surface (local contact plane) rather than the generally used normal component referred to the initial contact plane, then its value will always be less than unity. Figure 8.43 illustrates the effect of the change in orientation of the local contact plane upon the normal coefficient of restitution. Suppose that the sphere rebounds with a rebound velocity V_r at an apparent rebound angle θ'_r and the local contact plane is inclined at an angle β , as shown in Fig. 8.43. The true rebound angle $\theta_r = \theta'_r + \beta$ and

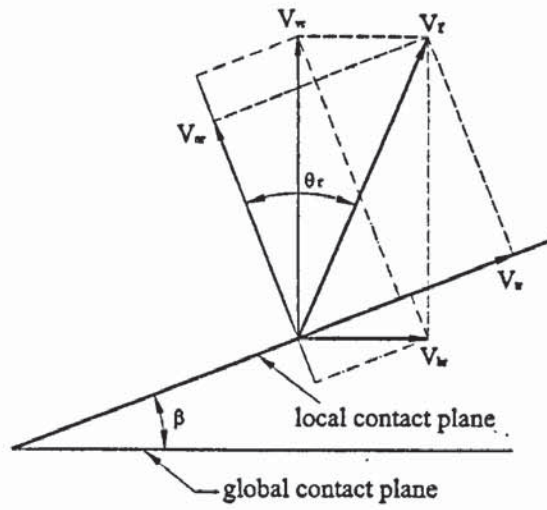


Fig. 8.43 The effect of the change in orientation of the local contact plane on the rebound of particles.

$$V_{vr} = V_r \cos \theta_r' \quad (8.9a)$$

$$V_{hr} = V_r \sin \theta_r' \quad (8.9b)$$

Similarly, the normal and tangential components of rebound velocity V_r , with respect to the local contact plane are obtained:

$$V_{nr} = V_r \cos(\theta_r' + \beta) \quad (8.10a)$$

$$V_{tr} = V_r \sin(\theta_r' + \beta) \quad (8.10b)$$

Also from Fig. 8.43

$$V_{nr} = V_{vr} \cos \beta - V_{hr} \sin \beta \quad (8.11a)$$

$$V_{tr} = V_{vr} \sin \beta + V_{hr} \cos \beta \quad (8.11b)$$

The true coefficients of restitution are defined as

$$e_n = V_{nr} / V_{ni} \quad e_t = V_{tr} / V_{ti} \quad (8.12a)$$

and the apparent coefficients as

$$e_n' = V_{vr} / V_{ni} \quad e_t' = V_{hr} / V_{ti} \quad (8.12b)$$

Consequently

$$e_n = e_n' \cos \beta - e_t' \tan \theta \sin \beta \quad (8.13a)$$

$$e_t = e_n' \cot \theta \sin \beta + e_t' \cos \beta \quad (8.13b)$$

It can be seen that e_n is generally less than e_n' . As an example, the coefficients of restitution for RP impacts with a fixed initial normal velocity $V_{ni} = 5.0m/s$ at $\theta = 85^\circ$ shown in Fig. 8.42 are introduced into Eq.(8.13) to illustrate how the true coefficients of restitution (e_n, e_t) depend on the inclined angle β . The result is shown in Fig. 8.44. It is

clear that the true normal coefficient of restitution e_n reduces sharply as the inclined angle increases, and when the inclined angle β is as small as 0.2° , the true normal coefficient of restitution e_n is reduced to a value less than unity. The true tangential coefficient of restitution essentially remains constant at the value equal to the apparent tangential coefficient of restitution. This indicates that the effect of the change in the orientation of local contact plane on the apparent normal coefficient of restitution is much more significant than on the apparent tangential coefficient of restitution.

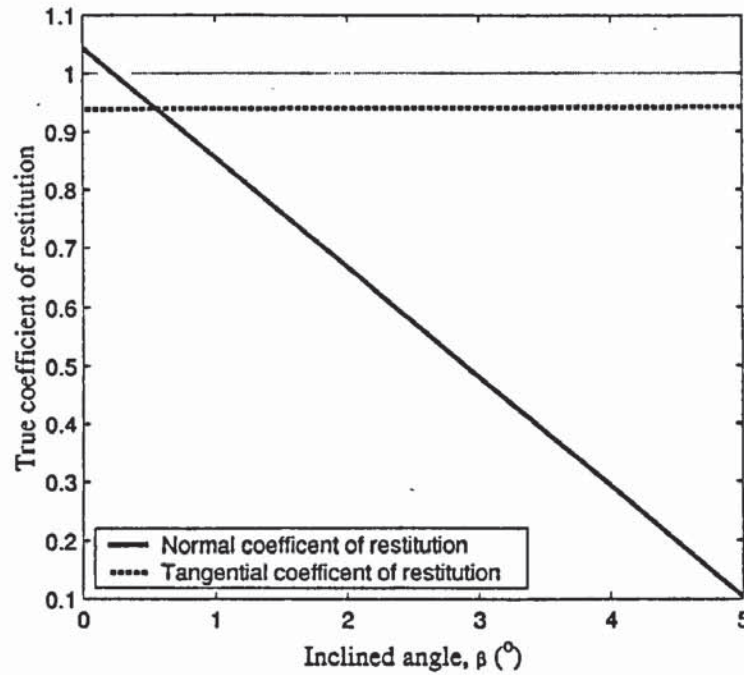


Fig. 8.44 Effect of contact plane inclination on the true coefficients of restitution for the RP impact with $V_{ni} = 5.0\text{m/s}$ at $\theta = 85^\circ$.

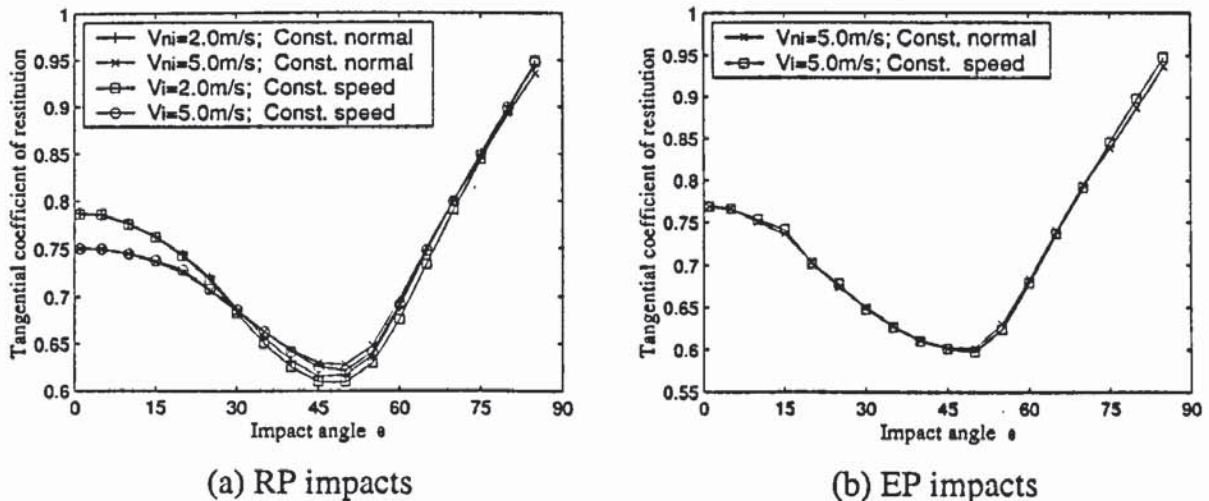


Fig. 8.45 The variation of tangential coefficient of restitution with impact angle for impacts involving plastic deformation in the substrate with $\mu = 0.3$.

The corresponding tangential coefficients of restitution for RP and EP impacts are shown in Fig. 8.45. It is clear that the tangential coefficient of restitution for impacts with fixed initial normal velocity components and fixed initial speeds are similar. The minimal tangential coefficient of restitution is obtained at around 45° for all impact cases considered. The minimal value increases as the normal component of initial velocity increases. Similar to PR and PE impacts, when the impact angle approaches zero, the limit value of the tangential coefficient of restitution decreases with the increase of initial normal velocity component.

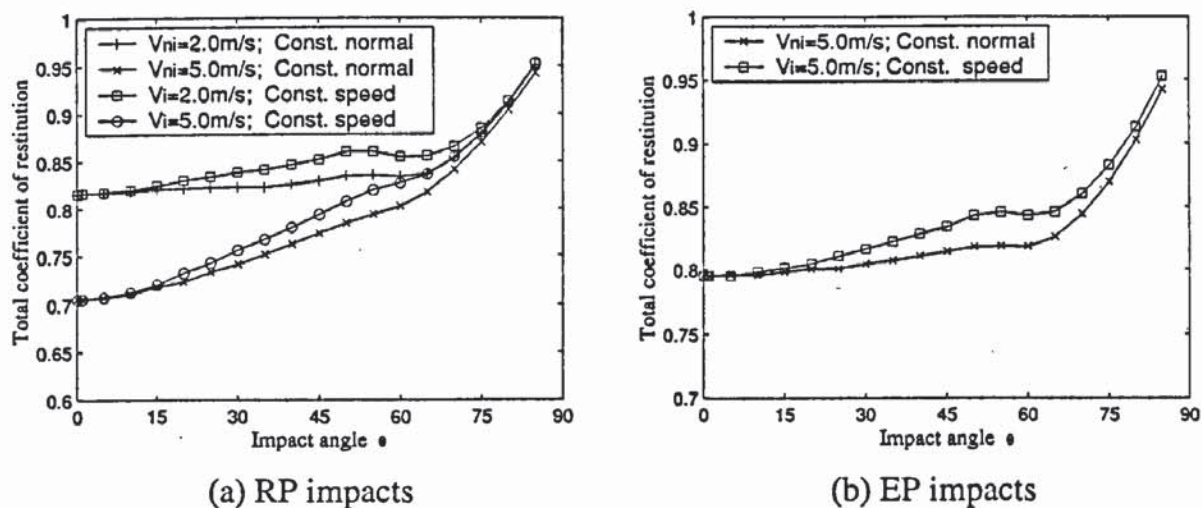


Fig. 8.46 The variation of total coefficient of restitution with impact angle for impacts involving plastic deformation in the substrate with $\mu = 0.3$.

Physically, a normal coefficient of restitution greater than unity seems to imply that the system gains energy during the impact. This is obviously not correct. The cause of this is the change in contact orientation as explained before. Figure 8.46 shows the total coefficients of restitution. As is expected, the total coefficient of restitution is always less than unity. This indicates that there is no gain of extra kinetic energy.

The decrease of the normal coefficient of restitution at the intermediate impact angles for plastic oblique impacts with fixed initial normal velocity component indicates the effect of friction. This feature also appears in the results for plastic oblique impacts with fixed initial speed. In order to clarify this feature, normal RP impacts were also simulated using the same value of the normal component of initial velocity. Figure 8.47 shows the comparisons of the normal coefficients of restitution for the normal and oblique impacts. Since the initial normal velocities are identical, the normal coefficients of restitution are expected to be the same if the tangential response has no effect on the normal impact behaviour. However, it can be seen from Fig. 8.47 that the results for normal and oblique impacts are

not close at intermediate and large impact angles. This clearly demonstrates that the tangential interaction does affect the normal response of the sphere.

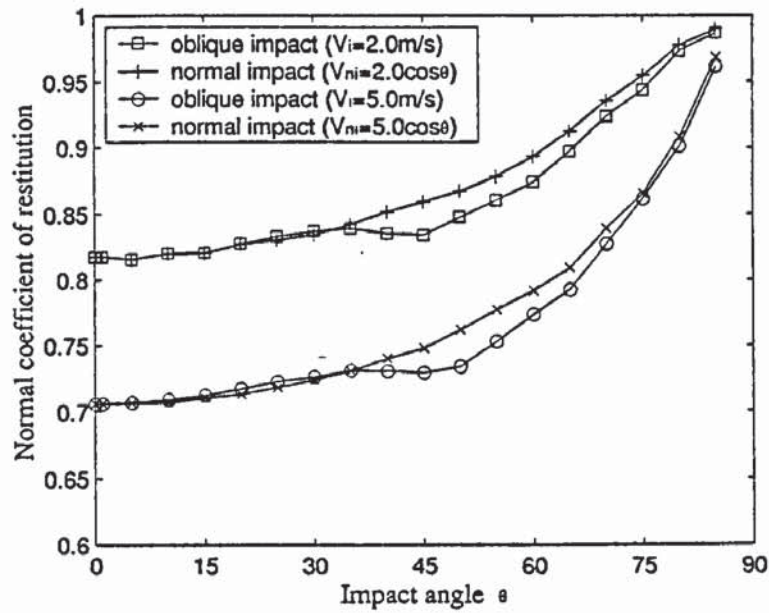


Fig. 8.47 Comparison of the normal coefficient of restitution obtained for (i) oblique impacts with fixed initial speeds and (ii) normal impacts with the same initial normal velocity ($\mu = 0.3$).

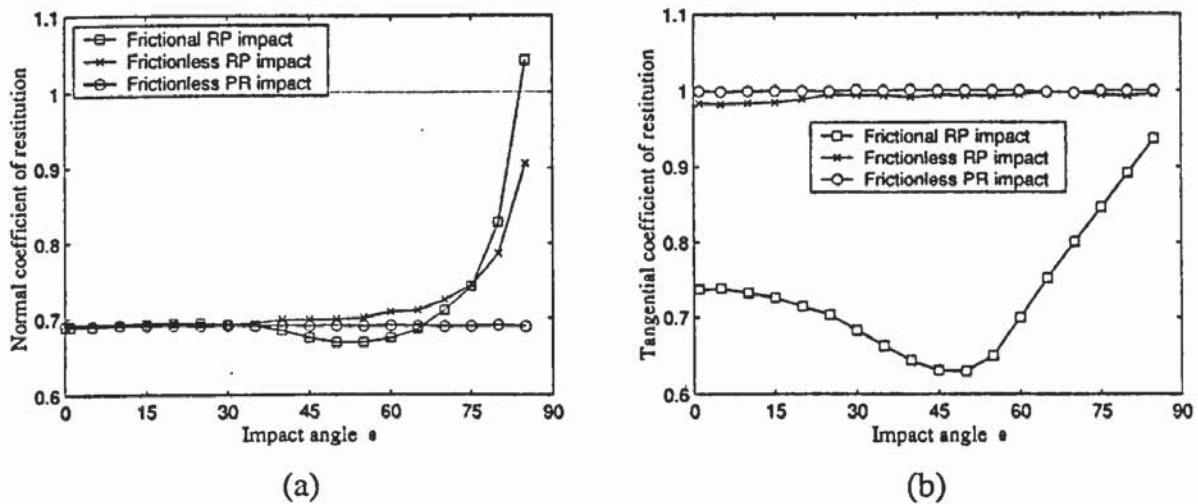


Fig. 8.48 The (a) normal and (b) tangential coefficients of restitution of frictional ($\mu = 0.3$) and frictionless RP and PR impacts with a fixed initial normal velocity of $V_{ni} = 5.0\text{m/s}$.

In theory, if there is no interface friction, the normal coefficient of restitution for PR and RP impacts should be the same and do not vary with impact angle if the initial normal velocity component is fixed. In addition, the tangential coefficient of restitution should always equal unity since there is no friction force. However, this appears not to be true if the orientation of the local contact plane is changed due to plastic deformation of the substrate as shown in Fig. 8.4. The FEA results for the normal and tangential coefficients of restitution for frictionless RP and PR impacts with a fixed initial normal velocity

$V_{ni} = 5.0\text{ m/s}$ are shown in Figs. 8.48a and 8.48b, respectively. Also superimposed are the results for frictional ($\mu = 0.3$) RP impacts with the same initial normal velocity component. As expected, the normal coefficient of restitution for frictionless PR impact does not vary with impact angle and the tangential coefficient of restitution is always equal to unity. However, different results are obtained for frictionless RP impacts. It is apparent from Fig. 8.48 that, although the normal coefficient of restitution remains essentially constant at low impact angles, it apparently increases with impact angle at large impact angles. Nevertheless, the tangential coefficient of restitution is essential close to unity as expected.

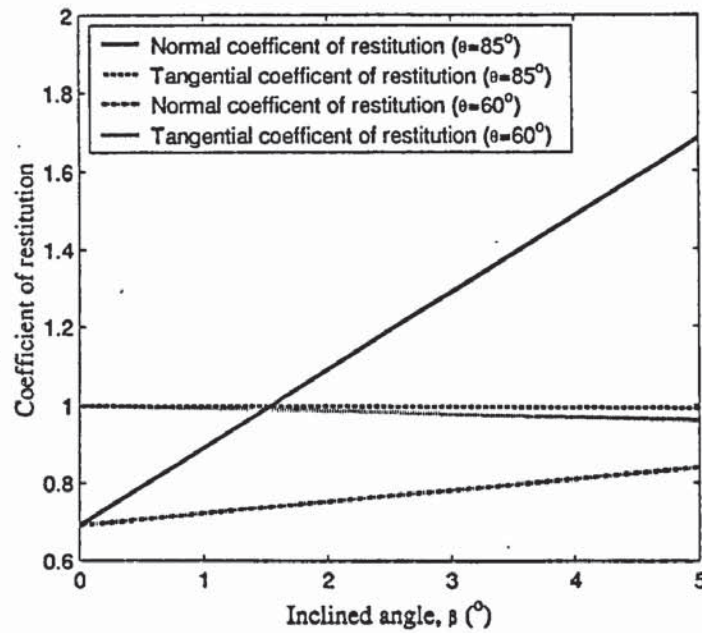


Fig. 8.49 Effect of the change in orientation of the local contact plane on the coefficients of restitution for frictionless RP impacts.

The apparent variation of the normal and tangential coefficients of restitution for frictionless RP impacts is primarily due to the change in orientation of the local contact plane. The effect of the change in orientation of the local contact plane on the coefficients of restitution for frictionless RP impacts is illustrated in Fig. 8.49. For various values of β , coefficients of restitution are obtained from Eq.(8.13), in which it is assumed that the true coefficients of restitution have values identical to those for normal impact, i.e., $e_n = 0.692$ and $e_t = 1.0$. It can be seen that the apparent normal coefficient of restitution is very sensitive to the inclined angle and increases as the inclined angle increases. In addition, the rate of increase is more significant for impacts at higher impact angles. The effect of the inclined angle on the apparent tangential coefficient of restitution is smaller.

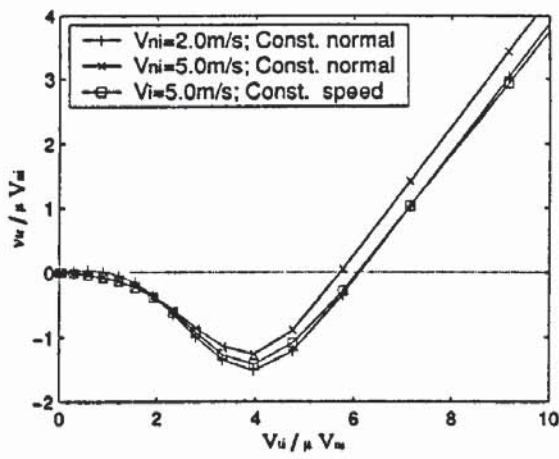
It can be seen from Fig. 8.48 that the normal coefficient of restitution for frictional and frictionless RP and frictionless PR impacts are close at low impact angles, but they begin to diverge at intermediate impact angles, at which the normal coefficient of restitution begins to reduce for frictional RP impacts due to the effect of friction. Due to the change in orientation of the local contact plane, the normal coefficients of restitution for both frictionless and frictional RP impact appear to increase with inclined angle at large impact angles, as discussed above.

8.8 Reflection angle of the contact patch

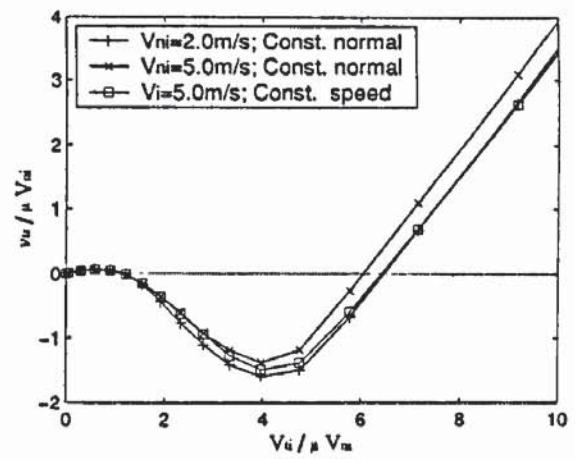
8.8.1 Impacts involving plastic deformation in the sphere

Figure 8.50 shows the reflection angle of the contact patch for PR and PE impacts. It can be seen that the overall behaviour for these two impact cases are similar. Negative reflection angles are produced at small impact angles, similar to the elastic oblique impacts. In addition, when the impact angle is approaching to zero, positive reflection angles are obtained for only PR impacts with a fixed initial normal velocity of $V_{ni} = 2.0m/s$ and all PE impacts. However, no positive reflection angle is obtained for PR impacts with a fixed initial normal velocity of $V_{ni} = 5.0m/s$. This corresponds to the results obtained for the tangential coefficient of restitution shown in Fig. 8.41 since the reflection angle of the contact patch is positive only when $e_t > 5/7$, see Eq.(7.17). It is clear that with the increase of the initial normal velocity, the segment of the curve at large impact angles shifts leftwards. It is suggested that, at high impact angles, the higher the normal coefficient of restitution, the lower the dimensionless reflection angle of the contact patch, i.e., the reflection angle of the contact patch depends on the normal coefficient of restitution.

To take the normal coefficient of restitution into account, both the dimensionless reflection angle of the contact patch and the dimensionless impact angle can be normalised by $(1+e_n)/2$, as suggested by Eq.(7.14). Figure 8.51 shows the variation of the normalised reflection angle of the contact patch with the normalised impact angle. At large impact angles, the curves of the normalised reflection angle against normalised impact angle fall on the same straight line, given by Eq.(7.32), as expected (see Ning 1995).

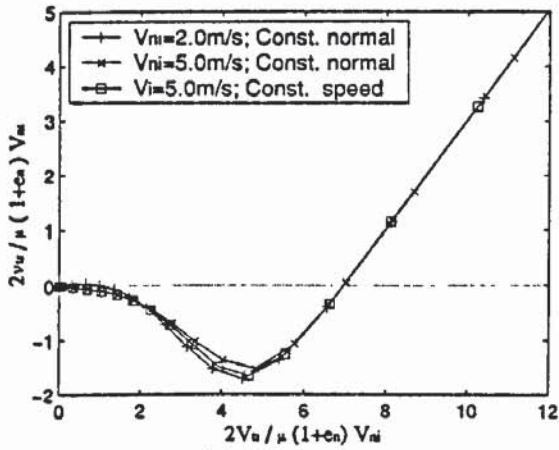


(a) PR impacts

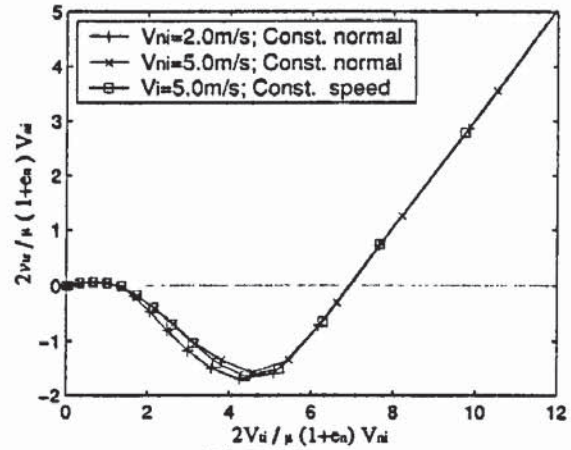


(b) PE impacts

Fig. 8.50 The variation of the dimensionless reflection angle of contact patch with dimensionless impact angle for impacts with plastic spheres ($\mu = 0.3$).



(a) PR impacts

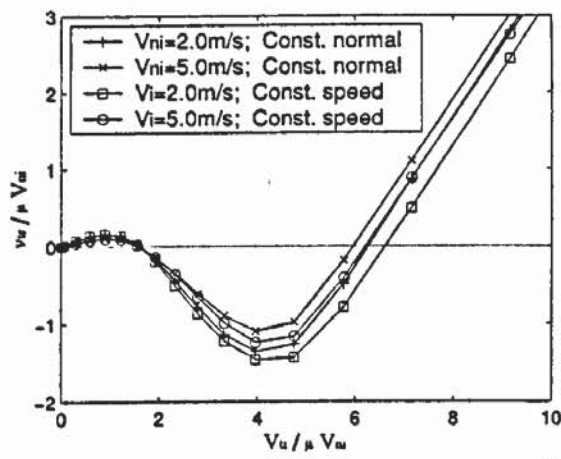


(b) PE impacts

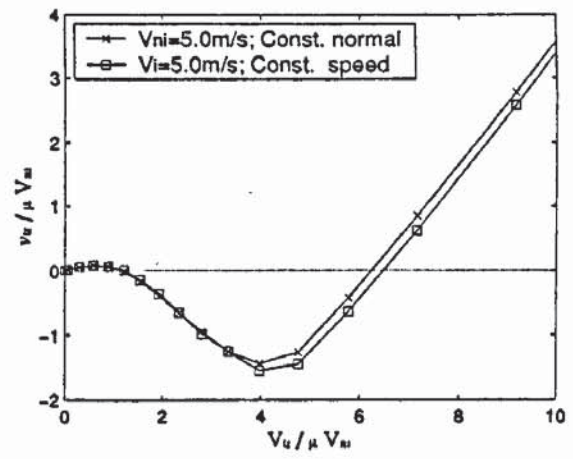
Fig. 8.51 The variation of the normalised reflection angle of contact patch with normalised impact angle for impacts with plastic spheres ($\mu = 0.3$).

8.8.2 Impacts involving plastic deformation in the substrate

Figure 8.52 shows the variation of the dimensionless reflection angle of the contact patch with dimensionless impact angle for impacts with plastic substrates under various initial velocity conditions. Again, similar patterns can be observed for RP and EP impacts. The corresponding normalised reflection angle of the contact patch is plotted against the normalised impact angle in Fig. 8.53. It can be seen that at large impact angles the results follow on the same line given by Eq.(7.32).

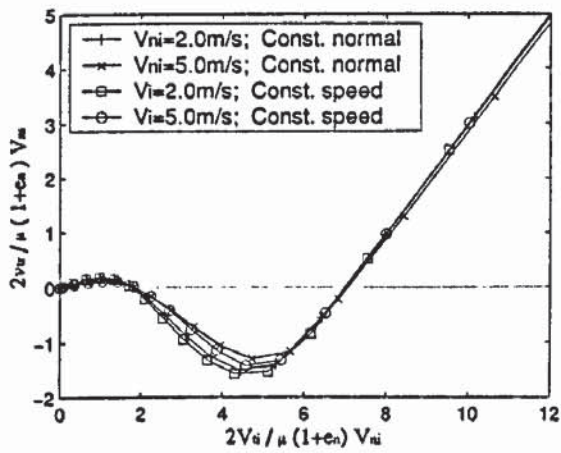


(a) RP impacts

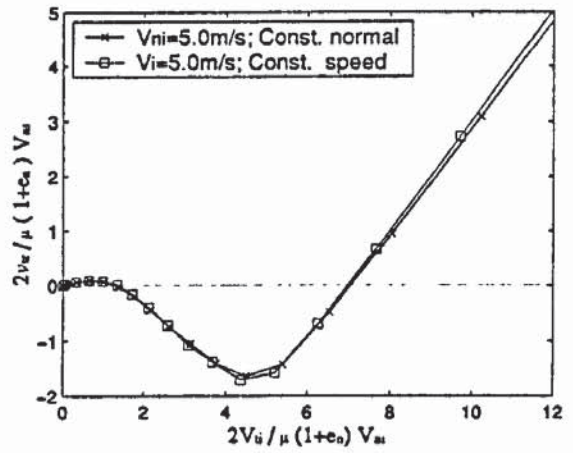


(b) EP impacts

Fig. 8.52 The variation of the dimensionless reflection angle of contact patch with dimensionless impact angle for impacts with plastic substrates ($\mu = 0.3$).



(a) RP impacts



(b) EP impacts

Fig. 8.53 The variation of the normalised reflection angle of contact patch with normalised impact angle for impacts with plastic substrates ($\mu = 0.3$).

8.9 Rebound angular velocity

The presence of friction over the interface leads to rotation of the sphere, which will absorb some initial kinetic energy. It is physically understood that the angular velocity varies in time during the impact. Nevertheless, we concentrate our attention on the rebound angular velocity, ω_r , from which one can determine how much initial kinetic energy is converted to rotational kinetic energy during the impact.

8.9.1 Impacts involving plastic deformation in the sphere

Figure 8.54 shows the variation of rebound angular velocity with impact angle for PE and PR impacts. Again, the overall patterns for PR and PE impacts are similar. For impacts

with a fixed initial speed, the rebound angular velocity reaches its maximum at around 50° . Afterwards it decreases with impact angle. However, for impacts with a fixed initial normal velocity component, the rebound angular velocity increases with impact angle until the impact angle reaches around 60° . Then it remains essentially unchanged. The range of impact angles at which the rebound angular velocity either remains unaltered or decreases corresponds to the range of impact angles where sliding occurs throughout the impact. According to Eq.(7.30), the rebound angular velocity is proportional to the initial normal velocity when sliding occurs throughout the impact. In contrast to impacts with a fixed initial normal velocity component, the normal component of the initial velocity decreases with the increasing impact angle, if we keep the initial speed constant. That is why the rebound angular velocity decreases for impacts with a fixed initial speed at large impact angles.

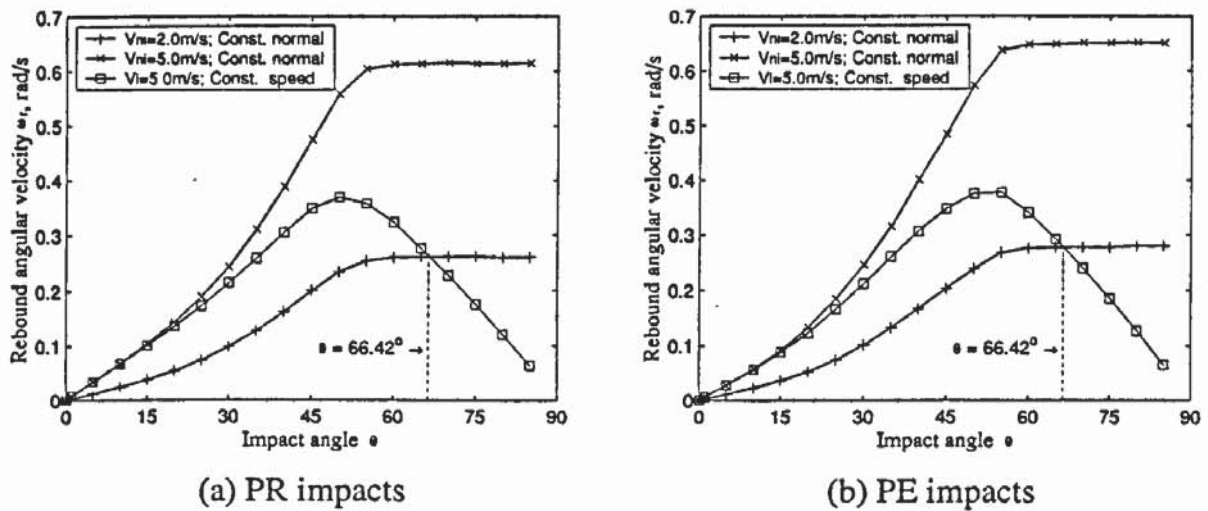


Fig. 8.54 The variation of the rebound angular velocity with impact angle for impacts with plastic spheres ($\mu = 0.3$).

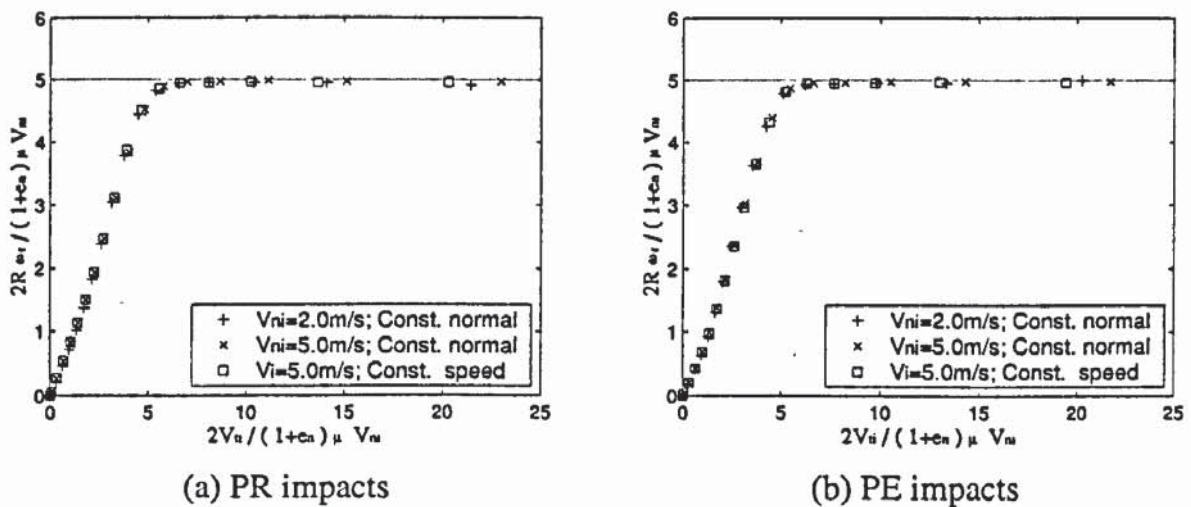


Fig. 8.55 The variation of the normalised rebound angular velocity with normalised impact angle for impacts with plastic spheres ($\mu = 0.3$).

However, according to Eq.(7.30), if the rebound angular velocity is normalised by $\mu(1 + e_n)V_{ni}/2R$, the normalised rebound angular velocity should be a constant of 5 for impacts throughout which sliding occurs. This is illustrated in Fig. 8.55 that shows the variation of the normalised rebound angular velocity with normalised impact angle. It is clear that the results for all impact cases coalesce to form a single curve, corresponding to Fig. 8.36 and Eq.(7.11).

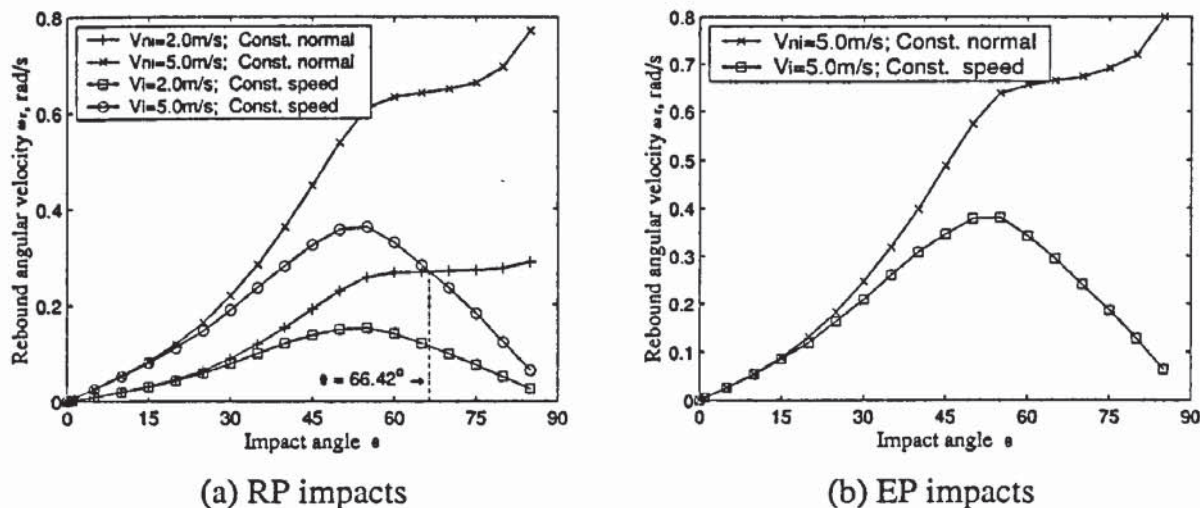


Fig. 8.56 The variation of the rebound angular velocity with impact angle for impacts with plastic substrates ($\mu = 0.3$).

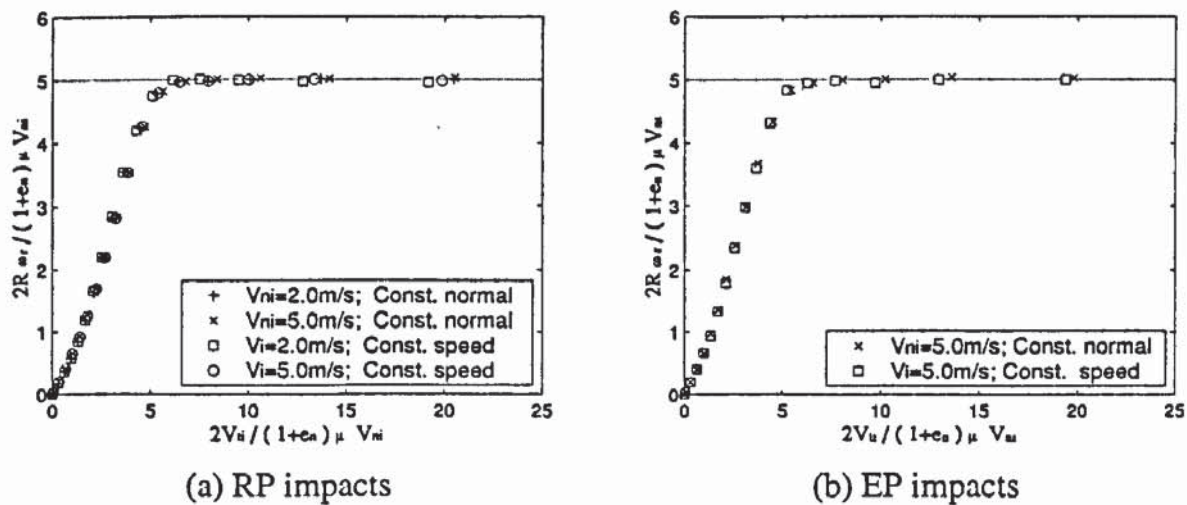


Fig. 8.57 The variation of the normalised rebound angular velocity with normalised impact angle for impacts with plastic substrates ($\mu = 0.3$).

8.9.2 Impacts involving plastic deformation in the substrate

The rebound angular velocity at various impact angles for RP and EP impacts are shown in Fig. 8.56. It can be seen that the difference between the two cases are at high impacts

angles. This is attributed to the effect of the change in the local contact plane orientation as explained in Fig. 8.42.

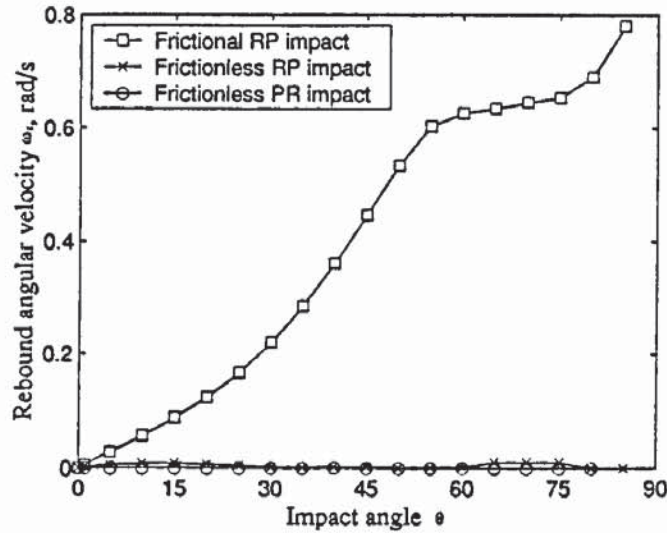


Fig. 8.58 The variation of the rebound angular velocity with impact angle for frictional ($\mu = 0.3$) and frictionless impacts.

Figure 8.57 shows the corresponding normalised rebound angular velocity versus the normalised impact angle. It is interesting to note that the results for all impact cases merge together and the normalised rebound angular velocity is equal to 5 at large impact angles. This implies that the increase of the rebound angular velocity with impact angle for impacts with fixed initial normal velocity components at large impact angles is due to the increase of the normal coefficient of restitution (see Fig. 8.42). Figure 8.58 shows the comparisons of the rebound angular velocity between frictional RP, frictionless RP and PR impacts. As expected, the rebound angular velocities for frictionless impacts are essentially zero. This indicates that the change in orientation of the local contact plane does not affect the rebound angular velocity, although it significantly affects the normal response.

8.10 Summary

In this chapter, the rebound behaviour of a sphere during the oblique impacts involving plastic deformation has been intensively investigated. The effect of friction and plastic deformation has been explored.

The similarity between the results of the impacts with the same body specified as either rigid or elastic indicates that the introduction of the idealistic rigid body does not change the overall impact behaviour and the rigid body is just the special case of elastic bodies.

For impacts in which only the sphere deforms plastically, the interface friction plays an important role. It not only dissipates some kinetic energy by doing frictional work but also transfers some kinetic energy into rotational kinetic energy. Furthermore, it enhances the plastic deformation of the sphere so that more kinetic energy is dissipated by plastic deformation, which has not been clearly addressed in literature.

For impacts with a plastic substrate, the plastic deformation of the substrate significantly affects the impact behaviour in such a way that not only some kinetic energy is dissipated by plastic deformation and interface friction, but also the orientation of the local contact plane changes during the impact. This is significant for high speed glancing impacts during which sliding occurs throughout the impact duration. The contact plane inclination leads to misinterpretation of the rebound kinematics if calculations/measurements of the contact forces and rebound velocities are based on the vertical and horizontal components.

Chapter 9 Conclusions

In this chapter, conclusions related to the impact behaviour of particles during normal and oblique impacts are drawn based on the finite element analysis. The main achievements during this study are highlighted followed by a discussion of the limitations and prospects for future work.

9.1 Normal impacts of particles

The normal impact process can be divided into two phases: compression and restitution. For elastic normal impacts, the duration of compression is identical to that of restitution and the total impact duration decreases as the impact velocity increases. For normal impacts involving plastic deformation, the duration of compression is insensitive to the impact velocity, especially when the impact velocity is sufficiently high. The restitution phase is essentially elastic, and the duration of impact is found to decrease with impact velocity.

For elastic normal impacts with small deformation, the impact behaviour can be properly predicted by Hertz theory. However, when the deformation becomes significant, the contact stiffness is higher. For normal impacts with plastic deformation, the contact stiffness is less than that predicted by Hertz theory. The contact pressure is significantly flattened when plastic deformation is involved, and the contact pressure distribution can be approximately described by a Hertzian elliptical distribution with a cut-off over the central contact area, with the cut-off pressure in the range between $1.6Y$ and $3.0Y$.

For the normal impact of particles, the initial kinetic energy is transformed into three parts: rebound kinetic energy, energy dissipated by stress wave propagation, and energy dissipated by plastic deformation. The energy loss due to stress wave propagation is found to depend upon how many times the wave can be reflected back to the initial contact point before the particles bounce off. It has been demonstrated that energy loss due to the stress waves can be ignored if the longitudinal wave can reflect back to the impact point more than three times. For the impact of a small particle with a massive body in which no

reflection of stress waves occurs, the energy loss depends on the impact velocity with a power law of 3/5. However, the energy loss due to stress wave propagation is trivial since the impact velocity required to initiate plastic deformation is normally far less than that required to induce significant energy loss due to stress wave propagation.

During plastic normal impacts, the energy loss due to plastic deformation becomes significant and increases with impact velocity. For the impact of elastic-perfectly plastic particles, finite-deformation plastic impact is addressed and the criteria for the transition from elastic-plastic impacts to the finite-deformation plastic impact have been proposed in terms of the impact velocity and the material properties. The coefficient of restitution is found to depend mainly upon V_{ni}/V_{y0} for the elastic-plastic impact of elastic-perfectly plastic particles and to be proportional to $(V_{ni}/V_{y0})^{-1/4}$ at high velocities, which is well predicted by LWT theory. During finite-deformation plastic impact, the coefficient of restitution is found to be proportional to $[(V_{ni}/V_{y0})/(E^*/Y)]^{-1/2}$. The impact of elastic-plastic particles with work hardening produces a higher coefficient of restitution than that in the elastic-plastic impact without work hardening.

9.2 Oblique impacts of particles

The contact area during the oblique interaction of spheres consists of two parts: a stick region and a surrounding slip region. The tangential traction for elastic contacts of bodies with similar elastic materials can be predicted by Mindlin's theory, according to which the tangential traction is estimated by the multiplication of the friction coefficient with the normal contact pressure, with a negative traction superimposed in the stick region. The dissimilarity of the material properties results in the traction distribution skewing towards the leading edge of the contact area. It is found that the tangential traction distribution during plastic oblique impact also consists of a stick region and a slip region, and the tangential traction distribution can be simplified in the same way as for elastic oblique impact except that the normal contact pressure distribution approximates to that of a Hertzian elliptical distribution with a cut-off.

The contact deformation plays a significant role in the oblique impact of particles. For elastic oblique impacts, the impact behaviour strongly depends on the contact deformation

when sliding does not occur throughout the impact. For impacts throughout which sliding occurs, the effect of contact deformation becomes negligible and the rebound behaviour can be predicted by an analytical solution.

For plastic oblique impacts, in which only the sphere deforms plastically, the interface friction plays an important role. It not only dissipates some kinetic energy by doing frictional work but also transfers some kinetic energy into rotational kinetic energy. Furthermore, it enhances the plastic deformation of the sphere so that more kinetic energy is dissipated by plastic deformation. This phenomenon has not been clearly addressed in the literature.

For impacts with a plastic substrate, the plastic deformation of the substrate significantly affects the impact behaviour in such a way that, in addition to some kinetic energy being dissipated by plastic deformation and interface friction, the orientation of the local contact plane changes during the impact. It is demonstrated that the change in the orientation of local contact plane significantly affects the apparent impact behaviour. This is significant to experimentalists studying high speed glancing impacts since they will invariably measure the vertical and horizontal rebound velocities.

Coupling between the normal and tangential responses is negligible for oblique elastic impacts. However, it is found that the tangential response does affect the normal response for oblique plastic impacts, in that the normal coefficient of restitution varies with impact angle even when the normal component of the impact velocity is not changed.

9.3 Limitations and future work

Several topics are worthy of consideration for future work on contact/impact of particles. The normal impact behaviour of elastic-perfectly plastic particles has been comprehensively discussed in this thesis. It is expected that a simplified model could be developed on the basis of the present study and could be incorporated into DEM. It is also useful that an analytical model for plastic oblique impacts would be established based on the present analysis of frictional contacts of plastic bodies under tangential loading.

In addition, the effect of work hardening is an important factor when dealing with contact/impact of real particles. It would be useful to deliver a rigorous analytical solution for normal impacts of elastic-plastic particles with work hardening. Furthermore, it is worth considering work hardening with a power law stress-strain relation, rather than the simple bilinear stress-strain law as assumed in this study.

Impacts with interface energy are of fundamental interests in chemical, pharmaceutical and processing engineering. Hence, it would be useful to develop finite element methods that could model interface energy realistically in order to investigate the impact behaviour of adhesive particles.

This study has mainly considered impacts between a sphere and a substrate, in which only one body deforms plastically. It would also be useful to investigate the contact/impact problems with both bodies deforming plastically, particularly, when the two bodies have different material properties.

In this study, we assume that the particle does not rotate before impact, i.e., no initial rotation has been considered. Further investigation of oblique impacts with initial rotation can be carried out to investigate how the initial rotational kinetic energy transforms during the impact. This would be useful to fully understand the transformation of kinetic energy during oblique impacts.

References

- [1] Adams, G.G. & Mosonovsky, M., 2000, "Contact modelling---forces", *Tribology Int.*, **33**, 431-442.
- [2] Adams, G.G. & Tran, D.N., 1993, "The coefficient of restitution for a planar two-body eccentric impact", *Trans. ASME, J. Appl. Mech.*, **60**, 1058-1060.
- [3] Akyuz, F.A. & Merwin, J.E., 1968, "Solution of nonlinear problem of elastoplasticity by finite element method", *AIAA Journal*, **6**, 1825.
- [4] Andrews, J.P., 1930, "Experiment on impact", *Proc. Phys. Soc.*, **43**, 8-17.
- [5] Bathe, K.J., 1982, *Finite Element Procedures in Engineering Analysis*, Prentice-hall, Englewood Cliffs, New Jersey.
- [6] Bathe, K.J. & Wilson, E.L., 1976, *Numerical Methods in Finite Element Analysis*, Prentice-hall, Englewood Cliffs, New Jersey.
- [7] Bentall, R.H. & Johnson, K.L., 1967, "Slip in the rolling contact of two dissimilar elastic rollers", *Int. J. Mech. Sci.*, **9**, 389-404.
- [8] Bhushan, B., 1996, "Contact mechanics of rough surfaces in tribology: single asperity contact", *Appl. Mech. Rev.*, **49**, 275-298.
- [9] Bitter, J.G.A., 1963, "A study of erosion phenomena, part I", *Wear*, **6**, 5-21.
- [10] Bondareva, V.F., 1971, "Contact problem for elastic spheres", *P.M.M.*, **35**, 37-45.
- [11] Brach, R.M., 1988, "Impact dynamics with applications to solid particle erosion", *Int. J. Impact Eng.*, **7**, 37-53.
- [12] Brach, R.M., 1989, "Rigid body collisions", *Trans. ASME, J. Appl. Mech.*, **56**, 133-138.
- [13] Bridges, F.G., Hatzes, A. & Lin, D.N.C., 1984, "Structure, stability and evolution of Saturn's rings", *Nature*, **309**, 333-335.
- [14] Brilliantov, N.V., Spahn, F., Hertzsch, J.M. & Poschel, T., 1996, "The collision of particles in granular systems", *Physica A*, **231**, 417-424.
- [15] Bryant, M.D. & Keer, L.M., 1982, "Rough contact between elastically and geometrically identical curved bodies", *Trans. ASME, J. Appl. Mech.*, **49**, 345-352.
- [16] Chang, W.R., Etsion I., & Bogy D.B., 1987, "An elastic-plastic model for the contact of rough surfaces", *Trans. ASME, J. Tribology*, **109**, 257-263.
- [17] Chang, W.R. & Ling, F.F., 1992, "Normal impact model of rough surfaces", *Trans. ASME, J. Tribology*, **114**, 439-447.
- [18] Chaudhri, M.M., Hutchings, I.M. & Makin, P.L., 1984, "Plastic compression of spheres", *Phil. Mag. A*, **49**(4), 493-503.
- [19] Chaudhri, M.M., 1987, "The plastic deformation of single asperities by hard flats", *Inst. Mech. Engrg. Conf. Publ.*, **C158**, 1003-1012.
- [20] Clough, R.W. & Penzien, J., 1993, *Dynamics of Structures*, McGraw-Hill, Inc., London.

- [21] Conway, H.D., 1971, "The effects of friction on normal contact stresses", *Trans. ASME, J. Appl. Mech.*, **38**, 1094-1095.
- [22] Conway, H.D., Engel, P.A. & Lee, H.C., 1972, "Force-time investigations for the elastic impact between a rigid sphere and a thin layer", *Int. J. Mech. Sci.*, **14**, 523-529.
- [23] Crook, A.W., 1953, "A study of some impacts between metal bodies by a piezo-electric method", *Proc. R. Soc. London*, **A212**, 377-390.
- [24] Davies, R.M., 1949, "The determinations of static and dynamic yield stresses using a steel ball", *Proc. R. Soc. London*, **A197**, 416-432.
- [25] Fisher, H.D., 1975, "The impact of an elastic sphere on a thin elastic plate supported by a Winkler foundation", *Trans. ASME, J. Appl. Mech.*, **42**, 133-135.
- [26] Follanabee, P.S. & Sinclair, G.B., 1984, "Quasi-static normal indentation of an elasto-plastic half-space by a rigid sphere-I: analysis", *Int. J. Solids Structures*, **20**, 81-91.
- [27] Francis, H.A., 1976, "Phenomenological analysis of plastic spherical indentation", *Trans. ASME, J. Eng. Mater. Tech.*, **98**, 272-281.
- [28] Goldsmith, W., 1960, *Impact*, Arnold, London.
- [29] Goldsmith, W. & Lyman, P.T., 1960, "The penetration of hard-steel spheres into plane metal surfaces", *Trans. ASME, J. Appl. Mech.*, **27**, 717-725.
- [30] Goodier, J.N., Jahsman, W.E., & Ripperger, E.A., 1959, "An experimental surface-wave method for recording force-time curves in elastic impacts", *Trans. ASME, J. Appl. Mech.*, **26**, 3-7.
- [31] Goodman, L.E., 1962, "Contact stress analysis of normally loaded rough spheres", *Trans. ASME, J. Appl. Mech.*, **29**, 515-522.
- [32] Goodman, L.E., & Keer, L.M., 1965, "The contact stress problem for an elastic sphere indenting an elastic cavity", *Int. J. Solids Structures*, **1**, 407-415.
- [33] Gorham, D. A. & Kharaz, A. H., 2000, "Measurement of particle rebound characteristics", *Powder Technology*, **112**, 193-202.
- [34] Haines, D.J. & Ollerton, E., 1963, "Contact stress distribution on elliptical contact surfaces subjected to radial and tangential forces", *Proc. I. Mech. E.*, **177**, 95-108.
- [35] Hallquist, J.O., 1991, *LS-DYNA3D Theoretical Manual*, Livermore Software Technology Corporation, California, USA.
- [36] Hamilton, G.M. & Goodman, L.E., 1966, "The stress field created by a circular sliding contact", *Trans. ASME, J. Appl. Mech.*, **33**, 371-376.
- [37] Hardy, C., Baronet, C.N. & Tordion, G.V., 1971, "The elasto-plastic indentation of a half-space by a rigid sphere", *Int. J. Num. Methods Eng.*, **3**, 451-462.
- [38] Hertz, H., 1896, *Miscellaneous Papers by H. Hertz*, Eds. Jones & Schott, Macmillan and Co., London.
- [39] Hill, R., 1950, *The Mathematical Theory of Plasticity*, Oxford Univ. Press, London.
- [40] Hill, R., Storakers, B. & Zdunek, A.B., 1989, "A theoretical study of the brinell hardness test", *Proc. R. Soc. London*, **A423**, 301-330.
- [41] Hills, D.A., Nowell, D. & Sackfield, A., 1993, *Mechanics of Elastic Contacts*, Butterworth-Heinemann Ltd., Oxford.

- [42] Hong, T. & Saka, N., 1991, "Finite element analysis of an elastic-plastic two-layer half-space: normal contact", *Wear*, **148**, 47-68.
- [43] Hughes, T.J.R., 1987, *The Finite Element Method-Linear Static and Dynamic Finite Element Analysis*, Prentice-hall, Englewood Cliffs, New Jersey.
- [44] Hughes, T.J.R., Taylor, R.L., Sackman, J.L., Curnier, A. & Kanoknukulchai, W., 1976, "Finite element method for a class of contact-impact problems", *Comput. Methods Appl. Mech. Eng*, **8**, 249-276.
- [45] Hunter, S.C., 1957, "Energy absorbed by elastic waves during impact", *J. Mech. Phys. Solids*, **5**, 162-171.
- [46] Hutchings, I.M., 1979, "Energy absorbed by elastic waves during plastic impact", *J. Phys. D: Appl. Phys.*, **12**, 1819-1824.
- [47] Hutchings, I.M., Macmillan, N.H. & Rickerby, D.G., 1981, "Further studies of the oblique impact of a hard sphere against a ductile solids", *Int. J. Mech. Sci.*, **23**, 639-646.
- [48] Hutchings, I.M., Winter, R.E. & Field, J.E., 1976, "Solid particle erosion of metals: the rebound of surface material by spherical projectiles", *Proc. R. Soc. London*, **A348**, 379-392.
- [49] Johnson, K.L., 1962, "Tangential tractions and microslip in rolling contact", In *Rolling Contact Phenomena*, Bidwell (Ed.), Elsevier, New York, 6.
- [50] Johnson, K.L. & Jefferis, J.A., 1963, "Plastic flow and residual stresses in rolling and sliding contact", *Proc. I. Mech. E. Symp. On Rolling Contact Fatigue*, Institute of Mechanical Engineers, London, 54-65.
- [51] Johnson, K.L., 1968, "An experimental determination of the contact stresses between plastically deformed cylinders and spheres", in *Engineering Plasticity*, Cambridge University Press, Cambridge, 341-361.
- [52] Johnson, K.L., Kendall, K. & Roberts, A.D., 1971, "Surface energy and the contact of elastic solids", *Proc. R. Soc.*, **A324**, 301-313.
- [53] Johnson, K.L., 1983, "The bounce of 'superball'", *Int. J. Mech. Engng. Education*, **111**, 57-63.
- [54] Johnson, K.L., 1985, *Contact Mechanics*, Cambridge University Press.
- [55] Johnson, K.L., 1997, "Adhesion and friction between a smooth elastic spherical asperity and a plane surface", *Proc. R. Soc. London*, **A453**, 163-179.
- [56] Johnson, K.L., 1998, "Mechanics of adhesion", *Tribology International*, **31**, 413-418.
- [57] Johnson, K.L., 2001, Private communication.
- [58] Kalker, J.J., 1967a, "On the rolling contact of two elastic bodies in the presence of dry friction", PhD Thesis, Technical University of Delft.
- [59] Kalker, J.J., 1967b, "A strip theory for rolling with slip and spin", *Proc. Kon. Ned. Akad. van Wetenschappen*, **B70**, 10-62.
- [60] Keller, J.B., 1986, "Impact with friction", *Trans. ASME, J. Appl. Mech.*, **53**, 1-4.
- [61] Kharaz, A.H. & Gorham, D.A., 2000, "A study of the restitution coefficient in elastic-plastic impact", *Phil. Mag. Letters*, **80**, 549-559.
- [62] Kharaz, A.H., Gorham, D.A. & Salman, A.D., 1999, "Accurate measurement of particle impact parameters", *Meas. Sci. Technol.*, **10**, 31-35.

- [63] Ko, P.L., 1985, "The significance of shear and normal force components on tube wear due to fretting and periodic impacting", *Wear*, **106**, 261-281.
- [64] Kolsky, H., 1963, *Stress Waves in Solids*, New York: Dover.
- [65] Kral, E.R., Komvopoulos, K., & Bogy, D.B., 1993, "Elastic-plastic finite element analysis of repeated indentation of a half-space by a rigid sphere", *Trans. ASME, J. Appl. Mech.*, **60**, 829-841.
- [66] Kral, E.R., Komvopoulos, K., & Bogy, D.B., 1995a, "Finite element analysis of repeated indentation of an elastic-plastic layered medium by a rigid sphere, part I: surface results", *Trans. ASME, J. Appl. Mech.*, **62**, 20-28.
- [67] Kral, E.R., Komvopoulos, K., & Bogy, D.B., 1995b, "Finite element analysis of repeated indentation of an elastic-plastic layered medium by a rigid sphere, part II: subsurface results", *Trans. ASME, J. Appl. Mech.*, **62**, 29-42.
- [68] Kral, E.R. & Komvopoulos, K., 1996a, "Three-dimensional finite element analysis of surface deformation and stresses in an elastic-plastic layered medium subjected to indentation and sliding contact loading", *Trans. ASME, J. Appl. Mech.*, **63**, 365-375.
- [69] Kral, E.R. & Komvopoulos, K., 1996b, "Three-dimensional finite element analysis of subsurface stresses and shakedown due to repeated sliding on an layered medium", *Trans. ASME, J. Appl. Mech.*, **63**, 967-973.
- [70] Labous, L., R, Rosato, A.D. & Dave, R.N., 1997, "Measurements of collisional properties of spheres using high-speed video analysis", *Phys. Rev. E*, **56**, 5717-5725.
- [71] Lee, C.H., Masaki, S. & Kobayashi, S., 1972, "Analysis of ball indentation", *Int. J. Mech. Sci.*, **14**, 417-426.
- [72] Levy, G. & Parry, A.A., 1980, "Studies of impact phenomena", *Wear*, **64**, 83-99.
- [73] Lewis, A.D. & Rogers, R.J., 1988, "Experimental and numerical study of forces during oblique impact", *Journal of Sound and Vibration*, **125**, 403-412.
- [74] Li, L.Y., Thornton, C. & Wu, C.Y., 2000, "Impact behaviour of the elastoplastic sphere with a rigid wall", *Proc. I. Mech. E.*, **214C**, 1107-1114.
- [75] Li, L.Y., Wu, C.Y. & Thornton, C., 2001, "A theoretical model for the contact of elastoplastic bodies", Submitted for publication.
- [76] Lim, C.T. & Stronge, W.J., 1994, "Frictional torque and compliance in collinear elastic collisions", *International Journal of Mechanical Science*, **36**, 911-930.
- [77] Liu, C. & Paul, B., 1989, "Rolling contact with friction and non-Hertzian pressure distribution", *Trans. ASME, J. Appl. Mech.*, **56**, 814-820.
- [78] Love, A.E.H., 1952, *A Treatise on the Mathematical Theory of Elasticity*, 4th Edn., Cambridge University Press, Cambridge.
- [79] Matthews, J.R., 1980, "Indentation hardness and hot pressing", *Acta Metal.*, **28**, 311-318.
- [80] Maw, N., Barber, J.R. & Fawcett, J.N., 1976, "The oblique impact of elastic spheres", *Wear*, **38**, 101-114.
- [81] Maw, N., Barber, J.R. & Fawcett, J.N., 1981, "The role of elastic tangential compliance in oblique impact", *Trans. ASME, J. Lub. Tech.*, **103**, 74-80.

- [82] Mesarovic, S.Dj. & Fleck, N.A., 1999, "Spherical indentation of elastic-plastic solids", *Proc. R. Soc. London*, A455, 2707-2728.
- [83] Mesarovic, S.Dj. & Fleck, N.A., 2000, "Frictionless indentation of dissimilar elastic-plastic spheres", *Int. J. Solids Structures*, 37, 7071-7091.
- [84] Mindlin, R.D., 1949, "Compliance of elastic bodies in contact", *Trans. ASME, J. Appl. Mech.*, 16, 259-268.
- [85] Mindlin, R.D. & Deresiewicz, H., 1953, "Elastic spheres in contact under varying oblique force", *Trans. ASME, J. Appl. Mech.*, 20, 327-344.
- [86] Morton, W.B. & Close, L.J., 1922, "Notes on Hertz' theory of contact problems", *Philosophical Magazine*, 43, 320.
- [87] Ning, Z., 1995, *Elasto-Plastic Impact of Fine Particles and Fragmentation of Small Agglomerates*, PhD Thesis, The University of Aston in Birmingham.
- [88] Oden, J.T., 1972, *Finite Elements of Nonlinear Continua*. McGraw-Hill, New York.
- [89] Poritsky, H., 1950, "Stress and deflexions of cylindrical bodies in contact with application to contact of gears and of locomotive wheels", *Trans. ASME, J. Appl. Mech.*, 17, 191-201.
- [90] Randall, C.W., 1989, *The Application of Contact Mechanics to the Numerical Simulation of Particulate Material*, PhD Thesis, The University of Aston in Birmingham.
- [91] Reed, J., 1985, "Energy losses due to elastic wave propagation during an elastic impact", *J. Phys. D: Appl. Phys.*, 18, 2329-2337.
- [92] Rickerby, D.G. & Macmillan, N.H., 1980, "On the oblique impact of a rigid sphere against a rigid-plastic solid", *Int. J. Mech. Sci.*, 22, 491-494.
- [93] Rogers, L.N. & Reed, J., 1984, "The adhesion of particles undergoing an elastic-plastic impact with a surface", *J. Phys. D: Appl. Phys.*, 17, 677-689.
- [94] Sackfield, A. & Hills, D.A., 1983, "Some useful results in the tangentially loaded Hertzian contact problem", *J. Strain Anal.*, 18(2), 107-110.
- [95] Sackfield, A. & Hills, D.A., 1988, "Sliding contact between dissimilar elastic bodies", *J. Tribology*, 110(4), 592-596.
- [96] Sen, S., Aksakal, B. and Ozel, A., 1998, "A finite element analysis of the indentation of an elastic-work hardening layered half-space by an elastic sphere", *Int. J. Mech. Sci.*, 40(12), 1281-1293.
- [97] Sheldon, G.L. & Kanhere, A., 1972, "An investigation of impingement erosion using single particles", *Wear*, 21, 195-209.
- [98] Shih, C.W., Schlein, W.S. & Li, J.C.M., 1992, "Photo-elastic and finite element analysis of different size spheres in contact", *J. Mater. Res.*, 7, 1011-1017.
- [99] Sinclair, G.B. Follanbee, P.S. & Johnson, K.L., 1985, "Quasi-static normal indentation of an elasto-plastic half-space by a rigid sphere-II: results", *Int. J. Solids Structures*, 21, 865-888.
- [100] Singh, K.P. & Paul, B, 1974, "Numerical solution of non-Hertzian elastic contact problems", *Trans. ASME, J. Appl. Mech.*, 41, 484-490
- [101] Smith, C.E., 1991, "Predicting rebounds using rigid-body dynamics", *Trans. ASME, J. Appl. Mech.*, 58, 754-758.

- [102] Smith, C.E. & Liu, P.P., 1992, "Coefficients of restitution", *Trans. ASME, J. Appl. Mech.*, **59**, 963-969.
- [103] Smith, J.O. & Liu, C.K., 1953, "Stresses due to tangential and normal loads on an elastic solid with application to some contact stress problems", *Trans. ASME, J. Appl. Mech.*, **21**, 157-166.
- [104] Sondergaard, R., Chaney, K., & Brennen, C.E., 1990, "Measurements of solid spheres bouncing off flat plates", *Trans. ASME, J. Appl. Mech.*, **57**, 694-699.
- [105] Stronge, W.J., 1990, "Rigid body collisions with friction", *Proc. R. Soc. London*, **A431**, 169-181.
- [106] Stronge, W.J., 1993, "Two-dimensional rigid-body collisions with friction", *Trans. ASME, J. Appl. Mech.*, **60**, 564-566.
- [107] Stronge, W.J., 1994, "Planar impact of rough compliant bodies", *Int. J. Impact Eng.*, **15**(4), 435-450.
- [108] Stronge, W., 1995, "Theoretical coefficient of restitution for planar impact of rough elasto-plastic bodies", *ASME, AMD, Impact, Waves and Fracture*, **205**, 351-362.
- [109] Stronge W.J., 2000, *Impact Mechanics*, Cambridge University Press.
- [110] Sundararajan, G. & Shewmon, P.G., 1987, "The oblique impact of a hard ball against ductile, semi-infinite target materials-experiment and analysis", *Int. J. Impact Eng.*, **6**, 3-22.
- [111] Tabor, D., 1948, "A simple theory of static and dynamic hardness", *Proc. R. Soc. London*, **A192**, 247-274.
- [112] Tabor, D., 1951, *Hardness of Metals*, Oxford University Press, Oxford.
- [113] Tabor, D., 1970, "The hardness of solids", *Proc. Inst. Phys. F, Phys. Tech.*, **1**, 145-179.
- [114] Tabor, D., 1986, "Indentation hardness and its measurement: some cautionary comments", in *Microindentation Techniques in Materials Science and Engineering*, ASTM STP 889, Blau, P.J. & Lawn B.R. (Eds.), American Society for Testing and Materials, Philadelphia, USA. 129-159.
- [115] Tangena, A.G. & Hurkx, G.A.M., 1985, "Calculations of mechanical stresses in electrical contact situations", *IEEE Transactions on Components, Hybrids, and Manufacturing Technology*, **CHMT-8**(1), 13-20.
- [116] Tataru, Y., 1989, "Extensive theory of force-approach relations of elastic spheres in compression and in impact", *Trans. ASME, J. Eng. Mat. Tech.*, **111**, 163-168.
- [117] Thornton, C., 1997, "Coefficient of restitution for collinear collisions of elastic-perfectly plastic spheres", *Trans. ASME, J. Appl. Mech.*, **64**, 383-386.
- [118] Thornton, C., & Ning, Z., 1994, "Oblique impact of elasto-plastic spheres", *Proc. 1st Int. Particle Technology Forum*, AIChE Publications, **2**, 14-19.
- [119] Thornton, C. & Ning, Z., 1998, "A theoretical model for the stick/bounce behaviour of adhesive, elastic-plastic spheres", *Powder Technology*, **99**, 154-162.
- [120] Thornton, C. Ning, Z., WU, C.Y., Nasrullah, M. & Li, L.Y., 2001, "Contact mechanics and coefficient of restitution", in *Granular Gases*, Poschel, T. & Luding, S., (eds.), Springer-Verlag, Berlin, 184-194.

- [121] Thornton, C. & Randall, C.W., 1988, "Applications of theoretical contact mechanics to solid particle system simulation", In *Micromechanics of Granular Materials*, Satake, M. & Jenkins, J.T., (Eds.), Elsevier, Amsterdam, 133-142.
- [122] Thornton, C. & Yin, K.K., 1991, "Impact of elastic spheres with and without adhesion", *Powder Technology*, **65**, 153-166.
- [123] Tillett, J.P.A., 1954, "A study of the impact on sphere of plates", *Proc. Phys. Soc.*, **B67**, 677-688.
- [124] Timoshenko, S. & Goodier, J.N., 1951, *Theory of Elasticity* (3rd Edn.), McGraw-Hill, New York.
- [125] Timothy, S.P. & Hutchings, I.M., 1986a, "The impact of a soft metal sphere on a hard metal target: I. deformation of the sphere", *Philosophical Magazine A*, **54**, 93-102.
- [126] Timothy, S.P. & Hutchings, I.M., 1986b, "The impact of a soft metal sphere on a hard metal target: I. deformation of the target", *Philosophical Magazine A*, **54**, 103-113.
- [127] Villaggio, P., 1996, "The rebound of an elastic sphere against a rigid wall", *Trans. ASME, J. Appl. Mech.*, **63**, 259-263.
- [128] Vu-Quoc, L. & Zhang X., 1999, "An elastoplastic contact force—displacement model in the normal direction: displacement-driven version" *Proc. R. Soc. London*, **A455**(1991), 4013-4044.
- [129] Vu-Quoc, L., Zhang, X., & Lesburg, L., 2000, "A normal force-displacement model for contacting spheres, accounting for plastic deformation: force-driven formulation", *Trans. ASME, J. Appl. Mech.*, **67**(2), 363-371.
- [130] Walton, O.R. & Braun, R.L., 1986, "Viscosity, granular-temperature, and stress calculations for shearing assemblies of inelastic, frictional disks", *J. Rheology*, **30**, 949-980.
- [131] Walton, O.R., 1992, "Numerical simulation of inelastic, frictional particle-particle interactions", in Roco, M.C. (ed.), *Particulate Two-Phase Flow*, Ch. 25, Butterworth-Heinemann, Boston.
- [132] Whirley, R.G., & Engelmann, B.E., 1992, *DYNA2D, a Nonlinear, Explicit, Two-Dimensional Finite Element Code for Solid Mechanics: User Manual*, Lawrence Livermore National Laboratory, University of California, USA.
- [133] Whirley, R.G., & Engelmann, B.E., 1993, *DYNA3D, a Nonlinear, Explicit, Three-Dimensional Finite Element Code for Solid and Structural Mechanics: User Manual*, Lawrence Livermore National Laboratory, University of California, USA.
- [134] Whittaker, E.T., 1904, *A Treatise on the Analytical Dynamics of Particles and Rigid Bodies*, Cambridge University Press, London.
- [135] Wang, Y. & Mason, M.T., 1992, "Two-dimensional rigid-body collisions with friction", *Trans. ASME, J. Appl. Mech.*, **59**, 635-642.
- [136] Wu, C. Y., Li, L. Y. & Thornton C., 2001 "Finite element analysis of the oblique impact behaviour of particles", *Proc. of the 9th annual conference of ACME*, University of Birmingham, 85-88.
- [137] Yigit, A.S. & Christoforou, A.P., 1994, "On the impact of a spherical indenter and an elastic-plastic transversely isotropic half-space", *Composites Engineering*, **4**, 1143-1152.

- [138] Yin, K.K., 1992, *Numerical Modelling of Agglomerate Degradation*, PhD Thesis, The University of Aston in Birmingham.
- [139] Yu, M.M.H., Moran, B. & Keer, L.M., 1995, "A direct analysis of three-dimensional elastic-plastic rolling contact", *Trans. ASME, J. Tribology*, **117**, 234-243.
- [140] Zener, C., 1941, "The intrinsic inelasticity of large plates", *Phys. Rev.*, **59**, 669-673.
- [141] Zhao, Y., Maietta, D.M. & Chang, L., 2000, "An asperity microcontact model incorporating the transition from elastic deformation to fully plastic flow", *Trans. ASME, J. Tribology*, **122**, 86-93.
- [142] Zhong, Z.H., 1993, *Finite Element Procedures for Contact-Impact Problems*, Oxford University Press, Oxford.
- [143] Zienkiewicz, O.C. & Taylor, R.L., 1989, *The Finite Element Method*, 4th Edn. McGraw-Hill, New York.

Appendix A Finite Element Methods for Contact/Impact Problems

A.1 Introduction

In this appendix, we will briefly discuss some aspects involved in finite element methods for contact/impact problems. The emphasis will be placed on those aspects of FEM for contact/impact problems which are distinct from the standard FEM. The general equations for contact/impact problems are presented first in the next section. Then the temporal discretisation used in FEM is discussed in Section A.3. In Section A.4, the contact modelling techniques are described. The finite element codes DYNA2D/DYNA3D, which are employed in this study, are then presented.

A.2 General formulations for contact/impact problems

Since most contact processes in engineering applications are dynamic in a restrictive sense, here we consider only the dynamic case involving two bodies in the general sense. Suppose the material properties are time-independent, while the deformation is time-dependent. The contacting system configuration considered is shown in Fig. A.1. The contact problem is an initial-boundary-value problem in which two arbitrary bodies B^1 and B^2 interact according to the principles of the mechanics of continuous media. Each body has a smooth boundary ζ^i ($i=1, 2$), on which three distinct parts can be classified: a prescribed displacement boundary ζ_d^i , a prescribed force boundary ζ_f^i , and a contact boundary ζ_c^i . The contact occurs only when

$$A = \zeta^1 \cap \zeta^2 = \zeta_c^1 \cup \zeta_c^2 \neq \emptyset \quad (\text{A.1})$$

The governing equations for the motion of the body i ($i=1, 2$) can be written as (Hallquist, 1991)

$$\sigma_{jk,k}^i + b_j^i = \rho^i \ddot{u}_j^i \quad (j=1, 3 \text{ and } k=1, 3) \quad (\text{A.2})$$

where σ_{jk} is the Cauchy stress component, the comma denotes covariant differentiation, b_j is the j th component of the body force vector \mathbf{b} , ρ is the mass density of the material,

and \ddot{u}_j is the j th component of the acceleration vector. Note that σ_{jk} , b_j and \ddot{u}_j are a function of position vector \mathbf{x} and time t . In Eq.(A.2), the superscript i denotes a quantity defined for body i ($i=1, 2$). For simplicity, we will omit the superscript i in the following except when specified otherwise.

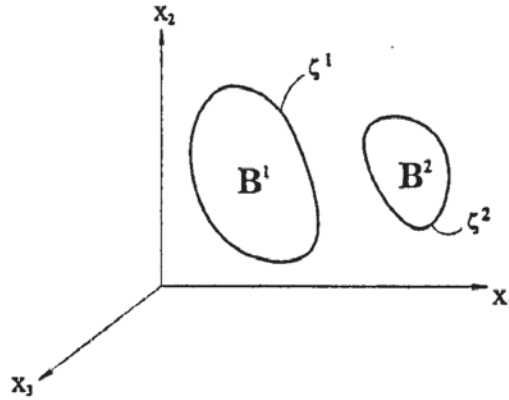


Fig. A.1 The contacting system configuration.

For a given contacting system, Eq.(A.2) should satisfy the initial conditions

$$u_j(\mathbf{x}, 0) = \bar{u}_j(\mathbf{x}) \quad (j=1, 3) \quad (\text{A.3a})$$

$$\dot{u}_j(\mathbf{x}, 0) = \dot{\bar{u}}_j(\mathbf{x}) \quad (j=1, 3) \quad (\text{A.3b})$$

for the whole displacement field $\mathbf{u}(\mathbf{x}, t)$ and velocity field $\dot{\mathbf{u}}(\mathbf{x}, t)$ at time $t=0$, and the prescribed boundary conditions

$$u_j(\mathbf{x}, t) = \bar{u}_j(\mathbf{x}, t) \quad \mathbf{x} \in \zeta_d \quad (j=1, 3) \quad (\text{A.4a})$$

$$\sigma_{jk}(\mathbf{x}, t)N_j = \bar{q}_j(\mathbf{x}, t) \quad \mathbf{x} \in \zeta_f \quad (j=1, 3; k=1, 3) \quad (\text{A.4b})$$

where $u_j(\mathbf{x}, 0)$ and $\dot{u}_j(\mathbf{x}, 0)$ denote the j th component of displacement and velocity fields at time $t=0$, respectively. $\bar{u}_j(\mathbf{x})$ and $\dot{\bar{u}}_j(\mathbf{x})$ are the corresponding prescribed initial values. N_j is the j th component of unit outward surface normal on the boundary ζ_f . $\bar{u}_j(\mathbf{x}, t)$ and $\bar{q}_j(\mathbf{x}, t)$ are prescribed displacement components and boundary traction components, respectively.

Equation (A.2) should also satisfy the following contact conditions on the boundary ζ_c :

$$g(\mathbf{x}, t) \geq 0 \quad (\text{A.5a})$$

$$p(\mathbf{x}, t) = \sigma_{jk}(\mathbf{x}, t) \cdot N_j \leq 0 \quad (\text{A.5b})$$

$$g(\mathbf{x}, t)p(\mathbf{x}, t) = 0 \quad (\text{A.5c})$$

where $g(\mathbf{x},t)$ is the gap between the contact surfaces, $p(\mathbf{x},t)$ is the normal component of contact stress in the outward normal direction of the surface. Equation (A.5a) is referred to be as the impenetrability condition, which means the two bodies cannot penetrate into each other. Equation (A.5b) indicates that only compressive contact stress is allowed at the contact interface for general contact/impact problems. Equation (A.5c) indicates that if $g(\mathbf{x},t)$ is non-zero, $p(\mathbf{x},t)$ must be zero and if $g(\mathbf{x},t)$ is zero, $p(\mathbf{x},t)$ must be non-zero.

Equations (A.2)-(A.5) constitute the mathematical model for the contact problem. To solve the contact problem is to find a displacement field $\mathbf{u}(\mathbf{x},t)$ so that the conditions in Eqs.(A.2)-(A.5) are all satisfied. Hamilton's law of varying action can be used to give an integral counterpart of the contact problem with reference to both the temporal and spatial domain. After integration of the kinetic energy by parts, Hamilton's law of varying action leads to a statement of virtual work for the initial-value problem according to

$$\int_{t_1}^{t_2} \left\{ \sum_{i=1}^2 (\delta E^i + \delta T^i - \delta W^i) + \delta W_c \right\} dt = 0 \quad (\text{A.6})$$

which is the weak form of the equilibrium equations. In Eq.(A.6) t_1 and t_2 denote the time instant, δE , δT and δW are the virtual internal, kinetic and external work, respectively. δW_c denotes the virtual work done by the contact force and appears in Eq.(A.6) only when Eq.(A.1) is satisfied, i.e., the contact takes place. In Eq.(A.6)

$$\delta E = \int_{\varphi} \sigma_{jk} \delta e_{jk} d\varphi \quad (\text{A.7a})$$

$$\delta T = \int_{\varphi} \rho \ddot{u}_j \delta u_j d\varphi \quad (\text{A.7b})$$

$$\delta W = \int_{\varphi} b_j \delta u_j d\varphi + \int_{\zeta_f} \bar{q}_j \delta u_j ds \quad (\text{A.7c})$$

$$\delta W_c = \int_{\lambda} \mathbf{q}_c (\delta \mathbf{u}^1 - \delta \mathbf{u}^2) ds \quad (\text{A.7d})$$

where summations on j and k are assumed with j and k ranging from 1 to 3, δe_{jk} denotes the components of virtual strain, δu_j is the component of virtual displacement, and φ denotes the spatial domain occupied by the contacting body, and \mathbf{q}_c is the contact traction vector.

Equation (A.6) forms the basis for the space-time discretization of the contact problem. Using finite difference and finite element methods, the time and space domains are divided into sub-domains, time steps and finite elements to carry out the integrations in Eq.(A.6). The time integration of the equations of motion can be performed using certain schemes,

which will be described in the following section. Integrations over the space domain in Eq.(A.6) are carried out on individual elements and assembled to obtain an equation system for the whole space domain. The finite elements can be of different types, such as 2D isoparametric solid element, axisymmetric element, solid element, shell element, beam element, etc. and can be of different material properties. For some contact/impact problems, the geometry non-linearity and material non-linearity may need to be handled in finite element procedures. A detailed description of element formulation and the algorithm to deal with the spatial integrations can be found in Zienkiewicz and Taylor (1989), Hughes (1987), Bathe (1982) and Oden (1972), among others. We will concentrate on the time integration method and the modelling of the contact conditions, which are the most distinct characteristics of the finite element technique for contact/impact problems.

For any specific point in time, a statement of equilibrium can be obtained by using finite element discretization of Eq.(A.6) and given in terms of the discrete nodal displacements as follows:

$$M\ddot{u}(t) + C\dot{u}(t) + Ku(t) = F(t) \quad (\text{A.8a})$$

$$F(t) = F_s(t) + F_c(t) \quad (\text{A.8b})$$

where M is the mass matrix, C is the damping matrix, K is the stiffness matrix, $u(t)$, $\dot{u}(t)$ and $\ddot{u}(t)$ are the nodal displacement, velocity and acceleration vectors, respectively, $F(t)$ is the external load vector, which consists of two parts: $F_s(t)$ as in the standard finite element procedure and $F_c(t)$ denoting the contribution of the contact force to the load vector. In practical applications, it is difficult or impossible to determine the element damping parameters for general finite element assemblies, in particular because the damping properties are frequency dependent. Therefore, the damping matrix C is generally not assembled from element damping matrices, but is constructed using the mass matrix and stiffness matrix of the complete element assemblies together with experimental results on the amount of damping. Among many formulations used to construct a damping matrix, Rayleigh damping is generally assumed in finite element methods, which is of form

$$C = \bar{\alpha}M + \bar{\eta}K \quad (\text{A.8c})$$

where $\bar{\alpha}$ and $\bar{\eta}$ are constants to be determined from two given damping ratios corresponding to two unequal frequencies of vibration (Bathe and Wilson 1976).

Equation (A.8) characterises the finite element solution for contact/impact problems. To solve Eq.(A.8), time integration schemes are required to find correlations of nodal

displacement, velocity and acceleration. Furthermore, special techniques must be developed to model the contact condition since neither the total number of contacting nodes nor the contact force are known before the solution is found. This requires that a certain contact searching procedure must be employed to find the true contacting nodes and a contact constraint method must be used to enforce the contact condition for solving the unknown contact force. The contact modelling techniques will be discussed in section A.4.

A.3 Time integration methods

In engineering dynamic analyses, four different methods are commonly used to carry out time integrations. These four methods are the direct integration method, the central difference method, the Newmark method and Wilson- θ method. In the following, we briefly review the central difference method and the Newmark method. For detailed description of the above time integration methods, readers are referred to Bathe and Wilson (1976) and Clough and Penzien (1993), among many others.

In the following discussion, we shall assume that the contact force vector is known. Then the problem becomes to find the displacement, velocity and acceleration vector, $\mathbf{u}(t)$, $\dot{\mathbf{u}}(t)$ and $\ddot{\mathbf{u}}(t)$, for any discrete points in time t from $t=0$ to $t=T$. We further assume that $\mathbf{u}(t)$, $\dot{\mathbf{u}}(t)$ and $\ddot{\mathbf{u}}(t)$ are known at time $t=0$ and equal to \mathbf{u}_0 , $\dot{\mathbf{u}}_0$ and $\ddot{\mathbf{u}}_0$, respectively. The time span considered is then subdivided into n equal time intervals Δt ($=T/n$) and the time integration scheme employed is to establish an approximate solution at times $0, \Delta t, 2\Delta t, \dots, t - \Delta t, t, t + \Delta t, \dots, T$.

A.3.1 The central difference method

The central difference method is one effective procedure to carry out the time integration in Eq.(A.6). It is assumed in the central difference method that

$$\ddot{\mathbf{u}}(t) = \frac{1}{\Delta t^2} \{ \mathbf{u}(t - \Delta t) - 2\mathbf{u}(t) + \mathbf{u}(t + \Delta t) \} \quad (\text{A.9})$$

$$\dot{\mathbf{u}}(t) = \frac{1}{2\Delta t} \{ \mathbf{u}(t + \Delta t) - \mathbf{u}(t - \Delta t) \} \quad (\text{A.10})$$

The errors in the expansion of Eqs.(A.9) and (A.10) are identical of order $(\Delta t)^2$ (Bathe and Wilson 1976). The displacement solution for time $t + \Delta t$ is obtained by considering Eq.(A.8) at time t and using Eqs.(A.9) and (A.10) as follows

$$\left(\frac{1}{\Delta t^2}M + \frac{1}{2\Delta t}C\right)u(t + \Delta t) = F(t) - \left(K - \frac{2}{\Delta t^2}M\right)u(t) - \left(\frac{1}{\Delta t^2}M - \frac{1}{2\Delta t}C\right)u(t - \Delta t) \quad (\text{A.11})$$

It can be seen that the solution of $u(t + \Delta t)$ is based on the equilibrium conditions at time t without solving Eq.(A.8) at time $t + \Delta t$. For this reason the time integration procedure is called an explicit integration method. An alternative procedure is an implicit integration method, such as the Newmark method to be discussed in the next subsection.

It is clear that using the central difference method, the calculation of $u(t + \Delta t)$ involves $u(t)$ and $u(t - \Delta t)$. To calculate the solution at time Δt , $u(-\Delta t)$ is hence required, which can be obtained by using Eqs.(A.9) and (A.10)

$$u(-\Delta t) = u_0 - \Delta t \dot{u}_0 + \frac{\Delta t^2}{2} \ddot{u}_0 \quad (\text{A.12})$$

where u_0 , \dot{u}_0 and \ddot{u}_0 are known.

A very important consideration in the use of the central difference method is that it is conditionally stable, *i.e.*, the time-step size Δt must be smaller than a critical value, Δt_{cr} , to satisfy the stability condition. Δt_{cr} can be calculated from the mass and stiffness properties of the entire element assemblage. Let ω_m denote the highest frequency component in the discretised system, the stability condition with the central difference method is then that (Hallquist 1991)

$$\Delta t \leq \frac{2}{\omega_m} \left(\sqrt{1 + \xi^2} - \xi \right) \quad (\text{A.13})$$

where ξ is the corresponding damping ratio.

A.3.2 The Newmark method

In the Newmark method, two parameters $\bar{\beta}$ and γ are introduced and can be used to control stability and accuracy of the integration. Briefly, the algorithm is given by

$$\dot{\mathbf{u}}(t + \Delta t) = \dot{\mathbf{u}}(t) + [(1 - \gamma)\ddot{\mathbf{u}}(t) + \gamma\ddot{\mathbf{u}}(t + \Delta t)]\Delta t \quad (\text{A.14})$$

$$\mathbf{u}(t + \Delta t) = \mathbf{u}(t) + \dot{\mathbf{u}}(t)\Delta t + \left[\left(\frac{1}{2} - \bar{\beta} \right) \ddot{\mathbf{u}}(t) + \bar{\beta}\ddot{\mathbf{u}}(t + \Delta t) \right] \Delta t^2 \quad (\text{A.15})$$

In addition to Eqs.(A.14) and (A.15), to solve the displacements, velocities and accelerations at time $t + \Delta t$, the equilibrium equations (A.8) at time $t + \Delta t$ are also required:

$$\mathbf{M}\ddot{\mathbf{u}}(t + \Delta t) + \mathbf{C}\dot{\mathbf{u}}(t + \Delta t) + \mathbf{K}\mathbf{u}(t + \Delta t) = \mathbf{F}(t + \Delta t) \quad (\text{A.16})$$

Solving from (A.15) for $\ddot{\mathbf{u}}(t + \Delta t)$ in terms of $\mathbf{u}(t + \Delta t)$ and then substituting for $\ddot{\mathbf{u}}(t + \Delta t)$ into (A.14), we obtained equations for $\ddot{\mathbf{u}}(t + \Delta t)$ and $\dot{\mathbf{u}}(t + \Delta t)$, each in terms of the unknown displacements $\mathbf{u}(t + \Delta t)$ only. These two relations for $\ddot{\mathbf{u}}(t + \Delta t)$ and $\dot{\mathbf{u}}(t + \Delta t)$ are substituted into (A.16) to solve for $\mathbf{u}(t + \Delta t)$, then, using Eqs.(A.14) and (A.15), $\ddot{\mathbf{u}}(t + \Delta t)$ and $\dot{\mathbf{u}}(t + \Delta t)$ can also be determined. The Newmark method demands a solution of the equation system at $t + \Delta t$ to obtain the displacements at $t + \Delta t$. It is hence an implicit method.

Newmark method is unconditionally stable when $\bar{\beta} \geq 1/4$ and $\gamma \geq 1/2$. For detailed analysis of stability for Newmark method, readers are referred to Bathe and Wilson (1976) and Clough and Penzien (1993). Note that even in an unconditionally stable method, the time-step size must be limited so that accuracy and convergence can be satisfied.

A.4 Contact modelling techniques in finite element methods

With the finite element method, contact boundaries are approximated by collections of polygons for three-dimensional (3D) problems. For two-dimensional (2D) problems, the contact boundaries are approximated by collections of lines. For the 3D cases, the polygons are normally either 3-vertex triangular facets or 4-vertex quadrilaterals according to different elements used. The polygons composing the contact boundaries are referred to as contact segments. Each edge of the contact segment is defined to be a contact edge. A node on the contact edge or the contact segments is referred to as a contact node. A contact surface is defined as the collection of all the contact segments that approximate a complete physical boundary. Note that a contact body may consist of more than one contact surface. Similarity, there may be more than one contact body in a contact system. Therefore a hierarchical relation can be established among a contact system, a contact body, a contact

surface, a contact segment, a contact edge and a contact node, which are called contact hierarchies. Figure A.2 illustrates the hierarchical contact system.

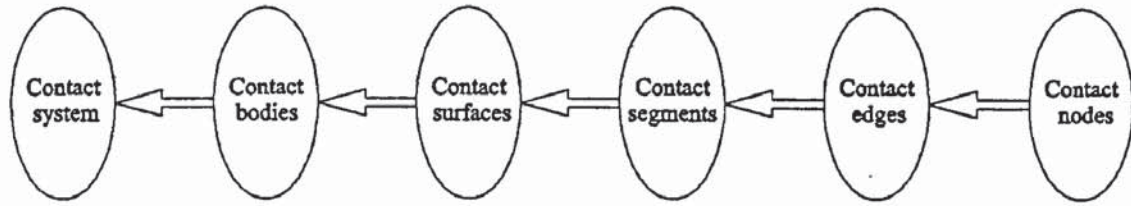


Fig. A.2 A hierarchical contact system.

Two types of contact can be classified: single surface contact and foreign contact. A single surface contact occurs when a surface makes contact with itself, while the foreign contact is defined as the contact between two different contact surfaces of either a single body or two contacting bodies. Here we only consider the foreign contact. In the foreign contact, one of the contact surfaces is specified as a slave surface, the other a master surface. The contact algorithms based on this specification are known as master-slave algorithms. We refer interested readers to Zhong (1993) and Hallquist (1991) for more information on the single surface contact.

In this section, the contact modelling procedures used in finite element methods will be described. First of all, the finite element discretisation of the contact surfaces will be described, followed by the discussion of the contact search algorithms. Finally the commonly used contact constraint methods (the kinematic constraint method and the penalty method) will be presented. We shall drop the argument t in the parentheses for all quantities for simplicity, except when specified otherwise, bearing in mind that all quantities are functions of time t since we are considering the general dynamic cases.

A.4.1 Finite element discretization of contact interfaces

As mentioned above, the contact surface is divided into collections of 3-nodes or 4-nodes contact segments for 3D problems and lines for 2D problems in finite element methods. The geometry of the 4-node contact segment can be defined using an iso-parametric coordinate system shown in Fig. A.3a as follows

$$\mathbf{x}(\xi, \eta) = \sum_{i=1}^4 \phi_i(\xi, \eta) \mathbf{x}_i \quad (\text{A.17})$$

where $\phi_i(\xi, \eta)$ denote the shape function corresponding to contact node i on the contact segment and \mathbf{x}_i the position vector of node i . The shape functions are defined as

$$\phi_1(\xi, \eta) = (1 - \xi)(1 - \eta)/2 \quad (\text{A.18a})$$

$$\phi_2(\xi, \eta) = (1 + \xi)(1 - \eta)/2 \quad (\text{A.18b})$$

$$\phi_3(\xi, \eta) = (1 + \xi)(1 + \eta)/2 \quad (\text{A.18c})$$

$$\phi_4(\xi, \eta) = (1 - \xi)(1 + \eta)/2 \quad (\text{A.18d})$$

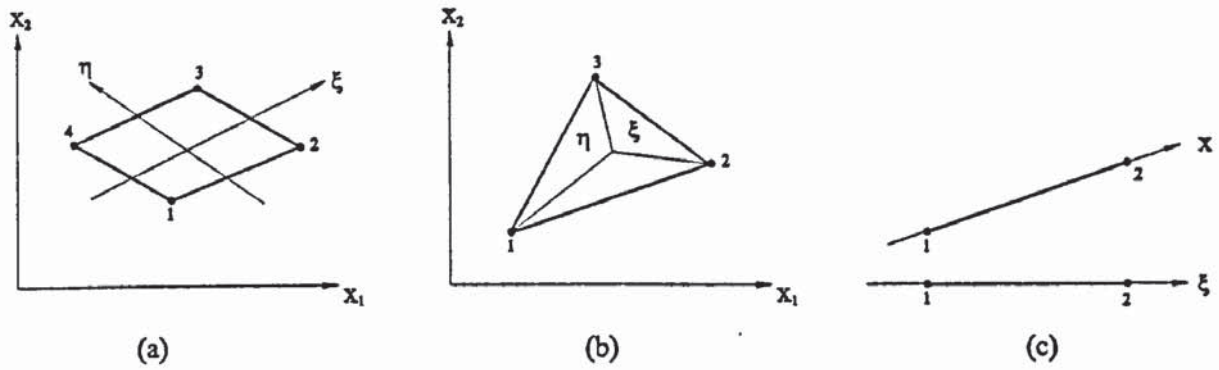


Fig. A.3 (a) A 4-node contact segment. (b) A 3-node contact segment (c) A line segment.

The geometry of the 3-node contact segment is defined as

$$\mathbf{x}(\xi, \eta) = \sum_{i=1}^3 \phi_i(\xi, \eta) \mathbf{x}_i \quad (\text{A.19})$$

The shape functions are defined as follows (Zhong 1993)

$$\phi_1(\xi, \eta) = \frac{\xi}{A} \quad (\text{A.20a})$$

$$\phi_2(\xi, \eta) = \frac{\eta}{A} \quad (\text{A.20b})$$

$$\phi_3(\xi, \eta) = 1 - \frac{\xi}{A} - \frac{\eta}{A} \quad (\text{A.20c})$$

where A is the area of the segment and ξ and η are area coordinates defined as in Fig. A.3b, in which the local node numbering of the segment is also shown.

Using an iso-parametric coordinate system shown in Fig. A.3c, the geometry of the line segment in 2D problems can be defined as

$$\mathbf{x}(\xi) = \sum_{i=1}^2 \phi_i(\xi) \mathbf{x}_i \quad (\text{A.21})$$

where the shape functions are defined as

$$\phi_1(\xi) = (1 - \xi)/2 \quad (\text{A.22a})$$

$$\phi_2(\xi) = (1 + \xi)/2 \quad (\text{A.22b})$$

To calculate the virtual work due to the contact traction (see Eq.(A.7d)), we need to know the contact traction distribution over the contact surface. However the contact traction distribution is not known prior to the solution of the problems. In the finite element procedure, the contact traction is usually regarded as a primary unknown and as an ordinary external load exerting on the contact body. The contribution of the contact traction is actually via contact nodes to exert unknown nodal forces. It is obvious that the problem can be simplified by directly taking the unknown nodal forces instead of the unknown contact tractions as primary unknowns. In this way, the discrete formulation of the contact problem can be derived (see, for example, Hughes *et al.* 1976; Zhong 1993; Hallquist 1991). Once the contact nodal forces are determined, the contact traction can be calculated directly from the nodal force, which will be discussed in Section A.4.4.

In the discrete formulation, only contacts at discrete contact nodes are considered. Contact loads are then concentrated forces at the discrete contact nodes. The virtual work due to the contact loads can now be calculated by

$$\delta W_c = \sum_{i=1}^{n_c} \delta w_{ci} \quad (\text{A.23})$$

where n_c is the total number of slave nodes, δw_{ci} denotes the virtual work produced by the concentrated contact force at slave node i , and is given by

$$\delta w_c = f_{cj} (\delta \bar{u}^2 - \delta u^1) \cdot N_j \quad (j=1 \text{ to } 3) \quad (\text{A.24})$$

where f_{cj} is the j th component of the contact nodal force, δu^1 and $\delta \bar{u}^2$ are the virtual displacements of the slave node and the corresponding contacting point on the master segment, respectively. $\delta \bar{u}^2$ can be evaluated by

$$\delta \bar{u}^2 = \sum_{i=1}^n \phi_i \delta u^2 \quad (\text{A.25})$$

where ϕ_i is the shape function corresponding to master node i on the master segments and δu^2 is the virtual displacement of the master nodes. The following notation is introduced to obtain a matrix expression for $\delta \bar{u}^2 - \delta u^1$:

$$\mathbf{u}_c = \{u_1^1 \quad u_2^1 \quad u_3^1 \quad u_{11}^2 \quad u_{12}^2 \quad u_{13}^2 \quad \dots \quad u_{n1}^2 \quad u_{n2}^2 \quad u_{n3}^2\}^T \quad (\text{A.26a})$$

$$\mathbf{Q}_c = \begin{bmatrix} -1 & 0 & 0 & \phi_1 & 0 & 0 & \dots & \phi_n & 0 & 0 \\ 0 & -1 & 0 & 0 & \phi_1 & 0 & \dots & 0 & \phi_n & 0 \\ 0 & 0 & -1 & 0 & 0 & \phi_1 & \dots & 0 & 0 & \phi_n \end{bmatrix} \quad (\text{A.26b})$$

Then Eq.(A.24) can be written as

$$\delta W_c = \delta \mathbf{u}_c^T (\mathbf{Q}_c^T \hat{N}_j f_{cj}) = \delta \mathbf{u}_c^T \mathbf{F}_c \quad (j=1 \text{ to } 3) \quad (\text{A.27})$$

where

$$\hat{N}_j = \{N_{j1} \quad N_{j2} \quad N_{j3}\} \quad (\text{A.28a})$$

$$\mathbf{F}_c = \mathbf{Q}_c^T \hat{N}_j f_{cj} \quad (\text{A.28b})$$

where N_{jk} denotes the k th component of boundary unit vector N_j . \mathbf{F}_c is a nodal force vector contributed by the contact at the corresponding contact node.

Substituting Eq.(A.27) into (A.23), we have

$$\delta W_c = \sum_{i=1}^{n_c} \mathbf{F}_{ci} \delta \mathbf{u}_{ci} \quad (\text{A.29})$$

The penetration of the slave node can be calculated as follows

$$p = (\bar{\mathbf{x}}^2 - \mathbf{x}^1) \cdot N_1 \quad (\text{A.30})$$

where \mathbf{x}^1 and $\bar{\mathbf{x}}^2$ are the position vectors of the slave node and the corresponding contacting points in the master segment, respectively. N_1 denotes the normal component of boundary unit vector N_j . In terms of the displacements, equation (A.30) can be rewritten as

$$\begin{aligned} p(t) &= (\bar{\mathbf{x}}^2(t - \Delta t) - \mathbf{x}^1(t - \Delta t)) \cdot N_1(t) + (\bar{\mathbf{u}}^2(t) - \mathbf{u}^1(t)) \cdot N_1(t) \\ &= p(t - \Delta t) + \hat{N}_1^T \mathbf{Q}_c \mathbf{u}_c(t) \end{aligned} \quad (\text{A.31})$$

The relative velocity of the slave node to the corresponding contacting points in the master segments is

$$\dot{\mathbf{u}} = \dot{\mathbf{u}}^1 - \dot{\bar{\mathbf{u}}}^2 = -\hat{N} \mathbf{Q}_c \dot{\mathbf{u}}_c \quad (\text{A.32})$$

where

$$\hat{N} = \{N_1 \quad N_2 \quad N_3\}^T \quad (\text{A.33a})$$

$$\dot{u}_c = \{\dot{u}_1^1 \quad \dot{u}_2^1 \quad \dot{u}_3^1 \quad \dot{u}_{11}^2 \quad \dot{u}_{12}^2 \quad \dot{u}_{13}^2 \quad \dots \quad \dot{u}_{n1}^2 \quad \dot{u}_{n2}^2 \quad \dot{u}_{n3}^2\}^T \quad (\text{A.33b})$$

Similarly, the relative acceleration \ddot{u} can be obtained as

$$\ddot{u} = -\hat{N}Q_c\ddot{u}_c \quad (\text{A.34})$$

where \ddot{u}_c is the time derivative of \dot{u}_c .

It can be seen from Eqs.(A.29)-(A.34) that after the finite element discretization the solution for the contact condition demands the total number n_c of the contacting slave nodes and the contact force F_c to be known *a priori*, which means that algorithms have to be developed to find the total number of contacting slave nodes and to determine the contact nodal force. The former is the task of contact searching procedures and will be discussed in the next subsection, while the latter requires certain contact constraint methods, which will be considered in Subsection A.4.3.

A.4.2 Contact searching procedure

After the finite element discretization of the contact boundary condition, the issue becomes to find segments in contact. There are many possible procedures to search the contacting segments, such as a master-slave algorithm, single-surface algorithm, and so on. Among these methods, the master-slave algorithm is a commonly used method. We shall discuss this method here. The objective of the master-slave method is to determine the total number of contacting slave nodes n_c and for each contacting slave node to find the corresponding contacting point in the master segment.

To determine n_c , a trial-and-error procedure has been widely used. In this procedure, it is supposed that the solution at time $t - \Delta t$ is known, then the total number of contacting slave nodes n_c at time $t - \Delta t$ is known. In addition, the position of a contact node in relation to all the contact segments is known at time $t - \Delta t$. Then it is possible to select new potential contact nodes at time t based on the information on the position of the contact nodes at time $t - \Delta t$. Where a new potential contact node is referred to as a contact node whose distance to any master segment/edge/node is smaller than a prescribed control

distance l_c , which can be specified either on the basis of the relative velocities $\dot{\mathbf{u}}_c$ of the contact boundaries as

$$l_c = \Delta t \dot{\mathbf{u}}_c(t - \Delta t) \cdot \mathbf{N}_1(t - \Delta t) \quad (\text{A.35})$$

or to be zero. In Eq.(A.35), \mathbf{N}_1 is a unit normal vector at a potential target point. The searching for the potential contacting slave nodes is performed in three phases (Zhong 1993). In the first stage, a master node that is closest to the slave node being considered is to be found. In the second stage, a master segment that contains that master node and is closest to the slave node is to be found as a target segment. Finally, the shortest distance between the slave node and its target master segment is to be calculated. If the distance is smaller than l_c , the slave node is then considered to be in contact with the master segment and regarded as a new potential contacting slave node.

Denote the total number of new potential contacting slave nodes at time $t - \Delta t$ by Δn_c , then the total estimated number of contacting slave nodes at time t is

$$\tilde{n}_c(t) = n_c(t - \Delta t) + \Delta n_c(t - \Delta t) \quad (\text{A.36})$$

It is obvious that \tilde{n}_c is a trial selection of contacting slave nodes, in which errors can be introduced. The errors can be found when an approximate solution based on the trial selection is obtained. Specifically, by enforcing the contact conditions at all the contact slave nodes, it may be found that the contact forces at some of the trial nodes are contradictory to physical conditions, which means that the mechanical contact condition is violated. A trial node that does not satisfy the mechanical contact condition is named as an error node. To obtain a correct solution, all the error nodes must be taken away from the trial selection, we then have the updated trial selection. The updated trial selection is used to update the solution at time t . If no error nodes are found, the updated selection is regarded as the true selection. Otherwise, the error node must be taken away and a new solution is obtained again at time t . This procedure is repeated until the trial or updated trial selection does not contain error nodes any more. Then the contacting number of slave nodes are found at time t and denoted by $n_c(t)$.

Now consider the searching for the corresponding target point in the master segment for each contacting slave node. Consider a slave node, n_s , sliding on a piecewise smooth master surface and assume that a search of the master surface has located the master node, n_m , lying nearest to n_s . Figure A.4 depicts a portion of a master surface with nodes n_s ,

and n_m labelled. If n_s and n_m do not coincide, n_s can usually be shown to lie in a segment s_i via the following tests (Hallquist 1991):

$$(N_i \times s) \cdot (N_i \times N_{i+1}) > 0 \quad (\text{A.37a})$$

$$(N_i \times s) \cdot (s \times N_{i+1}) > 0 \quad (\text{A.37b})$$

where vectors N_i and N_{i+1} are along edges of s_i and point out from n_m (see Fig. A.5). Vector s is the projection of the vector g , which is a vector beginning at n_m and ending at n_s , onto the plane being examined.

$$s = g - (g \cdot m)m \quad (\text{A.38})$$

where for segment s_i

$$m = \frac{N_i \times N_{i+1}}{|N_i \times N_{i+1}|} \quad (\text{A.39})$$

Since the sliding constraints keep n_s close but not necessarily on the master surface and n_s may lie near or even on the intersection of two master segments, the inequalities of equations (A.37) may be inconclusive, i.e., they may fail to be satisfied or more than one may give positive results. When this occurs n_s is assumed to lie along the intersection which yields the maximum value for the quantity

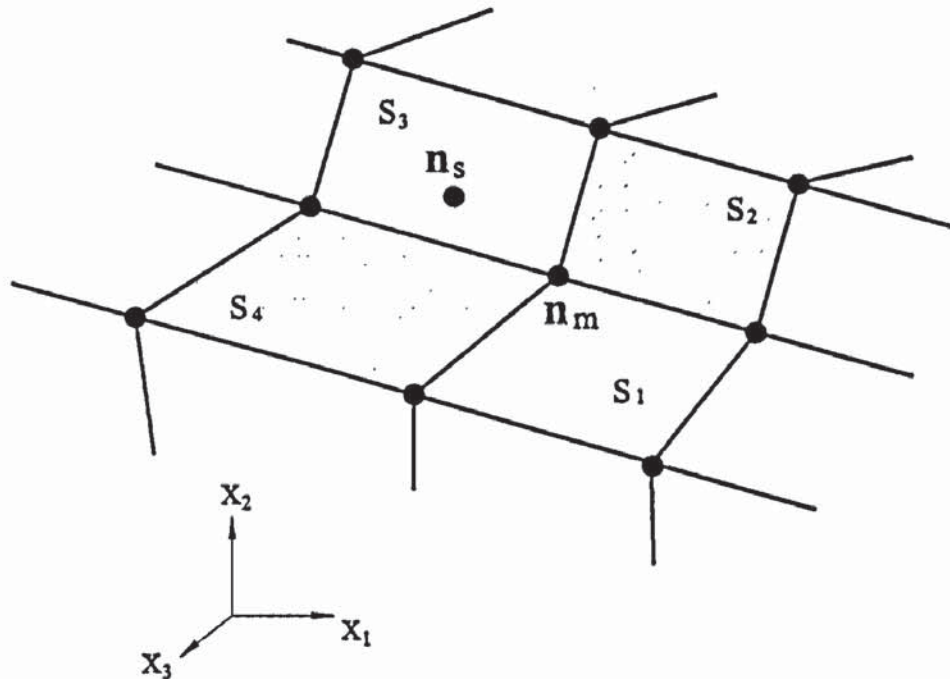


Fig. A.4 Illustration of the contact searching.

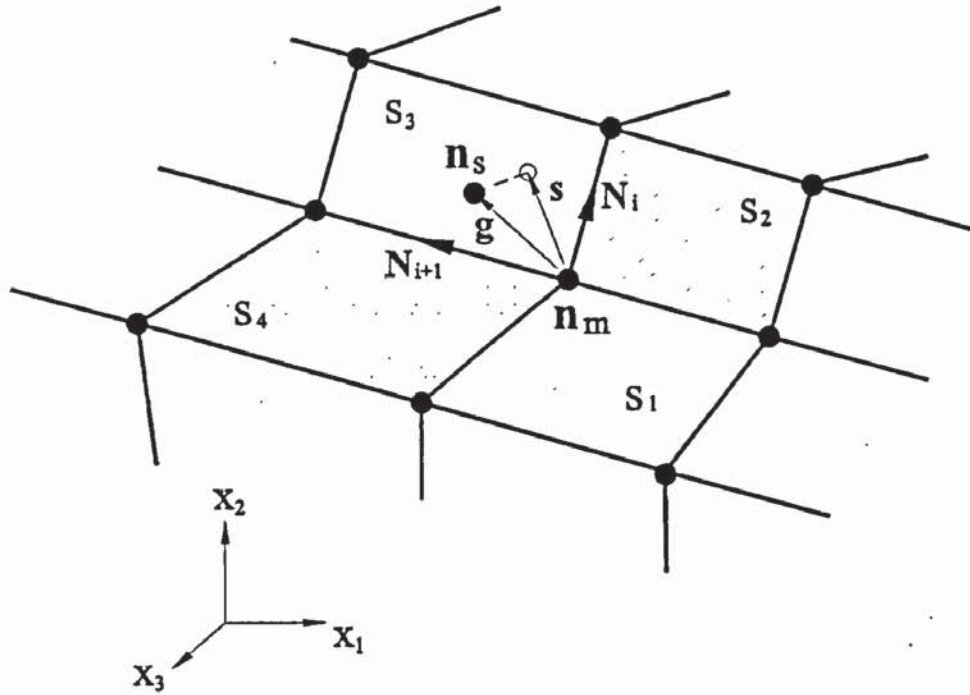


Fig. A.5 Projection of g onto master segment s_i .

$$\frac{g \cdot N_i}{|N_i|} \quad (i=1,2,3,4,\dots) \quad (\text{A.40})$$

Now consider that a master segment s_i has been located for slave node n_s , and that n_s is not identified as lying on the intersection of two master segments. Then the contact target point, defined as the point on the master segment which is closest to n_s , can be identified as follows.

With the finite element discretisation, each master segment s_i can be given by

$$r = x(\xi, \eta)N = \sum_{i=1}^3 x_i(\xi, \eta)N_i \quad (\text{A.41})$$

where $x(\xi, \eta)$ is defined in Eqs.(A.17)-(A.22) for various segments. And r represents a master segment that has a unique normal whose direction depends continuously on the points of s_i .

Let \mathbf{t} be a position vector drawn to slave node n_s , and assume that the master surface segment s_i has been identified with n_s . The contact target point coordinates (ξ_c, η_c) on s_i must satisfy

$$\frac{\partial r}{\partial \xi}(\xi_c, \eta_c) \cdot [\mathbf{t} - \mathbf{r}(\xi_c, \eta_c)] = 0 \quad (\text{A.42a})$$

$$\frac{\partial r}{\partial \eta}(\xi_c, \eta_c) \cdot [\mathbf{t} - \mathbf{r}(\xi_c, \eta_c)] = 0 \quad (\text{A.42b})$$

The physical problem is illustrated in Fig. A.6, which shows n_s lying above the master surface. Equations (A.42) can be readily solved for ξ_c and η_c . One way to accomplish this is to solve Eq.(A.42a) for ξ_c in terms of η_c , and substitute the results into Eq.(A.42b). This yields a cubic equation in η_c , which can be solved numerically.

A.4.3 Contact constraint method

Once a potential contacting slave node and the corresponding target point on the master segment are found, contact constraints must be imposed to model the contact boundary conditions. Two basic methods are commonly used to enforce the contact constraints: the kinematic constraint method and the penalty method. Fundamental differences between these two methods are discussed in the following.

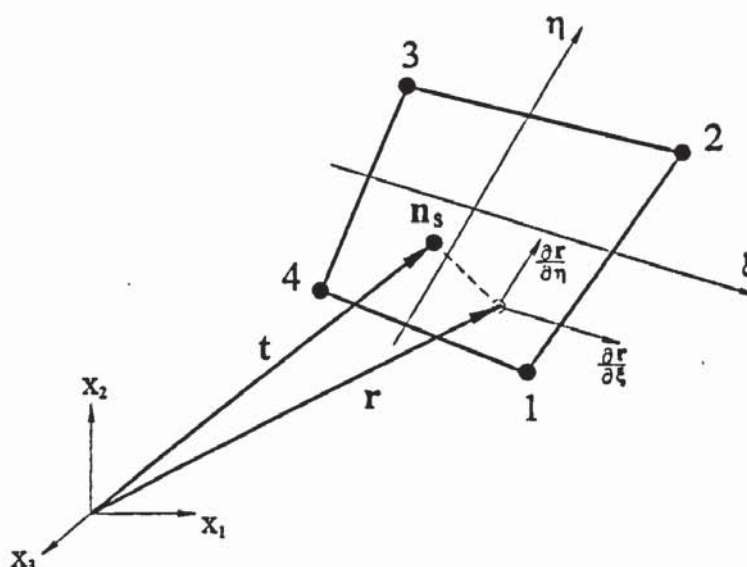


Fig. A.6 Location of contact target point when n_s lies above master segment.

A.4.3.1 Kinematic constraint method

The kinematic constraint method is also known as the Lagrange multiplier method. With this method, constraints are enforced on the global equations by a transformation of the nodal displacement components of the slave nodes along the contact interface. With the finite element discretisation of the contact surface, the impenetrability of contact Eq.(A.5a) can be expressed using Eq.(A.31):

$$p(t) = p(t - \Delta t) + \hat{N}_1^T \mathbf{Q}_c \mathbf{u}_c(t) = 0 \quad (\text{A.43})$$

Equation (A.43) applies to a single contacting slave node. Since there are n_c contacting slave nodes, there will be n_c contact constraints; each is expressed in the form of Eq.(A.43). Those n_c contact constraints can be assembled to obtain

$$p(t) = \mathbf{Q} \mathbf{u}(t) + p(t - \Delta t) = 0 \quad (\text{A.44})$$

in which

$$p(t) = \{p_1(t) \quad p_2(t) \quad \dots \quad p_i(t) \quad \dots \quad p_{n_c}(t)\}^T \quad (\text{A.45a})$$

$$\mathbf{Q} = \sum_{i=1}^{n_c} [\hat{N}_1^T \mathbf{Q}_c] \quad (\text{A.45b})$$

$$p(t - \Delta t) = \{p_1(t - \Delta t) \quad p_2(t - \Delta t) \quad \dots \quad p_i(t - \Delta t) \quad \dots \quad p_{n_c}(t - \Delta t)\}^T \quad (\text{A.45c})$$

where \sum indicates the standard finite element assembly procedure. Since all contacting slave nodes are identified after the contact searching process, Eq.(A.44) can be established explicitly.

With the kinematic constraint method, a Lagrange multiplier vector $\lambda(t)$ is used to replace the contribution of the contact force to the load vector $\mathbf{F}_c(t)$ in Eq.(A.8). Equation (A.8) can then be rewritten as

$$M\ddot{\mathbf{u}}(t) + C\dot{\mathbf{u}}(t) + K\mathbf{u}(t) + \mathbf{Q}_L^T \lambda(t) = \mathbf{F}_s(t) \quad (\text{A.46})$$

where, for the contacting slave nodes, \mathbf{Q}_L has the same components as \mathbf{Q} defined in Eq.(A.45b) (for others, the components of the \mathbf{Q}_L are zero). The components of the Lagrange multiplier vector $\lambda(t)$ are the contact forces. The Lagrange multiplier method proceeds by treating $\lambda(t)$ as unknown and solving Eqs.(A.44) and (A.46) simultaneously.

It is apparent that the contact constraint condition is enforced exactly in the kinematic constraint method. However, since we are only concerned with the enforcement of contact constraint on the slave nodes, problems may arise with this method when the master surface zone is finer than the slave surface zone, in which certain master nodes can penetrate through the slave surface without resistance. To minimize such problems, the more coarsely meshed surface should be chosen as the master. The disadvantage of the kinematic constraint method is that the introduction of new unknown Lagrange multipliers λ requires additional storage and computation. A more efficient method, the penalty method, was therefore developed.

A.4.3.2 Penalty method

In the penalty method, penetrations between contacting boundaries are allowed to happen. Then contact forces are calculated by using a penalty function

$$F_c(t) = \alpha_p p(t) \quad (\text{A.47})$$

where α_p is a diagonal matrix consisting of penalty parameters, $p(t)$ is the penetration vector given by

$$p(t) = Qu(t) + p(t - \Delta t) \quad (\text{A.48})$$

It is clear that the penetration vector $p(t)$ is a function of the displacement vector $u(t)$.

The penalty method uses an explicit approach to enforce the contact constraints. Figure A.7 illustrates the procedure used in the penalty method to enforce the contact constraints, in which only a single slave node that is about to come into contact with a fixed master surface is shown. In the increment n , the slave node comes into contact with the master surface and penetrates a distance \tilde{p} into the master surface at the end of the increment n . This penetration is allowed and no action is taken to avoid the penetration in the increment n . However, in the next increment $n+1$, an interface "spring" is inserted automatically between the slave node and the master surface to minimise the contact penetration. The force associated with the interface spring is equal to the spring stiffness multiplied by the penetration distance \tilde{p} . The interface spring stiffness is normally determined by the multiplication of a penalty parameter $\tilde{\alpha}$ with the stiffness of the contacting bodies.

Because the penalty method seeks to resolve contact penetration that exists at the beginning of each increment and the contact force is directly computed by introducing the penalty parameters, its explicit nature is obvious.

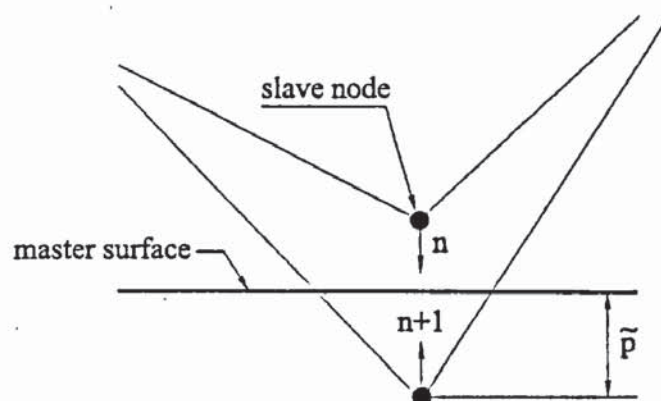


Fig. A.7 Illustration of the penalty method.

With the penalty method, no new unknowns are introduced and the contact constraints are enforced explicitly. Therefore no extra storage is required and the computations can be performed effectively. Since the penetrations introduced by the penalty method are controlled by the penalty parameters, the accuracy of the solution obtained using the penalty method depends on the choice of the penalty parameters. Too small penalty parameters may lead to too large penetrations, which may cause unacceptable errors. Too big penalty parameters may produce severe numerical problems in the solution process or simply make a solution impossible. Thus the penalty parameters must be chosen carefully to control the penetrations below a certain level.

A.4.4 Calculations of the contact traction

In finite element procedures for contact/impact problems, it is common that concentrated forces at discrete contacting nodes are used and solved instead of the contact traction that actually exerts over the contact boundary. However, in some engineering applications, the contact traction is of primary concern. So it is necessary to determine the contact traction from the nodal contact forces. This can be done in two ways: one is to convert the nodal contact forces to the contact tractions by a tributary area method; the other is to calculate the contact traction from boundary element stresses. It was shown by Hughes *et al.* (1976) that the contact tractions are given more accurately by the nodal contact forces than by the

element stresses. Therefore, in this study, all contact tractions are calculated from the nodal contact forces by the tributary area method.

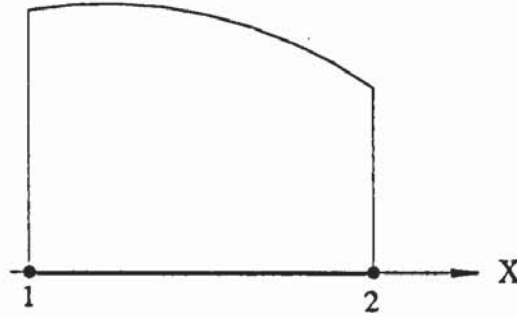


Fig. A.8 The contact traction over a contact segment.

Consider now the possible errors appeared in the calculation of contact tractions by using the tributary area method. For simplicity, we shall assume that a contact segment with two contact nodes is subjected to a contact traction in a 2D space as shown in Fig. A.8. The contact traction can be described by the following function (Zhong 1993):

$$p(x) = p_0 + cx^n \quad (\text{A.49})$$

where p_0 , c and n are constants. The nodal force is then as follows:

$$F_1 = \frac{1}{2} p_0 l + \frac{c}{(n+1)(n+2)} l^{n+1} \quad (\text{A.50a})$$

$$F_2 = \frac{1}{2} p_0 l + \frac{c}{(n+2)} l^{n+1} \quad (\text{A.50b})$$

where l is the length of the contact segment. Equations (A.50a) and (A.50b) give

$$p_0 = \frac{2}{nl} [(n+1)F_1 - F_2] \quad (\text{A.51a})$$

$$cl^n = \frac{(n+1)(n+2)}{nl} (F_2 - F_1) \quad (\text{A.51b})$$

Suppose now that the traction distribution in Eq.(A.49) is approximated by the following linear distribution:

$$\hat{p}(x) = \hat{p}_0 + \hat{c}x \quad (\text{A.52})$$

The nodal forces can then be obtained as follows

$$F_1 = \frac{1}{2} \hat{p}_0 l + \frac{\hat{c}}{6} l^2 \quad (\text{A.53a})$$

$$F_2 = \frac{1}{2} \hat{p}_0 l + \frac{\hat{c}}{3} l^2 \quad (\text{A.53b})$$

From Eqs.(A.53a) and (A.53b), it can be found that

$$\hat{p}_0 = \frac{2}{l} (2F_1 - F_2) \quad (\text{A.54a})$$

$$\hat{c} l = \frac{6}{l} (F_2 - F_1) \quad (\text{A.54b})$$

Then the errors of the traction at node 1 and node 2 can be obtained by

$$\varepsilon_1 = \hat{p}_0 - p_0 = -\frac{2(n-1)}{(n+1)(n+2)} cl^n \quad (\text{A.55a})$$

$$\varepsilon_2 = \hat{p}_0 + \hat{c} l - (p_0 + cl^n) = -\frac{n(n-1)}{(n+1)(n+2)} cl^n \quad (\text{A.55b})$$

It is clear that the approximated tractions are always smaller than the real ones if n is greater than unity, and the error is related to the length of the segment (the size of the finite elements).

In addition, another type of error can be introduced at the edge of the contact boundary. We shall again consider a 2D case for simplicity. Figure A.9a shows two neighbouring contact segments, where one segment is in full contact and the other only in partial contact. By assuming a linear distribution of contact traction over a complete contacting segment, we have to assume either a linear traction (Fig. A.9b) or zero (Fig. A.9c) over the partial contacting segment. It is clear that errors are introduced in both cases. Obviously, both types of error can be reduced by refining the mesh on the contact boundary.

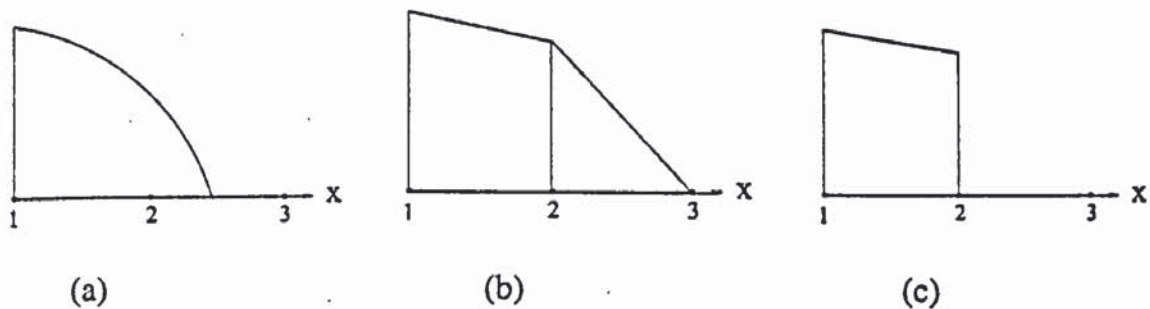


Fig. A.9 Possible errors in calculation of contact tractions at the contact edge.

A.5 Introduction of DYNA2D/DYNA3D (Whirley and Engelmann 1992, 1993)

DYNA2D/DYNA3D are non-linear, explicit, 2D and 3D finite element codes for analysing the transient dynamic response of solids and structures. They were originated and developed by Dr. John O. Hallquist of the Methods Development Group at the Lawrence Livermore National Laboratory (LLNL), USA, in the 1970s. Since then DYNA2D/DYNA3D have been used extensively and applied to a wide variety of large deformation transient dynamic problems by many analysts. DYNA2D/DYNA3D have also been advanced sufficiently to investigate contact/impact problems.

DYNA2D/DYNA3D are based on a finite difference discretisation of time and a finite element discretisation in two- and three- spatial dimensions. The explicit central difference method is used to integrate the equation of motion in time. The central difference method is only conditionally stable, and stability is governed by the time step size Δt . Physically, the limit of the time step size is essentially the time required for an elastic stress wave to propagate across the shortest dimension of the smallest element in the mesh. This maximum time-step may be equivalently related to the period of the highest free vibration mode of the finite element mesh. DYNA2D/DYNA3D automatically calculate the maximum time step size at each step of the solution, and adjusts the time step accordingly to minimize the number of time steps used in a solution. This feature minimizes the cost of the analysis while assuring that stability is maintained. DYNA2D/DYNA3D use a lumped mass formulation for efficiency. This produces a diagonal mass matrix M , which means that no simultaneous system of equations need be solved. Thus DYNA2D/DYNA3D do not form and solve the large matrix equation and do not require iteration at each time step.

The finite element formulations used in DYNA2D/DYNA3D are chosen for their accuracy, speed, and robustness in large deformation and non-linear problems. In an explicit analysis there are many small time steps, so it is important that the number of operations performed at each step be minimized. This consideration has largely motivated the use of elements with one-point Gaussian quadrature for the element integration. The four-node solid element and eight-node "brick" solid element with one-point Gauss integration are then chosen as the basic continuum finite elements in DYNA2D/DYNA3D. This approach gives rise to spurious zero energy deformation modes, or "hourglass modes", within the element. Spurious hourglass modes are then stabilized using an "hourglass viscosity" or an

“hourglass stiffness”. The element is hence stabilized to eliminate the spurious modes while retaining legitimate deformation modes. Displacements within the element are interpolated using bi-linear/tri-linear interpolation functions and the constitutive equations are evaluated once per element per time step based on the state at the centre of the element. This element is valid for large displacements and large strain.

As explicit codes, DYNA2D/DYNA3D are appropriate for problems where high rate dynamics or stress wave propagation effects are important. A transient dynamic problem requires the specification of initial conditions in order to be completely defined. In DYNA2D/DYNA3D, initial conditions are specified as initial velocities. All initial velocities may be set to zero, or the initial velocity of every node or a subset of nodes may be explicitly defined. DYNA2D/DYNA3D also contain a number of options for modelling the wide range of boundary conditions encountered in engineering analysis. Nodes may be constrained either from translation in the global coordinate system or to move only along an arbitrary but specified line by specifying in the node input.

DYNA2D/DYNA3D contain a robust and efficient capability for modelling the mechanical interaction of two bodies or two parts of a single body. In DYNA2D/DYNA3D, a slideline is defined in the input file by a list of nodes lying along the interface. One side of the interface is referred to as the slave surface and the other side the master surface. Several different options are offered for defining the behaviour of “slidelines” in a wide variety of situations. All DYNA2D/DYNA3D slidelines accommodate arbitrarily large relative motions. One of these options is a special purpose capability for treating interaction between a body and a rigid surface, for which “rigid wall/body” are defined to represent rigid surfaces/bodies. This permits modelling unilateral contact without requiring discretisation of the target surface, and thus is considerably effective. Among other options, the following are actually general slideline definitions:

- (1) Sliding only (kinematic formulation)
- (2) Tied (kinematic formulation)
- (3) Sliding with separation (kinematic formulation)
- (4) Sliding with separation and friction (penalty formulation)
- (5) Sliding with separation and no friction (penalty formulation)
- (6) Single surface slideline (penalty formulation)

As indicated in the parenthesis, two formulations are used and the main difference is the method employed to enforce the contact constraints (see Section A.4.3). The kinematic

method used in DYNA2D/DYNA3D is based on “node on surface” concept. Only slave nodes are restricted from penetrating the master surface and check if there is no penetration through any of the master segments for this slideline. Therefore it is important that the master surface should be chosen as the more coarsely meshed surface. The penalty method formulations are symmetric treatments in that the designation of the two surfaces as slave or master are interchanged, and the contact algorithm is applied a second time. Thus each surface goes through the penalty contact algorithm once as a master surface and once as a slave surface. This symmetric approach has been found to greatly increase the robustness and reliability of slidelines based on the penalty method. For these slidelines, the designation as master or slave surface is not important. The detailed descriptions of the above interfaces can be found in Whirley and Engelmann (1992, 1993).

A.7 Summary

In this appendix, we have briefly discussed the distinct aspects of finite element methods for solving contact/impact problems. We have focused on the general formulations for contact/impact problems, the time integration methods, and the contact modelling techniques. We have also introduced the capabilities and characteristics of the finite element codes, DYNA2D and DYNA3D, employed in this study.

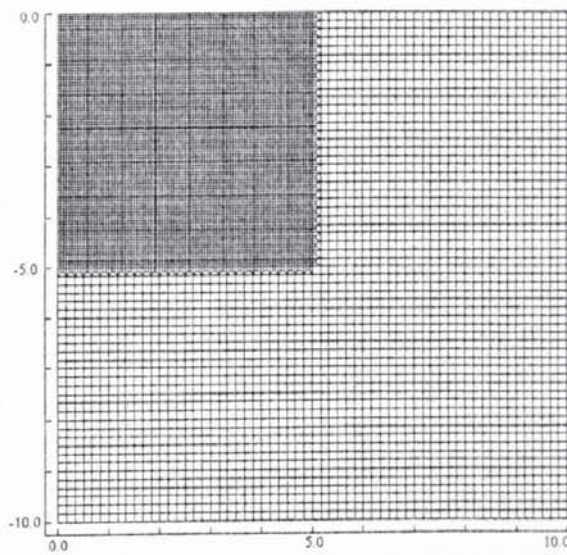
Appendix B Significance of the Substrate Size in FE Simulations of the Normal Impact of a Sphere with a Half-Space

B.1 Introduction

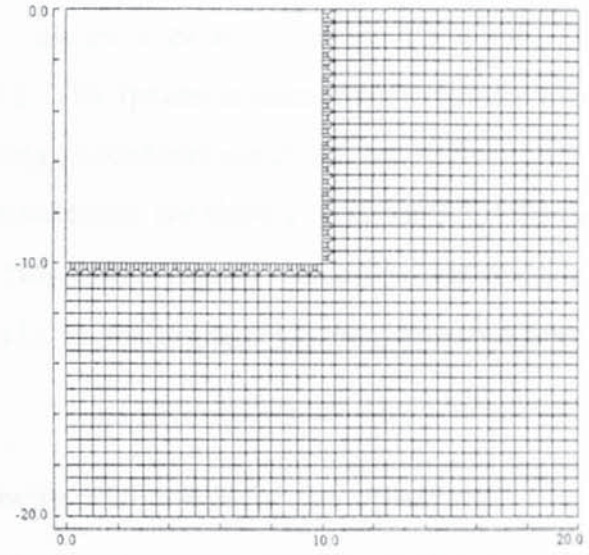
In FE simulations of the normal impact of a sphere with a half-space, it is crucial to select an appropriate dimension for the substrate, so that it can not only represent a half-space but also keep the computation as efficient as possible. To achieve this, it is recognised that, on the one hand, the substrate should be large enough to eliminate the constraints of boundary conditions; on the other hand, it should not be unnecessarily large, which may cost more computer power. It is also understood that the influence of the constrained boundaries is related not only to the substrate size but also to the loading conditions and material properties. In addition, the stress wave propagation is an unavoidable phenomenon during the impact, which, however, was ignored in all theoretical models in literature for simplicity. In order to make proper comparison with these theoretical models, we expect that the effect of the stress wave would be negligible and the deformation can be regarded as quasi-static in the FE simulations. This requires that the stress waves can traverse in the substrate many times during the impact, as suggested by Love (1952). This in turns requires that the substrate should not be too large, since the velocities of the stress waves are constant for a given material properties and the reflection times of the stress waves are then inversely proportional to the substrate size. Therefore, it is important to choose such an appropriate substrate in FE simulations of the normal impacts that not only the boundary conditions but also the stress wave has a negligible effect on the impact behaviour.

Motivated by this, preliminary studies of the normal impacts of a sphere with a substrate, which is assumed to be either elastic or elastic-perfectly plastic, of different sizes are carried out and presented here. The FE models considered are presented in Section B.2, and the effect of the substrate size on the impact response is discussed in Section B.3. Finally, the effect of stress wave is studied in Section B.4.

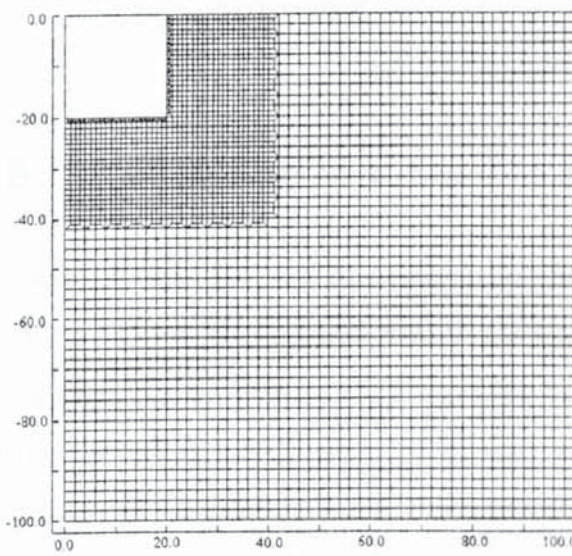
B.2 Finite element models



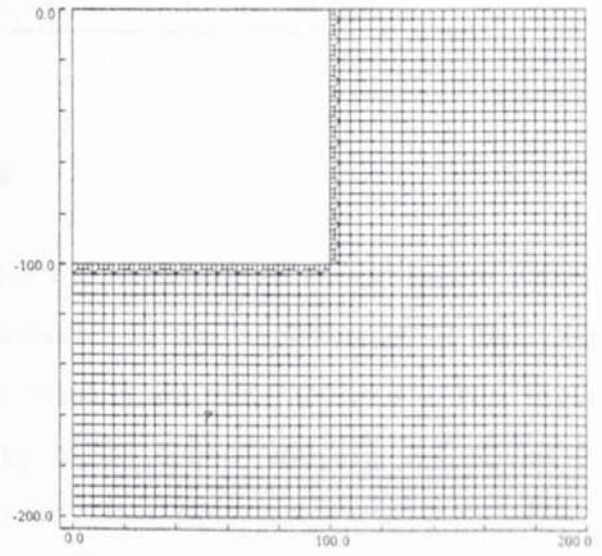
(a)



(b)



(c)



(d)

Fig. B.1 Finite element meshes for the substrate of: (a) $R \times R$; (b) $2R \times 2R$; (c) $10R \times 10R$ and (d) $20R \times 20R$. (unit: μm)

The analysis model for the normal impact of a sphere with a substrate is shown in Fig. 3.4. Four different sizes are chosen for the substrate: $L = R$, $2R$, $10R$ and $20R$, where $R = 10\mu\text{m}$ is specified to the radius of the sphere. To minimise the effect of the finite element mesh, a larger substrate is constructed by keeping the meshes for the previous smaller model unaltered and extending it using a graduated mesh for the sake of computing effectiveness. Therefore, for these four substrates, the meshes within the same region are identical. For example, the meshes in the region of $10\mu\text{m} \times 10\mu\text{m}$ for the substrate of

$20\mu\text{m}\times 20\mu\text{m}$ are identical to those for the substrate of $10\mu\text{m}\times 10\mu\text{m}$, and so on. The finite element meshes for these four substrates are shown in Fig. B.1, in which only meshes for extended region from the previous smaller one are shown for clarity. The total number of elements and nodes are shown in Table B.1. The sphere is discretised with the meshes shown in Fig. 3.3b. The finite element modelling procedures are discussed in Section 3.3.2. The material properties for the sphere and the substrate are shown in Table 3.2. In order to cover a wide range of the impact velocity, two initial impact velocities are considered: $V_{ni} = 5.0\text{m/s}$ and $V_{ni} = 150\text{m/s}$. $V_{ni} = 150\text{m/s}$ is the highest velocity employed in this study.

Table B.1 The number of elements and nodes for the substrates

The size of the substrate	Number of elements	Number of nodes
$R\times R$	10,980	11,161
$2R\times 2R$	12,300	12,481
$10R\times 10R$	15,760	16,001
$20R\times 20R$	17,735	18,002

B.3 The influence of substrate size

The FEA results are shown in Figs. B.2-B.6 for the impact of an elastic sphere with an elastic substrate. Figure B.2 shows the time histories of the displacement at the sphere centre. The corresponding time histories of the velocity are presented in Fig. B.3. Figure B.4 illustrates the evolutions of kinetic energy of the sphere and Fig. B.5 shows the evolutions of the contact force. Force-displacement relationships are shown in Fig. B.6. It can be seen that, regardless of the impact velocity, all results obtained with the substrate of size $10R\times 10R$ and $20R\times 20R$ are identical. This indicates that a substrate of size $10R\times 10R$ is larger enough to eliminate the influence of the boundary constraints and to represent a half-space for the wide velocity range considered, which is consistent with the analysis of Mesarovic and Fleck (1999) who pointed out that the outer boundary conditions are unimportant for FE models with a substrate larger than $L/R = 10$. For all the responses during the impact at $V_{ni} = 5.0\text{m/s}$, the differences among those obtained with four different substrates are so small that they can be ignored. It is implied that for low impact velocities even a small substrate (say, of size $R\times R$) can represent a half-space and further enlargement of the substrate size produce no significant effect on the results.

However for the impact at the high velocity of $V_{ni} = 150m/s$, the difference among the results obtained with different substrates becomes significant. At high velocities, two factors could affect the responses during the impact: one is the constraint of the boundary when the substrate is too small, the other is stress waves initiated by the impact when the substrate is large enough so that no stress wave reflects back to the contact point before the sphere rebounds. It is clear that significant energy loss can be observed for the impact with large substrates ($L \geq 10R$) at $V_{ni} = 150m/s$ (Fig. B.4b). This is obviously due to the effect of stress wave propagation, because when the size of the substrate is larger than $10R$, the shortest time for stress waves reflecting back to the contact point is about $39 \mu s$, but the duration of impact is only $23.7 \mu s$ at this impact velocity (see Fig. B.5b). This means that at high velocities the duration of the impact is very short; during this short period, the stress wave cannot reflect back to the initial impact point if the substrate is too large and part of the energy is thus dissipated. This also results in the divergence between the loading and unloading curves of force-displacement relationships as can be seen from Fig. B.6b. The area encompassed by the loading and unloading curves represents the magnitude of energy dissipated during the impact. The energy dissipation due to the stress wave will be discussed in next section in more details.

It is interesting to note that even for the impact at $V_{ni} = 150m/s$ the responses during the compression are very close among the impacts with the substrate of $L \geq 2R$. Bearing in mind the effect of stress waves, we may conclude that for the impact of an elastic sphere with an elastic substrate the effect of the boundary constraints can be neglected when the substrate size is large than the diameter of the sphere, and the divergence of the responses during the restitution are mainly due to the effect of stress wave.

Figures B.7-B.9 show the response of the elastic sphere during impacts with an elastic-perfectly plastic substrate of dimension $L = 2R$ and $L = 10R$ at $V_{ni} = 150m/s$. It is apparent that the results obtained from the impacts with different sized substrate are very close. This indicates that for the impact of an elastic sphere with an elastic-perfectly plastic substrate the substrate of size $L = 2R$ is large enough to eliminate the effect of the boundary constraints. This also implies that the effect of stress waves on the responses of the sphere during the impacts with an elastic-perfectly plastic substrate is negligible, which will be discussed further in next section.

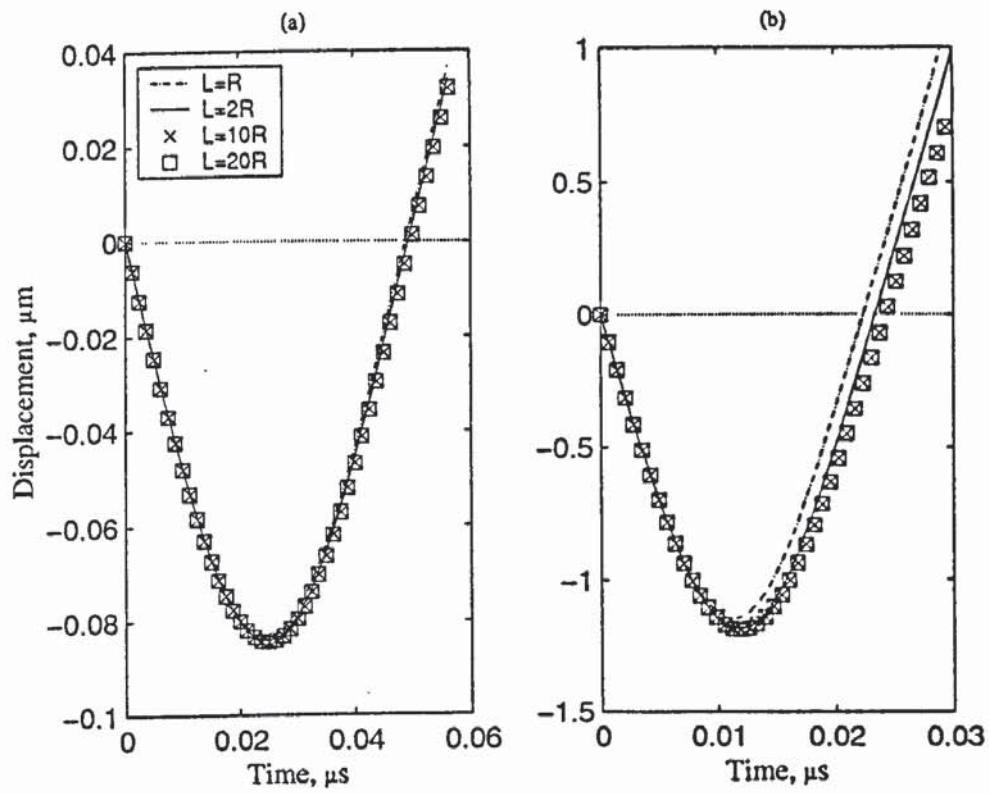


Fig. B.2 Time histories of displacement at the sphere centre for the impact of an elastic sphere with an elastic substrate of various sizes. (a) $V_{ni} = 5.0\text{ m/s}$; (b) $V_{ni} = 150\text{ m/s}$.

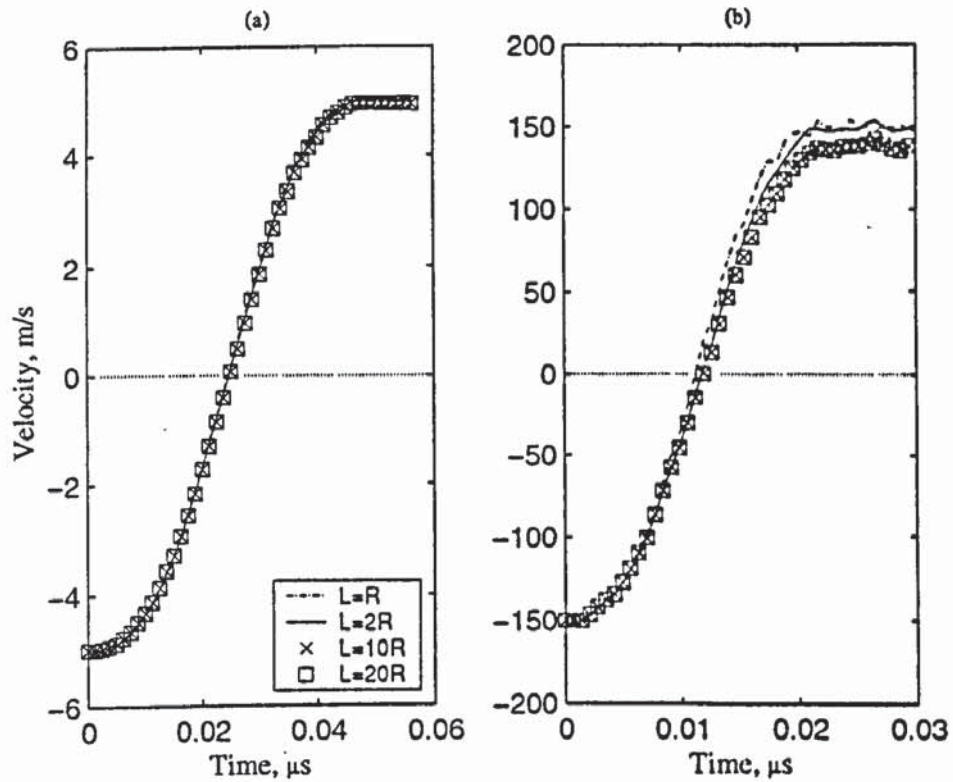


Fig. B.3 Time histories of velocity at the sphere centre for the impact of an elastic sphere with an elastic substrate of various sizes at: (a) $V_{ni} = 5.0\text{ m/s}$; (b) $V_{ni} = 150\text{ m/s}$.

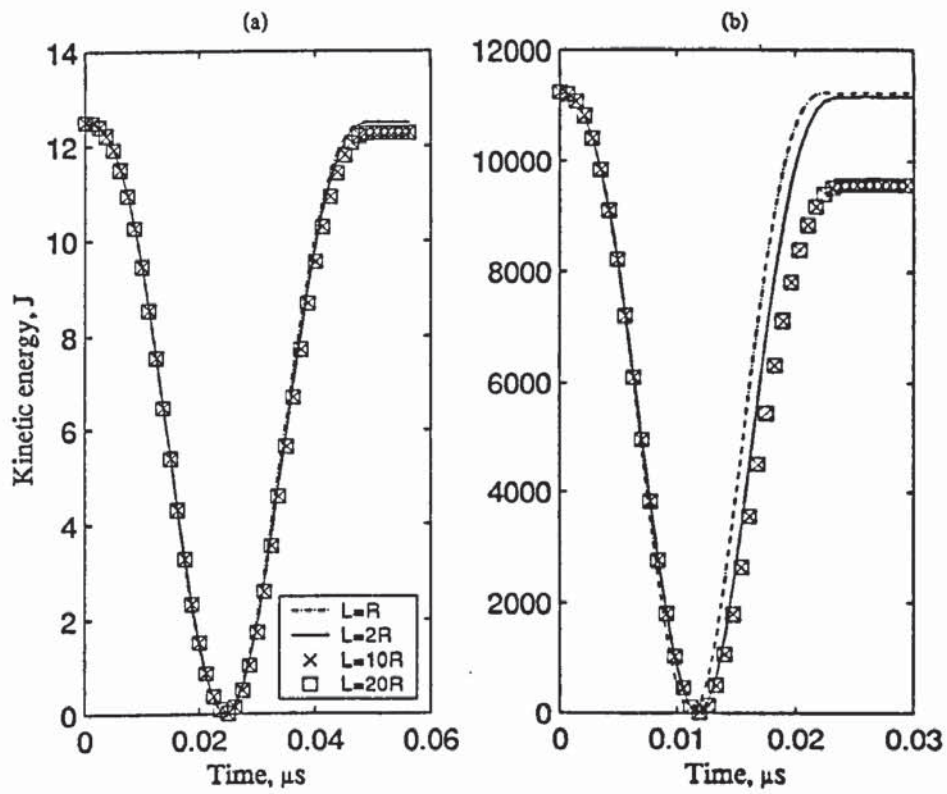


Fig. B.4 Time histories of kinetic energy of the sphere for the impact of an elastic sphere with an elastic substrate of various sizes at: (a) $V_{ni} = 5.0 \text{ m/s}$; (b) $V_{ni} = 150 \text{ m/s}$.

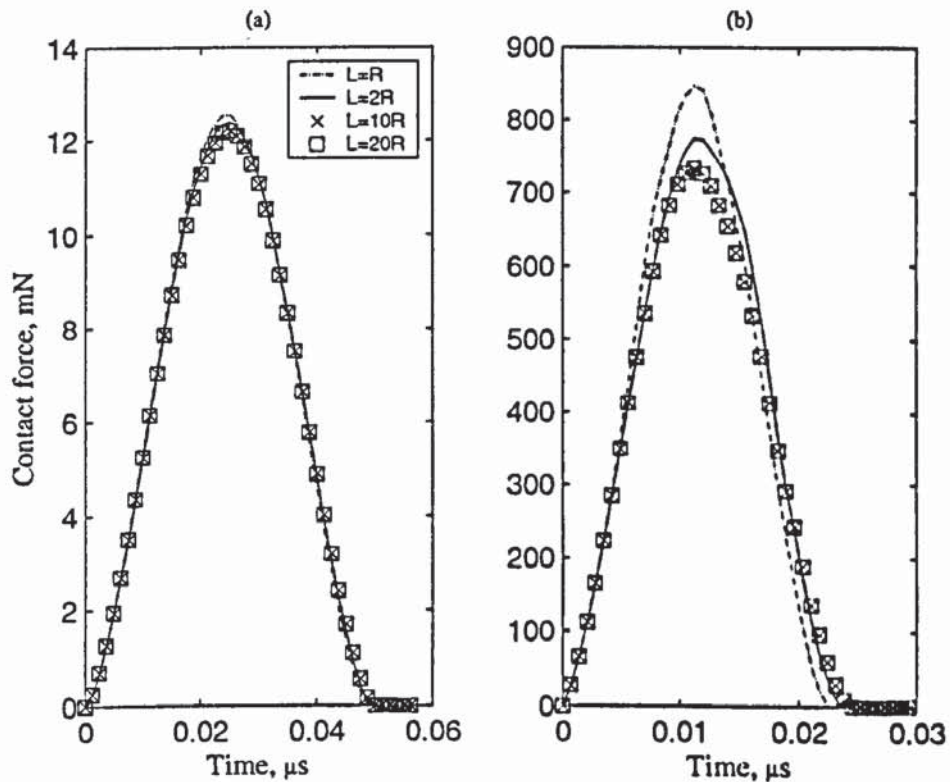


Fig. B.5 Time histories of contact force for the impact of an elastic sphere with an elastic substrate of various sizes at: (a) $V_{ni} = 5.0 \text{ m/s}$; (b) $V_{ni} = 150 \text{ m/s}$.

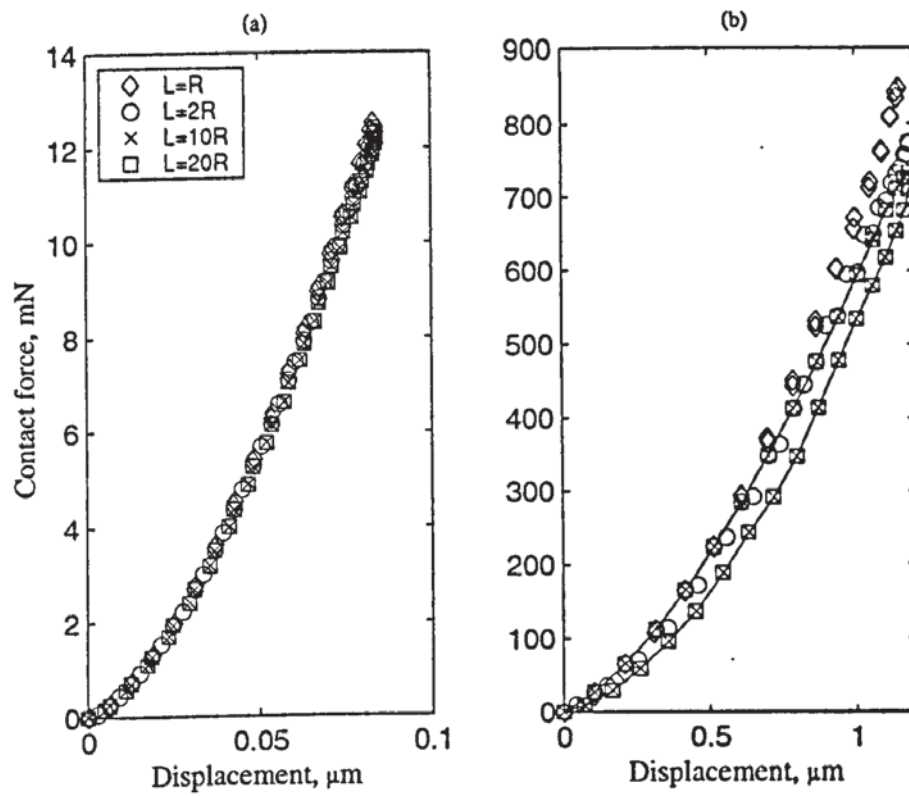


Fig. B.6 Force-displacement relationships for the impact of an elastic sphere with an elastic substrate of various sizes at: (a) $V_{ni} = 5.0 \text{ m/s}$; (b) $V_{ni} = 150 \text{ m/s}$.

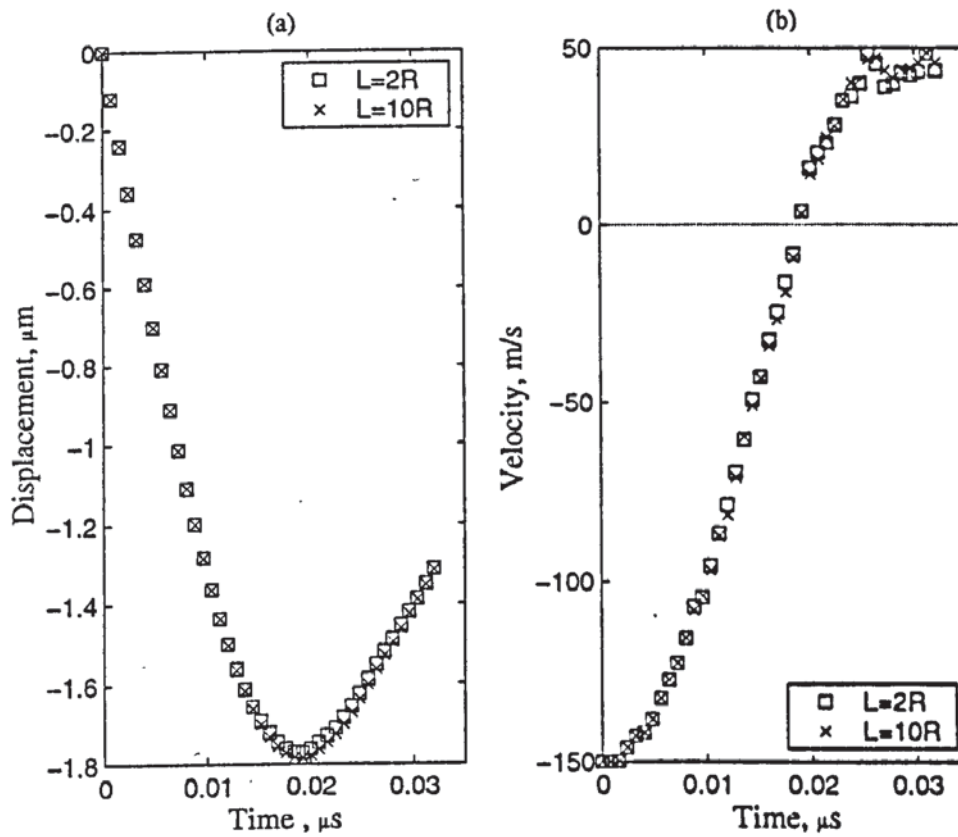


Fig. B.7 Time histories of (a) displacement and (b) velocity at the sphere centre for the impact of an elastic sphere with an elastic-perfectly plastic substrate of two different sizes at $V_{ni} = 150 \text{ m/s}$.

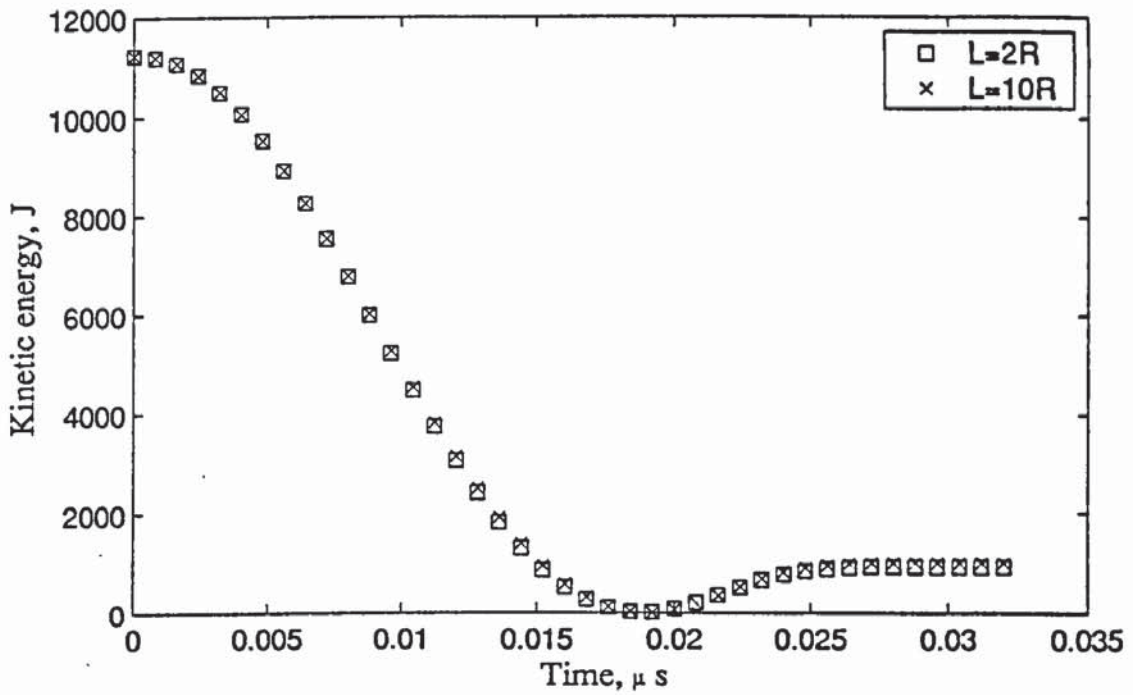


Fig. B.8 Time histories of kinetic energy of the sphere for the impact of an elastic sphere with an elastic-perfectly plastic substrate of two different sizes at $V_{ni} = 150m/s$.

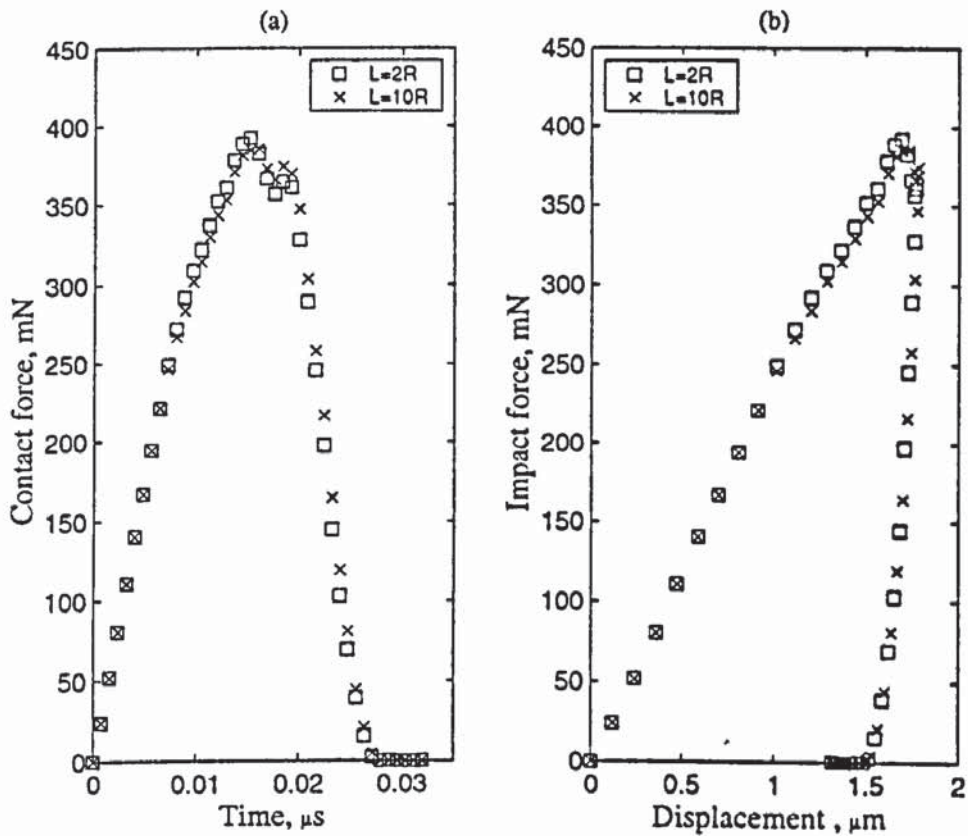


Fig. B.9 (a) Time histories of contact force and (b) force-displacement relationships, for the impact of an elastic sphere with an elastic-perfectly plastic substrate of two different sizes at $V_{ni} = 150m/s$.

B.4 The influence of stress waves

Figure B.10 shows the variation of the coefficient of restitution with initial impact velocity for the impacts of an elastic sphere with an elastic substrate. In this figure, two sets of results are presented for the same range of impact velocities: one is obtained from the simulations with a substrate of dimension $L = 2R$, while the other is obtained with a substrate of size $L = 10R$. It can be seen from Fig. B.10 that coefficients of restitution obtained for the two substrates are apparently different. For the impacts with a small substrate ($2R \times 2R$), the coefficient of restitution are essentially equal to unity when the impact velocity is less than 50m/s . Although the coefficient of restitution begins to deviate from unity, the deviation is very small, for instance, $e_n = 0.9956$ when $V_{ni} = 150\text{m/s}$. However, for the impacts with a large substrate ($10R \times 10R$), the coefficient of restitution always decreases with impact velocity and only when the impact velocity is very small is the coefficient of restitution close to unity. We attribute the different trends for the two substrates to the effect of the stress wave.

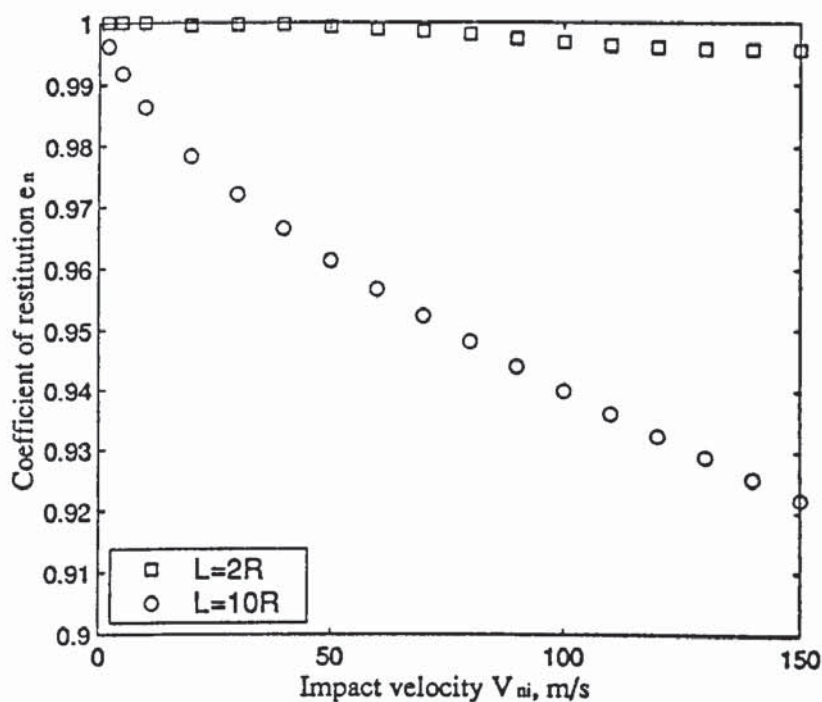


Fig. B.10 Coefficients of restitution for the impacts of an elastic sphere with an elastic substrate.

It is understood that it takes more time for the stress wave to reflect back to the initial contact point in the large substrate than in the small substrate. As for material properties selected, the time for the longitudinal wave to reflect back to the initial contact point in the sphere and the substrate of size $L = 2R$ is $\bar{T}_2 = 7.8 \times 10^{-3} \mu\text{s}$, while in the substrate of size

$L = 10R$, $\bar{T}_{10} = 39 \times 10^{-3} \mu s$. The energy loss due to the stress wave propagation depends strongly on how many times it can reflect back to the contact point before the sphere bounds off, which in turn depends on the duration of impact. It is also readily understood that the longer the impact duration, the more times for the stress wave to reflect back. Therefore it is necessary to determine the duration of impact. Table B.2 shows the duration of impacts for all impact velocities considered, in which we present the FEA results together with those given by Hertz theory (Eq.(2.15)). Note that the duration of impact obtained from FEA is determined by evaluating the instant when the contact force reduces to zero, for which the error is controlled by the time interval chosen arbitrarily before the test is run. For all cases considered here, the maximum error is $0.0016 \mu s$. It can be seen that the durations of impact obtained with finite element methods are comparable with those given by Hertz theory, and the longitudinal wave can reflect back to the initial contact points more than three times during the impact with a substrate of $L = 2R$ at all velocities considered. However, for the impacts with a substrate of $L = 10R$, the longitudinal wave can only reflect once at low velocities (say $V_{ni} \leq 10 m/s$), and at high velocity, no longitudinal wave reflects back to the initial contact point during the impact.

Table B.2 The duration of the impact

Impact Velocity (m/s)	The duration of impact (μs)		Number of reflections of stress wave	
	FEA	Hertz theory	$2R \times 2R$	$10R \times 10R$
2.0	0.0608	0.0604	7	1
5.0	0.0500	0.0503	6	1
10.0	0.0432	0.0438	5	1
20.0	0.0370	0.0381	4	0
30.0	0.0344	0.0352	4	0
40.0	0.0320	0.0332	4	0
50.0	0.0304	0.0317	4	0
60.0	0.0296	0.0306	3	0
70.0	0.0288	0.0297	3	0
80.0	0.0273	0.0289	3	0
90.0	0.0270	0.0282	3	0
100.0	0.0266	0.0276	3	0
110.0	0.0259	0.0271	3	0
120.0	0.0252	0.0266	3	0
130.0	0.0249	0.0262	3	0
140.0	0.0245	0.0258	3	0
150.0	0.0238	0.0255	3	0

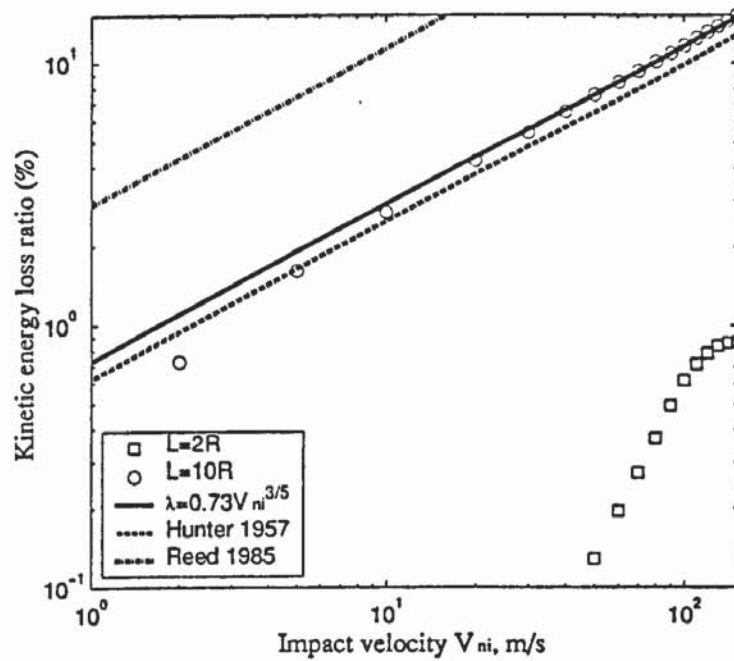


Fig. B.11 The variation of energy loss ratio λ with impact velocity for the impact of an elastic sphere with an elastic substrate.

Figure B.11 shows the variation of kinetic energy loss ratio λ with impact velocity for the impact of an elastic sphere with an elastic substrate of size $L = 2R$ and $L = 10R$, respectively. The energy loss ratio is defined as

$$\lambda = \frac{W_i - W_r}{W_i} \quad (\text{B.1})$$

It can be seen that the energy loss due to stress wave is generally small ($\leq 1\%$) and can be ignored during the impact with an elastic substrate of dimension $L = 2R$ at all velocities considered. However, for the impact with a substrate of dimension $L = 10R$, the energy loss due to stress waves increases with impact velocity, and when $V_{ni} > 20 \text{ m/s}$, at which no longitudinal wave reflects back to the initial contact point during the impact, FEA results show that λ is proportional to $V_{ni}^{3/5}$ with a proportional constant of 0.73. This is comparable with the predictions of Hunter (1957), whose analysis produced $\lambda = 0.62V_{ni}^{3/5}$ for the impact of a small sphere with a massive body.

Referring with Table B.2, it may be suggested that, for the impact of an elastic sphere with an elastic substrate, if the longitudinal wave can reflect back to the initial contact point more than three times during the impact, the effect of the stress wave is negligible. Otherwise the stress wave effect becomes significant.

Table B.3 The coefficient of restitution for the impact of an elastic sphere with an elastic-perfectly plastic substrate of different sizes

Impact velocity (m/s)	Coefficient of restitution, e_n		The difference
	$L = 2R$	$L = 10R$	
0.3	0.999	0.999	0.0
3	0.852	0.850	0.002
10	0.719	0.715	0.004
20	0.637	0.630	0.007
30	0.588	0.575	0.013
50	0.516	0.505	0.011
65	0.471	0.461	0.010
80	0.430	0.423	0.007
90	0.405	0.401	0.004
100	0.382	0.381	0.001
120	0.339	0.344	-0.005
130	0.320	0.327	-0.007
150	0.286	0.298	-0.012

Similar to the analysis for elastic impact, two series of tests were carried out for the impact of an elastic sphere and an elastic-perfectly plastic substrate: one was for the impact with a substrate of $L = 2R$ and the other for the impact with a substrate of $L = 10R$. The impact velocities were specified ranging from $0.3m/s$ to $150m/s$. The coefficients of restitution obtained from these two series of tests are compared in Table B.3, in which the coefficients of restitution are estimated by Eq.(4.6). It can be seen from Table B.3 that the differences in coefficients of restitution obtained from the two series of tests are very small and can be ignored, which is in contrast to the analysis for the impact of an elastic sphere with an elastic substrate as shown in Fig. B.10. This implies that the energy dissipation due to stress waves is negligible for the impact of an elastic sphere with an elastic-perfectly plastic half-space over a wide range of impact velocities regardless of the substrate size. This is because plastic deformation is very readily initiated for the impact of an elastic sphere with an elastic-perfectly plastic half-space as discussed in Chapter 5. The decrease of the coefficient of restitution with the increasing impact velocity shown in Table B.3 is hence mainly due to the effect of plastic deformation.

B.5 Summary

In this appendix, the significance of substrate size in FE simulations of the normal impact of a sphere with a half-space has been investigated. It has been shown that two factors need

to be considered when constructing the FE models: one is the effect of boundary constraints, which should be so insignificant that the substrate can actually represent a half-space; the other is the effect of stress wave which is unavoidable in physical impacts and depends very much upon the number of reflection of stress wave during the impact.

In summary, for the impact of an elastic sphere with an elastic substrate, the substrate of dimension $L = 10R$ is sufficiently large to eliminate the effect of the constrained boundary but the effect of the stress wave becomes significant at high velocities. And the substrate of size $L = R$ is only suitable for simulating the impact with low impact velocities. The substrate of $L = 2R$ is large enough to minimise the effect of the boundary constraints, and the effect of stress waves propagation is negligible. It has been shown that for the impact of an elastic sphere with an elastic-perfectly plastic substrate the substrate of size $L = 2R$ is also large enough to eliminate the effect of the boundary constraints, in addition, the energy dissipation due to stress waves is negligible over a wide range of impact velocities regardless of the substrate size.

Therefore it is suggested that, for all the impact velocities considered in this study, the substrate of size $L = 2R$ is large enough to eliminate the effect of the constrained boundary and the energy loss due to stress wave could also be ignored for both elastic and plastic impacts. It is thus used to investigate the impact over the velocity range considered in this study.

Appendix C Significance of the Substrate Size in FE Simulations of the Oblique Impact of a Sphere with a Half-Space

In order to examine if the size of the substrate used in the FE model for simulating the oblique impact of a sphere with a half-space (see Fig. 3.10) is large enough to eliminate the effect of the boundary constraints, an alternative FE model with a large substrate is constructed. The FE model is shown in Fig. C.1. The sphere, again, is of a radius $R = 10\mu\text{m}$. The spherical substrate is selected as $60\mu\text{m}$ in diameter, so $d/R = 6$. Because of geometrical and loading symmetries, only half of the model is meshed, and the mesh consists of 17,578 eight-node solid elements with 18,984 nodes in the sphere and 23,130 elements with 25,272 nodes in the substrate. Fine mesh is used in the vicinity of initial contact point in order to accurately describe the localised deformation. Nodes on the symmetry plane ($x=0$) are restricted in the x -direction. Nodes on outer boundary of the substrate are fixed.

The oblique impacts of a rigid sphere with an elastic substrate at various impact angles are simulated using two models shown in Fig. 3.10 ($L/R=1$) and Fig. C.1 ($d/R=6$), respectively. The sphere is assumed to be rigid and the substrate to be elastic with material constants shown in Table 3.5. The static and dynamic friction coefficients are assumed to be identical and remains constant at $\mu = 0.3$. The different impact angles are specified by keeping the initial normal velocity constant of $V_{ni} = 5.0\text{m/s}$. The results are shown in Figs. C.2-C.6. From these results, it is clear that the simulations using two different models produce the nearly identical results. Therefore, it may be concluded that further increase of the size of the substrate does not produce any change in the results, and the size of substrate selected in Section 3.4 should be large enough to eliminate the effect of the boundary constraints.

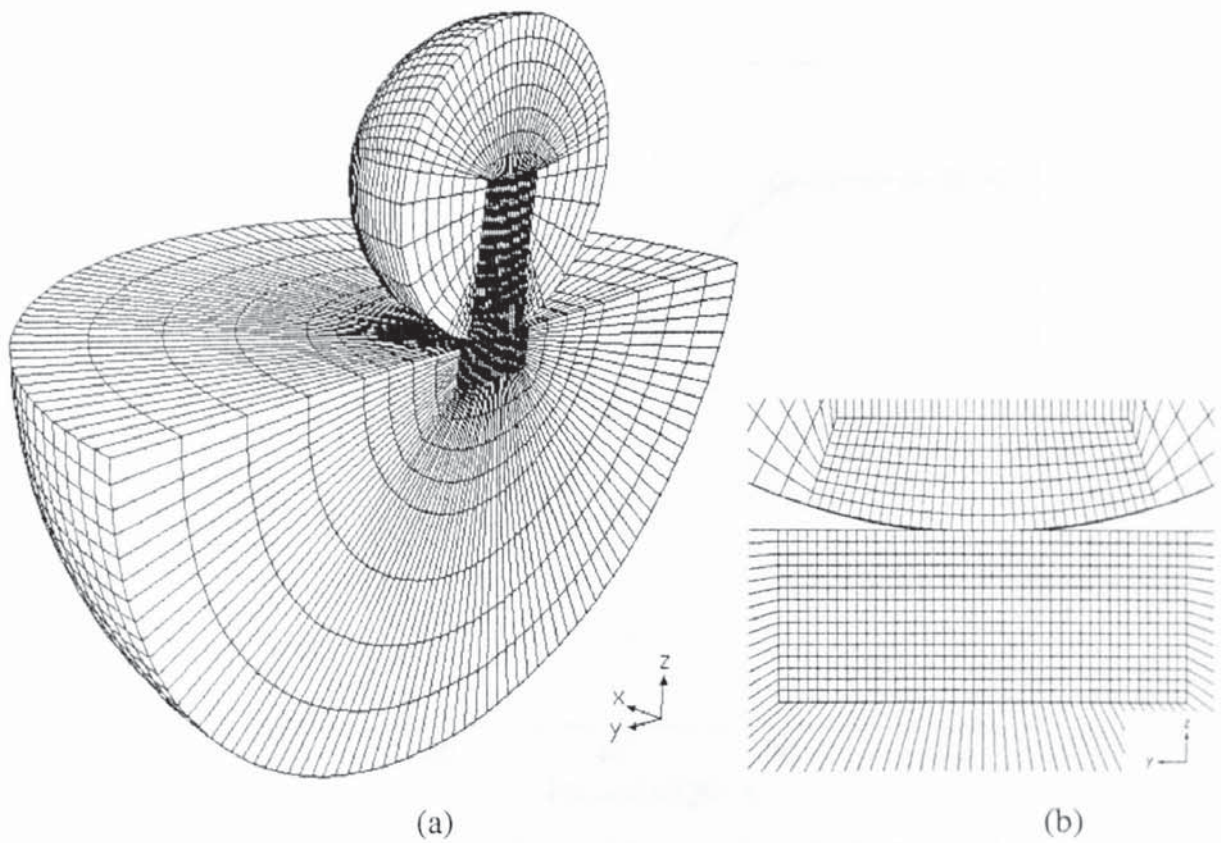


Fig. C.1 Finite element model with a large substrate ($d/r=6$): (a) the whole model; (b) a close view of the meshes in the contact region.

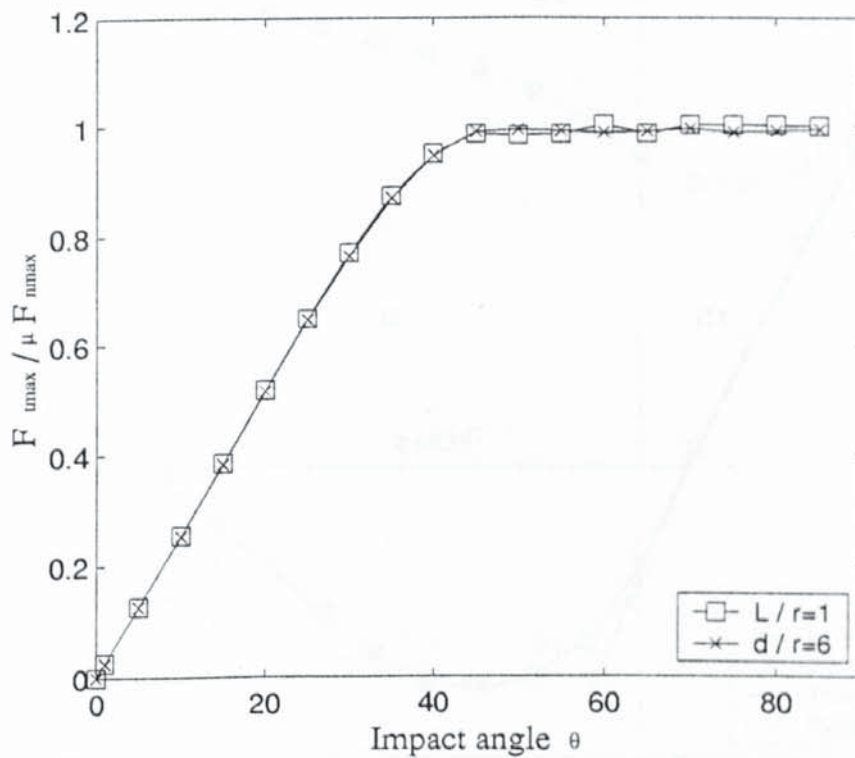


Fig. C.2 The variation of $F_{i,max} / \mu F_{n,max}$ with impact angle θ obtained using two different FE models.

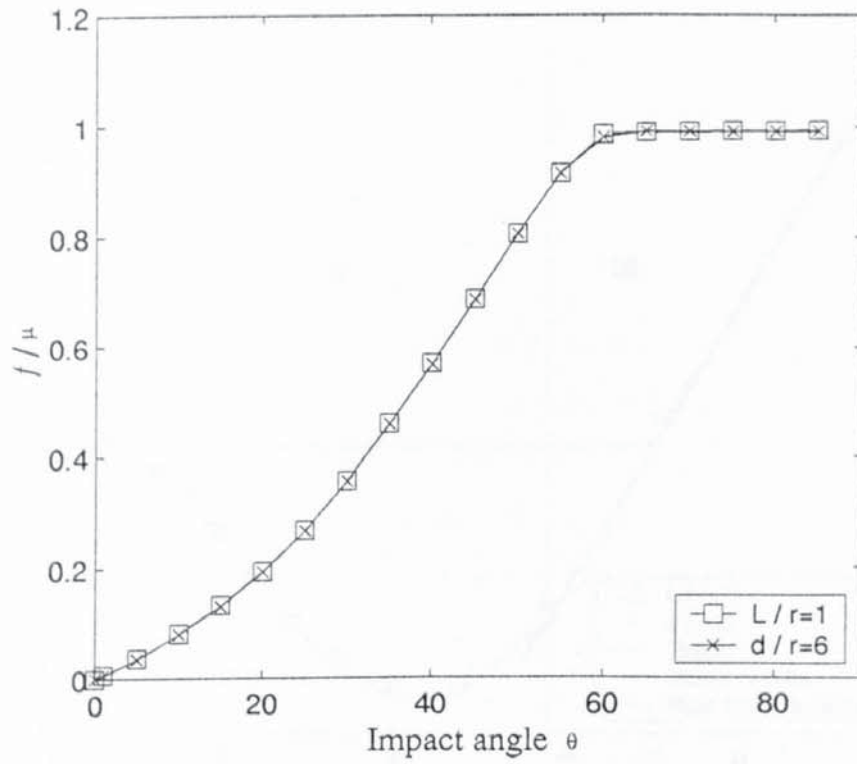


Fig. C.3 The variation of f/μ with impact angle θ obtained using two different FE models.

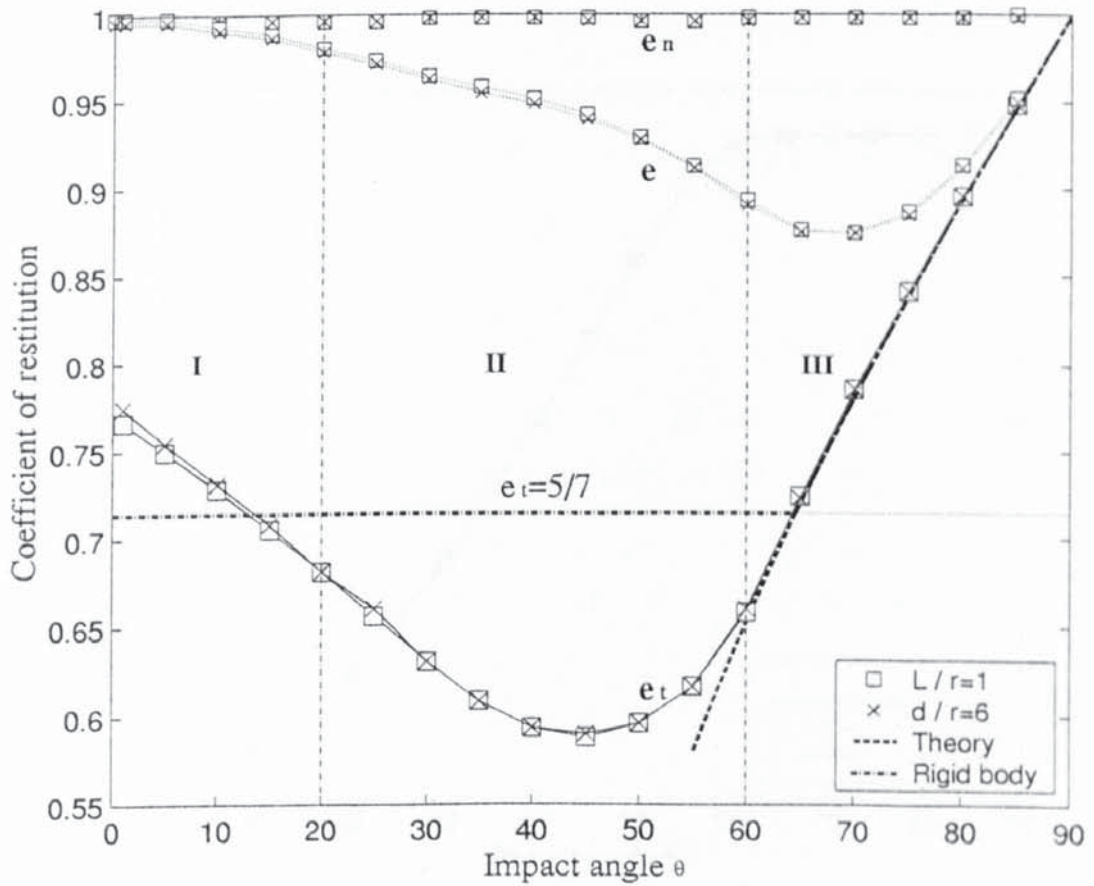


Fig. C.4 The coefficients of restitution at various impact angles obtained using two different FE models.

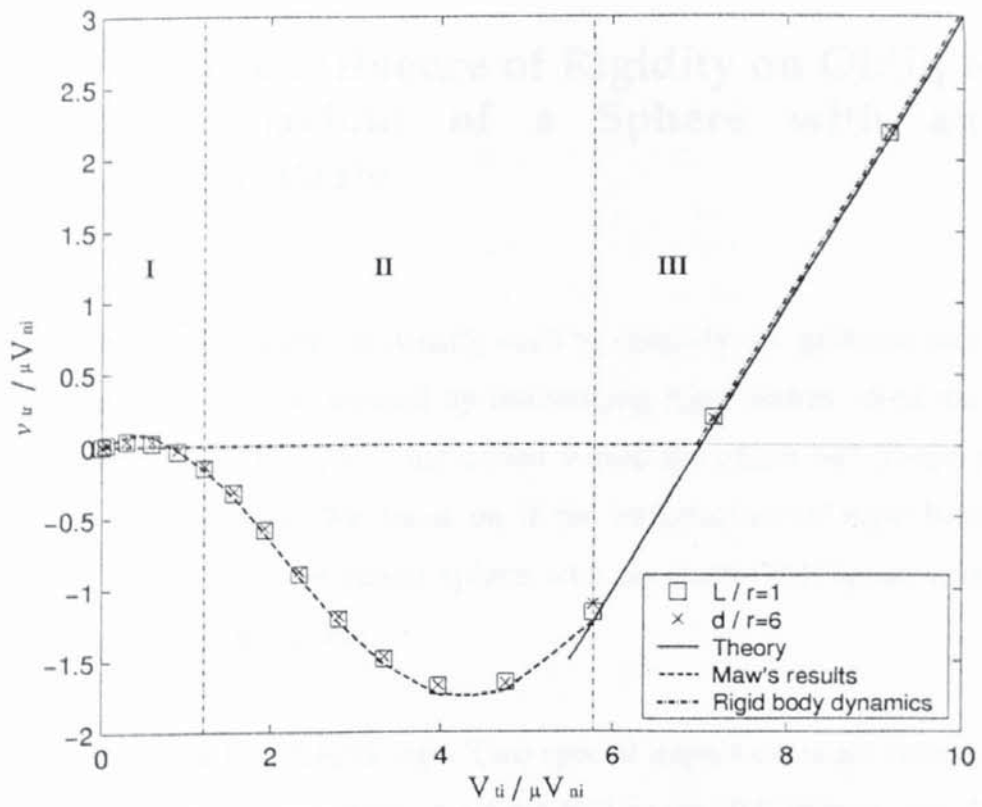


Fig. C.5 The variation of the normalised reflection angle at the contact patch with normalised impact angle obtained using two different FE models.

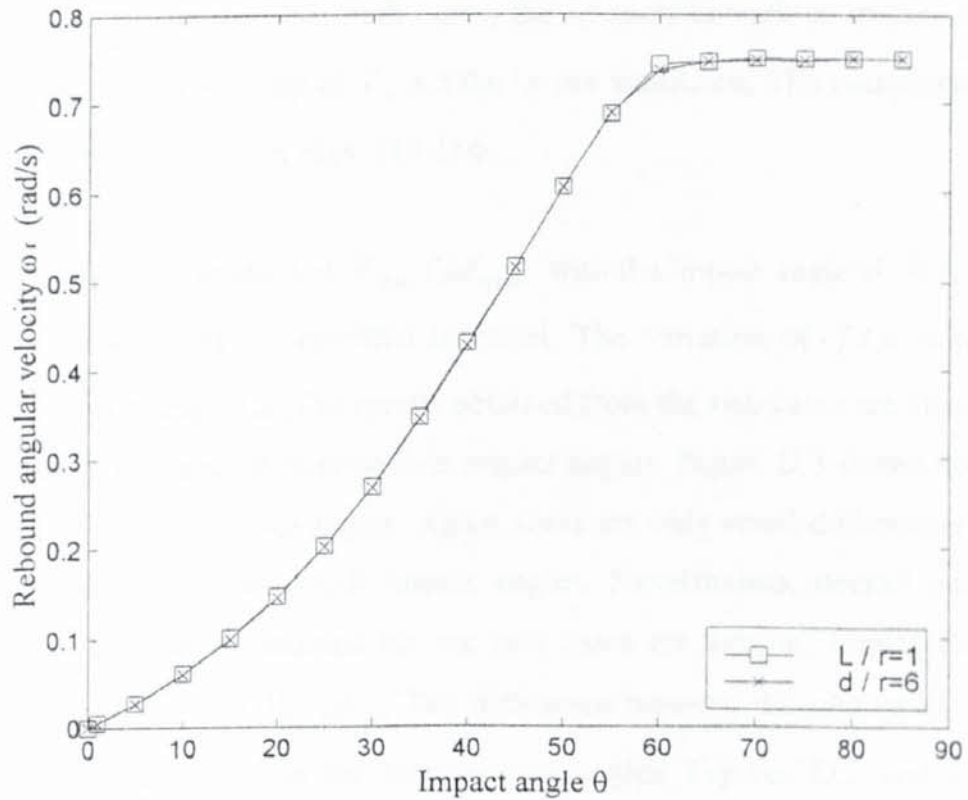


Fig. C.6 The rebound angular velocities at various impact angles obtained using two different FE models.

Appendix D The Influence of Rigidity on Oblique Impact Behaviour of a Sphere with an Elastic Substrate

In FE simulations, rigid bodies are usually used to simplify the problem and speedup the calculation. Questions may be aroused by introducing rigid bodies: does the use of rigid bodies affect the results? If so, to what extent would the effect be? These problems are investigated in this appendix. We focus on if the introduction of rigid body affects the oblique impact behaviour of an elastic sphere with an elastic half-space when the elastic sphere is replaced by a rigid sphere.

The FE model shown in Fig. 3.10 is used. Two special impact cases are investigated: one is for the impact of a rigid sphere with an elastic half-space (RE impact, see Table 3.4), as reported in Chapter 7 in more details, and the other is for the impact of an elastic sphere with the elastic half-space (EE impact). The elastic constants for these materials are shown in Table 3.5. The static and dynamic friction coefficients are assumed to be identical and remain constant at $\mu = 0.3$. For both cases, the impacts at various impact angles with a constant initial normal velocity of $V_{ni} = 5.0 \text{ m/s}$ are simulated. The comparisons of results for the two cases are shown in Figs. D.1-D.6.

Figure D.1 shows the variation of $F_{t \max} / \mu F_{n \max}$ with the impact angle θ . It is clear that the results for the two cases are essential identical. The variation of f / μ with the impact angle θ is shown in Fig. D.2. The results obtained from the two cases are close, except that there are small differences at intermediate impact angles. Figure D.3 shows the coefficients of restitution at various impact angles. Again, there are only small differences in tangential coefficient of restitution for small impact angles. Nevertheless, overall patterns for all coefficients of restitution obtained for the two cases are similar. Figure D.4 shows the variation of $v_{tr} / \mu V_{ni}$ with $V_{ti} / \mu V_{ni}$. The difference between the two cases is very small and is mainly concentrated in the intermediate angles. Figures D.5 and D.6 show the rebound angular velocities for the two cases. It is clear that the two cases give the similar rebound angular velocities.

Therefore, it is clear from Figs. D.1-D.6 that similar patterns are obtained for both EE and RE impacts. This implies that the use of a rigid sphere instead of an elastic one does not affect the overall behaviour of elastic oblique impacts. It is concluded the effect of rigidity on the oblique impact behaviour seems to be only marginal.

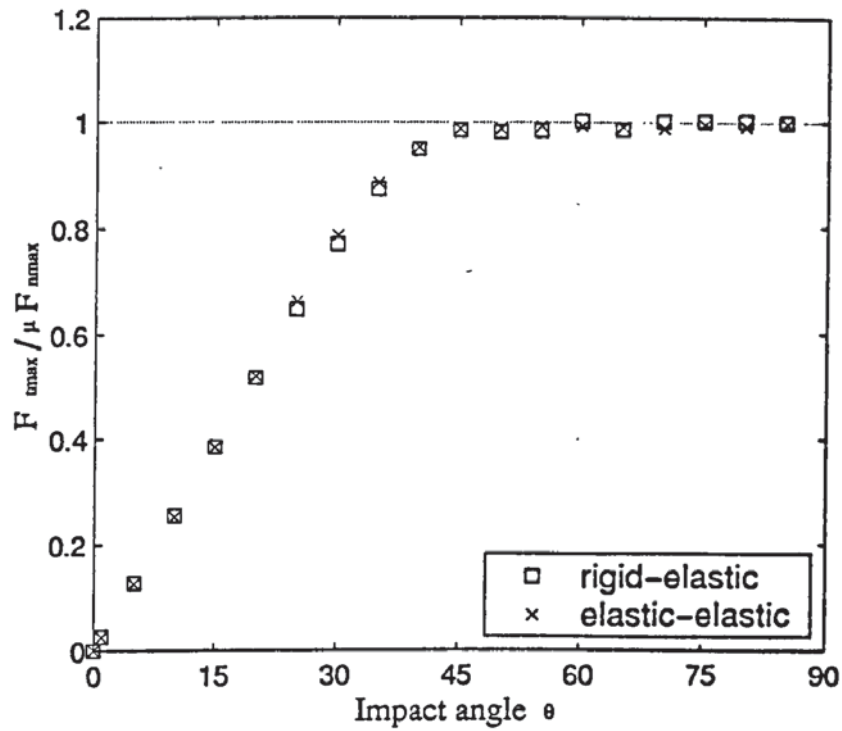


Fig. D.1 The variation of $F_{tmax} / \mu F_{nmax}$ with impact angle θ for different impact cases.

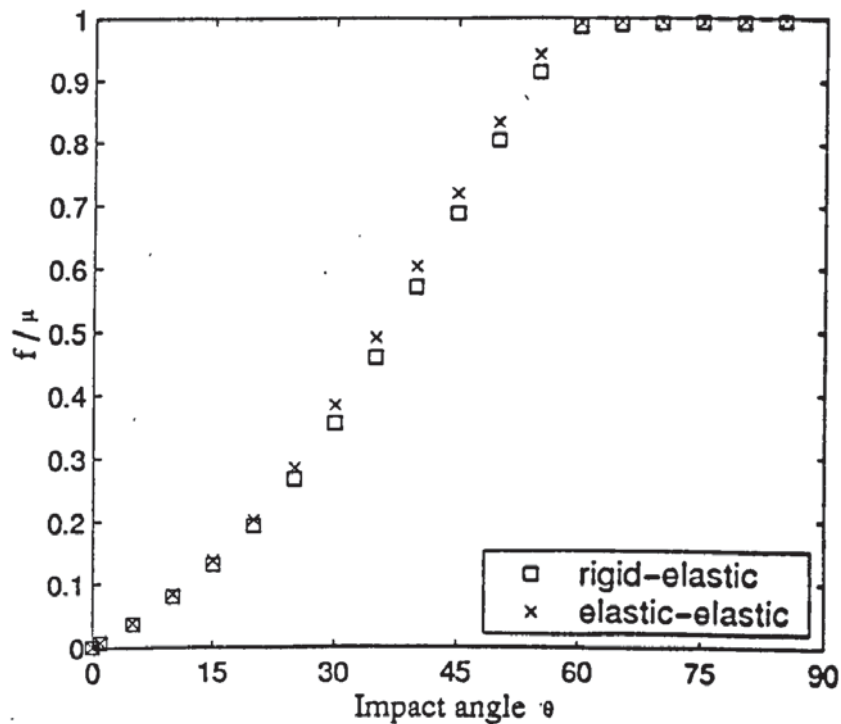


Fig. D.2 The variation of normalised impulse ratio f / μ with impact angle θ for different impact cases.

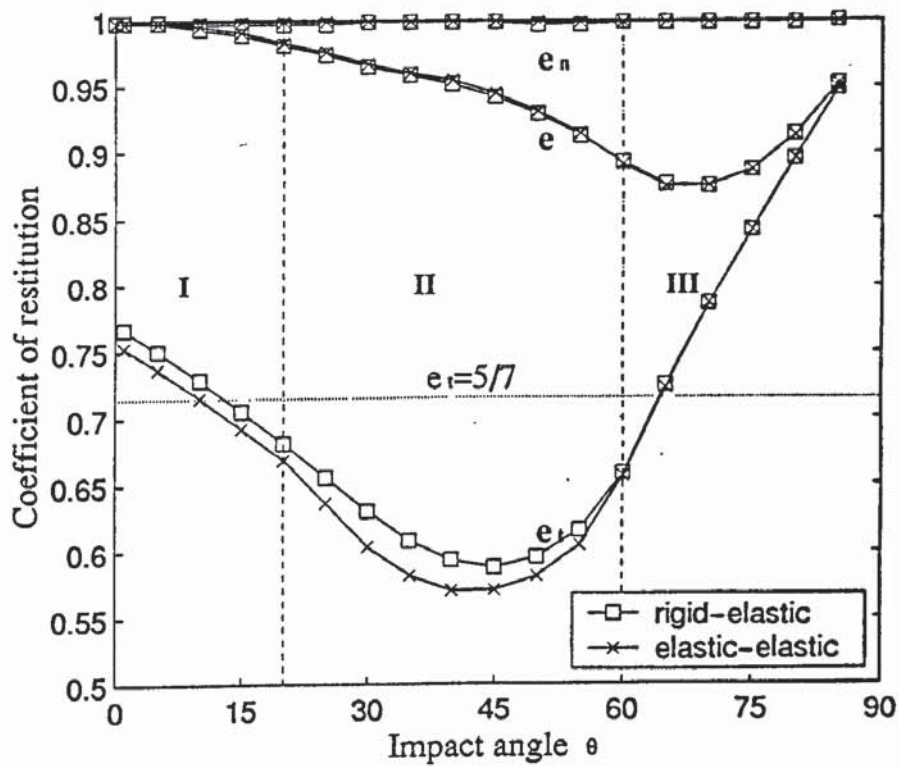


Fig. D.3 The coefficients of restitution at various impact angles for different impact cases.

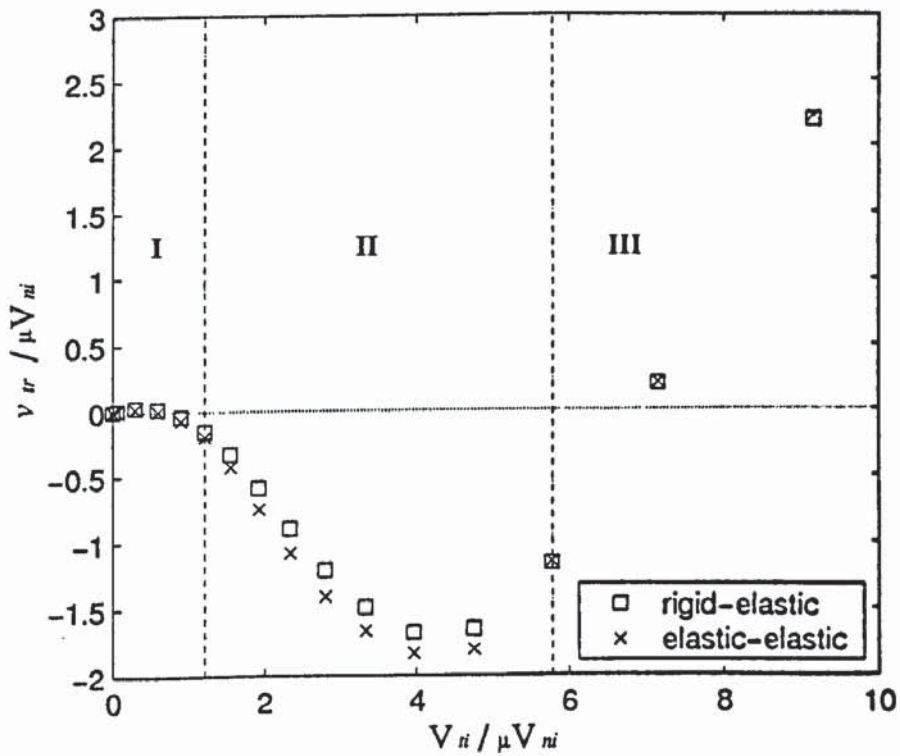


Fig. D.4 The variation of normalised reflection angle of the contact patch $v_{tr} / \mu V_{ni}$ with normalised impact angle $V_{ni} / \mu V_{ni}$ for different impact cases.

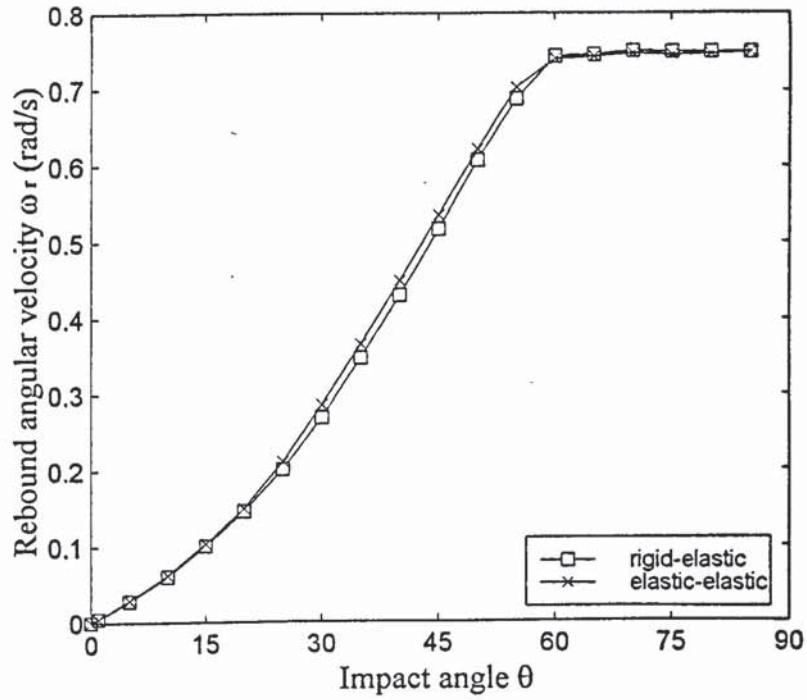


Fig. D.5 The rebound angular velocities at various impact angles for different impact cases.

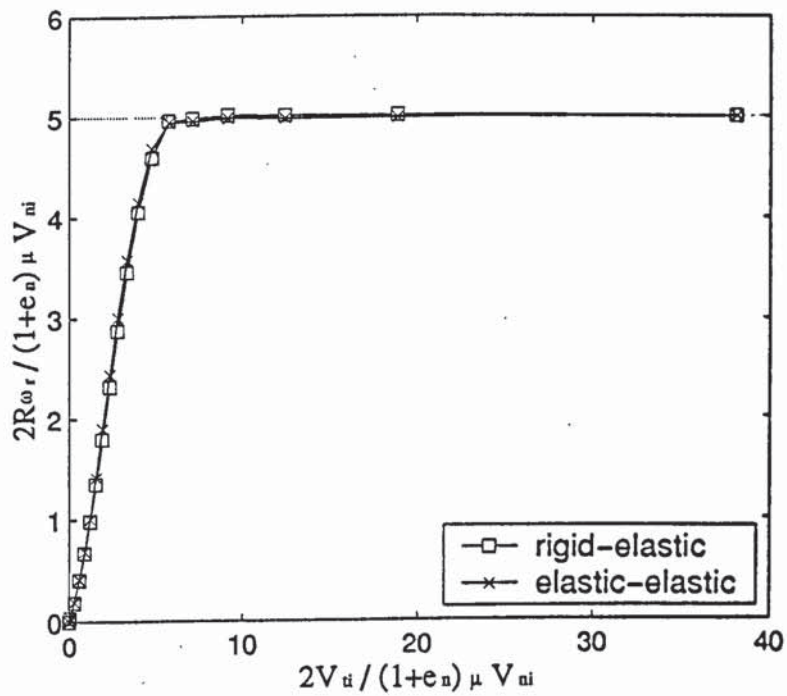


Fig. D.6 The normalized rebound angular velocity versus the normalized impact angles for different impact cases.